

# **Communications Demonstrations for Optical Ground Stations**

Skevos F. E. Karpathakis

*BSc, MEng, W.Aust.*



This thesis is presented for the degree of  
Doctor of Philosophy  
of The University of Western Australia

International Centre for Radio Astronomy Research

2024



*Resistant to advice,  
measure once, cut twice.*



## Thesis Declaration

I, Skevos Karpathakis, certify that:

This thesis has been substantially accomplished during enrolment in this degree.

The thesis is my own work and does not contain any material previously published or written by another person, except where due reference has been made in the text or Authorship Declaration.

This thesis does not contain material which has been submitted for the award of any other degree or diploma in my name, in any university or other tertiary institution.

In the future, no part of this thesis will be used in a submission in my name, for any other degree or diploma in any university or other tertiary institution without the prior approval of The University of Western Australia and where applicable, any partner institution responsible for the joint-award of this degree.

This thesis does not violate or infringe on any copyright, trademark, patent, or other rights whatsoever of any person.

SIGNED: .....  
DATE: .....  
*Skevos Karpathakis*  
*29/2/2024*



## Declaration of Contribution to Published Work

This thesis contains work that has been published in peer-reviewed journals. The details of these articles are described below, including a note describing the level of the author's contribution to the work described and the manuscript produced:

### **Atmospheric Turbulence Characterization with Simultaneous Measurement of Phase, Angle of Arrival, and Intensity in a Retroreflected Optical Link [1]**

*Benjamin P. Dix-Matthews, Skevos F.E. Karpathakis, Sascha W. Schediwy*

*Optics Letters, 48(21), 5519–5522 (2023), doi:[10.1364/OL.501346](https://doi.org/10.1364/OL.501346)*

**Chapter:** 3

**Contribution:** Experimental work - 40%, Manuscript preparation - 80%

### **High-bandwidth Coherent Optical Communication over 10.3 km of Turbulent Air [2]**

*Skevos F.E. Karpathakis, Benjamin P. Dix-Matthews, David R. Gozzard, Sascha W. Schediwy*

*Applied Optics, 62(23), G85-G89 (2023), doi:[10.1364/AO.491440](https://doi.org/10.1364/AO.491440)*

**Chapter:** 4

**Contribution:** Experimental work - 80%, Manuscript preparation - 90%

### **Demonstration of 100 Gbps Coherent Free-Space Optical Communications at LEO Tracking Rates [3]**

*Shane M. Walsh, Skevos F.E. Karpathakis, Ayden S. McCann, Benjamin P. Dix-Matthews, Alex M. Frost, David R. Gozzard, Charles T. Gravestock, Sascha W. Schediwy*

*Scientific Reports, 12, 18345 (2022), doi:[10.1038/s41598-022-22027-0](https://doi.org/10.1038/s41598-022-22027-0)*

**Chapter:** 5

**Contribution:** Experimental work - 30%, Manuscript preparation - 50%

DECLARATION OF CONTRIBUTION TO PUBLISHED WORK

---

**Ground-to-Drone Optical Pulse Position Modulation Demonstration as a Testbed for Lunar Communications [4]**

*Skevos F.E. Karpathakis, Benjamin P. Dix-Matthews, Shane M. Walsh, Ayden S. McCann, David R. Gozzard, Alex M. Frost, Charles T. Gravestock, Sascha W. Schediwy*  
*Drones, 7, 99 (2023), doi:10.3390/drones7020099*

**Chapter: 6**

**Contribution:** Experimental work - 50%, Manuscript preparation - 90%

I, Skevos F.E. Karpathakis, confirm that these proportional contributions are truthful and correct, and that permissions from all co-authors has been sought to allow publication of these works in this thesis.

SIGNED:  DATE: 27/2/24

I, Sascha W. Schediwy, certify that the student statements regarding their contribution to each of the works listed above are correct.

SIGNED:  DATE: 2024-02-27

We, as co-authors on one or more of these published works, endorse the students declaration and authorise inclusion of our co-authored work in their thesis.

Benjamin P. Dix-Matthews:		DATE: 27/02/2024
David R. Gozzard:		DATE: 27/02/2024
Shane M. Walsh:		DATE: 27/2/2024
Ayden S. McCann:		DATE: 29/02/2024
Alex M. Frost:		DATE: 27/02/2024
Charles T. Gravestock:		DATE: 27/02/2024

## Acknowledgements

This thesis was mostly written at The University of Western Australia’s Crawley campus on the banks of the Derbarl Yerrigan, on Whajduk Noongar land.

I have had a tremendously rewarding three years undertaking this PhD project and am extremely lucky to be able to get this thesis submitted ‘on time and under budget.’ Thanks should begin with my supervision team: Sascha Schediwy, David Gozzard, Gottfried Lechner, and Brett Nener. I greatly appreciate the vote of confidence these gentlemen provided by endorsing my PhD scholarship application with the SmartSat Cooperative Research Centre. Sascha, in particular, has opened so many doors for me; through this project and a previous appointment working on the Square Kilometre Array. Sascha has always been available to chat strategy and has shown me how to effectively execute projects. David has also been an enthusiastic advocate for my professional development, willing to talk through an array of technical problems beyond his comfort zone. Thanks also to Michael Clark from Thales Australia for his instructive guidance as an industry representative.

This thesis reports on a body of work undertaken within a tight-knit research and development team. As such, I must thank my colleagues working on free-space optical transmission. Ben Dix-Matthews has been a long-time friend and I have enjoyed our chats, spanning microwaves to macroeconomics. Thanks Alex Frost, for your infectious good attitude, Ayden McCann, for your inspirational work ethic, and Shane Walsh, for your creativity. Thanks Shawn McSorley for coaching in mathematics and the overhead press. Good luck to John Wallis and Josh Collier on their candidatures this year. Bonne chance also to my friend Nicolas Maron on his Australian adventure.

My research career began with the SKA, for which I owe Charles Gravestock many thanks. Charles did me a very good turn getting me into the research group at a time when I was fairly directionless. Together with Mike, Ed, Neethu, and Eric, they have a considerable task ahead of them (and an ngVLA follow-on!).

I am grateful for the friends and connections I made in the UWA Motorsport team. Without my UWAM experiences I would not have been a suitable candidate for this project. I would like to thank Alan Landman, Andre Van Vulpen, Andrew Parry, Ben Riley, Claudio Pizzirani, Dominik Ginter, Dylan Postans, Harley Olsthoorn, Henry Zhu, Jack Fischer, Lindsay Wood, Luke Di Dio, Mattison McGellin, Dirk Blom, Nicola Haste, Nick Favazzo, Praveen Sundaram, Peter Baskovich, Ryan Pallas, Sam Neilson, and Sam Turnbull. This list is not exhaustive! I must also thank Angus Tavner, as well as the faculty leadership team that provided crucial financial support to the team in 2017.

## ACKNOWLEDGEMENTS

---

Outside of the office, I am grateful to my parents, Judith and George, for supporting me throughout my education. In particular thanks to Mum for letting me post up in my childhood room over these last six months to complete my thesis. I also love and miss my sister, Cassandra and her husband, Patrick, who live far away, in a different city every year. They have been extremely generous in putting me up in fantastic places all over the world.

For over two years, I had an excellent rotation of housemates at Grosvenor Road. Thanks to Gaby O'Connor for her infinite understanding, James Royer for many missions, Simon Stobie for being very much like me, Anna Taleb-Bendiab for book chats, and Luca Ighina for feeling like an old friend. Thanks also Rhian Pearce, who spent a lot of time at Grosvenor, for deep chats and jogs.

I would also like to thank the following people for giving me reasons to leave the house. Nathan Giacci, Henri Crisp, Francis Follis, Johnny Perrone, Anjali Epanomitis, and Rachel Hao for good times in the inner North. Aimee Dodds and Sam Beard for making sure I attended all the right gallery openings. Miette Xamon and Manon Stoate for seeing all those French films with me. Alex O'Neil, Allan Williams, Chris Argile, Joel O'Mara, Michael Mayall, Angus Pyle, and Daniel Zampin for banter. Hoo. Michael Barblett, Peter Watson, and Jacob Colangelo for burgers and beers. Lucas Testar for the above but also for staying in Perth. Geordie Wilson for visiting Perth quite often. Julian Bocking for giving me a reason to visit Canberra. Nathan Batskos for sharing his unique perspectives with me. Mary Pensabene for staying in touch and lunch on Staten Island. Niall Smiles and Cathy Anderson for discussions about bike parts over biscuits. Matt Clark-Massera for his well-equipped garage well-considered opinions. Bliss Brosnan for her unbounded enthusiasm and know-how. Bruno Santarelli and Rob van Dieren for wisdom in all matters non-technical. Clive Reynoldson, Rob Harvey, Steve Drown, Arshad Omari, and Bruno (again!) for bike rides to Fremantle and coffee. Chelsea Somerville for walks in Hyde Park and plenty of tea.

This work has been supported by the SmartSat CRC, whose activities are funded by the Australian Government's CRC Program. I was the recipient of a SmartSat Cooperative Research Centre PhD scholarship and benefited from invitations to conferences, webinars, and other opportunities to present my research. This research is supported by an Australian Government Research Training Program (RTP) Scholarship. I would like to thank The Andy Thomas Space Foundation and EOS Space Systems for the generous provision of a research award in 2021. Thanks too, to the ICRAR board, for awarding me the Ken and Julie Michael Prize in 2023.

Finally, I want to thank Matt Christou for always being willing to share his experiences and for the push towards my next set of challenges below sea level.

## Summary

Earth's orbits are becoming increasingly crowded by new constellations of satellites with constantly improving sensors, which drives fierce competition for space communications bandwidth. The research undertaken in this thesis addresses this growing demand for space communications bandwidth, by developing new methods for commissioning optical communications ground stations. Space communications currently rely on free-space signals in the radio-frequency part of the electromagnetic spectrum. However, radio-frequency bandwidth is not keeping pace with the growing number of satellites and advancements in Earth observation sensor technologies. Additionally, radio-frequency signal beams diverge significantly on space-ground scales, thereby leading to overlapping interference, spectrum crowding, and a reduction in power efficiency. Free-space optical signals promise three-orders-of-magnitude of bandwidth increase and three-orders-of-magnitude reduced divergence, effectively eliminating spectrum crowding and enhancing their power efficiency over radio frequency signals. Optical ground stations on Earth will provide a point of contact for spacecraft equipped with free-space optical communications terminals. New optical ground stations require methods for testing and commissioning.

The current availability of spacecraft with optical communications terminals is extremely low. Therefore, accessible spacecraft proxies are extremely valuable to accelerate testing and development of the systems comprising the optical ground station. This thesis documents methods for demonstrating and commissioning optical ground station hardware, and also shows the conditions for translating commercial-off-the-shelf fibre communications equipment to the free-space domain. The following work towards this goal, and outcomes, are described herein:

- Simultaneous measurements of phase noise, angle-of-arrival variation, and intensity scintillation were taken on a retroreflected, or 'folded' link, established with a corner-cube retroreflector. Analytical models were formed to relate retroreflected links to point-to-point links. Comparing the experiment with the models validates the subsequent use of folded links for free-space optical communications experiments.
- Demonstration of 100 Gb/s coherent free-space optical communications over a 10.3 km retroreflected link. This was conducted on 52 wavelength-division multiplexing channels, demonstrating the extremely high bandwidth available to coherent free-space optical communications. No atmospheric stabilisation was used, showing the absolute limits of intensity scintillation compatible with commercial-off-the-shelf fibre networking equipment.

## SUMMARY

---

- Demonstration of 100 Gb/s coherent free-space optical communications to a drone carrying a corner-cube retroreflector. The drone was flown across the sky, requiring a prototype of an optical ground station to track the drone at angular rates equivalent to, or exceeding, the angular tracking rates required to maintain contact with a satellite in low-Earth orbit.
- Demonstration of high photon efficiency free-space optical communications to a drone-borne retroreflector. This demonstration provides a methodology for ground station operators to test their prototype systems for future lunar and deep-space missions.

These contributions advance knowledge in retroreflected free-space optical links and provide a roadmap for those who wish to test and commission their own optical communications ground stations.

## Contents

Declaration of Contribution to Published Work . . . . .	v
Acknowledgements . . . . .	vii
Summary . . . . .	ix
List of Figures . . . . .	xv
List of Tables . . . . .	xxi
List of Abbreviations . . . . .	xxiii
<b>1 Introduction</b>	<b>1</b>
1.1 History of Communications . . . . .	2
1.2 Space Communications . . . . .	4
1.3 Optical Ground Stations . . . . .	8
1.4 Thesis Outline . . . . .	11
<b>2 Technical Background</b>	<b>13</b>
2.1 Optical Communications . . . . .	15
2.2 Atmospheric Optical Communications . . . . .	23
2.3 Laser Safety . . . . .	32
<b>3 Atmospheric Turbulence Characterization in a Retroreflected Optical Link</b>	<b>35</b>
3.1 Abstract . . . . .	37
3.2 Introduction . . . . .	37
3.3 Materials and Methods . . . . .	38
3.4 Phase Noise . . . . .	39
3.5 Angle-of-Arrival Variation . . . . .	42
3.6 Scintillometry . . . . .	44
<b>4 High-Bandwidth Coherent Optical Communications Over 10.3 km of Turbulent Air</b>	<b>47</b>
4.1 Abstract . . . . .	49
4.2 Introduction . . . . .	49
4.3 Methods . . . . .	51
4.4 Results . . . . .	54
4.5 Discussion . . . . .	55
4.6 Conclusion . . . . .	56

## CONTENTS

---

<b>5</b>	<b>Coherent Free-Space Optical Communications at LEO Tracking Rates</b>	<b>59</b>
5.1	Abstract . . . . .	61
5.2	Introduction . . . . .	61
5.3	Methods . . . . .	64
5.4	Results and Discussion . . . . .	71
5.5	Conclusion . . . . .	77
<b>6</b>	<b>Ground-to-Drone Optical Pulse Position Modulation Demonstration as a Testbed for Lunar Communications</b>	<b>79</b>
6.1	Abstract . . . . .	81
6.2	Introduction . . . . .	81
6.3	Materials and Methods . . . . .	83
6.4	Results . . . . .	88
6.5	Discussion and Conclusion . . . . .	89
<b>7</b>	<b>Conclusion</b>	<b>91</b>
7.1	Summary of Work . . . . .	91
7.2	Significance of the Work . . . . .	92
7.3	Limitations of the Work . . . . .	93
7.4	Future Work . . . . .	95
7.5	Concluding Remarks . . . . .	98
	<b>References</b>	<b>99</b>
<b>A</b>	<b>Supplementary Material: Chapter 2</b>	<b>119</b>
A.1	Binary Representation of Information . . . . .	119
A.2	Amplitude Modulation . . . . .	121
A.3	Coherent Modulation . . . . .	122
A.4	Representative Link Budgets . . . . .	124
<b>B</b>	<b>Supplementary Material: Chapter 4</b>	<b>127</b>
B.1	Space Communication . . . . .	127
B.2	Results by Wavelength . . . . .	129
<b>C</b>	<b>Supplementary Material: Published Work</b>	<b>133</b>
C.1	Atmospheric Turbulence Characterization with Simultaneous Measurement of Phase, Angle of Arrival, and Intensity in a Retroreflected Optical Link . . .	135

C.2 High-Bandwidth Coherent Optical Communication over 10.3 km of Turbulent Air . . . . .	139
C.3 Demonstration of 100 Gbps Coherent Free-Space Optical Communications at LEO Tracking Rates . . . . .	144
C.4 Ground-to-Drone Optical Pulse Position Modulation Demonstration as a Testbed for Lunar Communications . . . . .	156



## List of Figures

1.1	Illustrations of three space mission scenarios pertinent to free-space optical communications: (a) geostationary telecommunications satellite acting as a relay to connect gaps in a terrestrial network, (b) Earth observation satellite in low-Earth orbit observing an area at one time, and communicating with a ground station at a later time, and (c) spacecraft in deep space communicating with a ground station on Earth. . . . .	5
2.1	Prototypical digital communication system using carrier modulation. . . . .	15
2.2	Schematic for a bit-error rate tester using a pseudo-random binary sequence (PRBS) generator and checker. . . . .	16
2.3	A communication system using amplitude modulation. The electrical message signal, $m(t)$ , is modulated onto the optical frequency signal, resulting in the amplitude-modulated signal $s_{AM}(t)$ . . . . .	17
2.4	Comparison of time-series for baseband symbols in (a) optical on-off keying and (b) pulse position modulation with four slots. . . . .	18
2.5	Graph showing the speed and photon efficiency scaling of a pulse-position modulation (PPM) system compared to an optical on-off keying (OOK) system. . . . .	19
2.6	Constellation diagrams for quadrature phase-shift keying with: (a) 15 dB signal-to-noise ratio (SNR) and (c) 9 dB SNR; (b) 16-quadrature amplitude modulation with 15 dB SNR and (d) 9 dB SNR. . . . .	21
2.7	A free-space optical link, with link budget gain and loss terms. $P_{tx}$ : fibre transmit power, $L_{imp}$ , implementation losses, $G_{tx}$ : transmitter telescope gain, $L_{fs}$ : isotropic free-space loss, $G_{rx}$ : receiver telescope gain, $L_{cpl}$ : fibre coupling loss, $P_{rx}$ : received power. . . . .	22
2.8	Illustration showing atmospheric turbulence structure with respect to a horizontal free-space optical transmitter. . . . .	24
2.9	Refractive index power spectral density (PSD), $\Phi_n$ , as a function of wavenumber, $\kappa$ , for the Kolmogorov and Greenwood-Tarazano models for refractive index structure, with fixed structure constant, $C_n^2$ . The Kolmogorov model is only defined between the wavenumbers corresponding to outer scale, $L_0$ , and inner scale, $l_0$ (not indicated). In the Greenwood-Tarazano model, the PSD is defined below $L_0$ . . . . .	25

LIST OF FIGURES

---

2.10 Graph showing the refractive index structure constant,  $C_n^2$ , versus height-above-ground,  $h$ . This is based on the Hufnagel-Valley 5/7 model, assuming a wind-speed of 21 m/s, and  $C_n^2$  of  $1.7 \times 10^{-14} \text{m}^{-2/3}$  at ground level. . . . . 26

2.11 Illustration of atmospheric channel for free-space optical communications in uplink, using an auxiliary aperture and downlink, receiving with the full-sized telescope aperture. . . . . 28

2.12 First order adaptive optics, or tip-tilt, system diagram illustrating the feedback connection between the quadrant photodetector and fast-steering mirror. Proportional-integral-derivative (PID) controllers are used to filter the quadrant photodetector signals. The system aids in pointing to the free-space-to-fibre coupler (FFC). . . . . 31

3.1 Apparatus for measuring phase noise, angle-of-arrival variation and scintillation. AOM: acousto-optic modulator, CCR: corner-cube retroreflector, PM: phase meter. . . . . 39

3.2 Phase noise power spectral densities for three measurement runs. Two analytical models are fitted to the low turbulence measurement (blue) in the region labelled **a**. The solid black line is the Kolmogorov spectrum model. The dashed black link is the Greenwood-Tarazano spectrum model. In the region labelled **b**, inflections due to outer scale effects are seen for the low and medium measurements. The dash-dot line follows a  $f^{-17/3}$  slope expected due to aperture averaging. . . . . 41

3.3 Angle-of-arrival power spectral densities for three measurement runs. Fitted dashed lines are provided for each run, showing  $f^{-2/3}$  slopes predicted by the Kolmogorov model. . . . . 43

3.4 Rolling measurement of turbulent structure constant,  $C_n^2$ , based on 100s samples of phase, angle-of-arrival and intensity measurements. Three separate measurements are given in (a) low, (b) medium, and (c) high turbulence. Error bars indicate the 90% confidence intervals for each parameter. For phase this is  $\pm 1.645\sigma$  calculated from the variance of the fit parameter. The angle-of-arrival and log-amplitude estimates depend on sub-sample variance,  $s^2$ , the value of which is bounded by  $\left[ s^2 \frac{N}{\chi^2(0.95,N)}, s^2 \frac{N}{\chi^2(0.05,N)} \right]$  where  $N$  is the number of independent samples, here defined as  $\frac{N_{total}}{2n_c}$ , where  $N_{total}$  is the total number of sub-samples and  $n_c$  is the time taken, in samples, for the autocorrelation to drop below  $e^{-2}$ . . . . . 45

4.1	Optical transceiver and terminal schematic for demonstration. BS: beam splitter, CCR: corner cube retro-reflector, DAQ: data acquisition, DCO: digital coherent optical module, EDFA: erbium-doped fibre amplifier, FFC: free-space to fibre collimator, FS PD: free-space photodetector, GBE: Galilean beam expander, PD: photodetector, PRBS: pseudo-random binary sequence. . . . .	51
4.2	Per optical wavelength, during low turbulence, measurements of ( <i>from top to bottom</i> ) scintillation index, mean single-mode fibre (SMF) coupling, wind-speed and direction, and proportions of lost, high bit-error rate (BER) and low BER transmissions. Wind-speed and direction recorded at Perth Airport, downward arrows point South, parallel to the transmission. . . . .	55
4.3	Measurements during low turbulence. Scatterplot of low bit-error rate (BER) transmission percentage and single-mode fibre (SMF) coupling versus scintillation index. . . . .	56
5.1	Schematic of the deployable optical terminal and experiment. Mon. PD: monitoring photodetector; FFC: fibre to free-space collimator; QPD: quadrant photodetector; CCR: corner-cube retroreflector; LED: light emitting diode; LoRa: ‘Long Range’ radio communication format; Tx: transmitter; Rx: receiver. .	64
5.2	<i>Left:</i> The optical breadboard layout. MV: Machine vision lens and camera; TTM: tip-tilt mirror; LM: static launch mirror; GBE: Galilean beam expander; QPD: quadrant photodetector; SBC: single board computer; PD: photodetector; BS: beam splitter. <i>Right:</i> The deployed optical terminal. Optics and MV are located on the far side of the breadboard. The TTM control electronics are visible on the lower left of the mount base. The telescope mounted on the left was not used for this experiment. . . . .	65
5.3	Block diagram showing interfaces between components during initial acquisition (blue) and continuous tracking (red). . . . .	66
5.4	Image from the machine vision tracking camera. The red cross shows the detected position of the beacon LEDs. The white circle shows the tip-tilt mirror actuation range, centred on the predetermined hotspot. . . . .	67
5.5	The drone in operation, with machine vision beacon LEDs visible on the gimbal-mounted optical payload. <i>Inset:</i> Close-up of the optical payload showing the beacon LEDs, corner-cube retroreflector (CCR), and camera. . . . .	70

LIST OF FIGURES

---

5.6 Map of flight area around the University of Western Australia campus in Perth, Western Australia. Red dot is the deployable optical terminal on the roof of the physics building, blue lines are static link paths, red line is the drone flight path during the 2022/04/21 flight. Map generated with OpenStreetMap data under the Open Database License (openstreetmap.org/copyright). . . . . 71

5.7 *Top*: Pre-forward error correction (FEC) bit-error rate (BER) versus received power. The black line is measurements taken in fibre, delineating best possible performance. The gray dots are measurements from two of the 2022/04/07 test flights, red dots are from the 2022/04/21 high-speed flight. *Bottom*: Histogram of received power. Gray is from two 2022/04/07 test flights, red is from 2022/04/21 high-speed flight. . . . . 72

5.8 *Left*: Time series for power (red) and log-scale bit-error rate (BER) (green) for rapid power modulation test of the communications module. *Right*: Scatter plot of (BER) versus power for modulation on (orange) and off (black). . . . . 73

5.9 Time series data. From top to bottom: -Line-of-sight distance between the deployable optical terminal and drone as calculated from GPS. -Drone horizontal velocity, as calculated from GPS. -Mount azimuth tracking rate, as calculated from mount (grey) and GPS (blue). -Machine vision tracking errors in azimuth (grey) and altitude (orange). -Received optical power from photodetector (blue) and communications module (red). -Bit-error rate after forward error correction (FEC) (green). Times of link dropout are delineated with a dotted line ( $t = 318$  s and  $t = 439$  s). . . . . 74

6.1 (a) Optical terminal. The upper-right box contains the free-space optics and machine vision system. The lower-left box is a tip-tilt mirror high voltage stage. The upper-left telescope is from an unrelated system. (b) Drone carrying the optical payload. *Inset*: close-up of the optical payload, consisting of LED array, pilot camera and corner-cube retroreflector. . . . . 84

6.2 Schematic of the free-space optical pulse-position modulation demonstration. CCR: corner-cube retroreflector; FFC: fibre-to-free-space collimator; FPGA: field programmable gate array; GBE: Galilean beam expander; PD: photodetector; PID: proportional, integral, derivative; SWIR: short-wave infrared; VOA: variable optical attenuator. . . . . 84

6.3 Bit-error rate versus signal-to-noise ratio (SNR) of 720 received 15120 bit 4-pulse-position modulation codewords. . . . . 89

7.1	Two aircraft used for high-altitude testing: (a) a fixed-wing aircraft and (b) a rotary-wing aircraft provided by the Police Air Wing of the Western Australia Police Force. . . . .	96
7.2	The locations of the TeraNet network of optical ground stations in Western Australia. TeraNet-1 and TeraNet-2 are based on 0.7 m telescopes and will be located in Perth and near Mingenew (383 km north of Perth), respectively. TeraNet-3 is a mobile optical ground station, based on a 0.4 m telescope mounted to a utility vehicle. It is planned to be located in New Norcia (132 km north-east of Perth), near ESA's deep space communications facility. . . . .	97
A.1	A continuous analog signal, dark blue, is sampled using three bits, and quantised as an output sequence of binary words. The quantised signal, light blue, can be reproduced by a computer at any time. . . . .	120
A.2	(a) an illustration of an electro-optical modulator (EOM), used to change the phase of an optical carrier; (b) a Mach-Zehnder modulator, using two EOMs to change the amplitude of an optical carrier through interference. . . . .	122
A.3	(a) An illustration of a dual-parallel Mach-Zehnder modulator (MZM), used in coherent modulation; (b) a constellation diagram for quadrature phase-shift keying, a coherent modulation technique; (c) an illustration of a coherent receiver, for recovering the in-phase and quadrature components of the coherently-modulated optical carrier. . . . .	123
B.1	Reflected power from a corner-cube retroreflector for range of deviation angles, relative to the reflected power from a perfectly-aligned, albeit clipped, Gaussian beam. . . . .	128
B.2	Scintillation index for a space downlink to a point receiver on the ground, various elevation angles. . . . .	129
B.3	$C_n^2$ profile along the line-of-sight to a satellite at three different elevation angles, using the Hufnagel-Valley 5/7 profile. . . . .	129



## List of Tables

2.1	Nominal ocular hazard distance (NOHD) for 1550 nm optical signals used in demonstrations. FFC: fibre-to-free-space coupler, GBE: Galilean beam expander.	33
3.1	Summary of turbulence regimes, with datum $L_0$ and $C_n^2$ values based on the observed phase noise spectra. The $C_n^2$ is fit to the spectrum from 90 mHz to 800 mHz.	41
4.1	Link budget for the 10.3 km folded laser range.	54
5.1	Mount parameters	65
5.2	Demonstration link budget	69
5.3	Atmospheric conditions in Perth for flight dates.	72
6.1	Link budget for retroreflected laser link to drone.	88
A.1	A selection of encodings from binary words to print characters in the ASCII encoding scheme.	120
A.2	Communication link budget for TBIRD to Optical Communications Telescope Laboratory.	125
A.3	Communication link budget for the Lunar Laser Space Terminal to ESA Lunar Laser Optical Ground Station.	126
A.4	Communication link budget for the Lunar Laser Space Terminal to NASA JPL Optical Communications Telescope Laboratory.	126
B.1	111.8 Gb/s Communications demonstration 2022-12-13.	129



**List of Abbreviations**

ADS-B	automatic dependent surveillance-broadcast
AO	adaptive optics
AoA	angle-of-arrival
ARQ	automatic repeat request
ASCII	American standard code for information interchange
BER	bit-error rate
BPSK	binary phase-shift keying
CCR	corner-cube retroreflector
CCSDS	Consultative Committee on Space Data Systems
COTS	commercial off-the-shelf
DCO	digital coherent optics
DPMZM	dual-parallel Mach-Zehnder modulator
DWDM	dense wavelength-division multiplexing
EDFA	erbium-doped fiber amplifier
EOM	electro-optic modulator
FEC	forward error correction
FFC	fiber-to-free-space collimator
FPGA	field-programmable gate array
FSM	fast-steering mirror
FSO	free-space optical
GEO	geostationary orbit
HPE	high photon efficiency
LCRD	Laser Communications Relay Demonstration
LEO	low-Earth orbit
LLCD	Lunar Laser Communications Demonstration
LLST	Lunar Laser Space Transmitter
LO	local oscillator
MPE	maximum permissible exposure
MV	machine vision
MZM	Mach-Zehnder modulator
NOHD	nominal ocular hazard distance
NRZ	non-return-to-zero

## LIST OF ABBREVIATIONS

---

O2O	Orion Artemis II Optical Communications System
O3K	optical on-off keying
OD	optical density
OGS	optical ground station
PID	proportional, integral, derivative
PPM	pulse-position modulation
PRBS	pseudo-random binary sequence
PSD	power spectral density
QAM	quadrature amplitude modulation
QPD	quadrant photodetector
QPSK	quadrature phase-shift keying
RF	radio frequency
SMF	single-mode fibre
SNR	signal-to-noise ratio
SPD	spatial position detector
TLE	two-line element
TT	tip-tilt
UWA	The University of Western Australia

---

---

## CHAPTER 1

---

# Introduction

This chapter summarises the milestones in near-instantaneous, long-distance communications, leading to increasing interconnectedness between societies. Historical developments in communications signal transmission are described for both wired and free-space links, and the advancements in these two types of links are shown to be closely intertwined.

### Chapter Contents

---

1.1	History of Communications . . . . .	2
1.2	Space Communications . . . . .	4
1.2.1	Telecommunications Satellites . . . . .	6
1.2.2	Earth Observation Satellites . . . . .	6
1.2.3	Space Exploration . . . . .	7
1.3	Optical Ground Stations . . . . .	8
1.3.1	Atmospheric Stabilisation . . . . .	8
1.3.2	Optical Ground Station Demonstrations . . . . .	9
1.3.3	Australia and New Zealand Optical Ground Station Network . . . . .	10
1.4	Thesis Outline . . . . .	11

---

## 1.1 History of Communications

The ability to communicate near-instantaneously over great distances extends the influence of individuals and societies and thus has been a technological pursuit with considerable consequences, particularly since the 19th century. Modern telecommunications, that is, near-instantaneous communications extending beyond line-of-sight or the reach of sound, underpins the dissemination of information for entertainment, industrial, and military purposes.

Before electrically-mediated communications, telegraphing information over long distances near-instantaneously was limited to visual or audible techniques, and, therefore, restricted to smaller-scale environments such as battlefields. The historian Polybius provides an account, from the fourth century BC, of a hydraulic semaphore using torchlight for synchronisation [5]. This invention allowed secure communication between Sicily and Carthage during the first Punic war, albeit with a very limited vocabulary due to the limited number of symbols possible with the semaphore. Other pre-19th century near-instantaneous telecommunications techniques included smoke signals, talking drums, and semaphore telegraph towers [6]. All of these may be characterised as low-bandwidth, referring to the quantity of information transferred in a given time. Long distance, high-bandwidth communications were limited to written text carried by couriers, and this was advanced by technological achievements, including mechanical reproduction with the movable type press and mechanisation [7]. This thesis, however, is concerned with the modern telecommunications paradigm and this began in earnest when the first practical telegraphs were realised in the 19th century.

Theories of electricity and magnetism emerged between the early and late modern periods, and provided the foundation for high-bandwidth, near-instantaneous communications beyond line-of-sight. An electrical telegraph was proposed as early as 1753 by an anonymous writer [8], and a working telegraph was realised in 1816 [9]. Application of electromagnetic theory to telegraphy [10] explained how electromagnetic fields propagate along a telegraph line at the speed of light (in the medium), leading to improved understanding and designs for the conductive media used in wired links. Hertz' discovery of free-space radio frequency (RF) radiation [11] paved the way for Marconi's demonstrations of free-space telegraphy [12], and this complemented wired telegraphy. At the cusp of the 20th century, the All Red Line network of telegraph lines girded the planet, connecting Commonwealth countries [13], and wireless telegraphy closed the gap where cables could not be lain [14]. Analog voice and video transmission followed telegraphy, along with improved techniques for modulation, transmission, and reception [15, 16].

In the mid-to-late 20th century, digital communications superseded analog communications and facilitated the beginning of the space age. This digital communications regime came about because of the discovery of information theory [17] and development of digital computing [18]. Information theory provided analytical tools to estimate the error-free capacity of any noisy wired or free-space communications link, using binary representation and error-correcting codes. Digital computers conveniently became available at the same time, to practically implement error-correcting codes [18]. At a similar point in history, the space race led to the use of artificial satellites for telecommunications and Earth observation, as well as space exploration [19]. For now, RF signals are the standard carrier signals for ground-space communications. Recently, however, the potential for significant improvements to ground-space communication, by using optical frequency signals, is now being realised [20–22].

Optical frequencies had been known to potentially provide higher bandwidths at longer distances than RF signals in both wired and free-space links. The possibility of low-loss optical fibres was proposed in the 1960s [23, 24], triggering the beginning of wired optical frequency links. With careful manufacturing, optical fibres could guide optical frequency signals with lower losses than wired RF links for equivalent distances. By the late 1980s, optical fibre technology had advanced sufficiently to support large-scale terrestrial networks [25]. Wired optical links now make full use of the spectrum available in the 1550 nm optical C-band, particularly due to improvements in modulation, detection, and amplification technologies [26]. However, the benefits of optical frequencies have not yet been fully realised in ground-space links because of the deleterious effects of atmospheric turbulence on optical transmission. Thus, free-space RF links remain the standard means of ground-space communications. Advancements in telecommunications [27], Earth observation [28, 29], and space exploration [30], demand increasing space-ground downlink bandwidth. The bandwidth available to RF signals is not anticipated to be able to fulfil this emerging demands. Furthermore, Earth's orbits are becoming more crowded because of reduced barriers-of-entry to satellite manufacturing and launch [31, 32]. Opportunities for RF downlink will become more costly and competitive as a result of crowding. These issues, along with advancements in optical frequency equipment for wired links, and advancements in atmospheric stabilisation technologies for astronomy, have renewed interest in free-space optical (FSO) communications for spacecraft. The following sections outline the specific applications to benefit from FSO communications, the challenges, and the current state of the art.

## 1.2 Space Communications

In the middle of 2024, approximately 10,300 active artificial satellites supporting scientific and commercial activities were recorded in the Space Track database [33]. Other spacecraft are sent beyond Earth's orbit on scientific exploration missions. Regardless of their objective, all spacecraft must be able to communicate with Earth. Other than the requirement to survive the physical conditions of outer space, a spacecraft's ability to transmit and receive communications to, and from, Earth is arguably the most important design requirement.

FSO communications poses a comparative advantage over free-space RF communications. Primarily, FSO communications will enhance space communications with orders-of-magnitude larger bandwidth than RF signals. Divergence is another important property for communications signals, describing the spreading angle of the signal wavefront propagating from a transmitter aperture. Divergence angle is proportional to the ratio of wavelength-to-aperture size of the transmitter [34]. For a given aperture size, RF beams diverge at significantly greater angles than FSO beams, and the implications of this to space communications are discussed.

Three space communications scenarios motivated this project. They are introduced in this paragraph, with details provided in subsequent subsections, and Figure 1.1 provides illustrations of each case. Figure 1.1a depicts communication with telecommunications satellites in geostationary orbit (GEO), approximately 35,000 km above Earth [35]. These satellites bridge gaps in terrestrial networks by consolidating information from multiple users into feeder links to ground stations. Next, Figure 1.1b depicts communication with Earth observation satellites, carrying out scientific or commercial missions in low-Earth orbit (LEO), approximately 500 km [35]. Depending on the specifics of the orbit, multiple data downlinks per day may be required to offload the data collected from an Earth observation satellite [36]. Last, Figure 1.1c represents communication with spacecraft in the process of space exploration. This scenario involves extremely long distances, from cislunar space approximately 300,000 km from Earth and beyond [30, 37, 38].

These three scenarios share common characteristics, contrasting with other FSO applications, such as inter-satellite links and quantum communications. First, they all involve optical transmission through atmospheric turbulence. Inter-satellite links avoid the atmosphere completely and therefore do not necessitate atmospheric stabilisation technologies. Second, they utilise technologies compatible with existing communications infrastructure. Quantum optical communications systems are currently experimental and thus are not salient in discussions of existing infrastructure.

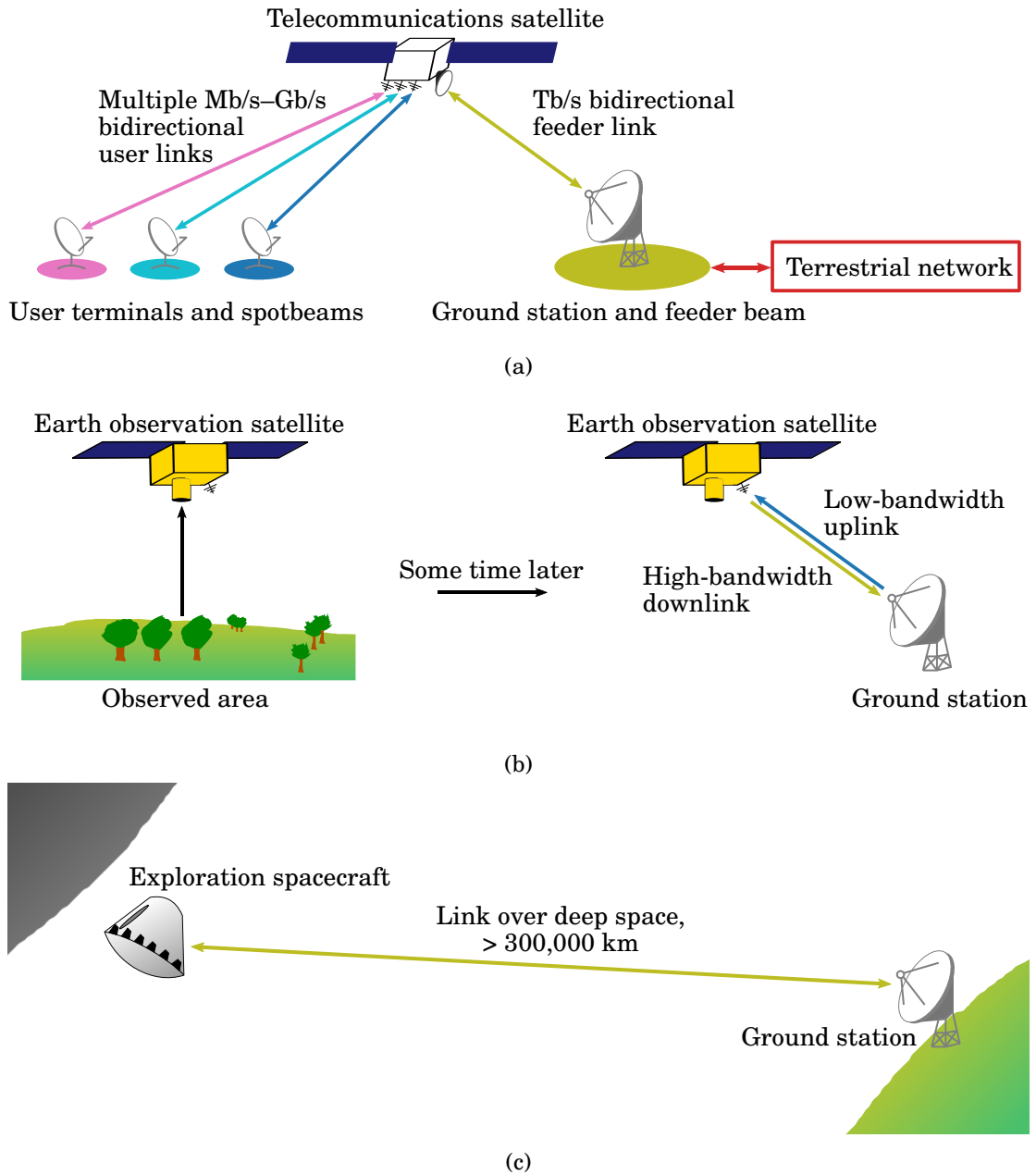


Figure 1.1: Illustrations of three space mission scenarios pertinent to free-space optical communications: (a) geostationary telecommunications satellite acting as a relay to connect gaps in a terrestrial network, (b) Earth observation satellite in low-Earth orbit observing an area at one time, and communicating with a ground station at a later time, and (c) spacecraft in deep space communicating with a ground station on Earth.

### 1.2.1 Telecommunications Satellites

The RF signals of modern GEO satellites have carrier frequencies in the K/Ka-band and Q/V-band, spanning 20 GHz to 50 GHz [27]. Also, at GEO distances, small angular pointing errors at either end can lead to large deviations. Free-space transmissions at identical or neighbouring frequencies can interfere, due to pointing errors and beam divergence. Figure 1.1a depicts a telecommunications satellite operating as a relay to bridge gaps in a terrestrial network. As shown in the left-hand-side of Figure 1.1a, multiple narrow RF spotbeams are used to cover neighbouring areas with overlapping channels, efficiently re-using the limited spectrum. Total throughput on the order of 1 Tb/s for all aggregated user links is possible, with careful design of the spotbeams [27], but this requires a feeder link to match. Feeder links, depicted in the right-hand-side of Figure 1.1a, involve relatively larger beams and a single ground segment receiver and cannot re-use the spectrum in the same way as user links, ultimately limiting the utilisation of advances in user link techniques.

Modern terrestrial fibre-optic communication equipment, on the other hand, operates with carrier frequencies in the optical C-band, on the order of 193 THz [39]. A transition to FSO communication will greatly improve the effectiveness of telecommunications satellites, because of the relatively higher available bandwidth and lower beam divergence than currently-used RF carrier signals. The optical C-band is divided into 102 channels with 50 GHz spacing. The entire channel bandwidth can be used without cross-channel interference, leading to potential throughput over 10 Tb/s [40, 41]. The European Data Relay System, operating at 1064 nm is a pioneering FSO communications relay network currently using a fraction of the available bandwidth to optical signals to support EU space activities [42]. Progressing to fibre-like technology for telecommunications satellite feeder links will allow the growing user demand to be met.

### 1.2.2 Earth Observation Satellites

Earth observation satellites are spacecraft equipped with sensors for capturing imagery and other spectral data. They typically occupy LEO, close enough to the ground for high resolution observations, but high enough to avoid significant atmospheric drag. Figure 1.1b depicts an Earth observation mission. The satellite manoeuvres to observe a predefined area and collects imagery. Later, the satellite will make contact with a ground station to downlink the imagery, and to receive instructions for future manoeuvres. The following paragraphs explain why FSO communications for downlinks from LEO is becoming increasingly desirable.

Opportunities to launch sub-1000 kg satellites to LEO are becoming more frequent and cheaper [32]. Being closer to Earth, LEO also suits smaller and cheaper satellites, assembled from modern, low-cost consumer microelectronics [31] less resistant to the harmful radiation seen at higher orbits. Additionally, LEO is becoming occupied by constellations of small commercial telecommunications satellites, such as Starlink [43, 44], in addition to Earth observation satellites. Communications signals transmitted by all satellites diverge, with divergence angles proportional to their wavelength-to-aperture ratios. This divergence can lead to interference, if two nearby satellites are transmitting at similar frequencies. The telecommunications satellites, discussed in the Section 1.2.1, are able to produce narrow RF beams by carrying transmitters with large apertures. For Earth observation satellites, using FSO communications may be a more suitable solution, because optical frequencies provide a wavelength-to-aperture ratio around 10,000 smaller than RF for the same aperture size, mitigating the interference issue arising from an increasingly populated LEO.

At the same time, the volume of data captured by Earth observation sensors is beginning to exceed the bandwidth available with RF communication [36, 45, 46] and beyond the ability of edge processing on orbit [47]. FSO communications promises to alleviate this second issue, because, as stated, optical frequencies have much more bandwidth available than RF. The possibility of terabytes of downlink volume per day, using FSO communications, was shown in the TBIRD mission [22].

### 1.2.3 Space Exploration

Space exploration missions are currently supported by deep space ground station networks operated by NASA [48], ESA [49] and commercial providers, such as Goonhilly Earth Station [50]. Deep space networks rely on RF communications and dish antennas with diameters on the order of 30 m. NASA's Deep Space Network currently provide speeds up to 150 Mb/s using the Ka band [48]. However, the rate is also contingent on the design of the spacecraft's communication system and the link distance, dropping off rapidly on interplanetary scales. Boroson, advocating for deep space optical communications systems, notes the state-of-the-art RF downlink rate from Mars was 6 Mb/s and, with a back-of-the-envelope calculation, shows it would take decades to transmit even a relatively low resolution map of Mars' surface at this rate [37]. Trends in photonics and optical technology are predicted to lead to Mars–Earth data rates on the order of Gb/s [30]. The Lunar Laser Communications Demonstration (LLCD) was the first successful demonstration of optical communications beyond GEO, achieving data rates up to

622 Mb/s from lunar orbit. This result is to be followed by a 250 Mb/s downlink demonstration from the Orion crew module as part of the Artemis II mission [51]. In December 2023, NASA's Psyche mission demonstrated 265 Mb/s downlink of a pre-recorded video from a spacecraft 31 million kilometres away [52]. Another deep-space optical communications terminal was also designed for an asteroid impact mission [38], and may be repurposed for a space weather monitoring mission at the L5 Lagrange point [53]. Deep-space optical communications is perhaps the most standardised mission scenario of the three described, with a longstanding CCSDS standard for high photon efficiency (HPE) signalling [54, 55]. The HPE standard emphasises simplicity and maximising the number of bits-per-photon-received on the ground.

### 1.3 Optical Ground Stations

Spacecraft communications are supported by ground stations on Earth. RF communications are at a level of maturity and ubiquity where all but the most specialised applications can be supported by commercial off-the-shelf (COTS) solutions, including services from commercial ground station providers [50]. However, optical ground station (OGS) systems are mostly bespoke. An OGS is embodied by an optical telescope, constructed from refracting or reflecting elements. Its purpose is to focus light from space-borne transmitters onto a detector. The detector converts the optical signal to an electrical one, with electronic communication systems downstream. Atmospheric turbulence reduces the amount of optical power coupled to these detector elements, necessitating stabilisation systems to suppress the effects of atmospheric turbulence.

#### 1.3.1 Atmospheric Stabilisation

Atmospheric temperature and humidity variations lead to variations in refractive index along the path of an optical signal [56]. Wind transverse to the path also introduces time variation to the refractive index structure. This leads to three negative, time-varying, effects on FSO beams – random phase noise fluctuations, angle-of-arrival (AoA) variation, and scintillation. It is necessary to develop and use stabilisation technologies, capable of measuring and compensating for these deleterious effects to ensure robust FSO communications.

Phase noise, or 'zeroth order' fluctuations, are caused by random changes in the refractive index, and therefore the speed of light, in each turbulent eddy in the atmosphere. Optical signal speed in a medium is a function of refractive index, so the net

time-of-flight along the path changes with time, observed as phase noise. Atmospheric phase noise sensing and correction is of interest in the field of frequency metrology [57, 58], where optical clock comparisons between low-phase-noise optical signal sources can be disturbed by time-of-flight fluctuations in the atmosphere [59]. In communications, atmospheric-induced phase noise is insignificant compared to the intrinsic phase noise of communications-grade lasers [60].

Changes in refractive index also cause angular, or ‘first order’ fluctuations, so propagating optical signals experience time-varying changes in the AoA of the beam. The signal intensity at a receiver varies with time as the signal is steered on and off the receiver. Atmosphere-induced AoA variations are compounded by spacecraft and OGS vibrations, adding additional pointing errors. AoA variation can be detected with imaging sensors, sensitive to incoming beam position, such as the quadrant photodetector (QPD) [57]. These sensors can feed back to active optical elements, such as a fast-steering mirror (FSM), to correct for measured angular deviations; this arrangement is referred to as first order adaptive optics (AO), or a tip-tilt (TT) system.

Scintillation occurs under sufficiently strong turbulence, where the wavefront of the optical signal is affected by ‘higher order’ fluctuations. High order fluctuations appear as speckle at the receiver. Qualitatively, the time-varying speckle leads to time variation in the intensity of the optical signals, referred to as scintillation [61]. Under speckle, the atmosphere limits the angular resolution of the OGS telescope, limiting the light-collecting power of larger apertures. Higher order AO technologies may be used to suppress speckle, and therefore stabilising scintillation occurring under strong turbulence. Traditionally, these AO systems use a specialised wavefront sensor to measure the time-of-flight across sections of a signal and feed back to a deformable mirror in the signal path, changing the time of flight of sections of the signal [62]. This stabilises the variations in signal power entering subsequent systems and improves the injection of optical signals into fibre. AO systems are highly applicable to OGS operations to enable high fibre-coupling efficiency, and therefore high-speed space-to-ground communications.

### 1.3.2 Optical Ground Station Demonstrations

OGS networks are not yet ubiquitous globally, and only a small number of space-ground FSO communications demonstrations have been conducted in the last three decades. In 1995, Japan’s NICT reported on the earliest downlink with an OGS for their pioneering FSO space-to-ground transmission from GEO at 1.024 Mb/s [63]. Further OGS operations by NICT, Germany’s DLR, and the United States’ NASA JPL demonstrated FSO downlink

from a satellite in LEO at 50 Mb/s [64–67]. In 2013, NASA demonstrated FSO downlink from the Moon, at up to 622 Mb/s, during the LLCD, with collaboration from ESA [37, 68]. In the mid-late 2010s, DLR demonstrated two compact optical terminals in LEO, capable of downlinking at 200 Mb/s and 1 Gb/s, with a planned 10 Gb/s terminal [69]. Later, in 2022 and 2023, NASA demonstrated a record-breaking 200 Gb/s downlink from LEO with the TBIRD mission [70]. However, more OGS than have currently been demonstrated are required worldwide to ensure seamless coverage for satellites on the move, and future OGS constructors require methods to commission ground station hardware.

Being capable of testing and developing prototype OGS hardware on representative free-space links is a necessary and significant component of the efficient development of all future space optical communications systems, including OGS commissioning. In particular, atmospheric stabilisation technologies are needed to ensure fibre-like data rates are possible on free-space links. Prototype stabilisation technologies must therefore be demonstrated on terrestrial proxy links with characteristics analogous to space-ground links. This thesis describes communications demonstrations on terrestrial FSO links, following on from work by NASA [71], DLR [39, 40], and NICT [72] and providing instructive guidance on OGS commissioning activities.

### 1.3.3 Australia and New Zealand Optical Ground Station Network

An Australia and New Zealand OGS network has been proposed [62]. This collaboration will leverage the countries' unique position in the southern hemisphere and use site diversity to provide opportunities for handover under unsuitable local weather conditions. Sites include an astronomical observatory site at Mount Stromlo, Australian Capital Territory, managed by The Australian National University [73], a space situational awareness observatory at the Defence Science Technology Group campus in Edinburgh [74], South Australia, an OGS under development in New Zealand [62], and all three nodes of The University of Western Australia (UWA)'s TeraNet optical ground station network. As planned, TeraNet will comprise two fixed 0.7 m telescopes, and a mobile 0.4 m telescope mounted to a utility vehicle. The two fixed OGS will be situated at UWA and at the Mingenew Space Precinct, 300 km north of Perth. The mobile OGS will initially be deployed at ESA's deep space communications facility in New Norcia, Western Australia. Modelling based on meteorological records at these locations shows the nationwide network will offer virtually constant availability to satellites over Australia and New Zealand [75, 76]. This thesis describes work carried out during the development of TeraNet, the Western Australian OGS network within the larger continental project.

## 1.4 Thesis Outline

This thesis aims to address a shortfall in the availability of methods for validating OGS performance. To create novel methods, a series of capability demonstrations are undertaken. The capabilities demonstrated in the course of this project were developed in a linear fashion, with discrete, increasingly challenging milestones. Each chapter in this thesis describes the achievement of each milestone, starting from measurements of the atmospheric channel, to a demonstration of high-bandwidth communications to an orbiting pseudo-satellite.

**Chapter 2** provides a background of technical information to support the remaining body chapters of the thesis. This includes an overview of optical carrier signal modulation, atmospheric physics, and laser safety.

In **Chapter 3**, the physics of a retroreflected atmospheric link established between a transceiver and a corner-cube retroreflector (CCR) are explored [1], providing a basis for the subsequent demonstrations. The characteristics of a folded link are given through mathematical models and experimental results, and related to the point-to-point links found in real-life communications. Chapter 3 provides an experimentally-verified foundation for understanding the channel conditions documented in the latter chapters.

A demonstration of high-bandwidth coherent communications on a long-distance static link is then described in **Chapter 4** [2]. In this chapter, the link is characterised in terms of power scintillation. The link was shown to exhibit scintillation equivalent to modelled scintillation for a space-to-ground optical link from GEO. This demonstration shows the limit of possible scintillation to be incurred when deploying COTS fibre networking equipment over free-space.

**Chapter 5** then introduces a LEO satellite simulation [3]. This combines the demonstrated high-bandwidth coherent communications capability with a pseudo-satellite target. In this demonstration, the target was in motion, requiring the ground station to slew at angular rates equivalent to an overhead LEO pass. High-bandwidth COTS fibre networking equipment was again used in this demonstration to show how FSO communications can be readily integrated into existing infrastructure. The implications of this demonstration were realised shortly after completion in the recent NASA TBIRD mission [70].

In **Chapter 6**, the pseudo-satellite technique is modified to demonstrate communications using a HPE communications scheme [4]. This HPE demonstration used a weak light signal for an analogous link budget to previous [37], and upcoming [51] lunar laser communications deployments. These deployments leverage existing optical fibre equipment, fitting into existing communications infrastructure but pushing the technologies to the fullest extremes in photonic efficiency.

Finally, **Chapter 7** concludes the thesis. The chapter is devoted to summarising the accomplishments of the research project as well as the limitations of the techniques promoted herein. Further in-progress and planned avenues for development are also described.

---

---

## CHAPTER 2

---

# Technical Background

This chapter introduces concepts and references for communications and optical atmospheric transmission, pertinent to the later chapters describing FSO communications demonstrations. Digital communications involves binary format information exchange between computer systems. A layer model abstracts the functions of various parts of a communication system, enabling specialisation and compartmentalisation. For example, a user accessing satellite imagery from a computer does not need to know how the computer has used binary data to store the image, and does not need to know what physical signalling format was used to mediate the exchange of the binary data between itself and the satellite. This thesis is concerned with the physical layer where the binary units, bits, modulate a physically observable property of the carrier, propagate over a link, and are received and demodulated back into bits. Bits may be received in error as a consequence of noise on a link, so a test procedure and performance metrics used in subsequent chapters are presented here.

Concepts for FSO channels are introduced, including modulation and demodulation, telescope gains and atmospheric turbulence. Detailed supplementary material, particularly on the implementation of modulation and demodulation functions, is provided in Appendix A. Physical layer quantities are summarised in a link budget comprising a sequence of gains and losses representing the physics of the components between the transmitter and receiver. Atmospheric turbulence and atmospheric stabilisation techniques are discussed, introducing models for the effect of turbulence on optical signals. Finally, the topic of laser safety when undertaking these demonstrations is addressed, to help guide future risk assessments.

## Chapter Contents

---

2.1	Optical Communications . . . . .	<b>15</b>
2.1.1	Digital Communications Using Carrier Modulation . . . . .	15
2.1.2	Amplitude Modulation . . . . .	16
2.1.3	Coherent Modulation . . . . .	19
2.1.4	Link Budget Analysis . . . . .	20
2.1.5	Fibre Coupling . . . . .	23
2.2	Atmospheric Optical Communications . . . . .	<b>23</b>
2.2.1	Atmospheric Turbulence . . . . .	23
2.2.2	Optical Signal Propagation in Turbulence . . . . .	26
2.2.3	Weak Turbulence . . . . .	27
2.2.4	Strong Turbulence . . . . .	28
2.2.5	Atmospheric Measurement and Stabilisation . . . . .	30
2.2.6	Spacecraft Proxies . . . . .	31
2.3	Laser Safety . . . . .	<b>32</b>
2.3.1	Engineering Controls . . . . .	33
2.3.2	Administrative Controls . . . . .	34
2.3.3	Personal Protection . . . . .	34

---

## 2.1 Optical Communications

### 2.1.1 Digital Communications Using Carrier Modulation

Modulated carrier signals are used for long-distance digital communications because of their advantageous physical propagation properties [77]. A prototypical digital communications system is shown in Figure 2.1, showing the carrier signal's position in a complete system. The originating digital message begins at the transmitter in binary format (examples of binary format usage are given in Appendix A). The binary bits to be transmitted are encoded as symbols in a 'baseband' signal. In the modulator, these baseband signals alter a physical property of the carrier signal, such as amplitude or phase, allowing it to convey the encoded bits over a long distance. At the receiving end, the carrier signal is demodulated to retrieve the baseband signal. The received baseband signal is then sampled and the symbols are decoded into the digital message. Figure 2.1 also shows an additional undesirable 'noise' signal being added to the carrier, though noise may enter the system at any point, depending on the physics of the actual link. If the so-called signal-to-noise ratio (SNR) is sufficiently low, the resulting decoded symbols will be misinterpreted, leading to symbol errors, hence, bit errors. In the demonstrations described in Chapters 4, 5, and 6, the bit-error rate (BER) was the key metric for the performance of the equipment under test, so an explanation for the practical measurement of BER follows.

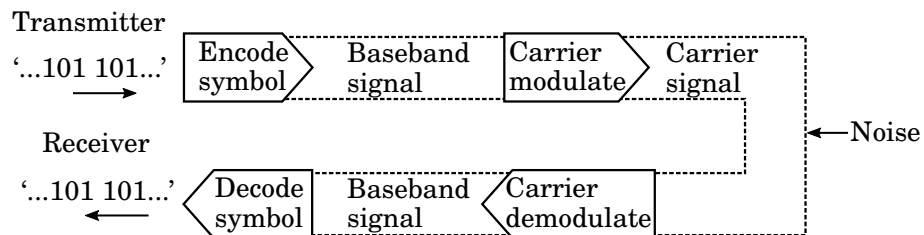


Figure 2.1: Prototypical digital communication system using carrier modulation.

BER is defined as the ratio of error bits to total received bits, and may be modelled analytically as a function of SNR [77]. In BER testing, measurements are taken using random data sourced from a pseudo-random binary sequence (PRBS) generator [78, 79]. A PRBS is type of binary-valued sequence with controllable periodicity. A key property of the PRBS is the ability to seed a PRBS generator with a sequence from a separate, remote PRBS generator, thus creating an independent and identical local sequence. Figure 2.2 provides a

schematic for BER testing using PRBS generators. A PRBS generator on the transmission side transmits a sequence over the link, and noise in the physical medium introduces bit errors. In the receiver, a second PRBS generator is seeded with a sub-sequence of incoming bits, with the exact quantity of bits required in the sub-sequence depending on the chosen PRBS implementation. Once the second PRBS is seeded, its output is logically compared with subsequent received bits. Any discrepancies between the two streams are counted, and this result can be read periodically and divided by the total number of bits received to calculate the BER.

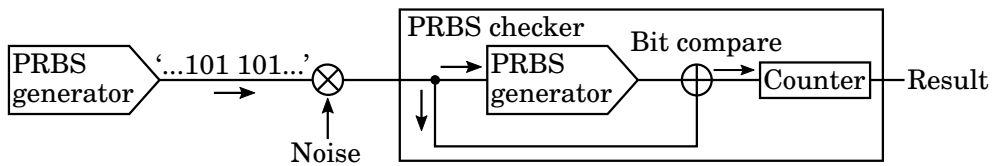


Figure 2.2: Schematic for a bit-error rate tester using a pseudo-random binary sequence (PRBS) generator and checker.

Chapters 4 and 5 describe BER measurements taken with COTS communications equipment, intended to demonstrate the technical readiness of the prototype OGS systems. In practice, the COTS equipment utilises forward error correction (FEC), a scheme for detecting and correcting bit errors in real time. FEC is a logical operation carried out on sequences of bits. For example, bits may be repeated to add redundancy, or interleaved to avoid losing information in bursts. A given FEC scheme has a threshold BER, below which a receiver can detect and correct all bit errors encountered. Thus, in Chapters 4 and 5, the BER measurements are compared with the FEC-correction thresholds of COTS systems [80] to measure the success or failure of transmissions.

This subsection established the method and metrics for testing communications performance. Sections 2.1.2 and 2.1.3 introduce aspects of amplitude modulation and coherent modulation, respectively. These are two optical signal modulation formats used in the FSO communications demonstrations described in Chapters 4, 5, and 6.

### 2.1.2 Amplitude Modulation

Amplitude modulation controls the intensity of the carrier signal to represent symbols. Figure 2.3 depicts the communications system of Figure 2.1 as an optical amplitude modulation system, with the electrical baseband signals in blue and the optical carrier signals in red. The amplitude-modulated signal,  $s_{AM}(t)$ , may be expressed as

$$s_{AM}(t) = A_m(t)A_L \cos(2\pi f_L t), \tag{2.1}$$

where  $A_L$  and  $f_L$  are the optical signal's amplitude and frequency, respectively, and  $A_m(t)$  is a function of the electrical baseband signal,  $m(t)$ , shown in Figure 2.3. A derivation of  $A_m(t)$ , and the amplitude modulator's operating principle is given in Appendix A. In FSO communications,  $A_m(t)$  equals either 1 or 0, corresponding to transmission or extinction of the carrier signal. At the receiver,  $s_{AM}(t)$  is demodulated by directing the optical signal onto a detector, recovering  $m(t)$  plus noise. The signal  $A_m(t)$  is also varied in time to encode symbols in different ways.

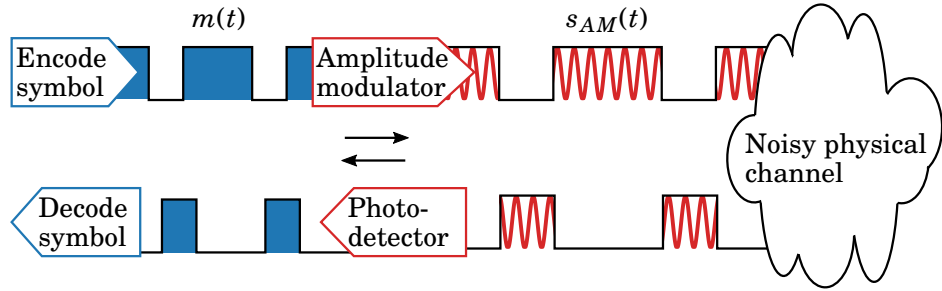


Figure 2.3: A communication system using amplitude modulation. The electrical message signal,  $m(t)$ , is modulated onto the optical frequency signal, resulting in the amplitude-modulated signal  $s_{AM}(t)$ .

Three types of symbol encoding relevant to FSO communications are optical on-off keying (OOK), pulse-position modulation (PPM), and non-return-to-zero (NRZ). The work described in Chapter 6 utilised PPM encoding, as the encoding is a modification of OOK, intended for HPE communication [54]. Figures 2.4a and 2.4b provide a visualisation of  $m(t)$  for OOK and PPM, to assist in understanding PPM through comparison with OOK, as this is the most general case of amplitude modulation. NRZ is standardised by the Space Development Agency [81] and may supersede the currently drafted OOK standard [82]. However, OOK and NRZ do not apply to the high bandwidth or HPE scenarios introduced in Chapter 1. Therefore, neither of the encoding techniques were utilised in any of the demonstrations described in this thesis. The remainder of this subsection is devoted to explanation of PPM by way of comparison to OOK, to aid in understanding the communications system described Chapter 6.

Both OOK and PPM encode bits as pulses in the carrier signal's amplitude, but differ in their temporal characteristics. In OOK the presence, or absence, of a pulse signifies a binary 1 or 0, respectively. The symbol period,  $T_s$ , in OOK is the duration of such a pulse, and the data rate,  $R$ , under OOK is therefore

$$R = \frac{1}{T_s}. \quad (2.2)$$

By contrast, PPM encoding utilises a longer symbol period, divided into  $m$  slots with

additional guard slots. An amplitude pulse may be transmitted in only one slot per symbol period, allowing  $m$  possible symbols to be transmitted, representing  $\log_2(m)$  bits-per-symbol. This improves the photon efficiency of the optical signal because more bits are transmitted per pulse than in O3K. High  $m$ -numbers are conducive to extremely long-distance links as they provide control over peak-to-average power ratio in deep-space communication systems with average power limited amplifiers. Figure 2.5 shows the increase in photon efficiency over O3K on the right-hand plot axis, for  $m$  from 4 to 512. For a fixed slot period, the data rate in PPM decreases with increasing  $m$ . The Consultative Committee on Space Data Systems (CCSDS) HPE standard [54] specifies  $m/4$  guard slots, with the same period as the slots. Thus, the data rate of a PPM system is

$$R = \frac{\log_2(m)}{(5/4)T_s m}. \tag{2.3}$$

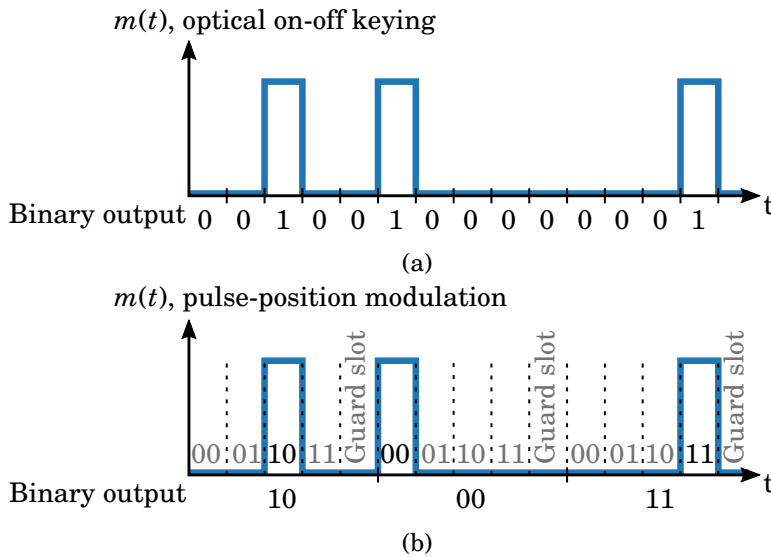


Figure 2.4: Comparison of time-series for baseband symbols in (a) optical on-off keying and (b) pulse position modulation with four slots.

Figure 2.5 shows Equation 2.3 relative to Equation 2.2 on the left-hand plot axis, for a PPM slot period equal to the O3K symbol period. As an example, in 2013, the LLCD demonstration used PPM to transmit data from cislunar space at 622 Mb/s, accounting for additional FEC bits, with  $m = 16$  slots and a 0.25 ns slot duration [37]. Per the background in Chapter 1, such a speed is a significant improvement over RF for deep-space communications, where large link distances result in minimal optical power at the receiver. Section 2.1.3 focuses on orbits around Earth, where link distances are orders-of-magnitude shorter, and thus orders-of-magnitude more optical power is

available. With more optical power on orbit, coherent modulation may be used to achieve data rates hundreds of times faster than with amplitude modulation.

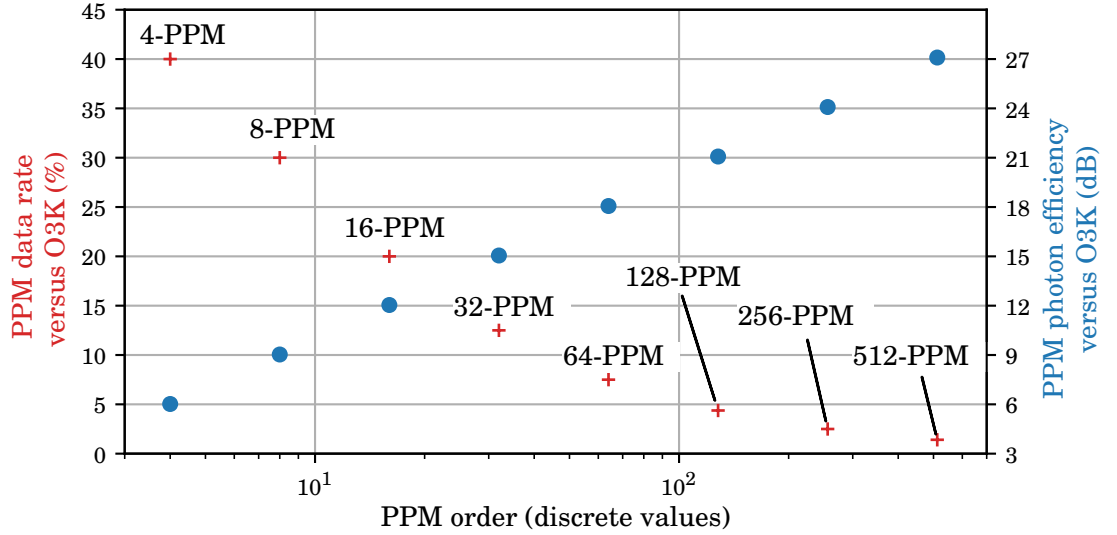


Figure 2.5: Graph showing the speed and photon efficiency scaling of a pulse-position modulation (PPM) system compared to an optical on-off keying (O3K) system.

### 2.1.3 Coherent Modulation

Coherent optical modulation enables high-bandwidth communications, with the entry point being a data rate of 100 Gb/s for COTS equipment [26]. A coherent modulator controls the phase and amplitude of an optical signal, while a coherent receiver senses these properties. Figures 2.6a and 2.6b depict the symbol constellations used in single-level quadrature phase-shift keying (QPSK) and the multi-level 16-quadrature amplitude modulation (QAM), respectively, along with the corresponding bit encoding. These symbols can be described mathematically by

$$s_{CM}(t) = I_m(t) \cos(2\pi f_L t) + Q_m(t) \sin(2\pi f_L t), \quad (2.4)$$

where  $I_m(t)$  and  $Q_m(t)$  are the in-phase and quadrature amplitudes, respectively. The amplitudes in Equation 2.4 are the axes in Figures 2.6a and 2.6b. Equation 2.4 also describes how a coherent modulator splits the carrier signal into the orthogonal in-phase and quadrature components, which are independently modulated by baseband signals. For further detail, the structure of a coherent modulator and receiver are given in Appendix A. Coherent modulation additionally provides polarisation discrimination, allowing two

orthogonal-polarised signals to share a channel, doubling the data rate of an  $m$ -level encoding to be,

$$R = 2 \frac{\log_2(m)}{T_s}. \quad (2.5)$$

The demonstrations described in Chapters 4 and 5 of this thesis were concerned with translation of COTS coherent fibre-optical communications equipment to FSO links. COTS coherent communications equipment primarily uses QPSK or QAM encoding; therefore, other coherent encoding techniques, such as polarisation-switching [83], were not considered. QPSK was selected over multi-level QAM, as it had a perceived advantage in low-SNR FSO links. Figures 2.6c and 2.6d show QPSK and 16-QAM constellations with low SNR. At low SNR, the 16-QAM constellation is more likely to incur symbol errors arising from amplitude and phase noise. This selection was validated by the recent TBIRD demonstration, where two COTS QPSK modems were used to downlink data from LEO at 200 Gb/s [70]. Sections 2.1.4 and 2.1.5 explain the link budget modelling used to select system parameters to achieve a desired SNR.

### 2.1.4 Link Budget Analysis

As discussed, a communications channel will exhibit a BER, and the use of FEC allows users to specify an acceptable BER. The probabilistic relationship between bit errors and received optical SNR can be analysed [26, 84]; therefore, a threshold power level can be calculated to achieve a likely BER. This provides a starting point for the link budget used to analyse FSO channel performance and drive engineering decisions. From the threshold power level, the system gains and losses can be summed to determine the necessary transmission power. Dynamic power variation will be encountered in practice; therefore, an additional link margin factor is added to the calculated link budget. Link budgets are given for each demonstration described in Chapters 3–6.

Figure 2.7 shows an FSO channel labelled with gain and loss terms encountered in the link budget. The initial optical signal power out of the transmission fibre is  $P_{tx}$ . Free-space loss,  $L_{fs}$  treats the optical signal as an isotropic radiation over the link distance,  $L$ ,

$$L_{fs} = \left( \frac{\lambda}{4\pi L} \right)^2. \quad (2.6)$$

The transmission telescope gain,  $G_{tx}$ , represents the directivity of the telescope. The gain is

$$G_{tx} = 16/\theta_{tx}^2, \quad (2.7)$$

where  $\theta_{tx}$  is the far-field full-angle beam divergence from the telescope. For a Gaussian beam from a diffraction limited telescope,  $\theta_{tx}$  is

$$\theta_{tx} = 4\lambda/(\pi\omega_d), \quad (2.8)$$

where  $\lambda$  is the optical wavelength and  $\omega_d$  is the  $1/e^2$  beam waist diameter. The resulting gain is

$$G_{tx} = \left(\frac{\pi\omega_d}{\lambda}\right)^2. \quad (2.9)$$

In practice, other implementation losses,  $L_{imp}$ , are incurred before and after the telescopes. For example, an optical beam splitter used for an AO system will reduce the optical signal power by approximately one half, or the secondary mirror support arms in a reflecting telescope will partially obscure the optical signal.

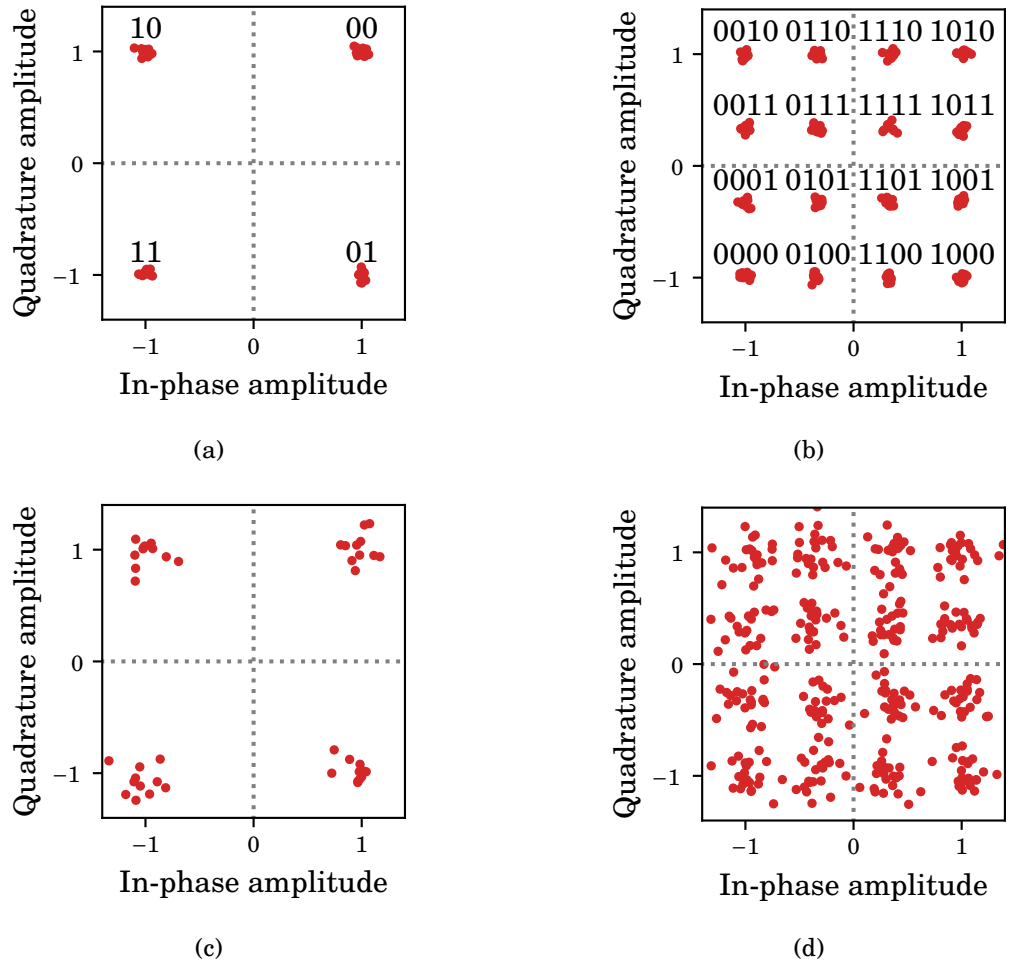


Figure 2.6: Constellation diagrams for quadrature phase-shift keying with: (a) 15 dB signal-to-noise ratio (SNR) and (c) 9 dB SNR; (b) 16-quadrature amplitude modulation with 15 dB SNR and (d) 9 dB SNR.

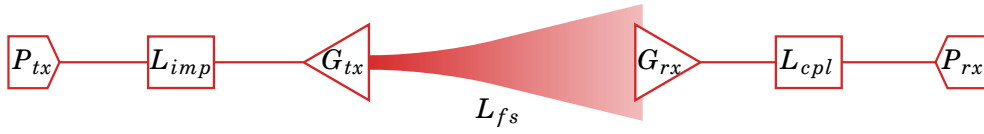


Figure 2.7: A free-space optical link, with link budget gain and loss terms.  $P_{tx}$ : fibre transmit power,  $L_{imp}$ , implementation losses,  $G_{tx}$ : transmitter telescope gain,  $L_{fs}$ : isotropic free-space loss,  $G_{rx}$ : receiver telescope gain,  $L_{cpl}$ : fibre coupling loss,  $P_{rx}$ : received power.

The receiver telescope, with diameter  $D_{rx}$ , applies a gain,  $G_{rx}$ , representing the directivity of the receiver. Assuming diffraction-limited performance, the receiver gain is

$$G_{rx} = \left( \frac{\pi D_{rx}}{\lambda} \right)^2. \quad (2.10)$$

The demonstrations described in this thesis were conducted on retroreflected, or ‘folded,’ links, which are a modified case of the point-to-point configuration illustrated in Figure 2.7. In a retroreflected link, a CCR is placed at the remote end and allows a single telescope to be used for transmission and reception. Co-locating the transmission and reception systems makes comparison of outgoing and incoming signals over long distances convenient, as feedback from a remote site would require dedicated fibre infrastructure. The on-axis loss term for the CCR is [85]

$$L_{ccr} = \rho_{ccr} \left( \frac{\pi D_{ccr}}{\lambda} \right)^2, \quad (2.11)$$

where  $\rho_{ccr}$  is the CCR’s surface reflectivity and  $D_{ccr}$  is its diameter. Multiplying  $L_{ccr}$  by the CCR area yields the optical cross section of the reflector [85]. However, power returned by a CCR is also sensitive to the incident angle. Furthermore, the CCR shape imparts complex distortions onto the optical signal wavefront, making it difficult to analytically model the true effects of the CCR. The link budget analyses described in Chapters 3–6 do not consider the optical cross section because of the complexity of these effects; hence, loss associated with the CCR is intended to be taken up in the link margin. Future work could address this through numerical simulations.

Finally a fibre coupling loss,  $L_{cpl}$ , is included to represent the optical signal power able to be coupled into the waveguide modes of the fibre. Fibre coupling is strongly dependent on the random effects of atmospheric turbulence and the stabilisation systems used to combat turbulence. Fibre coupling is discussed further in Section 2.1.5.

### 2.1.5 Fibre Coupling

The fibre coupling efficiency quantifies the amount of optical signal power lost when it is injected from the free-space receiver optics into an optical fibre. In FSO communications, optical fibre is required to carry optical signals from receiver optics to the detector. While non-fibre-coupled detectors may be used in low bandwidth communications, the three demonstrations described in Chapters 4, 5, and 6 utilised fibre-coupled equipment, so non-fibre-coupled detectors are not discussed further. These demonstrations also exclusively used single-mode fibre (SMF), a type of optical fibre capable of supporting only one spatial mode. This constraint on spatial mode is necessary in the coherent communications systems described in Chapters 4 and 5, as coherent detection relies on the received signal matching the spatial mode of the local oscillator signal for phase sensing [26]. HPE communication, relevant to Chapter 6, does not necessarily require an SMF-coupled detector, but one was used in the work described therein, because of the available equipment. The magnitude of  $L_{cpl}$  may be calculated from an overlap integral of the incoming FSO signal wavefront, and the mode field diameter of the SMF [86], determining how much of the signal is injected. Furthermore, FSO signals propagating through the Earth's turbulent atmosphere undergo time-varying wavefront distortions, so the  $L_{cpl}$  is constantly modulated as the overlap integral varies. An introduction to atmospheric physics follows, explaining the structure of eddies in the atmosphere, their evolution in time, and how this introduces the deleterious wavefront distortions in optical signals.

## 2.2 Atmospheric Optical Communications

### 2.2.1 Atmospheric Turbulence

The Earth's turbulent atmosphere is composed of eddies of air with varying temperature, humidity, and size, leading to refractive index variation. Figure 2.8 illustrates this regime of eddies of varying refractive index and varying size, along the FSO link. The outer scale,  $L_0$ , is the largest length scale where energy enters the channel, mainly due to wind shear along Earth's surface [87]. In horizontal propagation close to the Earth, the outer scale is approximately the altitude of the transmitter. The inner scale,  $l_0$ , is the beginning of the dissipation range, where energy in the eddies is lost to heat due to the viscosity of the air.

Spectral models describe the probabilistic distributions of the spatial scales of eddies with differing refractive index through power spectral density (PSD) functions [59, 87, 88]. The spectra are plotted against the reciprocal space wavenumber,  $\kappa$ , where  $\kappa = 2\pi/l$ , with  $l$

being length. Chapter 3 considers two such models, the Kolmogorov model and Greenwood-Tarazano model. The PSD for each model is shown in Figure 2.9, and the equations are as follows. The Kolmogorov PSD,  $\Phi_n(\kappa)$ , is defined between the  $\kappa$  values corresponding to the outer and inner scale lengths,

$$\Phi_n(\kappa) = 0.033C_n^2\kappa^{-11/3}, \quad 2\pi/L_0 < \kappa < 2\pi/l_0, \quad (2.12)$$

where  $C_n^2$  is the refractive index structure constant with units of  $m^{-2/3}$ . The Greenwood-Tarazano model extends the PSD definition below the outer scale,

$$\Phi_n(\kappa) = 0.033C_n^2(\kappa^2 + \kappa/L_0)^{-11/6}, \quad 0 < \kappa < 2\pi/l_0. \quad (2.13)$$

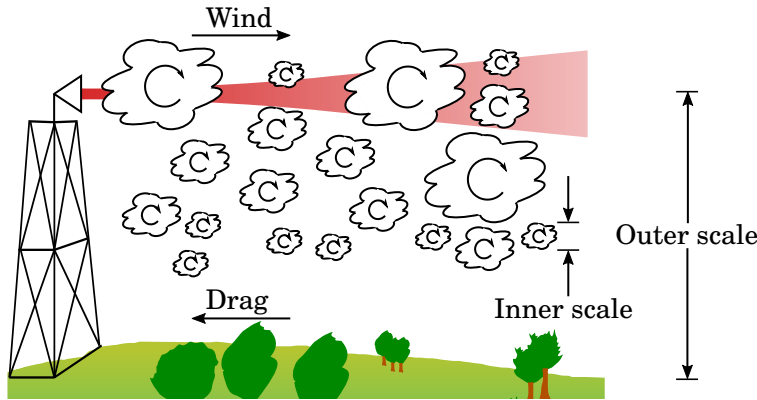


Figure 2.8: Illustration showing atmospheric turbulence structure with respect to a horizontal free-space optical transmitter.

In the Greenwood-Tarazano model, the outer scale defines an inflection point in the spatial PSD at low wavenumbers, as can be seen in Figure 2.9. Other models, not considered in this thesis, incorporate a high-wavenumber cut-off, in an attempt to capture the dissipation effect of the inner scale.

In the spectral models, the refractive index structure constant,  $C_n^2$ , scales the PSD and is a common means of specifying turbulence strength between deployments. However, different consideration is required for ground-ground and ground-space optical paths because the refractive index structure constant is dependent on height above ground. A commonly-used model for structure constant is the Hufnagel-Valley model [56],

$$C_n^2(h) = 0.00594(w/27)^2(10^{-5}h)^{10} \exp(-h/1000) + 2.7 \times 10^{-16} \exp(-h/1500) + A \exp(-h/100), \quad (2.14)$$

where  $h$  is the height above ground,  $w$  is a windspeed and  $A$  is the  $C_n^2$  at ground-level. Figure 2.10 shows the  $C_n^2$  profile using the Hufnagel-Valley 5/7 model, a common configuration when using the Hufnagel-Valley model, where  $w = 21$  m/s, and  $A = 1.7 \times 10^{-14} \text{ m}^{-2/3}$  [56].

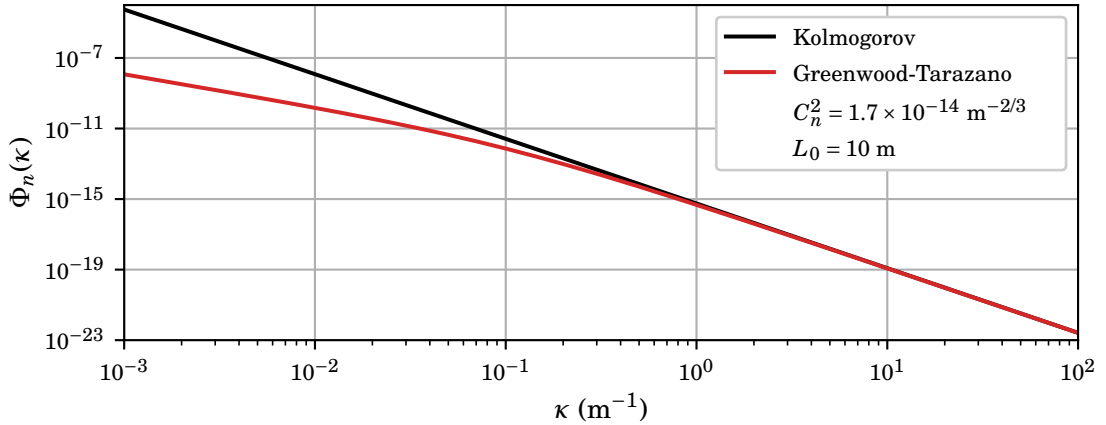


Figure 2.9: Refractive index power spectral density (PSD),  $\Phi_n$ , as a function of wavenumber,  $\kappa$ , for the Kolmogorov and Greenwood-Tarazano models for refractive index structure, with fixed structure constant,  $C_n^2$ . The Kolmogorov model is only defined between the wavenumbers corresponding to outer scale,  $L_0$ , and inner scale,  $l_0$  (not indicated). In the Greenwood-Tarazano model, the PSD is defined below  $L_0$ .

For ground-space optical links, typically above  $10^\circ$  in elevation, spectra must be evaluated in a series of layers with the varying  $C_n^2$  [88, 89]. For ground-ground paths at low elevation angles,  $C_n^2$  can be assumed to be constant and, therefore, only a single spectrum is required to characterise the refractive index structure. This assumption for ground-ground links is also convenient for later calculations involving path integrals of  $C_n^2$ . At optical frequencies,  $C_n^2$  can be estimated from spatially-distributed temperature measurements [59, 87]. However, distributed measurements are not usually possible, so it is desirable to be able to estimate atmospheric conditions from temporal measurements of FSO signals. Vice-versa, it is also desirable to use a known  $C_n^2$  to predict the dynamics of FSO signals in the atmosphere. Sections 2.2.2 describes the effects of atmospheric turbulence on optical signals. This starts with the relationship between FSO phase and AoA spectra and the spatial spectra of Equations 2.12 and 2.13.

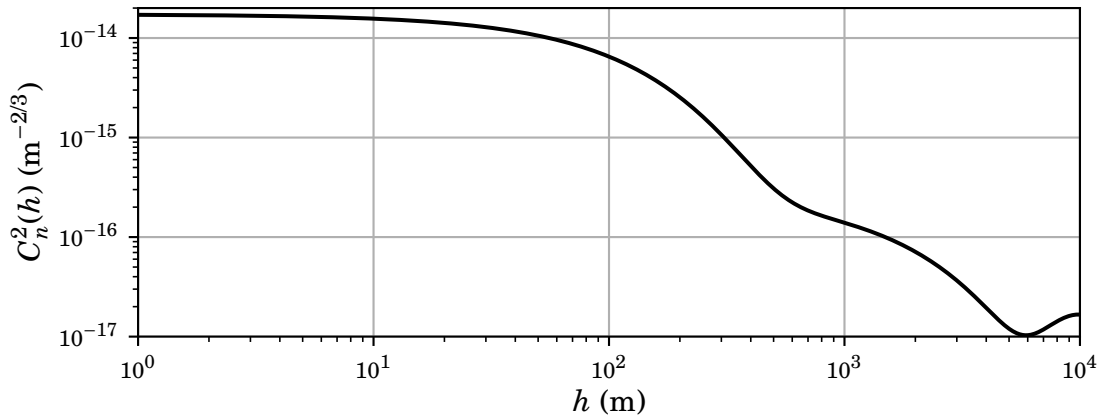


Figure 2.10: Graph showing the refractive index structure constant,  $C_n^2$ , versus height-above-ground,  $h$ . This is based on the Hufnagel-Valley 5/7 model, assuming a wind-speed of 21 m/s, and  $C_n^2$  of  $1.7 \times 10^{-14} \text{m}^{-2/3}$  at ground level.

## 2.2.2 Optical Signal Propagation in Turbulence

FSO signals propagating through Earth’s turbulent atmosphere experience deleterious effects due to the refractive index variation. The temporal statistics of atmospheric FSO signals are analysed by applying Taylor’s frozen turbulence hypothesis to the spatial spectra introduced in Section 2.2.1 [59, 88]. This assumes the refractive index structure is constant along the optical path, and a constant wind sweeps the turbulence perpendicular to the optical signal’s path. The frozen turbulence hypothesis is frequency limited, with a cut-off frequency proportional to the windspeed. Chapter 3 provides the mathematical results of this mapping, along with measurements of an FSO signal’s phase and AoA spectra. What follows here is a series of intuitive explanations for the effect of atmospheric turbulence on FSO signals.

As an FSO signal propagates through the atmosphere, it experiences refraction and diffraction effects to varying degrees due to the changes in refractive index between eddies and the diffraction-limiting effect of relatively small eddies, respectively [61, 87]. The relative contribution of each of these effects is dependent on the optical wavelength, link distance, and transceiver aperture size. A description of the turbulence strength can be loosely assigned depending on the dominant effect. Refraction tends to dominate under ‘weak’ turbulence, adding phase noise and inducing AoA variation. These are the zeroth order and first order disturbances described in Chapter 1. Diffraction becomes effective in ‘strong’ turbulence conditions, causing higher order disturbances and greatly degrading fibre coupling.

### 2.2.3 Weak Turbulence

Refraction occurs when an optical signal passes between regions of varying refractive index and therefore changes its velocity, advancing or retarding the signal's phase. Under weak turbulence, the inner scale is large compared to the first Fresnel zone, defined as

$$\sqrt{L\lambda}, \quad (2.15)$$

where  $L$  is the separation between the transmitter and receiver. Taylor's theory of frozen turbulence provides a PSD for the phase of a plane wave travelling through turbulence and this provides insight into the time-varying phase of the optical signal. Phase noise greatly affects interferometric measurements made with highly stable lasers [57, 58, 90] but is currently not a dominant effect in phase-dependent FSO modulation formats because of the relatively unstable optical sources in use [60]. However, refraction also induces an angular change to the direction an optical signals travels, according to Snell's law.

First order AoA variation is of interest in FSO communications because it directly impacts SNR by reducing received power. Chapter 3 describes how the AoA spectrum is derived by scaling the phase noise spectrum for a planar wavefront [88]. AoA changes close to the transmitter induce beam wander, thus steering the beam off the receiver. In ground-space links, the impact depends on the propagation direction, as follows with reference to Figure 2.11. Intuitively, as  $C_n^2$  decreases with increasing altitude, per Equation 2.14, the distribution of eddies tends towards greater a proportion of larger eddies compared to smaller eddies at higher altitudes. Ground-to-space uplink, shown on the left side of Figure 2.11, suffers from beam wander, as early contact with the atmosphere leads to gross pointing errors. The difficulty of atmospheric uplink pre-compensation makes it an active field of research [89, 91]. Smaller auxiliary apertures close to the ground station are often used for uplink because the greater wavefront divergence will offset beam wander at the expense of lower transmitter gain. In downlink from space-to-ground, an optical signal propagates through space initially, without experiencing atmospheric effects until it has widely diverged. Therefore, downlink signals do not experience the same magnitude of beam wander as uplink signals. This link geometry in downlink leads to high order wavefront variations contributing greatly to scintillation.

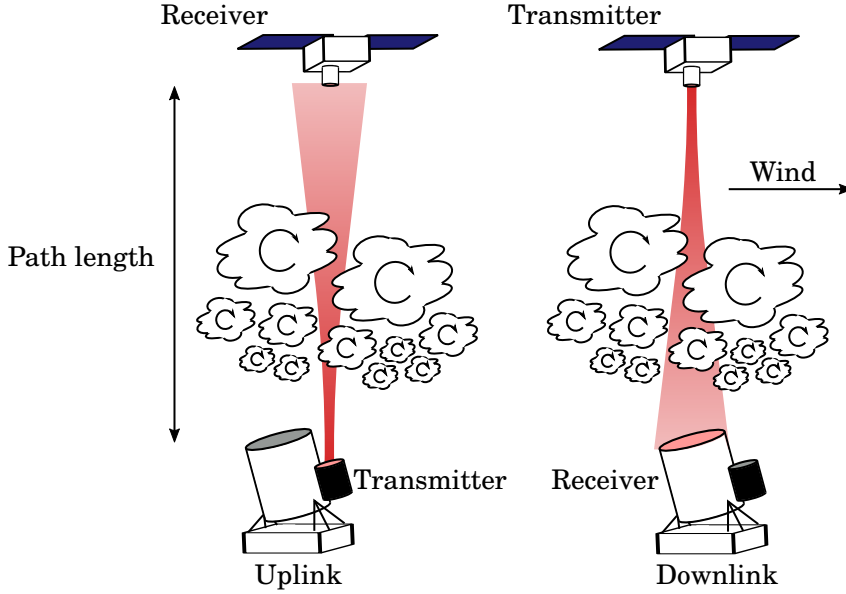


Figure 2.11: Illustration of atmospheric channel for free-space optical communications in uplink, using an auxiliary aperture and downlink, receiving with the full-sized telescope aperture.

### 2.2.4 Strong Turbulence

In strong turbulence, where the Fresnel zone, of Equation 2.15, is larger than the inner scale, diffraction effects are incurred in addition to the described refraction effects. The scale of eddies in strong turbulence leads to random focusing, defocusing, and phase shifts along the wavefront. This manifests as wavefront speckle, meaning random variations in amplitude and phase across the wavefront [56, 86]. Speckle is experienced in all atmospheric FSO propagation to some degree, regardless of turbulence strength. However, strong turbulence is considered to be in effect when the speckle causes reduction in the mean received intensity and significant variation in the intensity. A speckled wavefront imaged at a SMF tip will result in a low coupling efficiency from the overlap integral with the waveguide mode of the fibre [86]. For a quantitative definition, speckle size is often characterised in terms of the Fried parameter,  $r_0$ . For a plane wave,  $r_0$  is

$$r_0 = \left( 0.423k^2 \int_{Path} C_n^2(z) dz \right)^{-3/5}, \quad (2.16)$$

with  $k$  being the wavenumber at the optical signal's wavelength, that is,  $k = 2\pi/\lambda$ . The Fried parameter is a length scale describing the diameter of the smallest transverse subsection of the signal wavefront with no more than 1 radian of phase deviation. It implies a diffraction limit in observing the wavefront. On horizontal links the  $C_n^2$  is

assumed to be constant and the integral in Equation 2.16 becomes a product of  $C_n^2$  and path length,  $L$ . The Fried parameter over a given horizontal distance can therefore be equivalent to the Fried parameter of a much longer ground-space distance because of the rapid drop-off in  $C_n^2$  with altitude. The ratio of receiver aperture diameter-to-Fried scale,  $D/r_0$ , is commonly quoted to provide a normalised indication of turbulence strength observed by an optical receiver. Large receivers, with  $D/r_0$  greater than one, will observe many speckles, and the receiver will require higher order AO to couple the signal into fibre efficiently. A receiver with a  $D/r_0$  of one or less will generally experience only the refractive effects of atmospheric turbulence because it will only capture one speckle at a time.

Scintillation refers to temporal fluctuation in received optical power about a mean value. The mean received power of a scintillated wavefront will generally be lower than the received power predicted by a link budget. Additionally, random focusing and defocusing of the beam by smaller turbulent eddies leads to time-varying increasing and decreasing of power. A signal received through weak turbulence is not expected to exhibit temporal power variation due to negligible wavefront disturbances; however, scintillation is still observed at the receiver due to beam wander. Scintillation index,  $\sigma_I$ , can be measured from a receiver's photodetector voltage as

$$\sigma_I = \frac{\sigma_v^2}{\mu_v^2}, \quad (2.17)$$

where  $\sigma_v^2$  and  $\mu_v$  are the variance and mean of the voltage, respectively, assuming linear photodetector response. A scintillation index  $\ll 1$  is considered to indicate weak turbulence. Analytical expressions have been developed to model scintillation index from atmospheric conditions [56, 87, 92]. However, applying the correct expressions can be difficult because of the numerous different conditions regarding Fresnel zone size, aperture size, inner scale, and so on. Under strong turbulence in particular, the scintillation measurement will saturate, leading to underestimation of the  $C_n^2$  parameter, although expressions have been derived to account for this [92, 93]. Such models were used sparingly in this project. When scintillation indices were measured, they were intended to indicate the fluctuation conditions the optical signal was experiencing. Where relevant, consideration was given to the likelihood of saturation at the receiver aperture. As computing power increases into the future, it may become more practical to simulate specific atmospheric turbulence conditions using numerical simulation suites [94–96], rather than trying to adapt context-specific analytical models.

### 2.2.5 Atmospheric Measurement and Stabilisation

Techniques, particularly those from the field of optical astronomy, have been developed to measure and stabilise the effects of atmospheric turbulence on optical signals. Phase noise is directly measured through interferometry [58, 59, 88] and an example of phase noise measurement on a real link is given in Chapter 3. Phase variation may be stabilised by mechanical piston-like action in an optical element such as a FSM, or corrected in fibre using a photonic actuator, such as an acousto-optic modulator [57, 97]. In the case of the acousto-optic modulator, the frequency of the carrier is shifted and phase fluctuations are suppressed by phase-modulating the signal driving the modulator. This adds a deterministic phase rotation to the signal that can be removed by digital signal processing, while suppressing atmospheric phase noise fluctuations. However, phase noise is not significant to the communications-focused work in this thesis; therefore, phase noise stabilisation is not discussed further.

Measuring and stabilising AoA variation is significant to all of the demonstrations described in this work. Figure 2.12 depicts a first order AO system, also known as a TT system, comprising a FSM and a spatial position detector (SPD). Such a system measures AoA variation by sampling part of an incoming signal with a beam splitter, and directing the sampled signal to the SPD. An SPD reads the position of an incident optical signal and emits an electrical signal proportional to position. Two examples of an SPD are the QPD, and infrared-sensitive camera. A QPD provides an analog voltage readout, and typically provides lower latency and cost than a camera. On the other hand, a camera provides higher precision in the position determination. Usage of both has been reported in the literature, with the QPD used in systems with low  $D/r_0$  [39, 72], and cameras suited to large OGS systems with high  $D/r_0$  [68]. Sensed position signals are forwarded to proportional, integral, derivative (PID) controllers to drive the actuators of the FSM [57]. A fiber-to-free-space collimator (FFC) is used to couple the FSO signal into fibre, and so co-alignment of the QPD and FFC is critical. While Figure 2.12 indicates AoA correction with independent PID controllers per axis, an integrated multi-input, multi-output controller could be used to compensate for misalignment and unwanted coupling between the FSM axes.

TT systems are generally required in all levels of turbulence strength; however, in strong turbulence, speckle is modulated onto the wandering optical signal, requiring an additional layer of higher order AO stabilisation.

Higher order AO is required to maximise the fibre coupling of large telescopes in strong turbulence. Conventional AO systems use a wavefront sensor, capable of measuring the

phase of sections across an incoming wavefront, to control a deformable mirror shaped by an array of linear actuators [98]. AO systems are often found on astronomical telescopes, with large  $D/r_0$  ratios, to sharpen image quality closer to the diffraction limit of the aperture. In astronomy, a ‘guide star’ is required to provide a reference image for the wavefront sensor. However, in FSO communications, the incoming optical communications signal may be used as a guide star.

An alternative high order stabilisation technology, based on mode-converting devices, has emerged. A mode-converting device can decompose a speckled optical wavefront into multiple orthogonal waveguide modes. Each of these modes is then coupled into multiple SMF outputs. The multiple SMF outputs of the mode converting device each carries the same signal, with slight phase variations, and can be recombined [99, 100]. This technology promises a simpler system than conventional AO, without any moving parts, but remains experimental. No high-order stabilisation was used in this work. Turbulence bordering on weak-to-strong turbulence was experienced in the measurement campaigns and only first-order stabilisation was deployed.

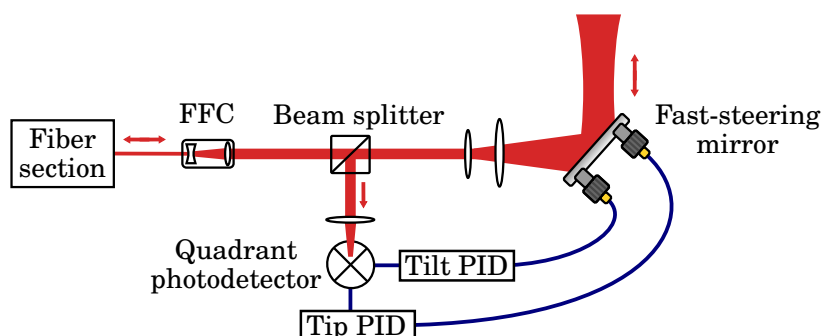


Figure 2.12: First order adaptive optics, or tip-tilt, system diagram illustrating the feedback connection between the quadrant photodetector and fast-steering mirror. Proportional-integral-derivative (PID) controllers are used to filter the quadrant photodetector signals. The system aids in pointing to the free-space-to-fibre coupler (FFC).

### 2.2.6 Spacecraft Proxies

FSO communications has not yet been widely taken up for day-to-day space missions. Furthermore, significant resources are required to make contact with any of the small number of spacecraft with optical terminals, making the endeavour risky for unproven hardware. This promotes the use of spacecraft proxies to fulfil the capability demonstration gap. Chapter 4 details the use of a CCR at one end of a relatively long horizontal link to simulate a GEO telecommunications satellite. This is extended to a

drone-borne CCR in the demonstrations reported in Chapters 5 and 6. In the corresponding demonstrations, the drone is subject to wind buffeting, adding additional AoA variation and requiring use of an astronomical telescope mount with altitude and azimuth control to increase the tracking range.

In the case of Chapter 5, the drone was required to act as a proxy for a LEO satellite. For a LEO satellite in a circular orbit at an altitude of 300 km, the tangential velocity,  $v_0$ , is calculated by rearranging Kepler's third law [101],

$$v_0 = \sqrt{GM_E/R_0}, \quad (2.18)$$

where  $G$  is the gravitational constant,  $M_E$  is the mass of the Earth, and  $R_0$  is the average distance from the centre of the Earth to the satellite. This yields a tangential velocity,  $v_0 = 7.73$  km/s. At the apex of flight over an OGS, taking the arctangent of the ratio of this velocity to the altitude corresponds to a maximum angular tracking rate of

$$\arctan(7.73/300) = 1.5^\circ/\text{s}. \quad (2.19)$$

The angular tracking rate is reduced for lower elevation angles. For example, at  $45^\circ$  the rate is

$$\arctan\left(\frac{7.73}{300\sqrt{2}}\right) = 1.0^\circ/\text{s}. \quad (2.20)$$

Tracking simulations were achieved by commanding the drone to slew back and forth within the allowable flight zone, while the telescope mount accelerated to the desired angular rate. Two key dissimilarities from a true LEO pass are the lack of appreciable Doppler shift at such tangential velocities and the relatively low possible geometric losses. However, this proxy method provides an extremely convenient means to have an OGS 'on sky' prior to significant investment of time and money.

## 2.3 Laser Safety

Optical signals are a hazard as they may cause permanent damage to human skin or eyes, possibly leading to blindness. In the apparatus described in this work, it is possible for unguided optical signals to be encountered at the output aperture of an optical terminal. Exposure may also result from an insufficiently sealed internal section of the optical terminal or from an energised and unconnected optical fibre. Calculations and risk controls based on the AS/NZS IEC 60825.14:2011 standard [102] follow. At 1550 nm, optical signals bypass the cornea and are absorbed by water in the eye, contributing to a maximum permissible exposure (MPE) of  $1000 \text{ Wm}^2$  for any exposure above 10 s. Skin

exposure is a secondary hazard to eye exposure at 1550 nm. Nominal ocular hazard distance (NOHD) is the minimum eye-safe distance for unprotected exposure to collimated optical signals from a laser source. For a Gaussian beam,

$$\text{NOHD} = \frac{1}{\theta} \sqrt{\frac{4P_o}{\pi \text{MPE}}} - \frac{a}{\theta}, \quad (2.21)$$

where  $\theta$  and  $a$  are the full-angle divergence and waist diameter of the beam, respectively, and  $P_o$  is the optical signal power. Table 2.1 provides the waist size, beam divergence, and NOHD for the power levels used in Chapters 4, 5, and 6. Divergence from an unconnected or broken fibre is modelled as having a waist diameter equivalent to the mode-field diameter of the fibre and divergence,  $\theta_{SMF}$ ,

$$\theta_{SMF} = \frac{\lambda}{\pi \text{MFD}/2}, \quad (2.22)$$

where MFD is the mode-field diameter, 10.4  $\mu\text{m}$  for the fibre in use [103]. In the case of the FFC and Galilean beam expander, the waist size and divergence were given by the manufacturer [104] and derived from the expansion ratio, respectively.

Table 2.1: Nominal ocular hazard distance (NOHD) for 1550 nm optical signals used in demonstrations. FFC: fibre-to-free-space coupler, GBE: Galilean beam expander.

		Fibre	FFC	15×GBE
	Spot diameter [m]	$1.04 \times 10^{-5}$	$1.60 \times 10^{-3}$	$2.40 \times 10^{-3}$
	Divergence [rad]	0.190	$1.30 \times 10^{-3}$	$8.70 \times 10^{-5}$
Ch. 3	NOHD (10 mW) [m]	0.019	1.5	No hazard
Ch. 4	NOHD (760 mW) [m]	0.16	23	82
Ch. 5 & 6	NOHD (30 mW) [m]	0.032	3.5	No hazard

Risk assessment procedures involve reasonable estimations of likelihood and severity of exposure to hazards, followed by implementation of controls. Ocular exposure from the FFC or beam expander were the hazards most likely to occur compared to other concerns, such as manual handling, trip hazards, or electrocution. Ocular exposure at the fibre tip or a broken fibre was also included but exposure to an energized, unconnected fibre was considered to be far less likely than the other sources, based on past experience. Once identified, engineering controls, administrative controls, and personal protective equipment were implemented, to the effect that the signals did not represent a hazard to nearby members of the public or pilots of aircraft overhead.

### 2.3.1 Engineering Controls

Engineering controls involve permanent physical mitigation or elimination of hazards. In the first two cases of Table 2.1, the optical signal exposure was hazardous, both out of the

fibre tip and FFC, while also being hazardous from the beam expander in the second case. As an engineering control, the optical path inside the terminal was enclosed, including enclosed beam traps on the unused ports of the beam splitters attached to the FFC. Optical signal emission was directed outdoors, and in the second case, the NOHD extended out of the building. In the second case, the outdoor hazard area reasonably encompassed by the ocular hazard was inaccessible, due to the height of the room relative to occupied structures nearby. Trees and buildings close to the ground also prevented observers on the ground within 82 m from observing the aperture. In the third case, involving outdoor demonstration in Chapters 5 and 6, a rigid enclosure was constructed to prevent specular reflections from the FFC escaping. It featured only one forward-facing aperture to allow the optical signal from the beam expander out.

### 2.3.2 Administrative Controls

Administrative controls were implemented through access control to the fifth-floor rooms hosting the equipment, preventing anyone without the appropriate laser safety training and approval from entering unaccompanied. This ensured any equipment operators were aware of the hazard and enforced competency requirements for risk exposure. The room also had local-regulation compliant warning signage at the entryway. It was also an administrative policy for windows in the room to be open, thus preventing any specular reflections from the outgoing signals.

### 2.3.3 Personal Protection

Laser safety goggles can be used to reduce the exposure of optical signals to below the MPE. Goggles require an optical density (OD) according to the maximum potential eye exposure,  $H_P$ ,

$$OD = \log_{10} \left( \frac{H_P}{MFD} \right). \quad (2.23)$$

The highest  $H_P$  case is calculated from the highest power used, in Chapter 4, and eye aperture diameter

$$H_P = \frac{760\text{mW}}{\pi(0.0035/2)^2} = 7.9 \times 10^4 \text{W/m}^2. \quad (2.24)$$

The required OD is then

$$OD = \log_{10} \left( \frac{7.9 \times 10^4}{1000} \right) = 1.9, \quad (2.25)$$

and goggles with an OD of 7 were procured to ensure eye safety. These were required to be worn by all room occupants during optical emission.

---

---

## CHAPTER 3

---

# Atmospheric Turbulence Characterization in a Retroreflected Optical Link

Chapter 3 concerns the physics of retroreflected optical links, also referred to as folded links, making use of a CCR. The work aimed to justify the subsequent use of folded links in demonstrations for commissioning OGS hardware. This was accomplished through analysis, using the models introduced in Chapter 2, validated with the results of a measurement campaign on a 2.4 km folded link exhibiting a range of turbulence strengths. Folded links differ from point-to-point links involving a transmitter and receiver at opposing ends—the optical signal passes through the same turbulent medium twice, and experiences wavefront clipping by the CCR. The incidence of AoA variation, despite atmospheric reciprocity in retroreflected links, makes the CCR extremely useful for testing the TT systems required in FSO communications. This work was also the first to simultaneously generate  $C_n^2$  estimations from three independent physical measurements. The outcomes of this work are also relevant to remote optical sensing such as range–rate measurement.

This chapter was published in the journal *Optics Letters*. I am a joint first author on the publication, contributing 40% to the experimental work and data analysis, and 80% to the manuscript preparation. I formulated analytical expressions for AoA and log-intensity, and processed the log-intensity data. Benjamin Dix-Matthews built the apparatus, conducted the experiment, and formulated the expressions pertaining to phase noise and AoA. I was responsible for technical translation of the results into a publication-quality manuscript.

## **Chapter Contents**

---

3.1	Abstract . . . . .	<b>37</b>
3.2	Introduction . . . . .	<b>37</b>
3.3	Materials and Methods . . . . .	<b>38</b>
3.4	Phase Noise . . . . .	<b>39</b>
3.5	Angle-of-Arrival Variation . . . . .	<b>42</b>
3.6	Scintillometry . . . . .	<b>44</b>

---

## Atmospheric Turbulence Characterization in a Retroreflected Optical Link

Benjamin P. Dix-Matthews, Skevos F. E. Karpathakis, Sascha W. Schediwy

Published in the journal *Optics Letters*

### 3.1 Abstract

FSO transmission through Earth's atmosphere is applicable to high-bandwidth data transmission and optical clock comparisons, among other uses. Fluctuations in the refractive index of the atmosphere limit the performance of atmospheric optical transmission by inducing phase noise, AoA variation, and scintillation. The statistics of these deleterious effects are predicted by models for the spatial spectrum of the atmospheric refractive index structure. We present measurements of phase fluctuations, AoA variations, and scintillation, taken concurrently and compared with models for the atmospheric refractive index structure. The measurements are also cross-compared by deriving independent estimates of the turbulence refractive index structure constant  $C_n^2$ . We find agreement within an order of magnitude for derived  $C_n^2$  values for all three metrics.

### 3.2 Introduction

Understanding how atmospheric turbulence affects the propagation of optical beams is important when attempting to transmit optical signals over long distances, with motivating applications including high-speed data transmission [2] and frequency comparisons between optical clocks [105, 106]. Horizontal or slanted optical links are used to connect terrestrial sites on the ground or in the air, and can be point-to-point [57, 107], folded with a mirror-relay [108], or folded with a retroreflector [109–111]. Folded links are advantageous for only requiring access, power, and substantial shelter at one site as transmission and reception hardware can be co-located, with retroreflected links having less stringent pointing requirements. For all these optical links, refractive index fluctuations caused by atmospheric turbulence perturb the propagation of optical beams. Several models have been developed to describe the spatial spectrum of these refractive index fluctuations based on turbulence theory. In this letter, we will focus on the Kolmogorov and Greenwood-Tarazano models [59, 88, 105].

These spatial spectrum models describe the physical structure of the refractive index fluctuations and are thus independent of any specific transmission signal. To determine the effect of the atmosphere on measurable quantities for a specific optical link architecture, the modelled refractive index fluctuations must be integrated over the optical propagation path. To derive temporal statistics, Taylor’s hypothesis of frozen turbulence [88,105] must be used to couple one spatial direction to the time axis by shifting the turbulence model transverse to the link direction at a specific wind speed. Analytically derived statistics for phase noise, AoA, and scintillation will drive engineering decisions for atmospheric optical transmission applications; however, these require understanding of the expected atmospheric turbulence strength. Thus, in-situ characterisation of the atmospheric turbulence conditions for a given optical link is important.

The strength of atmospheric turbulence is typically defined by the turbulence structure constant,  $C_n^2$ , which is obtained by comparing the predictions of atmospheric turbulence models with the statistics of experimentally measured quantities. Many commercial systems, known as scintillometers, rely on scintillation statistics to measure  $C_n^2$ , however, they have a tendency to saturate in high-turbulence regimes [112]. Improved systems relying on AoA measurements to determine turbulence strength have been demonstrated within the FSO communications community [112, 113]. An alternative method based on the measurement of optical phase-fluctuations has been demonstrated within the frequency metrology community [59]. The  $C_n^2$  measurements based on phase-fluctuation data agreed, within an order of magnitude, with independent temperature measurements taken by micrometeorological sensors. This previous investigation, conducted on a uniform range with distributed micrometeorological sensors, encourages the use of phase-fluctuation measurements on optical links where distributed sensors cannot be installed. However, this technique has not yet been compared to turbulence characterisation techniques based on AoA and intensity measurements. In this letter, we examine the agreement between the turbulence strength estimates derived from simultaneous phase, AoA, and scintillation measurements over a retroreflected link.

### 3.3 Materials and Methods

An apparatus for simultaneously measuring optical phase, AoA, and intensity was deployed over a 1.2 km horizontal atmospheric link to a 50 mm diameter CCR, as shown in Figure 3.1. Power levels are indicated at key locations. This apparatus comprises a 1550 nm fibre laser source launched into free-space via a 15× Galilean beam expander. The beam expander has a 43.5 mm diameter aperture, and the outgoing beam has a 17 mm

beam waist radius. In the free-space terminal, the reflected beam is split and partially directed to a QPD to measure AoA, via the voltages  $V_{\Delta x}^{meas}$  and  $V_{\Delta y}^{meas}$ , the difference in voltage between two opposite quadrants. The sum of the quadrant voltages is also recorded as  $V_{sum}^{meas}$ , to derive the scintillation. The remaining beam power is coupled back into SMF and beats with a prompt copy of the transmitted laser to measure the two-way phase shift,  $\phi^{\leftrightarrow}$ . The prompt copy of the laser passes an acousto-optic modulator to frequency-shift the signal, so the heterodyne interference beat can be input to a RF phase meter. QPD voltages were sampled at 1.25 kHz and the phase was sampled at 2 kHz. An anemometer was located on the rooftop, 4 m above the apparatus, recording wind speed and gusts at 300 s intervals.

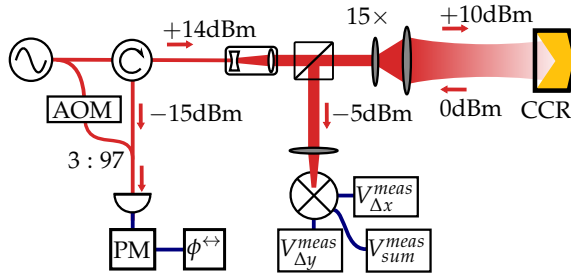


Figure 3.1: Apparatus for measuring phase noise, angle-of-arrival variation and scintillation. AOM: acousto-optic modulator, CCR: corner-cube retroreflector, PM: phase meter.

Three one-hour long measurements were taken under different turbulence conditions and are consistently labelled “low,” “moderate,” and “high” in the remainder of this letter for ease of reference. Phase, AoA, and intensity measurements in each of the low, moderate, and high data sets are compared with models derived from turbulence theory. Finally, rolling predictions of  $C_n^2$  are derived from the phase, AoA, and intensity measurements. The experimental data underlying the results presented in this letter are made publicly available in a repository [114].

### 3.4 Phase Noise

Phase fluctuations are a zeroth order disturbance induced by atmospheric turbulence. Refractive index fluctuations on length scales physically larger than the propagating optical beam will cause variations in the time-of-flight, and thus degrade the phase stability of the received optical beam. For a one-way transmission of a plane wave propagating through Kolmogorov turbulence [59, 88, 105], the single-sided power spectral

density (PSD) of phase noise is expected to be,

$$S_{\phi, \text{Kol}}^{-}(f) = 0.033k^2 C_n^2 L V^{5/3} f^{-8/3}, \quad (3.1)$$

where  $C_n^2$  is the turbulence structure constant for the index of refraction,  $L$  is the path length,  $V$  is the perpendicular wind speed,  $f$  is the Fourier frequency,  $k = 2\pi/\lambda$  is the optical wave-number, and  $\lambda$  is the optical wavelength.

Similarly, the Greenwood-Tarazano turbulence model for a plane wave results in an expected single-sided PSD of,

$$S_{\phi, \text{Gre}}^{-}(f) = 5.211k^2 C_n^2 L/V \int_0^\infty \left[ q_y^2 + \left( \frac{2\pi f}{V} \right)^2 + \frac{\sqrt{(2\pi f/V^2 + q_y^2)}}{L_0} \right]^{-11/6} dq_y, \quad (3.2)$$

where  $L_0$  is the outer scale of turbulence.

These phase noise models describe one-way propagation through atmospheric turbulence. For a two-way atmospheric link reflected by a CCR, the optical beam experiences a phase delay during forward propagation,  $\phi_-(t)$ , and backward propagation,  $\phi_-(t)$ . The phase delay caused by reflection off the CCR remains constant and may be ignored. Phase contributions at timescales below the round-trip time of the two-way link are reciprocal, and thus the total phase delay is  $\phi^-(t) = 2\phi_-(t)$ . Thus, the single-sided PSD of phase noise is,

$$S_{\phi}^{\leftrightarrow}(f) = 4S_{\phi}^{-}(f), \quad (3.3)$$

for  $f < 1/T$ , where  $T = L/c$  is the round-trip time of the link.

Figure 3.2 shows the three phase noise spectra observed, along with fitted lines for Kolmogorov (solid black) and Greenwood-Tarazano (dashed black) phase noise spectra for the low results. The low (blue) and medium (red) phase noise spectra in Figure 3.2 show the characteristic downward inflection at low frequencies of the Greenwood-Tarazano model, Equation 3.2, in the region labelled **b**. The high spectrum (orange) appears to follow the strict  $f^{-8/3}$  trend of the Kolmogorov model spectrum of Equation 3.1 for most of the spectrum with a more subtle downward inflection at low frequencies. Outer scale,  $L_0$ , is estimated by fitting each spectra to Equation 3.2 in the region **b**, and the estimates are given in Table 3.1. The estimates correspond to physically reasonable lengths, close to the approximately 30 m height-above-ground of the apparatus. The high spectrum (orange) in Figure 3.2 exhibits a  $f^{-17/3}$  roll-off above 200 Hz consistent with aperture averaging [88], before dropping to a white noise floor. An average  $C_n^2$  estimate was derived from each spectrum using a non-linear least-squares fit of Equation 3.3 between 90 mHz and

800 mHz, region **a** in Figure 3.2, where all the spectra closely follow the  $f^{-8/3}$  Kolmogorov trend, and do not contain any noise spurs. These values are given in Table 3.1. This technique is used to estimate rolling  $C_n^2$  from phase measurements later in this letter.

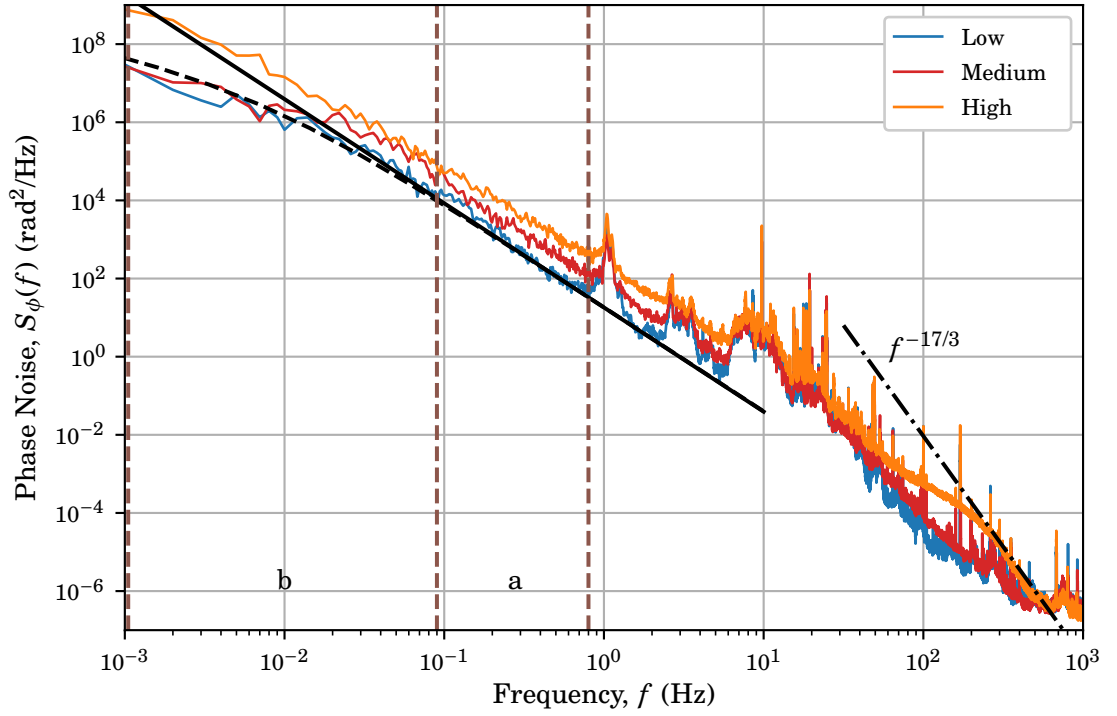


Figure 3.2: Phase noise power spectral densities for three measurement runs. Two analytical models are fitted to the low turbulence measurement (blue) in the region labelled **a**. The solid black line is the Kolmogorov spectrum model. The dashed black link is the Greenwood-Tarazano spectrum model. In the region labelled **b**, inflections due to outer scale effects are seen for the low and medium measurements. The dash-dot line follows a  $f^{-17/3}$  slope expected due to aperture averaging.

Table 3.1: Summary of turbulence regimes, with datum  $L_0$  and  $C_n^2$  values based on the observed phase noise spectra. The  $C_n^2$  is fit to the spectrum from 90 mHz to 800 mHz.

Name	$L_0$ [m]	$C_n^2$ [ $m^{-2/3}$ ]
Low	51.9	$1.25 \times 10^{-15}$
Medium	30.8	$4.84 \times 10^{-15}$
High	35.8	$1.52 \times 10^{-14}$

### 3.5 Angle-of-Arrival Variation

First order AoA variations lead to the optical beam wandering off-target. For a one-way link, the single-sided PSD of AoA fluctuations can be modelled in terms of the phase noise [88, 105],

$$S_{\alpha}^{-}(f) = (\lambda f/V)^2 S_{\phi}^{-}(f). \quad (3.4)$$

Relating the AoA for a two-way link with a CCR to the one-way AoA is more complicated than in the phase case. For a perfectly flat wavefront, variations in AoA during the forward propagation are cancelled in backward propagation, whether or not the beam underfills the CCR. However, for any other beam wavefront geometry, such as spherical or Gaussian, truncation at the CCR results in an additional AoA change not suppressed in the backward propagation, thus resulting in measurable AoA fluctuations over the two-way link [115]. Thus, the relationship between the one-way and two-way AoA fluctuations is  $\alpha_{\leftarrow}(t) = b\alpha_{\rightarrow}(t)$  where  $b$  is a constant dependent on the specific geometry of the free-space link. Thus,

$$S_{\alpha}^{-}(f) = b^2 S_{\alpha}^{-}(f), \quad (3.5)$$

where  $b \approx 0.74$ , from numerical modelling based on the method in Walsh, 2022 [115], of a 50 mm diameter CCR at a distance of 1.2 km, with beam waist radius of 17 mm and wavelength  $\lambda=1550$  nm.

If temporal information is not required, the expected AoA variance can be obtained from turbulence theory without the need for Taylor's hypothesis of frozen turbulence. For a one-way link, the expected AoA variance is,

$$\text{Var}[\alpha_{\rightarrow}] = 1.093 LC_n^2 D_r^{-1/3}, \quad (3.6)$$

provided that  $(L\lambda)^{1/2} \ll D_r$ , where  $D_r$  is the receiver diameter [112, 113]. The constant at the front of Equation 3.6 is associated with the spherical wave approximation. Thus, by taking into account the relationship between the one- and two-way AoA,

$$\text{Var}[\alpha_{\leftarrow}] = b^2 \text{Var}[\alpha_{\rightarrow}] = 1.093 b^2 LC_n^2 D_r^{-1/3}. \quad (3.7)$$

The AoA fluctuations of the retroreflected optical beam were measured using a QPD, where the incident angle is determined based on the voltage differences caused by the lateral deflections of the imaged beam. This QPD was at a focal point of the receiving optical system and operated in a regime where the returned optical beam was diffraction limited. The diameter of the imaged beam was significantly smaller than the full QPD size. In this regime, an incident AoA deflection in the  $x$ -axis by the diffraction-limited

angular resolution of the optical system will entirely shift the imaged spot between the QPD  $x$ -axis quadrants, causing the normalized voltage difference,  $\overline{V_{\Delta x}}$ , to span  $-1$  to  $+1$ . Thus, assuming linearity in the QPD response, the measured AoA deflections are given by,

$$\theta_{qpd}^x = \frac{\theta}{2} \overline{V_{\Delta x}}, \quad \theta_{qpd}^y = \frac{\theta}{2} \overline{V_{\Delta y}}, \quad (3.8)$$

where  $\theta = 1.22\lambda/D_r$  is the diffraction-limited angular resolution of the optical system,  $\lambda$  is the optical wavelength, and  $\overline{V_{\Delta x}}$  and  $\overline{V_{\Delta y}}$  are the measured  $x$  and  $y$  QPD voltage differences normalised from  $-1$  to  $+1$ . The normalized voltage difference measurements are  $\overline{V_{\Delta x}} = V_{\Delta x}^{meas}/V_{max}$  and  $\overline{V_{\Delta y}} = V_{\Delta y}^{meas}/V_{max}$  where  $V_{max}$  is a design parameter of the QPD. Equation 3.8 will change slightly if the coherence length,  $r_0 = (1.46k^2C_n^2L)^{-3/5}$ , is smaller than the receive aperture. In this case, the angular resolution of the optical system is no longer diffraction limited, and instead  $\theta \approx \lambda/r_0$ . For the high turbulence measurement in Figure 3.3 the atmospherically-limited angular resolution was used.

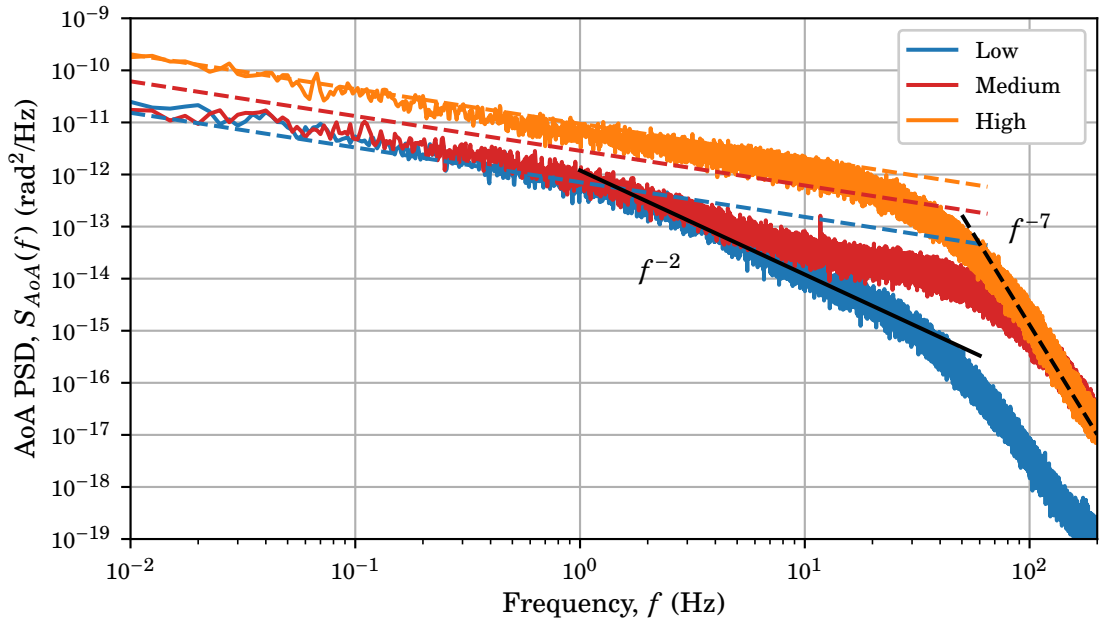


Figure 3.3: Angle-of-arrival power spectral densities for three measurement runs. Fitted dashed lines are provided for each run, showing  $f^{-2/3}$  slopes predicted by the Kolmogorov model.

Figure 3.3 shows the AoA spectra for the three measurements. The three dashed lines represent the expected AoA spectra given by Equation 3.4 assuming the  $C_n^2$  values provided in Table 3.1. Substituting Equation 3.1 into Equation 3.4 predicts an  $f^{-2/3}$  trend, and this is exhibited in all spectra between 10 mHz and 2 Hz. Beyond 2 Hz the low (blue) and medium

(red) spectra roll-off at  $f^{-2}$ , deviating from the expected trend, with the medium spectrum exhibiting an unexpected upwards inflection at 10 Hz. This behaviour is unlikely to be due to atmospheric effects, and may be caused by unexpected behaviour in the QPD, such as sensitivities to spot size and incident power. Similarly, the sharp  $f^{-7}$  roll-off exhibited by all spectra at high frequencies is likely due to the instrumentation. The medium spectrum is also lower than expected for the first two measurement decades, the cause of which we are unsure.

### 3.6 Scintillometry

Scintillation is caused by higher order wavefront fluctuations – when different sections of the wavefront pass through eddies with varying size and refractive index, before meeting at the receiver plane and interfering, thereby causing variation in received power. Scintillation specifically refers to the variance about the mean value [56], and is commonly expressed in terms of the variance of log-intensity,  $\sigma_{\ln,I}^2$ ,

$$\sigma_{\ln,I}^2 = \ln\left(1 + \frac{\sigma_v^2}{\mu_v^2}\right), \quad (3.9)$$

where  $\mu_v$  is the mean, and  $\sigma_v$  is the standard deviation of the voltage at the photodetector [93]. For a horizontal link with uniform  $C_n^2$ , the log-intensity variance is given by

$$\sigma_{\ln,I}^2 = 0.496C_n^2 k^{7/6} L^{11/6}. \quad (3.10)$$

Retroreflected links have been analysed in depth for laser ranging systems [56]. For this link geometry the scintillation of the retroreflected link is equivalent to a link of the round-trip distance. The sum voltage from each quadrant of the QPD,  $V_{sum}^{meas}$ , was used to calculate a rolling log-intensity variance for each dataset, based on Equation 3.9, and substituted into Equation 3.10, to estimate  $C_n^2$ , as shown in Figure 3.4. Rolling estimates of  $C_n^2$  based on phase and AoA measurements are also shown in Figure 3.4. The phase estimate is derived by fitting Equation 3.3 to region **a** in Figure 3.2. The AoA estimates are derived using Equation 3.7. Each rolling estimate is calculated from 100 s subsamples of the full measurement. A detailed explanation of the error bar derivation for these statistical processes, based on methods taken from frequency metrology [116], is provided in the caption.

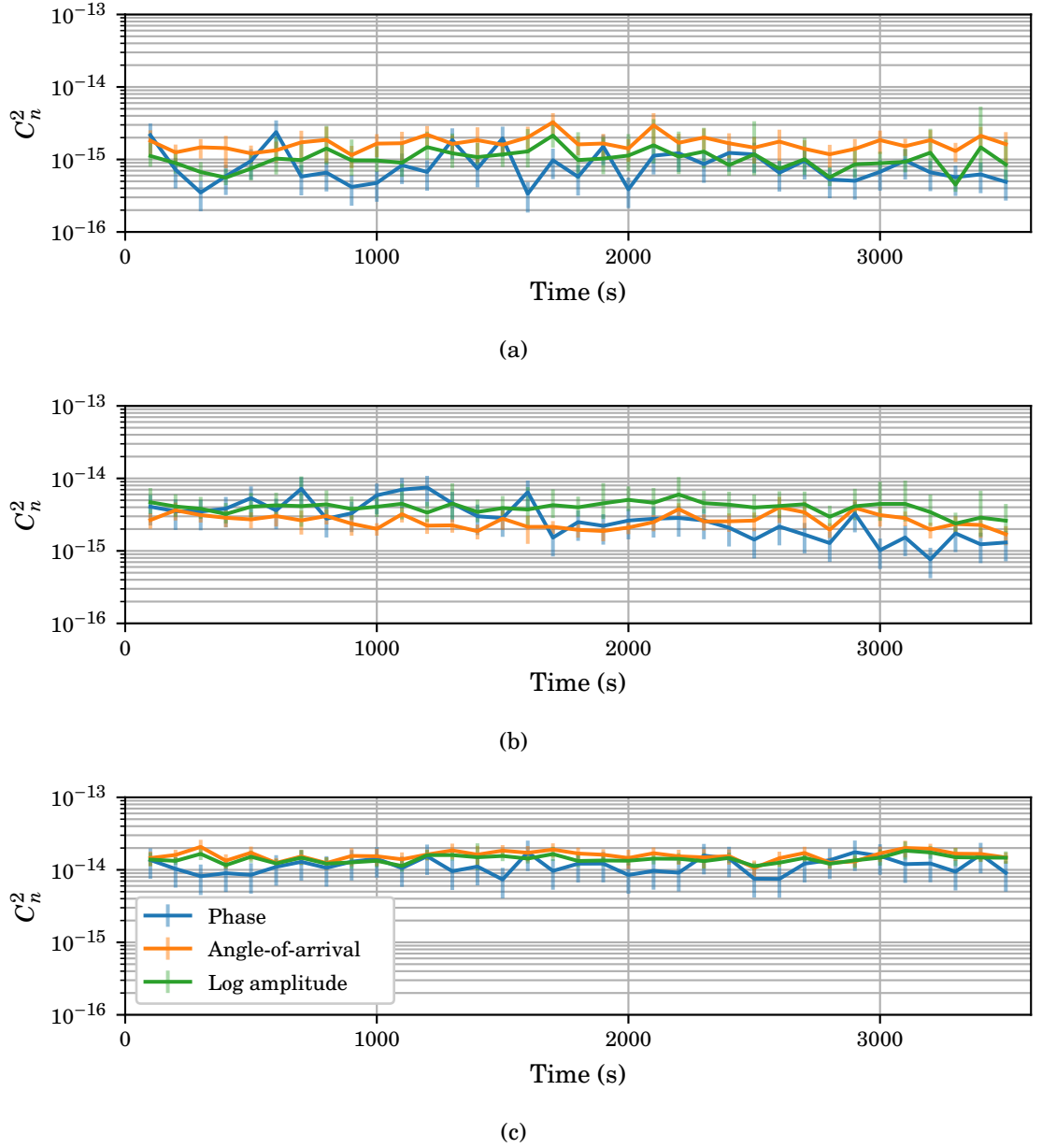


Figure 3.4: Rolling measurement of turbulent structure constant,  $C_n^2$ , based on 100 s samples of phase, angle-of-arrival and intensity measurements. Three separate measurements are given in (a) low, (b) medium, and (c) high turbulence. Error bars indicate the 90% confidence intervals for each parameter. For phase this is  $\pm 1.645\sigma$  calculated from the variance of the fit parameter. The angle-of-arrival and log-amplitude estimates depend on sub-sample variance,  $s^2$ , the value of which is bounded by  $\left[ s^2 \frac{N}{\chi^2(0.95, N)}, s^2 \frac{N}{\chi^2(0.05, N)} \right]$  where  $N$  is the number of independent samples, here defined as  $\frac{N_{total}}{2n_c}$ , where  $N_{total}$  is the total number of sub-samples and  $n_c$  is the time taken, in samples, for the autocorrelation to drop below  $e^{-2}$ .

The rolling  $C_n^2$  estimates are encouraging, reinforcing the case for future development of these turbulence characterisation techniques. Each measurement type agrees within an order of magnitude, with a maximum factor of 2.9 deviation between AoA and scintillation-derived  $C_n^2$  in all conditions, and up to a factor of 6.6 between phase and AoA during low turbulence. In high turbulence, each measurement agrees within a factor of 2.5. Within the disagreement between the measurements, no one measurement appears to be biased to over- or under-estimate the  $C_n^2$  in any of the three cases. Generally, the estimate based on phase noise has a lower tracking bandwidth, as it is based on PSD calculations involving averages over large time windows. The applicability of either technique will depend on the required time resolution, although the latter two measurements can be achieved with only one sensor device, the QPD. Anomalies in the AoA PSDs at high frequencies, as seen in Figure 3.3, has motivated us to consider replacing the QPD with a charge-coupled device.

---

## CHAPTER 4

---

# High-Bandwidth Coherent Optical Communications Over 10.3 km of Turbulent Air

Telecommunications satellites will benefit from the introduction of optical feeder links with downlink rates on the order of tens of terabits-per-second. Such feeder links may be realised using COTS coherent fibre-optic transceivers and dense wavelength-division multiplexing (DWDM) technologies currently used in broadband networks [40]. Horizontal FSO links over many kilometres exhibit equivalent integrated turbulence to space-to-ground links and have been used in initial trials with coherent FSO communications to determine possible data rates [40]. Of these, the VERTIGO demonstration of 1 Tb/s data rate over 53 km holds the record [41]. This chapter reports on the demonstration of a 100 Gb/s-class coherent FSO communications signal transmission over a 10.3 km folded link. In the demonstration, 52 DWDM channels were tested over a 3-hour period. At this distance, first order AO had no effect and was not used. The scintillation index was determined from measurements of received fibre-coupled optical power, providing insight into the fading statistics for a COTS coherent device at a given turbulence strength. Appendix B provides calculations for the scintillation at an OGS. This is compared with scintillation calculated from power measurements on the link described in the chapter. Results in the chapter are presented graphically. Appendix B includes a table of the results.

This chapter was published in the journal *Applied Optics*. I am the first author on the publication, contributing 80% to the experimental work and data analysis, and 90% to the manuscript preparation. This chapter was also submitted as a technical report to the SmartSat Cooperative Research Centre.

## Chapter Contents

---

4.1	Abstract . . . . .	49
4.2	Introduction . . . . .	49
4.3	Methods . . . . .	51
4.3.1	Coherent Transceiver . . . . .	51
4.3.2	Optical Terminal . . . . .	52
4.3.3	Channel Model . . . . .	52
4.3.4	Link Budget . . . . .	53
4.4	Results . . . . .	54
4.4.1	Transceiver Wavelength-Dependence Characterisation . . . . .	54
4.5	Discussion . . . . .	55
4.6	Conclusion . . . . .	56

---

## **High-Bandwidth Coherent Optical Communications Over 10.3 km of Turbulent Air**

Skevos F. E. Karpathakis, Benjamin P. Dix-Matthews, David R. Gozzard, Sascha W. Schediwy

Published in the journal *Applied Optics*

### **4.1 Abstract**

We demonstrate 111.8 Gb/s coherent optical communication throughput over a 10.3 km folded FSO link. Folded links are low-complexity to establish and provide a high uptime for testing equipment. The communications signals were sourced from an unmodified COTS transceiver intended for long-haul fibre networks. A potential DWDM line rate, up to 5.81 Tb/s, was demonstrated by testing 52 optical C-band channels over the course of an evening. In the future, such high-bandwidth communications will be used in feeder links from satellites in GEO. Optical power measurements of the received signal are compared with atmospheric theory to determine the turbulence strength exhibited, and therefore, the applicability of the terrestrial horizontal link to space-to-ground links. We show the high-uptime, 10.3 km laser range is suitable for testing high-bandwidth space-to-ground optical communications systems intended for links from GEO at 20-50° elevation.

### **4.2 Introduction**

Space-to-ground communication using wireless radio and microwave transmissions is facing a bandwidth bottleneck due to increasing quantities of data acquired in space, and beam crowding due to divergence at orbital distances [27]. FSO communications promises to address these emerging issues in traditional space communications, by offering improved bandwidth and lower divergence compared with wireless radio and microwave transmissions. Amplitude modulation was used in early FSO communication experiments, including the first space-to-ground FSO communication demonstration in 1995 [63]. Amplitude modulation has since been used in inter-satellite links [65], and in a cis-lunar space-to-ground link [37]. Coherent communication, using QPSK modulation, offers higher spectral efficiency than amplitude modulation, and future FSO communications from GEO- and LEO-to-ground can use coherent optical communication transceivers to capitalize on established, commonly-deployed, and interoperable terrestrial fibre

technology [26, 117]. In 2022, NASA's TBIRD satellite transmitted data from LEO at 200 Gb/s using two COTS 100 Gb/s coherent transceivers and DWDM [22, 70]. TBIRD successfully transmitted coherent optical signals through Earth's turbulent atmosphere, by using an automatic repeat request (ARQ) protocol. This ARQ protocol was developed using tests on a 3 km folded horizontal link [71].

Transceiver deployments over horizontal terrestrial FSO links are used to inform system design choices to mitigate the effects of turbulence, because horizontal links can exhibit atmospheric turbulence equivalent to, or exceeding, space-to-ground links [39]. In 2019, high-bandwidth coherent communications were demonstrated on a 10.45 km point-to-point link [40]. This demonstration utilised COTS transceivers as well as two optical combs, 200 Gb/s modulators, and DWDM to simulate simultaneous transmission by many coherent transceivers. In doing so, 13.16 Tb/s transmission was achieved, utilising the entire optical C-band, comprising centre wavelengths from approximately 1530 nm to 1564 nm. Other relevant demonstrations over terrestrial laser ranges have been conducted using bespoke communications systems. In a 2022 demonstration, a custom 128 Gb/s single-wavelength transceiver was tested over a 10 km folded laser range [118]. The highest-capacity, longest-distance terrestrial demonstration to date was also conducted in 2022 [41]. This was a point-to-point transmission over 53 km, achieving 1 Tb/s on a single-wavelength by using technologies developed specifically for FSO communications, including higher order AO and coherent beam combining. These publications all describe the likely use-case of high-bandwidth coherent communications to be feeder links from telecommunications satellites in GEO.

This paper presents 111.8 Gb/s coherent communications over a 10.3 km folded horizontal laser range, using a COTS coherent transceiver. Folded laser links are extensively modelled in literature and exhibit comparable channel statistics to point-to-point links when monostatic terminals are used [72], and exhibit AoA variability despite atmospheric reciprocity [115]. Folded links are also low-complexity to establish, compared to point-to-point links, and allow loopback for BER testing. We analyse measurements of the received power to characterize the link conditions and demonstrate applicability of this low-complexity arrangement to a satellite FSO communication scenario. Data was transmitted on 52 channels over a turbulent channel with scintillation indices equivalent to a GEO-to-ground link between 20-50° elevation angle.

## 4.3 Methods

### 4.3.1 Coherent Transceiver

The communications signal under test was generated by a COTS 111.8 Gb/s digital coherent optics (DCO) transceiver, employing dual-polarisation QPSK modulation, and intended for use in a long-distance optical transport network. Functionality is standardised in the management interface specification [119]. The DCO contains a PRBS generator and checker in its transmit and receive sections. The PRBS checker counts received bits and bit errors when enabled, and reports these quantities when disabled. The state of the PRBS checker may be toggled on the fly, allowing a real-time sub-sampling measurement of BER over the link. Figure 4.1 shows the logical mapping of these peripherals to the optical terminal.

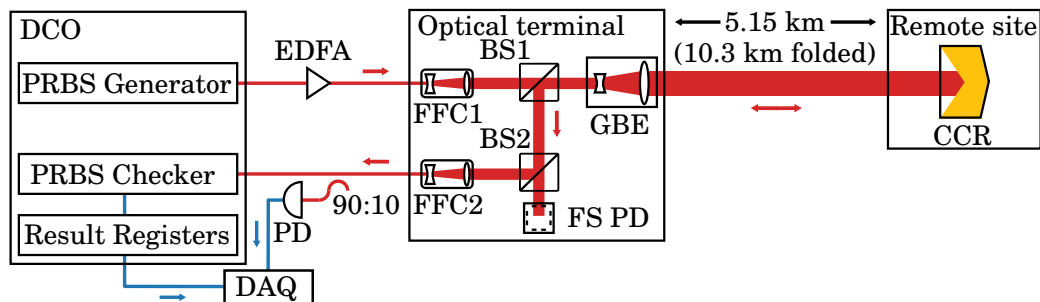


Figure 4.1: Optical transceiver and terminal schematic for demonstration. BS: beam splitter, CCR: corner cube retro-reflector, DAQ: data acquisition, DCO: digital coherent optical module, EDFA: erbium-doped fibre amplifier, FFC: free-space to fibre collimator, FS PD: free-space photodetector, GBE: Galilean beam expander, PD: photodetector, PRBS: pseudo-random binary sequence.

In this demonstration, each sub-sampled measurement is considered to represent a transmission, and the duration of each transmission is a free parameter requiring constraint. Transmissions with duration on the order of 10 ms are useful for characterizing link quality due to atmospheric turbulence causing "bursty" data loss on this time scale [40, 71]. As the PRBS checker provides bit-by-bit comparisons, it does not give insight into the FEC performance internal to the DCO. A pre-FEC BER threshold of  $4.5 \times 10^{-3}$  was selected as the threshold for FEC-correctable transmission, based on the standards for optical transport network FEC [80].

The DCO emission wavelength was varied in order to characterise total throughput available with DWDM and to search for any unexpected wavelength-dependent limitations. The laser inside the DCO is tuneable between 1568.77 nm and 1527.60 nm, or 191.1 THz

and 196.25 THz, in 50 GHz steps. Changing wavelength requires power-cycling the laser, approximately 60 s in duration. These processes, in conjunction with a 30 s measurement duration, limit the number of channels able to be tested during periods of low turbulence. An erbium-doped fiber amplifier (EDFA) was used to boost the DCO output to 26.8 dBm.

### 4.3.2 Optical Terminal

A schematic of the optical terminal is shown in Figure 4.1. The terminal takes a fibre-fed laser input from the DCO and EDFA, and collimates it to free-space via FFC1. The beam splitter, BS1, splits the collimated beam. Half of the transmitted beam is directed to the 50 mm Galilean beam expander, expanding the beam to a 34 mm  $1/e^2$  waist diameter. The 2.5" CCR reflects the beam back, and it passes BS1 before entering the receiver beam splitter, BS2. On passing BS2, half of the beam power is directed back into the collimator FFC2, to couple back into SMF for reception. Fibres with angled end-faces were used to reduce back reflections in fibre. Despite this, with the transmit powers used in this demonstration, a back reflection is observed on the return port of a fibre circulator when the common port was used for launch into an FFC. Thus, the beamsplitter BS2 and separate receive FFC are required to provide separate transmit and receive fibres, as reflections off the fibre end-face were observed to degrade the optical signal-to-noise ratio when the fibres were shared with a circulator. The other half of the received power is directed into a free-space photodetector to measure free-space power,  $P_{FS}$ . A 10% portion of the SMF-coupled power is directed to a fibre-coupled photodetector to measure received power,  $P_{rx}$ .

### 4.3.3 Channel Model

Measurements of the communication channel are used to determine the relevance of this demonstration to FSO space-to-ground communication. The link spans 5.15 km between the optical terminal site and the CCR. The optical terminal is located 29 m above sea level, and the CCR is located 3 m above sea level. This slant path primarily spans the Swan River, Western Australia, and turbulence strength is relatively high at this distance and altitude. Atmospheric turbulence causes random interference in the optical signal wavefront as well as additional divergence, leading to time-varying scintillation of the received power and reducing the coupling efficiency of the FSO signal back into SMF. Scintillation index,  $\sigma_I$ , is a measure of the scintillation in received optical power and is defined

$$\sigma_I = \frac{\sigma_{P_{rx}}^2}{\mu_{P_{rx}}^2}, \quad (4.1)$$

where  $\sigma_{P_{rx}}$  and  $\mu_{P_{rx}}$  are the standard deviation and mean of received power  $P_{rx}$ . For the folded link, the attenuation due to turbulence is the product of two correlated random variables representing the forward and backward paths, and is treated similarly to a conventional one-way link [72]. Turbulence is also characterized by the Fried parameter, a length scale decreasing with increasing turbulence along the link [56].

The relevance of horizontal links to uplink and downlink channels has been investigated by researchers from DLR [39]. They assert the 10 km ground-to-ground link most closely resembles an uplink because the atmospheric turbulence is close to the transmit aperture. The modelling supporting the demonstration suggested scintillation indices of 0.2 and 1 corresponded to ground-to-space uplink to GEO at  $30^\circ$  and  $10^\circ$  elevation, respectively. An elevation of  $30^\circ$  was stated to be the practical worst case for a GEO link. The aperture diameter in the modelling was not discussed. For the folded link concerned in this manuscript, with CCR at 5.15 km from the transmitter, calculations given in Appendix B shows that the Fried parameter is close to the beam  $1/e^2$  waist diameter and receiver aperture diameter. Figure B.1 in Appendix B shows angular deviations will not lead to significant power variation for this link geometry. Instead, power scintillation is dominated by speckle as the beam front passes through many turbulent eddies. Speckle dominates in the space-to-ground downlink direction, and causes degraded free-space-to-SMF coupling. Therefore, the folded link is primarily subject to the characteristic issue of downlinks and is relevant to this transmission direction. Further modelling in Appendix B, with a Hufnagel-Valley 5/7 profile [56] predicts scintillation indices between 0.1 and 0.4 for downlink from satellites at  $50^\circ$  and  $20^\circ$  elevation, respectively. This modelling is based on plane wave propagation to a point receiver at the ground, and ground station receiver apertures on the order of 50 cm to 100 cm will be subject to lower scintillation indices due to aperture averaging. The scintillation indices measured during this demonstration are compared with the 0.1–0.4 scintillation index values, to show applicability to a GEO feeder link.

#### 4.3.4 Link Budget

A link budget is given in Table 4.1. The DCO cut-off is approximately  $-33.0$  dBm of received optical power. Splitting losses are idealised to be 3 dB. For a transmit power of 26.8 dBm, a link margin of 28.3 dB accommodates excess losses due to misalignment, clipping, SMF coupling loss, and turbulence-induced fading. Additional loss will also be caused by scattering from sea-spray because the beam propagates close to the surface of the river.

Table 4.1: Link budget for the 10.3 km folded laser range.

Quantity	Value
Transmit power	26.8 dBm
Splitting loss (FFC1 to FFC2)	-9.00 dB
Geometric & clipping loss (optimum alignment)	-22.5 dB
Receiver cut-off power	-33.0 dBm
Link margin	28.3 dB

## 4.4 Results

Measurements were taken on 2022-12-13 between 17:55 and 20:43, while the scintillation index remained below 0.4. For each wavelength under test, scintillation index, mean SMF coupling, and proportion of BER measurements below the  $4.5 \times 10^{-3}$  FEC threshold are shown in Figure 4.2. A scatterplot of BER measurements below the FEC threshold and SMF coupling against scintillation index is shown in Figure 4.3. The wavelengths shown were increased in chronological order, providing a time-sampling of the atmospheric turbulence. Reported wind direction and speed during the 3 hour period is also given in Figure 4.2. Wind direction was predominantly parallel to the direction of beam propagation for the first half of the demonstration, and transverse to the beam for the second half, and wind speed ranged from 11.1 km/h to 27.8 km/h [120]. An additional 2 dB of transmit power was added at 20:15, increasing the power into FFC1 to 28.8 dBm, for wavelengths 193.10 THz and above, and causing a momentary increase in the proportion of BER above the FEC threshold. The minimum and maximum  $s_I$  were 0.110 and 0.346 for wavelengths 192.05 THz and 192.75 THz, respectively. Mean SMF coupling efficiency ranged between a maximum of -8.55 dB and a minimum of -11.9 dB, corresponding to percentages of transmissions above threshold of 84% and 20%, respectively. Table B.1 in Appendix B provides the full numerical results.

### 4.4.1 Transceiver Wavelength-Dependence Characterisation

For each wavelength used in the demonstration, loopback measurements of BER were taken in-fibre with fixed transmit power and attenuation. Of the first 10 channels, spanning 191.10 THz to 191.55 THz, BER decreased linearly from  $6.61 \times 10^{-4}$  to  $1.88 \times 10^{-4}$ . For the remaining 52 channels, spanning 191.60 THz to 194.15 THz, BER was randomly distributed within the range of  $1.05 \times 10^{-4}$  and  $2.11 \times 10^{-4}$ . This suggests a minor wavelength-dependence in the DCO or EDFA in the first 10 channels. Therefore the performance variation seen in Figure 4.2 was likely caused by changing atmospheric turbulence and not a wavelength-dependence in the DCO.

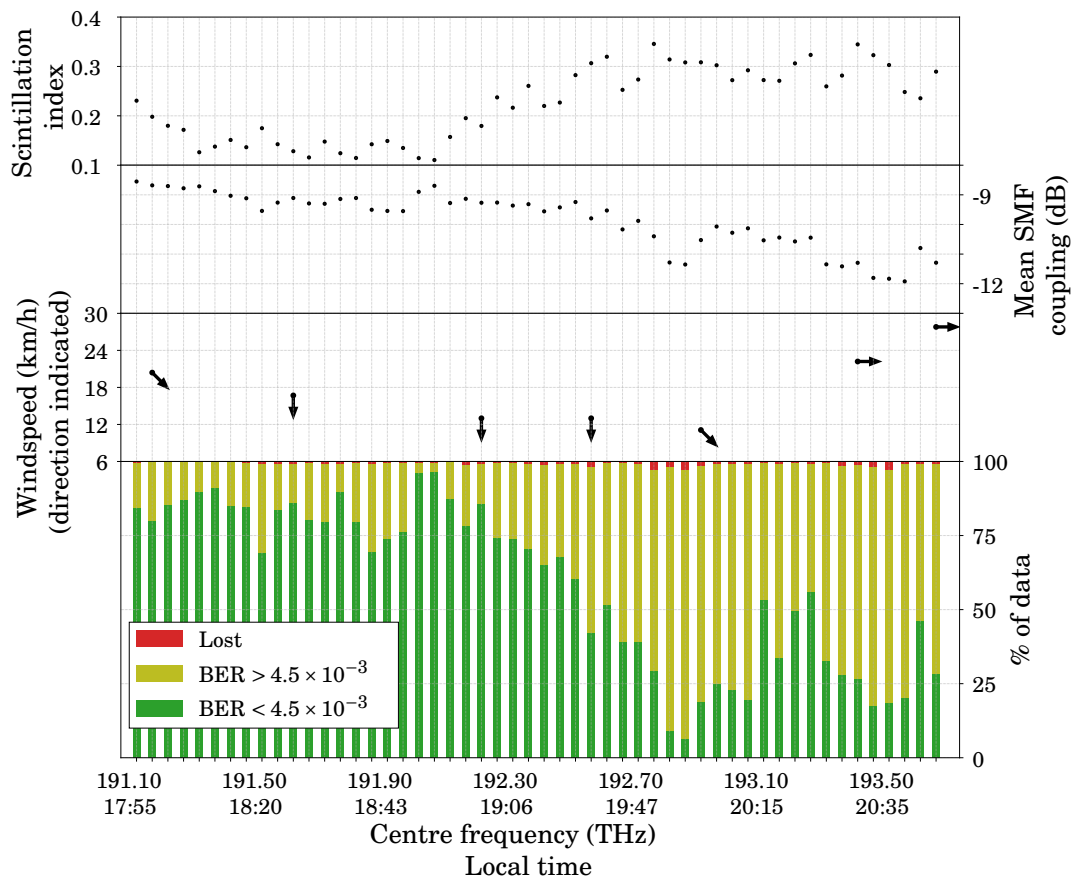


Figure 4.2: Per optical wavelength, during low turbulence, measurements of (*from top to bottom*) scintillation index, mean single-mode fibre (SMF) coupling, wind-speed and direction, and proportions of lost, high bit-error rate (BER) and low BER transmissions. Wind-speed and direction recorded at Perth Airport, downward arrows point South, parallel to the transmission.

## 4.5 Discussion

Scintillation indices measured show the relevance of this terrestrial link to a real ground-to-space laser link. The scintillation indices observed on 2022-12-13 spanned 0.1 to 0.4. These indices are equivalent to the scintillation indices modelled for GEO downlink to a point receiver on the ground at 20-50° elevation. A large proportion of transmissions for scintillation index values below 0.2 were below the FEC threshold, without any amplitude stabilisation. From Figure 4.3, the increasing scintillation index correlated with the decreasing SMF coupling efficiency, with a sharp drop-off around a scintillation index of 0.25. For the best performance under speckle, a higher order AO system must be employed to ensure robust reception, as in Dochhan, 2019 [40] or Bitachon, 2022 [41].

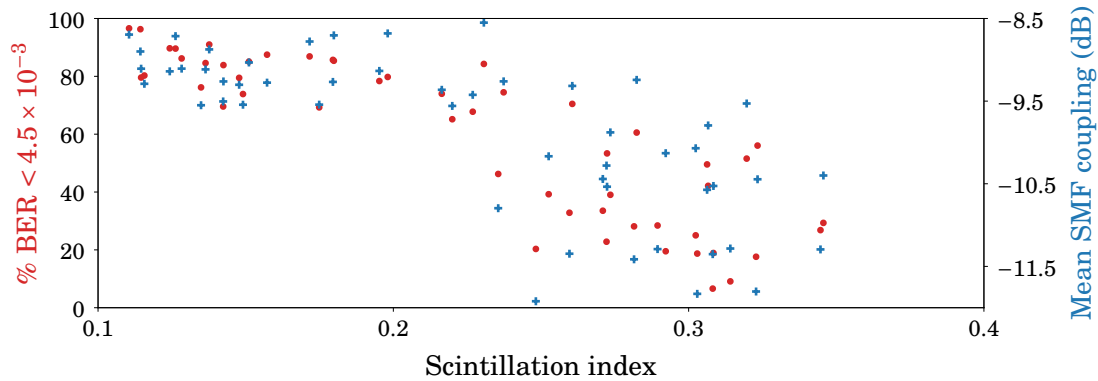


Figure 4.3: Measurements during low turbulence. Scatterplot of low bit-error rate (BER) transmission percentage and single-mode fibre (SMF) coupling versus scintillation index.

Additionally, at 20:00, a change in wind direction transverse to the link direction occurred close to the peak scintillation index observed at 19:50, along with a generally low number of transmissions below the FEC threshold between 19:55 and 20:15. The period of transverse wind may be more applicable to space communications than the period prior to 20:00 when the wind was parallel to the link, as winds encountered by a beam propagating from space-to-ground will necessarily travel transverse to the link. Also, wind generates sea spray on the surface of the river, resulting in additional power attenuation as the signal propagated close to the river surface. This effect will have led an increase in high BER transmissions, in addition to atmospheric turbulence. The scattering cannot be isolated from the power measurements, but will clearly be correlated with wind velocity and the strength of the turbulence.

As GEO and LEO transmissions both pass through the same atmosphere, this link also has relevance to transmission from LEO. On a given day, scintillation index for a LEO link will be higher than a GEO link because of the contribution of satellite slew rate to the pseudowind [56]. Furthermore, the Doppler shift imparted by the slew rate of a LEO satellite is not replicated by the stationary horizontal link.

## 4.6 Conclusion

High-bandwidth coherent communication over a 10.3 km folded link was demonstrated without atmospheric turbulence correction, in varying turbulence conditions. Scintillation index for the demonstration was derived and showed the relevance of the horizontal ground-to-ground link to a typical and worst-case ground-to-space link. Performance under

these conditions is challenging without employing a higher order AO system. However, transmission of data with BER below  $4.5 \times 10^{-3}$  is shown to be possible with unmodified fibre networking equipment, under the right conditions. A possible correlation between BER and wind direction was observed, and this may have implications for high-speed ground-to-ground FSO communication installations as an additional topic of interest.

The folded FSO link utilizing a CCR is a relatively low-complexity arrangement, compared to a point-to-point link. This link intrinsically has a higher accessibility and potential up-time for commissioning activities than a link to a satellite. Having shown the relevance of this link, it can be used for further research and development activities. This includes commissioning other communications equipment prior to deployment in a full-sized OGS. Furthermore, the decline in BER with the increasing scintillation index demonstrates the need for adaptive optics correction to overcome high order wavefront disturbances. As a priority, the optical terminal shown can be modified to incorporate a high order AO system, as the current arrangement clearly experiences speckle and performance would be improved with high order AO to correct the wavefront. The system could then be tested, with high uptime, on this link with statistics representative of space-to-ground conditions.



---

---

## CHAPTER 5

---

# Coherent Free-Space Optical Communications at LEO Tracking Rates

Earth observation satellites collecting imagery in LEO are constantly being improved, with higher fidelity sensors and smaller physical footprints. As the size of sensor data increases and the RF environment in LEO becomes increasingly crowded, FSO downlink from the tens-to-hundreds of gigabits-per-second promise to alleviate the inevitable bandwidth bottleneck. This chapter concerns a demonstration of 100 Gb/s-class coherent FSO communications to an aerial Earth observation satellite proxy at LEO tracking rates.

Pointing and tracking are significant challenges in FSO communications, owing to the relatively low divergence of optical frequency signals. Tracking the reflected signal from an aerial target makes this task more challenging, as the atmosphere-induced AoA variation is compounded with the vibration of the drone-borne CCR. This drone-based technique also exceeded the distance of similar reports at the time, extending the art by incorporating tracking with angular rates equivalent to the angular tracking rate required to communicate with a transiting satellite in LEO.

Chapter 5 was published in the journal, *Scientific Reports*; I was the second author on the publication. This work involved many systems working in tandem; therefore, it was the result of the work of several researchers. My contribution comprised 30% of the experimental work and analysis and 50% of the manuscript preparation. The astronomical mount and machine vision (MV) systems were programmed and operated during the demonstration by Shane Walsh and Ayden McCann. The optics system was assembled by Benjamin Dix-Matthews, Alex Frost, and David Gozzard. During the demonstration,

Benjamin Dix-Matthews was responsible for troubleshooting any issues with the optics. I conducted research to determine the criteria for successfully demonstrating coherent communications, selected an appropriate COTS module, and reverse-engineered it to be used as a real-time BER tester. During the demonstration, I was responsible for operating the communications module and TT system. David Gozzard piloted the drone and ensured compliance with the civil aviation authority. Shane Walsh was responsible for preparing the manuscript for publication in Scientific Reports, and I was responsible for the sections on the communications equipment, link budget, and interpretation of results. I also provided detailed feedback on the manuscript prior to submission, and during peer review. This chapter was also submitted as a technical report to the SmartSat Cooperative Research Centre.

### **Chapter Contents**

---

5.1	Abstract . . . . .	<b>61</b>
5.2	Introduction . . . . .	<b>61</b>
5.3	Methods . . . . .	<b>64</b>
5.3.1	Mount . . . . .	<b>66</b>
5.3.2	Machine Vision . . . . .	<b>66</b>
5.3.3	Coherent Communications . . . . .	<b>67</b>
5.3.4	Optics . . . . .	<b>68</b>
5.3.5	Drone . . . . .	<b>69</b>
5.3.6	Flight Operations . . . . .	<b>70</b>
5.4	Results and Discussion . . . . .	<b>71</b>
5.5	Conclusion . . . . .	<b>77</b>

---

## Coherent Free-Space Optical Communications at LEO Tracking Rates

Shane M. Walsh, Skevos F. E. Karpathakis, Ayden S. McCann, Benjamin P. Dix-Matthews, Alex M. Frost, David R. Gozzard, Charles T. Gravestock, Sascha W. Schediwy

Published in the journal *Scientific Reports*

### 5.1 Abstract

FSO communications are poised to alleviate the data-flow bottleneck experienced by spacecraft as traditional RF techniques reach their practical limit. While enabling orders-of-magnitude gains in data rates, optical signals impose much stricter pointing requirements and are strongly affected by atmospheric turbulence. Coherent detection methods, which capitalise fully on the available degrees of freedom to maximise data capacity, have the added complication of needing to couple the received signal into SMF. In this paper we present results from a coherent 1550 nm link across turbulent atmosphere between a deployable optical terminal and a drone-mounted CCR. Through 10 Hz machine vision optical tracking with nested 200 Hz TT adaptive optics stabilisation, we corrected for pointing errors and atmospheric turbulence to maintain robust SMF coupling, resulting in an uninterrupted 100 Gb/s optical data link while tracking at angular rates of up to 1.5 deg/s, equivalent to that of spacecraft in LEO. With the greater data capacity of coherent communications and compatibility with extant fibre-based technologies being demonstrated across static links, LEO-to-ground links of hundreds of gigabits-per-second can ultimately be achieved with capable ground stations.

### 5.2 Introduction

Communication at optical frequencies revolutionised terrestrial communications with the advent of optical fibre networks [121], but the same is not yet true of free-space applications, which are still dominated by RF communications. While the orders-of-magnitude increase in carrier frequency from RF (kHz–GHz) to optical frequencies (THz) enables a commensurate increase in data capacity, moving to the optical domain brings with it new challenges. Primary among these are the strict acquisition and tracking requirements [122], and the effect of atmospheric turbulence that significantly

influences optical beam propagation on millisecond timescales [87]. To realise the potential of FSO communications for ground-to-ground, ground-to-air, and ground-to-space links, the effects of atmospheric turbulence must be suppressed [123].

The most straightforward implementations of FSO communications modulate data on the intensity of light, such as simple O3K or PPM. These direct-detection methods only require a detector than can measure the intensity of the received light. Coherent detection methods, in contrast, maintain phase and polarisation information by mixing the received signal with a local oscillator (LO), giving extra degrees of freedom to encode data and capitalise fully on channel capacity [124] and compatibility with ubiquitous fibre-based technologies [125]. These coherent methods require coupling the received light into SMF, which at a diameter of 8–10 microns, is more susceptible to pointing errors and turbulence compared with the larger multi-mode fibre (> 50 microns) or free-space detectors used with direct-detection schemes [126].

Currently, Earth observation satellites produce data at such high volumes that on-board compression is often required before transmission to the ground using available RF bandwidth [28, 127], which is power intensive and can reduce data fidelity. For the case of LEO, the time a spacecraft is visible to any particular ground station is only a few minutes per day, further constraining data transfer. A LEO spacecraft could transmit data via a relay spacecraft, typically in GEO, but the increased transmission distance (~ 35,000 km versus ~ 1,000 km) further burdens the size, weight, and power of spacecraft communications systems. Relieving this bottleneck is the goal of NASA's TBIRD mission to develop cubesat-suitable optical terminals capable of 200 Gb/s coherent LEO-to-ground downlink [46].

The previous 5.6 Gb/s record for an optical data link between LEO-to-ground was demonstrated using coherent binary phase-shift keying (BPSK) between two DLR TESAT laser communication terminals, one on board the NFIRE spacecraft, and one on the ground at Tenerife, Spain [128]. These terminals were engineered for inter-satellite links, where atmospheric turbulence is not an issue and as such do not employ any active turbulence mitigation; only a reduction of the ground terminal aperture to reduce the effect of scintillation. The ~ 5 m beam size would ensure that the occurrence of deep fades due to beam wander at the ground terminal are negligible, but given turbulence in a ground-to-space link is concentrated at the ground, beam wander is significantly greater for the uplink than the downlink. This is reflected in the disparity in link quality, with the downlink remaining error free while the uplink showed a BER of  $\sim 10^{-5}$ , despite the identical hardware at each end. To push the data rates into the 100+ Gb/s regime requires, at a minimum, TT AO stabilisation to improve downlink fibre coupling efficiency and

pre-compensate uplink beam wander. Such ground stations are currently in development [129, 130] and have demonstrated AO-corrected SMF coupling from GEO [131], but to our knowledge TT AO stabilised coupling has only been demonstrated at the more challenging tracking rates of LEO by NICT in 2012 [132], and more recently by NASA in 2023 [70].

TT AO stabilised high-speed coherent optical links between the ground and airborne platforms have been demonstrated previously. Chen, 2018 [133] demonstrated a 100 Gb/s bi-directional QAM link between a ground station and light aircraft over 10–20 km link distance. Li, 2017 [134, 135] demonstrated an 80 Gb/s link to a drone mounted retroreflector across a 100 m round trip distance with simulated turbulence, using two orbital-angular-momentum (OAM) multiplexed 40 Gb/s QPSK links. These demonstrations reached angular tracking rates of  $\sim 0.2$  and  $\sim 0.1$  deg/s respectively, although maintaining fibre coupling at LEO-like tracking rates were not aims of those experiments.

The ultra-high capacity of coherent FSO communications has been demonstrated across static links by various groups. Parca *et al.* [136] used 16 channel QPSK to establish a 1.6 Tb/s link over 80 m between buildings. Feng *et al.* [137] used 3 channel QPSK to achieve 160 Gb/s over a 1 km link. The highest capacity link to date, by Docchan *et al.* [40], achieved 13.16 Tb/s with 54 channel QPSK with TT stabilisation across a turbulent 10.45 km link. Most recently, Guiomar *et al.* [138] achieved the highest spectral efficiency to reach 800 Gb/s in a single channel using probabilistic constellation shaping 64-ary QAM over 42 m.

To enable these high-capacity technologies for ground-to-space links requires a tracking system that can maintain SMF coupling in the presence of large angular velocities and atmospheric turbulence. In this paper, we present results of a coherent FSO link operating at 1550 nm between a deployable optical terminal and an airborne drone. Combining a TT AO system with concurrent closed loop MV tracking, we maintain the SMF coupled link at angular velocities up to  $\sim 1.5$  deg/s, representative of the apparent motion of spacecraft in LEO.

Our work uses the retroreflected signal serving as its own TT beacon [72, 115], which due to atmospheric reciprocity [139] allows our terminal to simultaneously demonstrate correction of the downlink beam to maintain fibre coupling as well as pre-compensation of the uplink to maintain pointing on target. An overview of the experiment is depicted in Figure 5.1. Our deployable optical terminal serves as a development test-bed for the TeraNet-1 OGS [140], and also as a standalone unit, which with further optimisation could facilitate Tb/s ground-to-ground, ground-to-air, and ground-to-LEO coherent optical links.

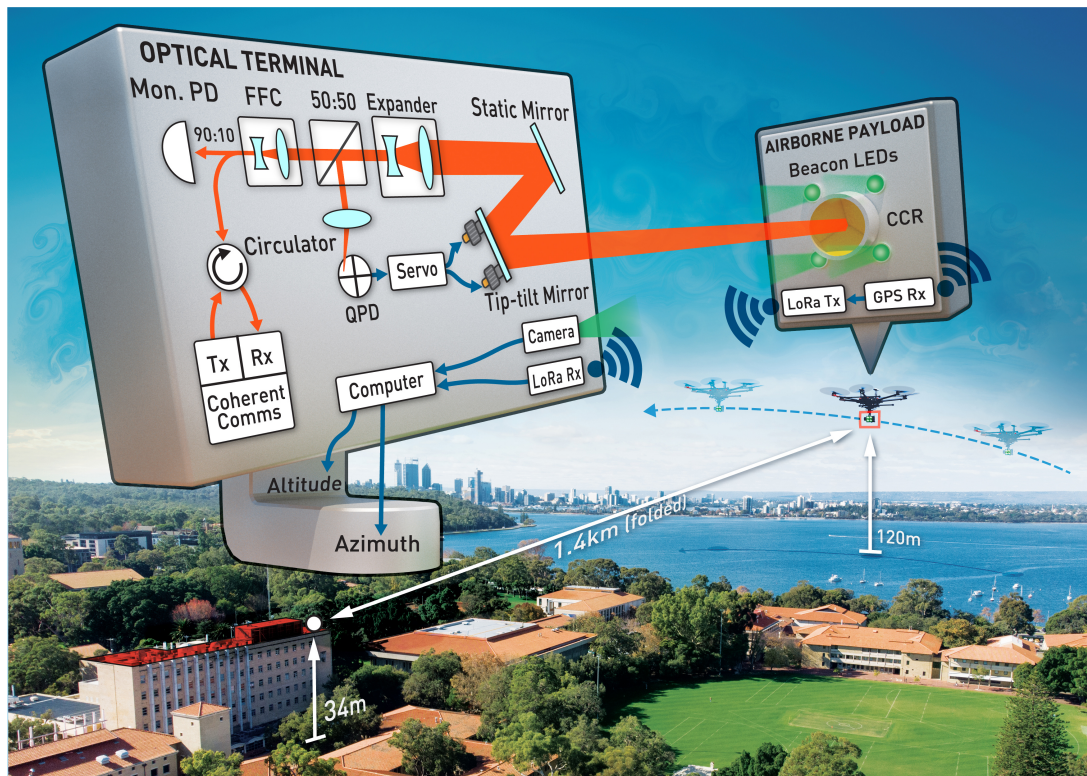


Figure 5.1: Schematic of the deployable optical terminal and experiment. Mon. PD: monitoring photodetector; FFC: fibre to free-space collimator; QPD: quadrant photodetector; CCR: corner-cube retroreflector; LED: light emitting diode; LoRa: ‘Long Range’ radio communication format; Tx: transmitter; Rx: receiver.

### 5.3 Methods

For this experiment our deployable optical terminal was located on the roof of the physics building at the UWA Crawley campus, approximately 34 m above sea level. An optical breadboard housing the optics, MV system, GPS receiver, and single board computer was fastened to the mount, shown in Figure 5.2. Electrical cables and optical fibre carried signals to the TT AO control electronics on the mount base and communications equipment housed in a separate enclosure. To simulate a satellite pass, we used a drone carrying an optical payload that includes a CCR, flying at an altitude of 120 m over the Swan River and a line-of-sight distance of 500–700 m for a folded link length of up to 1.4 km. Figure 5.3 details the interactions between components during the acquisition and tracking phases. CCRs installed at two fixed locations provided static links of 600 m and 2.4 km folded lengths, used for calibration and troubleshooting. A summary of the mount design parameters is presented in Table 5.1, and each subsystem is described in further detail in the following subsections.

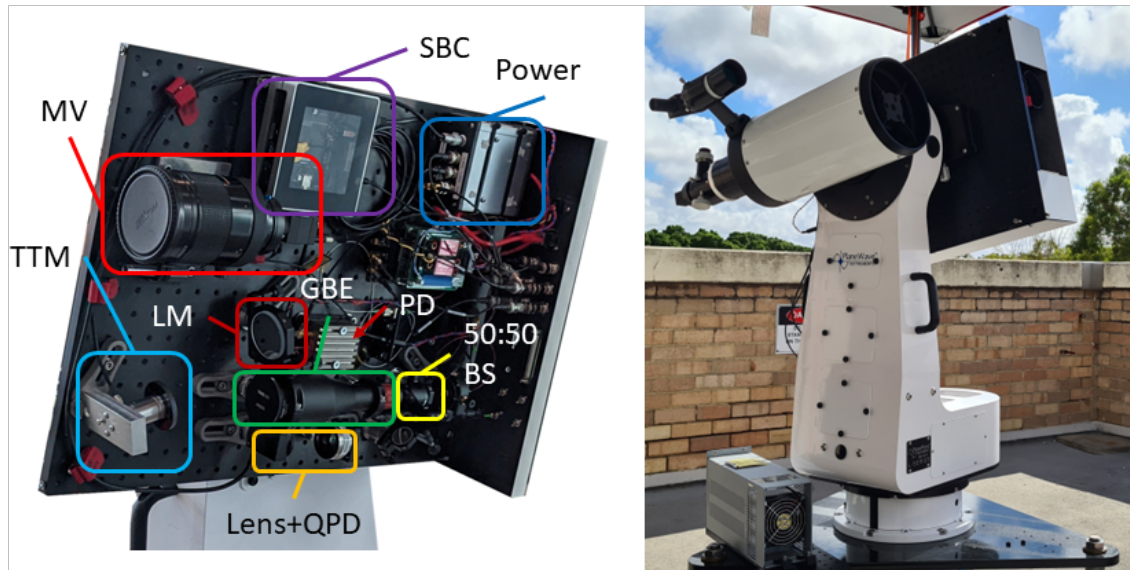


Figure 5.2: *Left*: The optical breadboard layout. MV: Machine vision lens and camera; TTM: tip-tilt mirror; LM: static launch mirror; GBE: Galilean beam expander; QPD: quadrant photodetector; SBC: single board computer; PD: photodetector; BS: beam splitter. *Right*: The deployed optical terminal. Optics and MV are located on the far side of the breadboard. The TTM control electronics are visible on the lower left of the mount base. The telescope mounted on the left was not used for this experiment.

Table 5.1: Mount parameters

Parameter	Value
Transceiver aperture	50 mm
Transmit laser	
Wavelength	1550 nm
Beam waist	17.1 mm
Power	11.7 dBm
Machine vision	
Focal length	500 mm
Field of view	$1.0^\circ \times 0.75^\circ$
Pixel scale	$9 \mu\text{rad}/\text{pixel}$
Mount command rate	10 Hz
Beacon wavelength	532 nm
TT AO	
Bandwidth	200 Hz
Mirror actuation range	$\pm 2 \text{ mrad}$
Mirror resolution	50 nrad

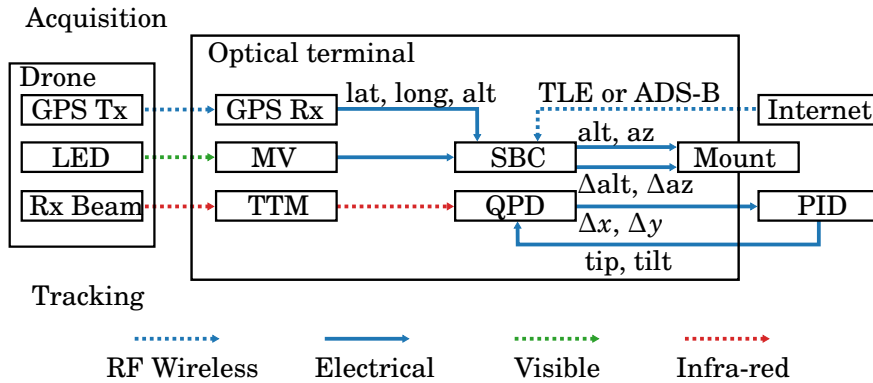


Figure 5.3: Block diagram showing interfaces between components during initial acquisition (blue) and continuous tracking (red).

### 5.3.1 Mount

Our deployable optical transceiver terminal was built around a PlaneWave Instruments L-350 precision altitude-azimuth astronomical mount. This mount provides smooth, accurate tracking and slew speeds of up to 50 deg/s for rapid acquisition. The mount is controlled by the remotely accessed single board computer located on the optical breadboard. Initial pointing of the mount can be provided by spacecraft two-line element (TLE) ephemeris or aircraft automatic dependent surveillance-broadcast (ADS-B) retrieved over the internet, or in the case of this experiment, from GPS coordinates transmitted from the drone via 921.2 MHz LoRa signal. The vendor-provided mount API natively accepts TLEs and calculates the mount path accordingly, while ADS-B and GPS coordinates are converted into mount altitude and azimuth coordinates by our bespoke software layer above the mount API.

### 5.3.2 Machine Vision

GPS and TLE coordinates are not sufficiently precise to point an OGS accurately enough to acquire its target. To provide an intermediate acquisition and tracking stage between TLE/GPS and the TT AO system, an MV system is used for optical closed loop control of the mount. We use a commercially available MV camera with an  $f = 500$  mm lens, giving a  $1.0^\circ \times 0.75^\circ$  field of view. An example image is shown in Figure 5.4. This is large enough to allow for errors in TLE/GPS-derived pointing, but with a fine  $9 \mu\text{rad}/\text{pixel}$  for tracking resolution. A broadband green filter was added to enhance the SNR of the drone's 532 nm beacon LEDs over the blue-sky background. An infrared MV scheme may possibly allow a higher quantum efficiency. However, a 532 nm scheme was ultimately chosen because of the availability of the constituent components.



Figure 5.4: Image from the machine vision tracking camera. The red cross shows the detected position of the beacon LEDs. The white circle shows the tip-tilt mirror actuation range, centred on the predetermined hotspot.

The response time of the mount limited the rate at which it could receive commands from the MV system to  $\sim 15$  Hz, but to avoid intermittent CPU bottlenecks on the single board computer we further limited the camera acquisition and command rates to 10 Hz. Each image was thresholded to detect the four beacon LEDs on the target that circumscribe the CCR. The pointing error is calculated from the pixel difference between the center of mass of the thresholded pixels and the “hotspot”; the pixel coordinates where the target must be located for the retroreflected laser to be coupled back into the SMF. The difference in pixel values are converted to errors in azimuth and altitude angles, and then fed to a software PID control loop to calculate offset rates, in arcseconds per second [141], to apply to the mount to maintain the target on the hotspot. The hotspot is determined pre-flight using the 600 m and 2.4 km static links. The camera was aligned on the mount such that the  $x$ -axis aligned with azimuth, and the  $y$ -axis with altitude.

### 5.3.3 Coherent Communications

The 1550 nm optical communications signal under test was generated by a COTS C form-factor pluggable 27.95 Gbaud dual-polarisation QPSK DCO module, with net line rate of 118.8 Gb/s, typical of high-capacity fibre-optical transport networks. This DCO module was controlled with an evaluation board, providing access to standardised pre-FEC BER and received power measurements with a 1 s minimum performance monitoring interval [119]. This 1 s sampling rate is suitable for deployment in fixed fibre networks, but will not capture amplitude shifts seen on a free space link due to the shorter atmospheric coherence time (a few to tens of milliseconds). In-fibre commissioning of the DCO module demonstrated the threshold power corresponding to a FEC-correctable BER

of  $4.5 \times 10^{-3}$  is approximately  $-30$  dBm (optional registers reporting optical SNR [119] were not implemented in this module). This BER value was taken to be the threshold for error-free communication, with the caveat that a 1 s period of reception averages out short duration bit error events over a free-space link and some instances may exceed the error-free threshold. Unfortunately, post-FEC BER nor QPSK constellations were available from this module.

As the DCO power measurements are taken at 1 Hz, fast power fluctuations due to atmospheric turbulence are subject to aliasing. Therefore, a 90:10 splitter sends 10% of the received light to a monitoring photodetector to capture received power information at 2 kHz. This sample rate is faster than the atmospheric coherence time, and allowed us to determine whether short duration deep fades due to turbulence or pointing errors were present; if signal is observed throughout the drone passes then the goal of robust SMF coupling is successful.

### 5.3.4 Optics

The communications signal is fibre-fed from the DCO module to the mount via an EDFA nominally providing 20 dB gain and  $< 5$  dB noise. The amplified output power was verified using a handheld power meter before feeding to the mount, where it is transmitted from a FFC as a beam of waist radius  $w_0 = 1.14$  mm. The beam is directed to a 50:50 beam splitter, needed for the TT AO correction of the returned beam, where 50% of the power is transmitted through the system. The transmitted portion of the beam is expanded by a  $15\times$  Galilean beam expander to a waist radius of  $w_0 = 17.1$  mm from an aperture diameter of 50 mm. We chose this beam size to be as large as possible to minimise divergence due to diffraction, while remaining smaller than the expected worst-case Fried Parameter size ( $r_0$ , typically on the order of  $\sim 10$  cm at 1550 nm for strong turbulence). In this regime, scintillation is negligible and first-order TT AO alone is sufficient to correct for atmospheric turbulence. The expanded beam is reflected off the piezo-electric FSM to a static launch mirror before exiting from the system. Note that in Figure 5.1, these two mirrors are swapped for graphical convenience, but this is functionally identical.

After propagating across the atmospheric channel to the drone, the beam is retroreflected and returned to the transceiver where it follows the reverse path through the optics. This time, at the beam splitter, the transmitted light is coupled back into the SMF to be sent to the communications module and monitoring photodetector, while the reflected light is focused onto a position sensitive QPD. Variations in AoA of the retroreflected beam imparted by turbulence and/or pointing errors are translated into

lateral spot movement on the QPD, which is used by the PID loop and control electronics to drive the FSM actuation to maintain the spot centering.

The TT AO system consists of a two-inch diameter mirror mounted to a commercial fast piezo TT platform and its associated electronics. The piezo platform has a specified closed-loop angular resolution of 50 nrad and actuation range of  $\pm 2$  mrad in two dimensions. During this experiment, the TT loop was operated at 200 Hz. Due to atmospheric reciprocity [139], the TT loop has the dual effect of correcting beam wander of the outgoing beam to maintain pointing, as well as correcting the AoA of the return beam to maintain fibre-coupling efficiency.

A link budget for the experiment is presented in Table 5.2. The in-fibre transmit power was limited to a maximum of 11.7 dBm to avoid saturation of the QPD and mitigate the effect of prompt reflections, largely from the refractive elements of the beam expander. The terminal optics imposed a combined 15.7 dB loss across transmission and reception, leaving 26 dB of link margin above the  $-30$  dBm threshold for pointing, geometric, and atmospheric losses.

Table 5.2: Demonstration link budget

<b>Parameter</b>	<b>Value</b>
In-fibre transmit power	11.7 dBm
Transmit beam split loss	-3 dB
Geometric and clipping loss	-1.7 dB
Receive beam split loss	-3 dB
Single-mode fibre coupling loss	-8 dB
Received power threshold for $10^{-4}$ BER	-30 dBm
Link margin	26 dB

### 5.3.5 Drone

To simulate the angular motion of a satellite in LEO, we use a professional grade drone carrying a gimbal-mounted optical payload consisting of a two-inch CCR to return the 1550 nm signal, four 532 nm beacon LEDs for MV tracking, and a camera for payload orientation. The drone also carries a GPS and barometric altimeter that relay coordinates to the optical terminal via LoRa for autonomous acquisition. The drone has a maximum horizontal velocity of 65 km/h, allowing us to easily mimic the  $\sim 1$  deg/s angular tracking rates of LEO across the  $\sim 700$  m distance to the optical terminal. Figure 5.5 shows the drone in flight with the payload LEDs illuminated (top), and a close up of the payload (bottom).

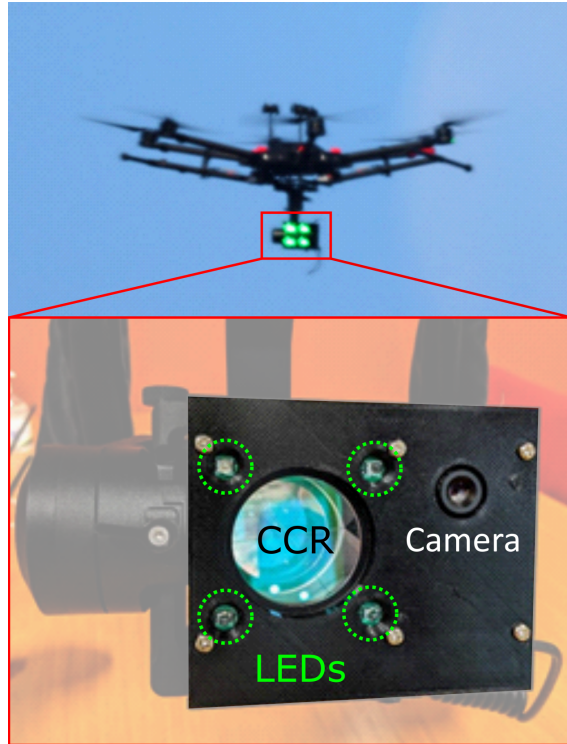


Figure 5.5: The drone in operation, with machine vision beacon LEDs visible on the gimbal-mounted optical payload. *Inset:* Close-up of the optical payload showing the beacon LEDs, corner-cube retroreflector (CCR), and camera.

### 5.3.6 Flight Operations

After take-off, the drone climbed to a regulation-limited 120 m altitude and moved into position over the Swan River, then adjusted the gimbal pointing so the beacon LEDs were oriented toward the mount. The onboard GPS module continuously transmitted the drone's position to the optical terminal computer, which was converted into altitude and azimuth angles to point the terminal at the drone. Once the LEDs were visible within the camera's field-of-view, the MV loop was closed and the mount pointing adjusted to acquire and maintain the drone beacons on the hotspot.

With the drone located on the MV hotspot, the laser was nominally incident on the CCR and signal was returned to the terminal. However, given the relatively short distance to the drone and its susceptibility to wind buffeting, return power was only intermittently observed until the TT loop was closed and signal was stable. The MV and TT loops ran concurrently to track the drone correcting for macroscopic motion, whether intentional or due to wind buffeting, as well as beam wander from atmospheric turbulence. The MV controlled the mount for high-amplitude, low-frequency ( $\gtrsim 1$  Hz) errors and the TT loop

controlled the FSM for low-amplitude ( $< 2$  mrad), high-frequency errors. With both tracking loops closed, we flew the drone in passes replicating the tracking rates needed for FSO links to spacecraft in LEO. Figure 5.6 shows a map of the drone flight path, which was limited in the north by obstructed line-of-sight, and to the south by dense marine traffic.



Figure 5.6: Map of flight area around the University of Western Australia campus in Perth, Western Australia. Red dot is the deployable optical terminal on the roof of the physics building, blue lines are static link paths, red line is the drone flight path during the 2022/04/21 flight. Map generated with OpenStreetMap data under the Open Database License ([openstreetmap.org/copyright](https://openstreetmap.org/copyright)).

## 5.4 Results and Discussion

Flights were conducted on 2022/04/07 and 2022/04/21, with the former being a series of test flights and the latter being the culminating “high-speed” flight. Atmospheric conditions for these dates are shown in Table 5.3. Figure 5.7 shows the BERs versus received optical power (top panel) for the flights with in-fibre measurements for reference, as well as histograms for the received power (bottom panel) for both days. During testing the received optical power ranged from  $-20$  dBm to  $-12$  dBm, implying total pointing, atmospheric, and other losses of 8 dB to 16 dB. However, on 2022/04/21 smoke was present due to controlled burns by the Parks and Wildlife Service; air quality monitoring from sites 16 km north and 18 km north-east reported peak  $\text{PM}_{2.5}$  densities over 150 and 200  $\mu\text{g}/\text{m}^3$  respectively, compared with average values for those sites of  $\sim 20$   $\mu\text{g}/\text{m}^3$ . The increased density of micron-sized particulates imposed an apparent additional loss of  $\sim 10$  dB due to

CHAPTER 5. COHERENT FREE-SPACE OPTICAL COMMUNICATIONS AT LEO TRACKING RATES

Mie scattering of the 1550 nm beam across the link, compared with the test measurements taken in the clearer PM<sub>2.5</sub> conditions on 2022/04/07. This reduced power resulted in an associated increase in BER. The measurements deviate from the in-fibre reference due to aliasing of the turbulence-induced power fluctuations occurring faster than the 1 Hz sampling rate.

Table 5.3: Atmospheric conditions in Perth for flight dates.

Parameter	2022/04/07	2022/04/21
Temperature (°C)	30	25
Relative humidity (%)	25	34
Pressure (hPa)	1014	1023
Wind speed (km/h)	15	17
Wind direction	W	N
Cloud cover (%)	18	10
Air quality (Peak PM <sub>2.5</sub> , µg/m <sup>3</sup> )		
Duncraig (16 km N)	< 10	160
Caversham (18 km NE)	10	> 200

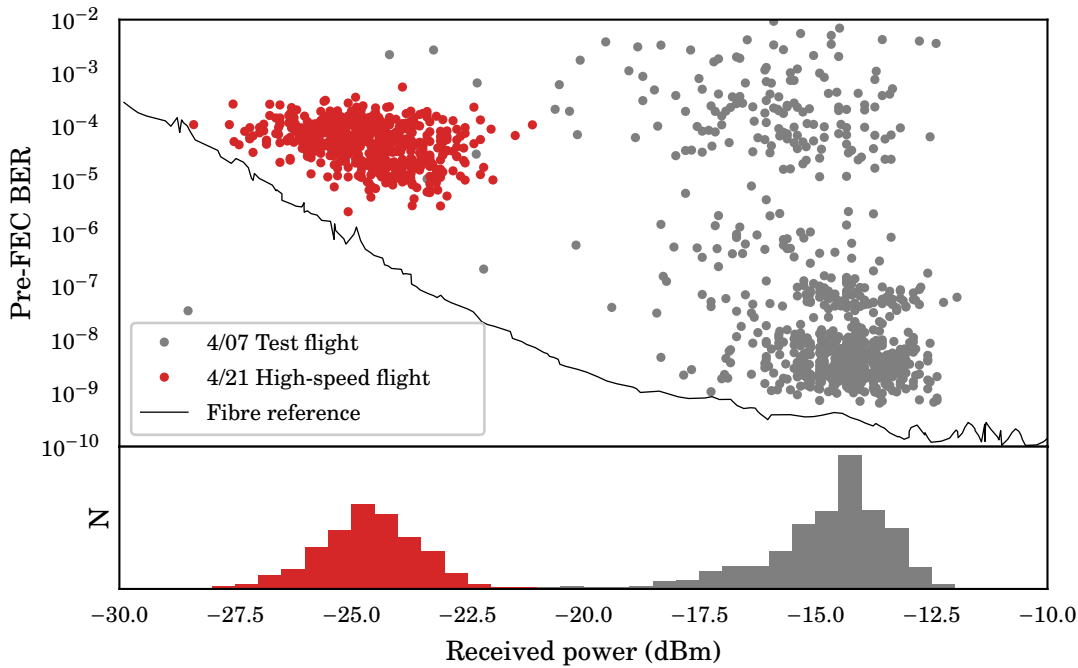


Figure 5.7: *Top*: Pre-forward error correction (FEC) bit-error rate (BER) versus received power. The black line is measurements taken in fibre, delineating best possible performance. The gray dots are measurements from two of the 2022/04/07 test flights, red dots are from the 2022/04/21 high-speed flight. *Bottom*: Histogram of received power. Gray is from two 2022/04/07 test flights, red is from 2022/04/21 high-speed flight.

In-fibre testing with a signal modulated by  $\pm 3$  dB at 220 Hz produced a two orders of magnitude increase in BER, with the aliased power measurements distributed near uniformly across the modulated range, as seen in Figure 5.8. We therefore conclude the clustering of points at the top right of Figure 5.7 is due to a period of particularly high turbulent variability across the link.

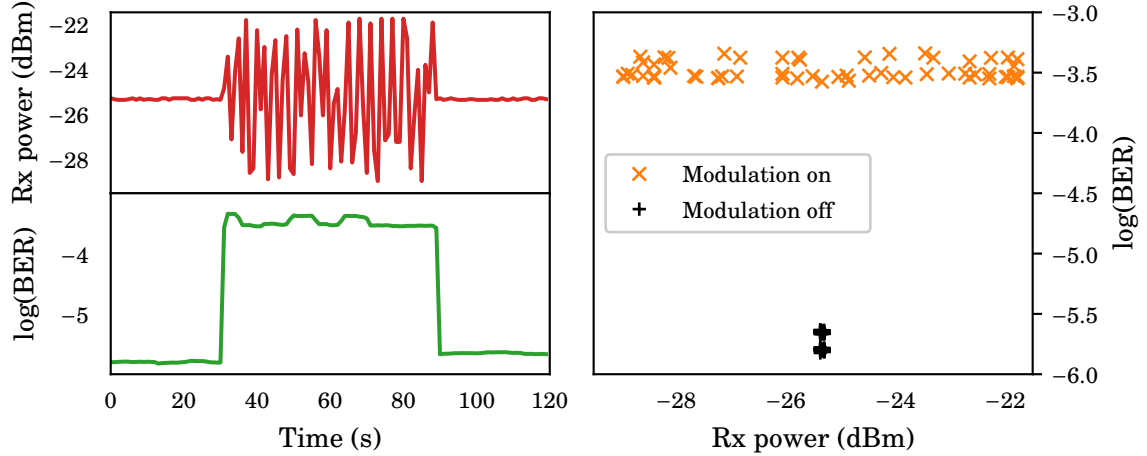


Figure 5.8: *Left*: Time series for power (red) and log-scale bit-error rate (BER) (green) for rapid power modulation test of the communications module. *Right*: Scatter plot of (BER) versus power for modulation on (orange) and off (black).

Figure 5.9 shows time-series data for the 2022/04/21 high-speed flight, showing drone-terminal distance, drone velocity, mount azimuth tracking rate, MV tracking error, received optical power, and pre-FEC BER. Drone distance and velocity were calculated from GPS coordinates, which also provide an independent measure of the mount azimuth tracking rate in addition to the values reported directly by the mount. The MV tracking errors are the offsets in milliradians between observed drone position and the hotspot.

The measurement series spans a total of eight drone passes over  $\sim 750$  s, with the longest uninterrupted link period of  $\sim 318$  s, or four drone passes. The link is only broken at the end of the fourth and sixth passes ( $t = 318$  s and  $t = 439$  s) when the drone decelerated abruptly at the flight area boundary, resulting in pointing errors too fast for the MV and too large for TT loops. When this occurred, the transmitted beam was longer incident upon the CCR, and therefore no signal was returned; it is not the result of turbulence or poor link quality. During these periods of interruption, the MV tracking remains active as long as the drone remains visible in the  $1.0^\circ \times 0.75^\circ$  field of view. When the tracking returns the drone to the hotspot, the TT loop is closed again.

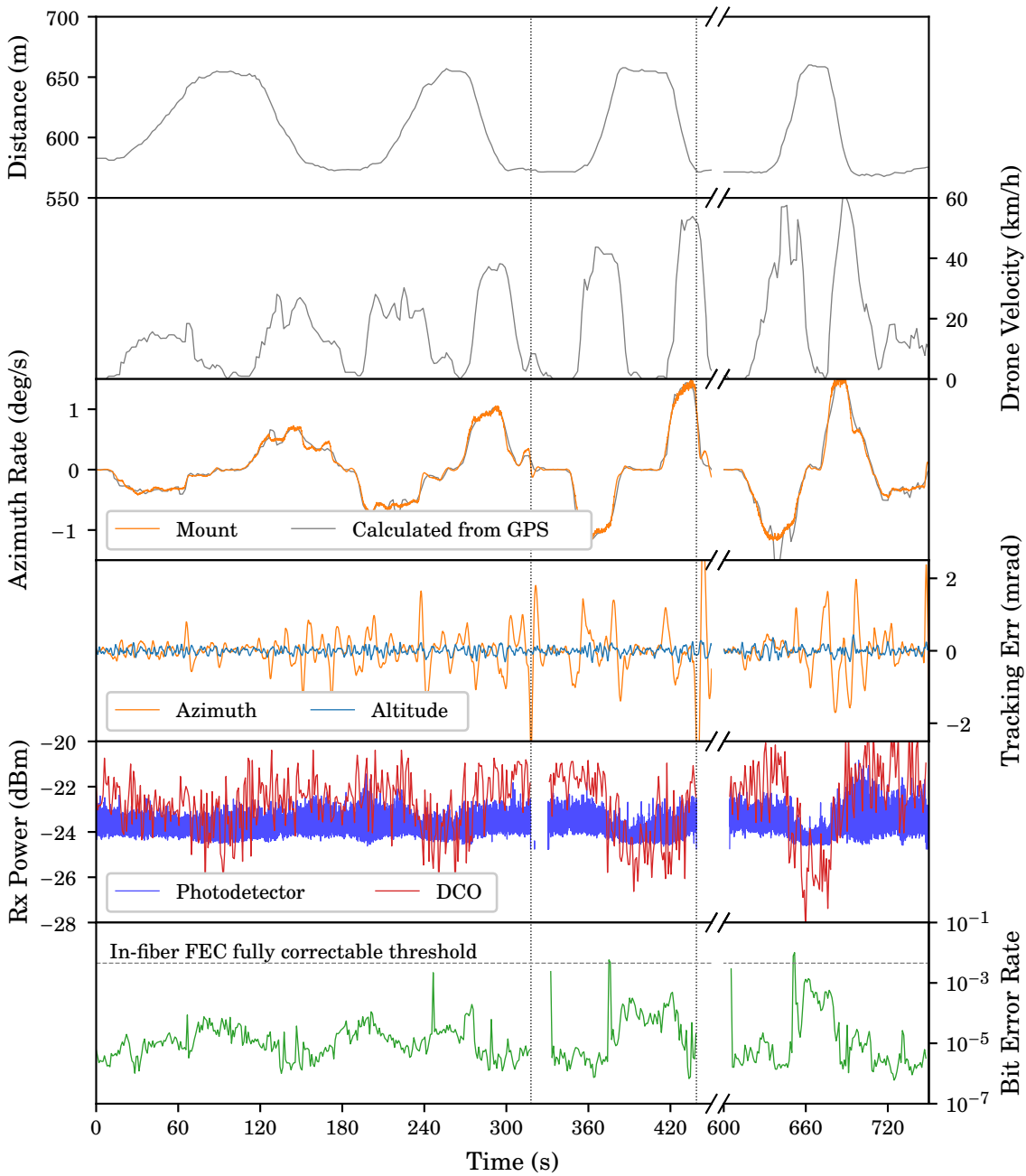


Figure 5.9: Time series data. From top to bottom: -Line-of-sight distance between the deployable optical terminal and drone as calculated from GPS. -Drone horizontal velocity, as calculated from GPS. -Mount azimuth tracking rate, as calculated from mount (grey) and GPS (blue). -Machine vision tracking errors in azimuth (grey) and altitude (orange). -Received optical power from photodetector (blue) and communications module (red). -Bit-error rate after forward error correction (FEC) (green). Times of link dropout are delineated with a dotted line ( $t = 318$  s and  $t = 439$  s).

During the flight, the drone ranged from around 550 m to 660 m line-of-sight distance. The drone reached a maximum speed of 60 km/h, corresponding to an azimuth tracking rate of 1.5 deg/s. The MV tracking errors show the effect of wind buffeting, with the azimuth error frequently spiking well above 1 mrad while the altitude error remains stable below 0.25 mrad.

The returned optical power and BER plots show the link was lost only when the MV error exceeded 2.5 mrad during the drone deceleration; somewhat greater than the manufacturer specified 2 mrad actuation limit of the FSM. The pre-FEC BER fluctuates between  $\sim 10^{-6}$  and  $\sim 10^{-3}$ . Given the millisecond scale of turbulence-induced atmospheric coherence time, instances of high BER will dominate the average within each 1 s sample. Therefore, the BER data are very likely pessimistic compared to what would be observed with shorter and more frequent sample periods, which conversely would likely resolve more spikes above the FEC-correctable threshold. However, we can infer that for a practical communications link, when the pre-FEC BER approached and exceeded the FEC-correctable threshold of  $4.5 \times 10^{-3}$ , reliable communication could still be established with an appropriate ARQ protocol at the data layer. With this in mind, the results serve as confirmation that robust data transmission was maintained throughout the flight. Given the presence of smoke induced power loss and the limitations of the DCO for free-space links, the important result is the maintaining of the SMF coupling, rather than the specific BER behaviour.

The monitoring photodetector, receiving only 10% of the returned signal, was operating near the lower limit of its dynamic range, where its response is non-linear, making measurements less accurate than the DCO reported values. The values shown in Figure 5.9 were shifted by +10.7 dB to account for the splitter and normalize the output to the DCO measurements. Due to the non-linearity it does not show the same variation in power as the DCO aliased measurements, but its 2 kHz sampling rate serves the critical purpose of showing that power fades are not occurring on timescales shorter than the 1 s DCO sample time; verifying that we maintained fibre coupling throughout the drone passes despite atmospheric turbulence, wind buffeting, and high angular velocity of the drone. To the best of our knowledge, this is the first such terrestrial demonstration of TT AO-stabilised robust SMF coupling at the angular tracking rates needed for coherent ground-to-LEO links.

It is not possible to quantify the turbulence strength observed across the drone link from the data available as the power measurements are post-TT correction and any AoA variations from turbulence are coupled with those from drone movement/vibration. Measurements without TT for comparison were also not possible as the TT loop was

required to keep the beam on the CCR in the presence of wind buffeting. However, given the fact that TT was sufficient to keep the beam centered on the QPD, we can conclude that scintillation was negligible and the integrated turbulence resulted in a Fried parameter size  $r_0$  larger than the receiver diameter of 50 mm. For the round trip link distance of 1.2 km at 1550 nm, this would correspond to an upper bound  $C_n^2$  of  $5 \times 10^{-14} \text{ m}^{-2/3}$  throughout the experiment, per Equation 2.16 for constant  $C_n^2$ .

In some respects, a low-altitude drone link is more challenging than a link to a spacecraft. At the  $\sim 600$  m link length, the change in beam size due to divergence is negligible such that at the drone it is still only on the order of the CCR size. The drone was subjected to wind buffeting, causing motion at the scale of tens of centimeters even in mild winds and moving the CCR in and out of the beam when the TT AO loop was not closed. This motion was faster than the MV could correct the mount pointing, meaning that the TT AO system was correcting for this in addition to AoA variations due to atmospheric turbulence. Furthermore, without a TLE spacecraft ephemeris providing an *a priori* coarse tracking path, the MV was responsible for tracking of the drone's large scale motion rather than making minor corrections to a pre-defined path. Despite these challenges the terminal maintained the link, with dropouts occurring only during abrupt deceleration of the drone as it approached flight boundaries, where the correction required was too rapid for the mount tracking and too large for the FSM. This situation is not analogous to any practical scenario of ground-to-LEO communications with a cooperative target.

A further drawback of the airspace and altitude restrictions on the drone was that tests were limited to tangential paths at a distance of  $> 550$  m. In this situation, the angular velocity is almost purely azimuthal, at a low altitude angle ( $\sim 8^\circ$ ). The mechanical azimuth rate of the mount needed to track a target on sky with a given angular velocity scales inversely with the cosine of the altitude angle, so the closer to zenith a satellite transits, the faster the azimuth axis must rotate. A more robust test would be a flight that transits close to zenith, more closely approximating the tracking demands on the mount axes where the required azimuth rate increases dramatically. We aim to address this in future experiments with light aircraft.

For this work we used the retroreflected beam as its own TT beacon, which provides an AoA error signal despite atmospheric reciprocity due to the truncation of the Gaussian beam at the CCR on the drone payload [115]. This was convenient as it minimised the size and weight requirements of the drone. For a real LEO downlink, the spacecraft would either transmit a dedicated beacon signal at a separate wavelength from the data signal, or a portion of the data signal could be siphoned to use as the TT (or higher order AO) beacon. In either scenario, the operation of the TT loop remains unchanged from this work.

Our terminal has demonstrated the tracking capability for maintaining coherent ground-to-LEO communications, but to develop the terminal into a system capable of real uplink and downlink to LEO requires some optimisations. The line-of-sight velocity of the drone in this experiment produced a Doppler shift of at most  $\sim 1$  MHz, whereas the Doppler shift seen from a spacecraft at 500 km altitude LEO is of order  $\pm 10$  GHz during each orbital pass. For this experiment Doppler shift was negligible compared to the  $\pm 1.8$  GHz accuracy of the DCO module, but for coherent communications from LEO, a local oscillator capable of sweeping across a  $\sim 20$  GHz frequency range would be required.

The MV system would also need to be tailored to the beacon being used by the spacecraft. The limiting factor for our drone flights were the positional uncertainty from the GPS at a relatively short distance, requiring a large field of view. A simple lens and visible camera were sufficient as the beacon LEDs provided ample signal. A spacecraft beacon would be significantly fainter and therefore the MV system might be incorporated within the larger receiver optics using a dichroic/other beam splitter to increase sensitivity and resolution. Depending on field-of-view constraints, separate coarse and fine MV systems may be needed [141]. It is possible the downlink signal itself could serve as both TT and MV beacons, which would require a camera sensitive at the signal wavelength. The demands placed on the MV for LEO would also be significantly less compared to the wind-buffed drone, meaning the control loop could operate at a slower rate and allow for longer integration time of the fainter beacon.

An increase in receiver aperture diameter is needed for more collecting power of the downlink signal, and an increase in transmitter aperture is needed to reduce beam divergence and geometric losses over the link distance to LEO. Aperture sizes of a few tens of centimeters are sufficient for ground-to-LEO links [21, 130, 141]. If the ratio of aperture size to Fried parameter  $D/r_0$  is greater than one, either due to large aperture or strong turbulence, higher order correction beyond TT is required to efficiently couple into SMF. This can be accomplished with traditional AO [133, 142], or with novel ‘passive’ methods such as photonic lanterns [143] or multi-plane light conversion [144]. In combination with atmospheric phase-stabilisation technology [57, 58, 97], such a deployable optical terminal could even facilitate secure ground-to-LEO continuously-variable quantum key distribution [145].

## 5.5 Conclusion

We have demonstrated a robust, high-bandwidth coherent FSO communications link between a deployable optical terminal and drone moving at LEO-like angular velocities.

Combining MV optical tracking and large actuation range TT AO, we maintained transmitted beam pointing and retroreflected beam AoA in the presence of atmospheric turbulence and macroscopic motion to sustain the 100 Gb/s link. SMF coupling is required for high capacity coherent communications, and ground stations with capabilities such as described here will relieve the data bottleneck between earth and LEO and provide ubiquitous fibre internet-like speeds to space.

---

---

## CHAPTER 6

---

# Ground-to-Drone Optical Pulse Position Modulation Demonstration as a Testbed for Lunar Communications

Improved communications beyond Earth's orbit requires optical signals modulated into HPE formats—transmitting as many bits as possible per photon. The PPM format introduced in Chapter 2 has been used in FSO communications to and from the Moon and beyond. In this work we demonstrate transmission and reception of PPM signals on a folded link to a hovering drone carrying a CCR. The SNR was intentionally kept at a low level to simulate the signal characteristics in a marginal, deep space mission. We proposed this technique as a method to commission OGS hardware for future deep space optical communications missions. This drone-based technique also exceeded the distance of similar reports at the time.

This chapter was published in the journal *Drones*. I was the first author on the publication and contributed 50% to the experimental work and analysis, and 90% to the manuscript preparation. The astronomical mount, optics systems, and drone piloting were existing infrastructure carried over from the work described in Chapter 5. I was responsible for modelling, designing, and operating the PPM system constructed from bulk photonic and electronic components. Following the demonstration, I post-processed the data and prepared the manuscript for publication. I also presented this work as a conference presentation at the International Astronautical Congress in Paris, France, during September 2022. This chapter was also submitted as a technical report to the Australian Space Agency.

## Chapter Contents

---

6.1	Abstract . . . . .	<b>81</b>
6.2	Introduction . . . . .	<b>81</b>
6.3	Materials and Methods . . . . .	<b>83</b>
6.3.1	Optical Systems . . . . .	<b>83</b>
6.3.2	Transmitter and Receiver Hardware . . . . .	<b>85</b>
6.3.3	Receiver Software . . . . .	<b>86</b>
6.3.4	Receiver Performance . . . . .	<b>86</b>
6.3.5	Demonstration Operations . . . . .	<b>87</b>
6.4	Results . . . . .	<b>88</b>
6.5	Discussion and Conclusion . . . . .	<b>89</b>

---

## **Ground-to-Drone Optical Pulse Position Modulation Demonstration as a Testbed for Lunar Communications**

Skevos F. E. Karpathakis, Benjamin P. Dix-Matthews, Shane M. Walsh, Ayden S. McCann, David R. Gozzard, Alex M. Frost, Charles T. Gravestock, Sascha W. Schediwy

Published in the journal *Drones*

### **6.1 Abstract**

FSO communication promises to bring fibre-like speeds to data transmissions between ground, sky and space. This is becoming more important in light of the increasing volume of data collected by aircraft and spacecraft. UWA is commissioning an OGS network to support FSO communications payloads. We propose retroreflected links to drones as a useful step towards further ground-to-sky and ground-to-space FSO communications demonstrations. In this paper, we describe the operation of a hardware testbed for a HPE optical communication physical layer. This testbed was deployed over a slanted free space link to a drone to verify sub-systems required in communication between an OGS and a spacecraft in cis-lunar space. Accomplishing this verification of the telescope pointing systems and communications systems would have otherwise been much harder or impossible without using a retroreflected drone link.

### **6.2 Introduction**

From the Apollo era to today, deep space communication is conducted using RF, with the Deep Space Network currently able to provide speeds up to 150 Mbit/s using the Ka band [48]. However, RF bandwidth presents a bottleneck to expanding deep-space communication capability for transmission of scientific data and other non-command-and-control communications.

FSO communication between space and ground will enable the return of larger science data payloads, larger telemetry payloads, and streaming high-definition video to Earth. Pioneering experiments in FSO communication include NICT's 1994 space-to-ground laser downlink [63] and several space-to-space laser links in the 2000s [20, 65, 146]. In the 2013 LLCD, NASA demonstrated Moon-to-Earth optical communication at downlink speeds up to 622 Mb/s, using the Lunar Laser Space Transmitter (LLST) [37]. In the Artemis II

Mission [147], a crew of NASA astronauts will orbit the Moon in the Orion spacecraft. This will be the first crewed lunar orbit since Apollo 17, over 50 years ago. The Orion Artemis II Optical Communications System (O2O) is the successor to the experimental LLST and will initially support space-to-ground downlink at speeds from 80 to 260 Mb/s and ground-to-space uplink at 20 Mb/s [51]. O2O will transmit information using the PPM format, standardised by the CCSDS in the 141.0-B-1 Recommended Standard [54].

Earth's atmosphere remains a challenge to FSO communication because of the deleterious effects of atmospheric turbulence on optical propagation. Techniques for mitigating turbulence and correcting optical wavefronts, such as adaptive optics, have been successfully applied in optical astronomy for decades [56]. Therefore, organisations specialising in optical astronomy and space situational awareness are showing interest in establishing OGS networks to support FSO communications, including several Australian institutes [62]. However, the limited accessibility of FSO communications-capable satellites in orbit remains a challenge for commissioning ground stations. Hardware testbeds in lieu of satellites and spacecraft are therefore useful for testing and verifying OGS systems and sub-systems.

Retroreflected laser links to drones are one such testbed and have been used by the frequency metrology community in preparation for tests of fundamental physics over satellite laser links [148, 149]. For communications purposes, the channel statistics of retro-reflected drone links have been analysed and tested for round-trip lengths up to 204 m [72]. A retroreflected communications link was demonstrated using orbital-angular momentum multiplexed light at 40 Gb/s over a round-trip distance of 100 m [134]. Extensions to this method are possible. For example, due to drone mobility, a drone may also be slewed, requiring the ground station to slew at equivalent angular rates to a LEO satellite, therefore simulating LEO satellite tracking [3]. However, in the context of lunar and deep-space communication, a stationary, hovering drone is more analogous to communication with FSO payloads in cis-lunar space, deep space or geosynchronous orbit. Furthermore, FSO communication demonstrations with stationary, long-distance drone platforms are also of interest to terrestrial network designers, as drones have been proposed as highly mobile nodes for FSO communication feeders in re-configurable networks for disaster recovery and urban centres [150, 151]. Numerical studies of drone-to-ground communication have also been conducted [152]. True drone-to-ground communication for space simulation or terrestrial communication remains difficult to accomplish due to size, weight and power requirements. One drone-to-ground demonstration was conducted with a drone-borne active optical payload linked and powered with a tether to conduct loopback measurements over the aerial link [153].

However, the provision of a tether limits the drone’s mobility and altitude, while also introducing vibration modes associated with tension in the tether. However, advances in retroreflected links have led to achievements in drone-to-ground communications. In one case a 560 m, 500 Mb/s drone-to-ground link was demonstrated by using a modulating retroreflector [154].

In this paper, we present a 1.3 km round-trip retroreflected drone link, using a hardware transceiver based on CCSDS 141.0-B-1. Using a drone in this scenario is presented as a highly accessible, high-uptime testbed for FSO communications and flight operations. PPM symbols were transmitted and received over a 1.3 km folded link formed between an optical terminal and an optical payload, including a CCR, mounted to a multi-rotor drone. AoA variations are exhibited by CCR-folded links despite atmospheric reciprocity [115], so the optical terminal must simultaneously demonstrate correction of the ‘downlink’ beam angle while pre-compensating for the ‘uplink’ beam pointing. The 4-PPM symbols with 8 ns slot widths were transmitted, received and demodulated for a line rate of 50 Mb/s, using COTS components.

## 6.3 Materials and Methods

Figure 6.1a shows a photograph of the optical terminal in panel, alongside Figure 6.1b, a photograph of the drone and drone-borne optical payload. Figure 6.2 shows a detailed schematic of the optical systems. As the link segment is a folded FSO range, the transmitter and receiver hardware are conveniently located in the same cabinet and are isolated in fibre with an optical circulator.

### 6.3.1 Optical Systems

The optical terminal is a precursor to a field-deployable mobile OGS. Coarse pointing with the terminal mount (L-350, Planewave Instruments, Adrian, MI USA) is achieved with an MV system, comprising a visible-light camera, lens and single board computer, used to image the drone and payload. The drone-borne optical payload includes a square array of visible-wavelength (green) beacon LEDs, arranged uniformly around the centre of the CCR. This beacon-camera arrangement feeds back to the MV system to automatically servo the mount when engaged, keeping the beam within the field of view of the optical terminal’s laser path. The field-of-view of the machine vision system is  $17.5 \times 13.1$  mrad, with an angular resolution of  $9 \mu\text{rad}$ .

CHAPTER 6. GROUND-TO-DRONE OPTICAL PULSE POSITION MODULATION DEMONSTRATION AS A TESTBED FOR LUNAR COMMUNICATIONS



Figure 6.1: (a) Optical terminal. The upper-right box contains the free-space optics and machine vision system. The lower-left box is a tip-tilt mirror high voltage stage. The upper-left telescope is from an unrelated system. (b) Drone carrying the optical payload. *Inset*: close-up of the optical payload, consisting of LED array, pilot camera and corner-cube retroreflector.

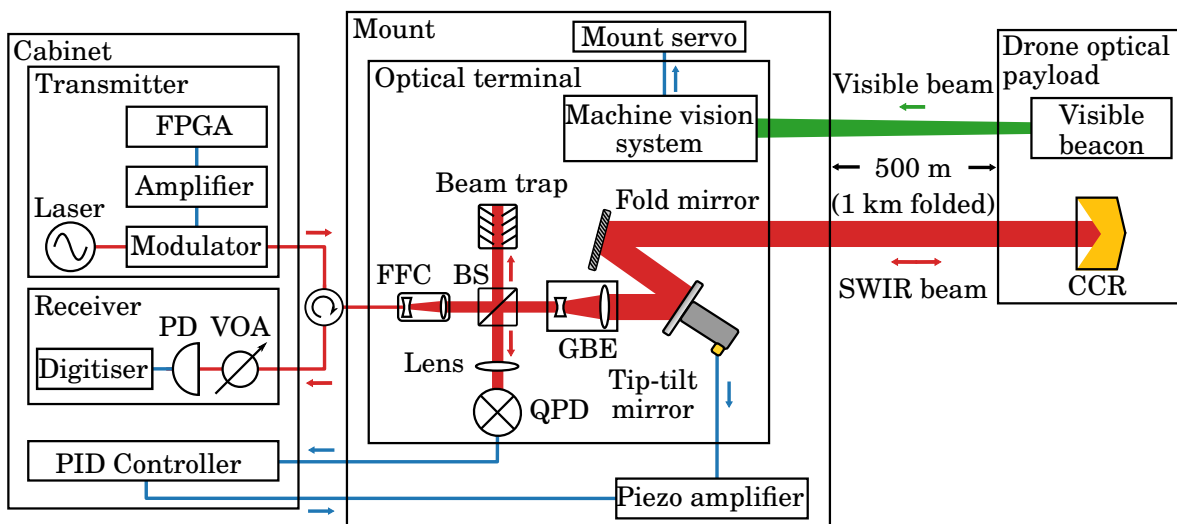


Figure 6.2: Schematic of the free-space optical pulse-position modulation demonstration. CCR: corner-cube retroreflector; FFC: fibre-to-free-space collimator; FPGA: field programmable gate array; GBE: Galilean beam expander; PD: photodetector; PID: proportional, integral, derivative; SWIR: short-wave infrared; VOA: variable optical attenuator.

The optical terminal also houses the FSO components for directing the laser beam. Optical signals from the transmitter are fed to the terminal using fibre. At the FFC, the signal is launched into free space. This beam passes through a 50:50 beam splitter to a Galilean beam expander with a clear aperture of 43.5 mm. The beam splitter is required to image the returning beam, so half of the outgoing power must be directed to a beam trap and is lost. The outgoing beam is then steered by the FSM and stationary fold mirror, out of the terminal. The incoming retroreflected beam follows the same path, but this time half of the power is coupled into the fibre via the FFC, and then to the optical receiver. At the link distance, no clipping due to beam divergence is caused by the aperture of the CCR or the Galilean beam expander. Half of the incoming beam is directed by the beam splitter to the imaging arm.

In the terminal's imaging arm, a lens focuses the incoming beam onto a 3 mm QPD with a field-of-view of  $2.9 \times 2.9$  mrad. Two position signals from the QPD are used to estimate AoA variations and are input into a PID controller (one for each of the pitch and yaw mirror axes) and output to the FSM piezo actuators. The mirror has an actuation range of 4 mrad, covering the QPD field of view. Co-alignment between the QPD and FFC means the FSM provides high-frequency, narrow field-of-view pointing for fibre coupling.

Finally, the drone-borne optical payload also carries a camera to assist the drone pilot in pointing the payload towards the optical terminal. The optical payload chassis is a 3D-printed enclosure and mounts to the COTS gimbal controlled using the drone's native software and controller.

### 6.3.2 Transmitter and Receiver Hardware

A PPM transmitter and receiver are implemented to demonstrate the capability of the system as a testbed for lunar FSO communications systems. A field-programmable gate array (FPGA) development board generates a PRBS, mapped to a 4- or 16-order PPM waveform output. A high-slew-rate amplifier matches the digital output on the development board to the modulation port of a high-extinction-ratio optical amplitude modulator. A fibre-coupled seed laser in the 1550 nm optical C-band is used, as it conveniently has polarisation-maintaining output fibre, avoiding polarisation-dependent losses in the modulator due to birefringence.

The transmitter PPM waveforms were measured over a 2 km fibre link in a lab environment to determine the minimum possible slot width due to bandwidth limitations of components. At 16 ns and 8 ns slot widths, the transmitted pulses exhibit well-defined edges shorter than 1 ns. At 8 ns width, the raw bitrates with 4- and 16-PPM mappings

(and guard slots) are 50 Mb/s and 25 Mb/s, respectively. PPM symbols with 4 ns slot widths were tested but appeared distorted, most likely by the electrical transmission properties of the physical interconnect between the FPGA pin and the driver amplifier, limiting the achievable slot clock speed and, therefore, data rate. For the demonstration, the PRBS was framed into 15120 bit codewords, using the 4-PPM format with an 8 ns slot width. A faster slot clock could be achieved with a purpose-built modulator electrical interface, to achieve the O2O-specified 260 Mb/s.

The receiver hardware comprises an SMF-coupled InGaAs photodetector (Menlo Systems FPD510-FC-NIR, typical to the coherent detection systems more often used by the group) and digitiser, with sufficient bandwidth to observe the PPM waveforms. An SMF-coupled detector was used as it was available, but a multi-mode fibre-coupled or free-space detector would be better suited, as PPM communication is not mode-selective. Slot and symbol synchronisation and demodulation are conducted offline in MATLAB. The incoming PRBS is used to measure the BER of a sequence of PPM symbols. As the incoming light is coupled to SMF, the PPM signal experiences fading from AoA variations caused by turbulence, wind-buffeting of the drone, and mechanical vibrations of the optical payload. A variable optical attenuator was also added ahead of the photodetector to manually control the link margin.

### 6.3.3 Receiver Software

The offline receiver achieves slot synchronisation for a codeword by edge detection, for an initial estimation of slot boundaries in the record of photodetector output voltage samples. Symbol synchronisation is then achieved by overlaying and summing a number of un-synchronised symbols and identifying the guard slot as the slot with the lowest cumulative sum. Maximum-likelihood demodulation of each symbol is implemented by summing the voltage values in each slot location and selecting the slot with the largest value. If the signal is lost at the beginning of a codeword, synchronisation fails and the codeword is discarded. However, if the signal is lost after a codeword is synchronised, the demodulator has an equal likelihood four-way decision on the pulse slot location for a given symbol.

### 6.3.4 Receiver Performance

For 4-PPM with a typical maximum-likelihood detector [155], errors arising from signal fade will lead to a BER,

$$BER = Q\left(\sqrt{SNR}\right), \quad (6.1)$$

where  $Q(x)$  is the  $Q$ -function. Analytical models for PPM error rates in terms of photodetector physics are complex to derive. In order to compare the demonstration data with this threshold, a simple model for SNR as a function of photodetector output voltage was developed for this demonstration. Three parameters are observed in the photodetector output voltage,  $v_d$ ,

$$v_d = v_s + v_o + v_n. \quad (6.2)$$

The photodetector voltage comprises the PPM signal amplitude,  $v_s$ , an offset voltage,  $v_o$ , and additive white noise fluctuations,  $v_n$ , with zero-mean and variance  $\sigma_n^2$ . The optical signal itself is assumed to be otherwise noiseless because of the high extinction ratio of the modulator. Therefore, the SNR for each readout is

$$\text{SNR} = \frac{\langle v_s^2 \rangle - \langle v_o^2 \rangle}{\sigma_n^2}, \quad (6.3)$$

where  $\langle v^2 \rangle$  is the mean squared value of the voltage corresponding to  $v_s$  or  $v_o$  sampled over the entire codeword.

### 6.3.5 Demonstration Operations

The optical terminal, transmitter and receiver were located on the roof of the Department of Physics building at The University of Western Australia at an altitude of around 34 m above sea level. The drone hovered at an altitude of 120 m (the maximum allowed by local regulations without exemptions), with a 650 m slant distance from the terminal site, completing the 1.3 km slanted folded link. While the drone was hovering, the pilot would use the optical payload camera to coarsely align the CCR with the optical terminal. At the optical terminal side, the drone was pulled into the MV system's field-of-view by slewing the mount while viewing the MV camera feed. Upon entering the field-of-view of the MV system, the tracking system could be engaged, automatically moving the mount to locate the CCR within the field-of-view of the QPD. The TT system then dynamically corrected pointing errors. Operating concurrently, the two pointing and tracking systems effectively maintained fibre coupling while the drone hovered in place. If the TT system was disengaged by disconnecting the PID controllers, the MV system was not able to couple the laser light back into the SMF on its own, due to the beam size, link distance, and wind buffeting of the drone.

## 6.4 Results

Results are presented for a drone flight conducted during the day on 18 March 2022, at 2:30 PM. The wind speed recorded nearby, at Perth Airport, was  $\approx 16.7$  km/h [156].

The link budget for the testbed is presented in Table 6.1. The optical sensitivity floor for the photodetector was determined to be  $-33$  dBm, corresponding to a mean output voltage of 1.4 mV. During measurements, the variable optical attenuator was adjusted such that the received power, after pointing losses, was near the threshold for error-free reception. Error-free reception occurred when the output voltage exceeded 2.9 mV, corresponding to an optical pulse power of  $-30.3$  dBm. With AoA correction and additional fixed attenuation, the average received power was maintained within a small margin of the detector’s sensitivity limit. Under one-third of the codewords were received with zero bit errors, confirming this intended marginal performance condition. At this link distance, the beam size is smaller than the Fried parameter and, therefore, scintillation due to turbulence was not expected to cause any fading in excess of the AoA errors caused by drone movement and beam wander.

Table 6.1: Link budget for retroreflected laser link to drone.

Parameter	Value
Transmit power	13.0 dBm
Modulator insertion loss	$-3.50$ dB
Circulator losses	$-2.40$ dB
Splitter loss (2 way)	$-6.00$ dB
Singlemode fibre coupling penalty	$-10.0$ dB
Receive power (error free)	$-30.3$ dBm
Combined pointing and variable attenuator loss	$-22.6$ dB
Mean photodetector sensitivity	$-33.0$ dBm
Error-free link margin	2.70 dB

To confirm receiver functionality, BER was compared to Equation (6.1) using observations for SNR per Equation (6.3). The portion of transmissions received with bit errors, caused by partial or complete signal fading arising due to pointing errors, allow the receiver performance to be characterized. Figure 6.3 shows the SNR as derived from Equation 6.3 and BER for 720 codeword transmissions, with each data point representing a single 15,120-bit codeword. This record has a BER measurement sensitivity floor of  $1/15,120$  errors per bit, and a ceiling at  $1/2$  errors per bit, caused by failure to demodulate, though pulses were present. For comparison, the theoretical BER, from Equation 6.1, is plotted alongside the data as a black line in Figure 6.3.

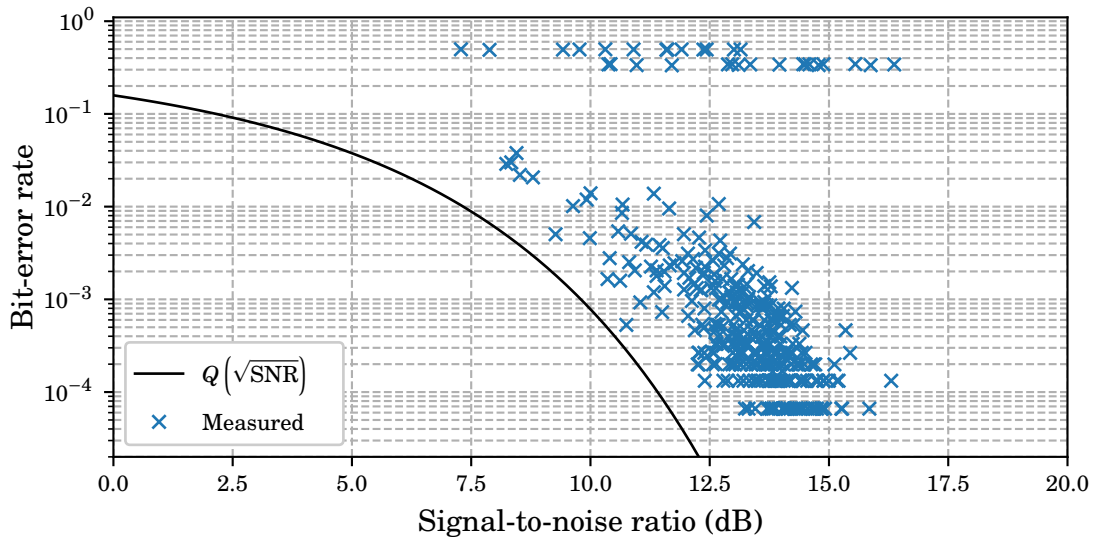


Figure 6.3: Bit-error rate versus signal-to-noise ratio (SNR) of 720 received 15120 bit 4-pulse-position modulation codewords.

## 6.5 Discussion and Conclusion

This demonstration involving a drone-borne CCR provided a useful return on experience towards FSO communications developments, including potential communication with O2O on a full-sized OGS. This was particularly true in the domain of flight operations, not otherwise accessible without enlisting the services of professional small aircraft operators, or operators of commercial high-altitude pseudo satellites, or the few FSO communication-capable satellites in orbit. The drone link demonstration required the coordination of equipment and planning of methods within the research group and was subject to scheduling with the aviation authority and local government as well as uncontrollable go/no-go conditions such as wind warnings and rain. In effect, the availability of the drone provided a scaled-back simulation of space operations.

Interpreting Equation 6.3 implies the optical sensitivity floor represented by  $v_o$  is analogous to background counts in photon-counting receivers, and a comparison may be drawn between the drone link and LLCD results [68]. Downlink results from [68] reported error-free communication at 38.55 Mb/s with a link margin of 13.5 dB between signal and background photon counts. Per Table 6.1, the error-free link margin for the demonstration was 2.70 dB. While it is not possible for this testbed to recreate the transmission powers and link losses of a lunar-to-ground link, the receiver may be similarly tested with the link margin at the limit of its sensitivity. This scales with detector technology, so a

photon-counting detector with a lower sensitivity floor may be integrated into a future iteration of the testbed, and the receive power adjusted to recreate the link margin conditions.

Figure 6.3 shows a main cluster of BER versus SNR results following the theoretical relationship, confirming the expected performance of the receiver. However, the demodulation algorithm implemented often failed to completely demodulate a codeword if too many early symbols were faded, or if the slot or symbols synchronisation had failed, causing ‘synchronised’ pulses to fall across slot boundaries. These cases account for the outlying clusters at the top of the graph, stratified around BERs of 0.5 and 0.33, and indicate further margin for improvement of the offline receiver algorithm before investing engineering time into a real-time receiver.

The 1.3 km retroreflected drone link presented can be extended with materials and methods previously demonstrated over shorter retroreflected links such as verification of atmospheric channel modelling [72]; demonstration of other communication formats [134]; or demonstrations of modulating retroreflectors [154]. Further extensions previously demonstrated include links to tethered drones, carrying active optical payloads [153], or drones moving in paths tangential to the ground station, thus requiring the ground station to track at angular rates equivalent to satellite tracking [140]. Furthermore, results from FSO communication demonstrations with stationary drones will be of interest to designers and analysts planning future terrestrial and disaster-response networks [150, 151].

The drone provided a testbed to perform technical verification of the prototype communications equipment, intended for a future lunar FSO communication link, over a real, time-varying channel. This also tests the mechanical robustness of the optical assembly and pointing systems. The effectiveness of the testbed is limited by dissimilarities to O2O in terms of PPM parameters and detector technology, as well as the relative differences in aperture sizes and optical power levels involved (intrinsically linked to detector technology and link distance). However, some of these limitations can be addressed with changes to the optics and launching the drone from a different location. Furthermore, without undertaking more fundamental demonstrations of capability, costly engineering upgrades to make the communications system more closely resemble O2O, such as the integration of photon-counting detectors, are risks and may not be supported by prudent systems engineering processes. The drone testbed will allow us to continue rapidly integrating and testing subsystems as work progresses to a more complete emulation of a cis-lunar communication system. Therefore, this paper supports the case for retroreflected drone links as useful testbeds for developing FSO communication capabilities while access to FSO communications payloads in orbits remains limited.

---

---

## CHAPTER 7

---

# Conclusion

This thesis investigates high-speed, fibre-like, optical communications carried out on FSO links, motivated by the growing demand for bandwidth in communications between space and ground. Three classes of space mission are positioned to benefit significantly from the advantages offered by FSO communications: telecommunications satellites in GEO, Earth observation satellites in LEO, and spacecraft exploring deep space. OGS installations around the world require proven atmospheric stabilisation systems to suppress the deleterious effects of atmospheric turbulence on FSO propagation. The reported demonstrations show how retroreflected links to stationary and airborne terrestrial targets may be used to develop and validate such atmospheric stabilisation systems. This chapter summarises the outcomes of each preceding chapter, outlines the significance of the body of work presented, and discusses future work planned to follow on from the thesis project.

### 7.1 Summary of Work

**Chapter 3** introduced the concept of a retroreflected atmospheric link, established between a transceiver and a CCR. Analytical models of statistics of phase noise, AoA variation, and intensity scintillation of practical point-to-point links are given and modified to describe retroreflected links. This modification was tested experimentally using simultaneous measurements of the three quantities on a real retroreflected atmospheric link. Good agreement was found between the simultaneous measurements, reinforcing the suitability of the modifications made to the analysis and encouraging the use of retroreflected links to test atmospheric optical systems for future use in point-to-point fashion.

Next, **Chapter 4** documented a demonstration of high-bandwidth coherent FSO communications at the limit of what is achievable without atmospheric stabilisation. COTS fibre communication equipment was used to show how very established, interoperable, technologies can be translated to this new domain. Optical intensity recordings were used to estimate the scintillation index during the demonstration, providing insight into the magnitude of power fluctuations encountered on a real atmospheric link and the ‘breaking point’ for unmodified, COTS equipment. The 10.3 km link was modelled to show equivalence, in terms of integrated turbulence, to a ground-to-GEO link and therefore has implications for future high-bandwidth telecommunications feeders using established networking equipment to meet future bandwidth demands.

A deployment of the same high-bandwidth coherent FSO communications technology to an aerial target tracking demonstration, simulating the downlink of sensor data from an Earth observation satellite in LEO, is detailed in **Chapter 5**. In this demonstration, atmospheric TT stabilisation was used to maintain fibre-coupling in a retroreflected link to a drone-borne CCR. The optical terminal was also mounted to an astronomical telescope mount, providing large-scale altitude and azimuth degrees of freedom. The telescope mount was required to track the flying drone at angular rates similar to a LEO pass. The fibre-coupling was sufficient to maintain a FEC-correctable BER in the communications signal for most of the flight, despite the relatively high tracking rates.

Finally, **Chapter 6** described works testing the capability of a prototype OGS to demonstrate a HPE optical modulation format. PPM signals were transmitted and received between the OGS and a drone-borne retroreflector hovering in place. The system was shown to work down to a theoretical minimum SNR and provided another example for commissioning technologies for the task of deep space FSO communication.

## 7.2 Significance of the Work

This body of work represents a significant contribution to the field of FSO communication through the development and validation of methods for commissioning prototype OGS hardware. Two key outcomes were (a) the advancement of commissioning methods involving retroreflected links and (b) creating coherent communications infrastructure for validating future high bandwidth FSO links.

Experimentally-validated models for retroreflected links were put forward in **Chapter 3**. The impact of **Chapter 3** is multifaceted. First, it validates recent modelling showing AoA variation in retroreflected links despite atmospheric reciprocity [115].

Second, the agreement between three sources of  $C_n^2$  measurement lead to high confidence in each individual metric. In particular, the model for phase noise modified for retroreflected links has applications to FSO range and rate measurements. An improved understanding of atmospheric turbulence-induced phase noise is key to enabling highly precise coherent techniques for measuring range and rate [109, 157]. Retroreflected links were used exclusively throughout the remaining works described in Chapters 4–6.

In the course of this project, the coherent communications DCO module proved to be of significant benefit, becoming a key piece of infrastructure. The DCO module was initially used in its COTS configuration for the airborne work described in Chapter 5. Later, the sampling technique was improved, while undertaking the work described in Chapter 4 to optimise the measurements for free-space links. Demonstrating capability with the DCO module is proving to be highly useful because high bandwidth FSO communications appears to be moving towards using such devices, with little-to-no modification, within an FSO networking stack [70, 71]. The limitations of this work are discussed in Section 7.3 and the follow-on work is described in Section 7.4 of this thesis.

### 7.3 Limitations of the Work

The limitations of the work described in this thesis present avenues for improvement of future research. First, as stated in Section 2.1.4, the CCR optical cross-section was omitted from all of the link budgets in the thesis due to the complexity of analytically modelling the effect of CCR's on an optical signal's wavefront. For example, the edges and facets of the CCR distort the optical signal wavefront, affecting its SMF coupling efficiency. This can be investigated using a numerical technique involving phase screen models for wavefront distortions [89]. Such a numerical study would contribute to the understanding of retroreflected link usage promoted by this thesis. This is possibly a minor concern, with conventional wisdom suggesting the imaged CCR facets do not contribute a significant fibre coupling loss compared to the diffraction losses associated with the CCR aperture itself.

Second, the results presented in Chapters 4 and 5 could have been supplemented with a more detailed analysis of FSO link statistics. Atmospheric FSO links are considered to be stationary over a 'coherence time' and measurements longer than this interval are biased by changing conditions. Links may be further characterised by the probability of fade and fades per unit time [72]. Coherence time in FSO links from LEO is on the order of 1 ms [158]. However, as a consequence of the equipment usage, BER measurements were taken over 20–30 ms intervals in Chapter 4 and one second intervals in Chapter 5.

Further work should incorporate concurrent photodetector measurements, taken at a rate of 1 kHz or greater, to calculate the link's coherence time, probability of fade, and fades per unit time. This would (a) add additional context to the reports of link conditions and (b) provide deeper insight into the DCO module's potential performance when transmitting realistic data packets with shorter duration than the atmospheric coherence time. Further characterisation could have been achieved by comparing the spectral properties of the demonstration links to the corresponding space communication scenarios. For example, the scintillation index comparison of Chapter 4 or the tracking rate comparison of Chapter 5 would both have been enhanced by comparison with theoretical frequency spectrum of coupled fibre power for each scenario.

Additionally, the CCR-based methods presented in this thesis, albeit convenient, do not capture the breakdown in reciprocity between uplink and downlink transmission in satellite-ground FSO links. In space-ground links, the point-ahead angle between uplink and downlink signals may exceed the isokinetic angle, meaning the signals experience uncorrelated first-order disturbances [159]. When the point-ahead angle exceeds the isokinetic angle, separate AO systems are required to stabilise the uncorrelated turbulence experienced in each direction. Terrestrial demonstrations involving CCRs do not capture this effect and cannot be used to verify the performance of point-ahead AO systems. Thus, the absence of a mechanism to reproduce point-ahead angle and measure its effects is another limitation of the methods developed for this project.

Finally, terrestrial retroreflected links to drones are not suitable for testing the tracking systems with full-sized OGS apertures, on the order of 0.7–1 m. As a consequence of the link geometry, the point-spread function of a 76 mm CCR on the tracking sensor of a full-sized OGS telescope will be close to, or exceed, the field-of-view of the sensor at practicable link distances. This arrangement makes tracking via closed-loop feedback feedback impossible. Furthermore, the arrangement of a full-sized OGS aperture with a separate, off-axis, uplink transmitter pointing at a drone-borne CCR may not be practical. However, it should be stated the intention of the technique is to develop tracking technology in an incremental manner with small-aperture systems. The CCR allows convenient development of many systems in the presence of atmospheric turbulence without the complication of a full-sized OGS. With the benefit of these experiences, a development team can begin to deploy a large aperture OGS in preliminary satellite FSO communications demonstrations with a high degree of confidence in the performance of the tracking systems and expected communications throughput.

## 7.4 Future Work

The work described in this thesis leads into two related future bodies of work. First, the OGS commissioning activities can be extended to higher-altitude links through use of light aircraft or helicopters. Second, the OGS hardware itself must be prepared for future operational use as part of an OGS network. The following concluding subsections outline ongoing work towards these two research and development themes. Additionally, Section 7.4.3 expands on additional FSO communications techniques that might employ an operational OGS network.

### 7.4.1 High-Altitude Tracking

Demonstrations of tracking and communications to a high altitude target was reasoned to be the next stage of this commissioning work. This stems from a need to test the dynamic tracking systems described in Chapter 5 with a larger range of motion, closer to a complete LEO satellite pass. Along with the larger range of motion, a longer link distance is sought, on the scale of the 10 km retroreflected link described in Chapter 4. Establishing long-distance links from a rooftop to ground targets is impossible at the current location due to ground clutter. Furthermore, downward slanted links over 5 km are often subject to turbulence exceeding ground-space links, due to the density of the atmosphere close to the ground. This makes high altitude links necessary to achieve the distance and tracking range requirements. However, the drone used in previous demonstrations has a limited flight time at altitudes exceeding 120 m. Therefore, the CCR must be borne by aircraft capable of flight around 3 km, such as the fixed-wing aircraft, shown in Figure 7.1a, or the rotary-wing aircraft, shown in Figure 7.1b. Flight tests have been conducted with these aircraft, again using a CCR to complete the retroreflected link [160]. I am a contributing author on a publication describing this work. Success in these high altitude tests was one of the final milestones in the process of achieving institutional support for the construction of TeraNet, a three-node OGS network in Western Australia, with an overview in Section 7.4.2.

### 7.4.2 TeraNet

TeraNet is an OGS network comprising two fixed ground stations and a mobile ground station mounted to a utility vehicle. Figure 7.2 provides a map of Western Australia showing the locations of the three nodes. TeraNet-1 and TeraNet-2 are the fixed ground stations, located in Perth and outside Mingeneu, respectively. These ground stations will

be based on 0.7 m telescopes; thus they have a large receiver gain. To support deep space optical communications, a high-sensitivity detector needs to be developed or procured. COTS solutions are available [161] for satellite networking using O3K, PPM, or NRZ. These solutions involve fibre-coupled detectors, so the 0.7 m apertures will require higher order AO in order to optimise fibre coupling. This is also an opportunity to investigate novel methods for higher order AO using mode-converting devices [99, 100]. Site characterisation will involve measurements of turbulence to tune the AO system, and also to take measurements of the background irradiance to determine the noise floor for weak light signals from deep space optical payloads. TeraNet-3, utilising a 0.4 m telescope, will initially be equipped with first-order AO, as the  $D/r_0$  will generally be lower than the fixed ground stations. TeraNet 3 is mobile, and intended to provide satellite connection in areas cut off from terrestrial networks. Figure 7.2 shows the initial location of TeraNet-3 at the ESA deep space facility in New Norcia. This location is advantageous as it allows TeraNet-3 to be tested while connected to existing space communications infrastructure, with terrestrial links back to other ESA facilities worldwide. TeraNet-3 is also being used to develop methods, based on daytime astronomical measurements, for accurate localisation in GPS-denied environments. Consideration for laser safety, particularly around aircraft, will be important to the development of the OGS network. Once commissioned, the three TeraNet nodes will be able to connect with future FSO-capable satellites. Furthermore, as part of an Australia and New Zealand OGS network [62], TeraNet will be able to participate in hand-off to and from other OGS nodes, providing seamless coverage over Australia.



Figure 7.1: Two aircraft used for high-altitude testing: (a) a fixed-wing aircraft and (b) a rotary-wing aircraft provided by the Police Air Wing of the Western Australia Police Force.

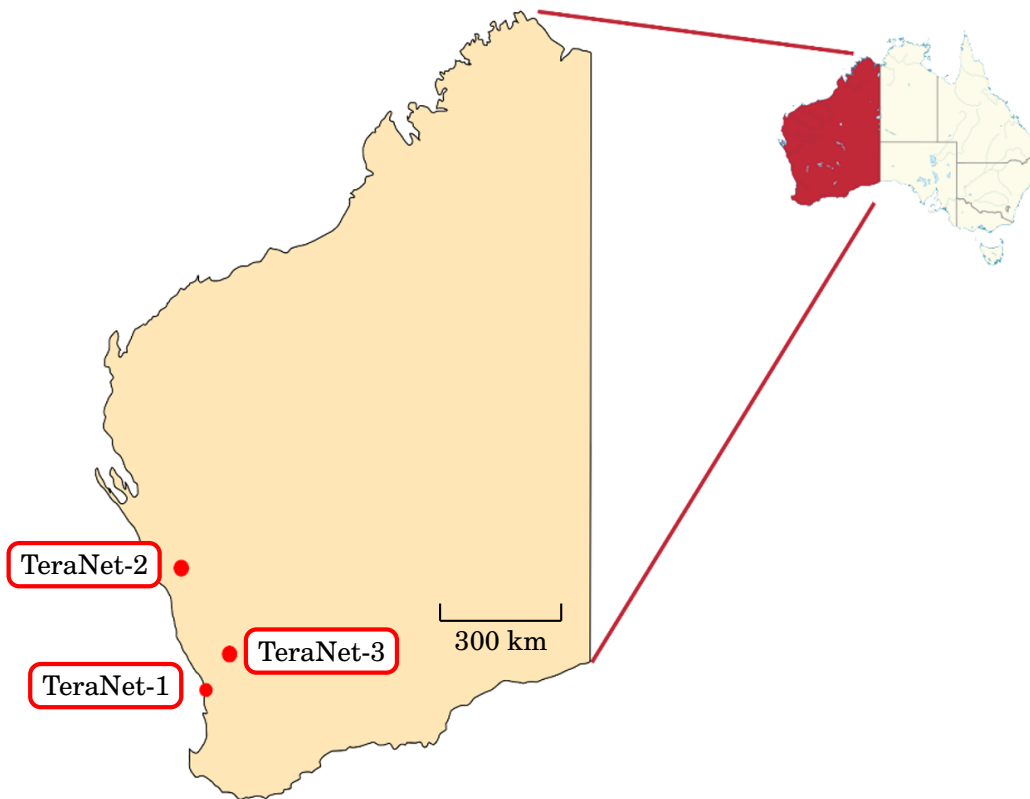


Figure 7.2: The locations of the TeraNet network of optical ground stations in Western Australia. TeraNet-1 and TeraNet-2 are based on 0.7 m telescopes and will be located in Perth and near Mingenew (383 km north of Perth), respectively. TeraNet-3 is a mobile optical ground station, based on a 0.4 m telescope mounted to a utility vehicle. It is planned to be located in New Norcia (132 km north-east of Perth), near ESA’s deep space communications facility.

### 7.4.3 Additional Techniques

Further thought may be given to demonstrating OGS technologies for relay networking. Relay networking between two OGS sites and a space-borne payload was demonstrated in the Laser Communications Relay Demonstration (LCRD) [162]. The terrestrial demonstration techniques described in this thesis could be adapted to simulation of relay networking by replacing the CCR with a retroreflecting prism or other optical relaying device. If a space payload were available, the TeraNet OGS network could support a multi-node demonstration similar to LCRD. Satellite-to-satellite relay networking also benefits from the increased bandwidth provided by FSO communications. The European Data Relay System [42] utilises optical inter-satellite links in the space segment and

LEO-to-ground capability was been demonstrated using laser terminals from the original equipment manufacturer, Tesat [65]. An operational TeraNet could participate in future activities linking sites around the globe. FSO signals are also a promising candidate for next-generation time and frequency transfer techniques with stability performance surpassing current RF time and frequency transfer techniques.

Transfer of time and frequency information between satellites and ground stations provides the basis of global navigation satellite systems. As a result of their higher frequency, optical signals have higher frequency stability than their RF counterparts, and FSO transmission technologies are being developed for next-generation timing networks [163, 164]. FSO frequency transfer may also be used to undertake tests of fundamental physics, by measuring the passage of time at different altitudes above Earth to high precision [97]. The CCR-based techniques described in this thesis are used to develop systems for frequency transfer [109, 110, 165]. This includes links to moving targets with means to measure and suppress Doppler shifts in the optical signal [166]. The quantum nature of light also leads to further applications of FSO transmission techniques to improved communications security.

FSO signals are an enabler for quantum communications. Quantum communications makes use of the quantum nature of light to transmit messages known only to the sender and receiver, thus providing a means to securely distribute security keys [167]. Such quantum key distribution is a burgeoning field and a terrestrial laser range can be used to trial the performance of distribution systems transmitting through atmospheric turbulence. Satellites employing quantum communications systems could also be used to relay quantum states between different locations on Earth for global quantum communications [168]. If equipped with an appropriate detector and optical source, TeraNet could support space-borne quantum payloads. Such activities would leverage experiences with systems used in classical communications, such as the single-photon detectors used in deep-space PPM.

### **7.5 Concluding Remarks**

OGS networks will support FSO communications with space to overcome emerging limitations of RF communications. This thesis documents FSO communications demonstrations using retroflected links to develop OGS hardware. The research outcomes encourage the further use of retroflected links for OGS development and have led to ongoing work, including attracting investment for the TeraNet OGS network.

---

## REFERENCES

---

- [1] B. P. Dix-Matthews, S. F. E. Karpathakis, and S. W. Schediwy, "Atmospheric turbulence characterization with simultaneous measurement of phase, angle of arrival, and intensity in a retroreflected optical link," *Optics Letters*, vol. 48, no. 21, pp. 5519–5522, 2023.
- [2] S. F. E. Karpathakis, B. P. Dix-Matthews, D. R. Gozzard, and S. W. Schediwy, "High-bandwidth coherent optical communication over 10.3 km of turbulent air," *Applied Optics*, vol. 62, p. G85, May 2023.
- [3] S. M. Walsh, S. F. E. Karpathakis, A. S. McCann, B. P. Dix-Matthews, A. M. Frost, D. R. Gozzard, C. T. Gravestock, and S. W. Schediwy, "Demonstration of 100 Gbps coherent free-space optical communications at LEO tracking rates," *Scientific Reports*, vol. 12, no. 1, pp. 1–12, 2022.
- [4] S. F. E. Karpathakis, B. P. Dix-Matthews, S. M. Walsh, A. S. McCann, D. R. Gozzard, A. M. Frost, C. T. Gravestock, and S. W. Schediwy, "Ground-to-drone optical pulse position modulation demonstration as a testbed for lunar communications," *Drones*, vol. 7, p. 99, 2023.
- [5] Polybius, "Book X," in *The Histories of Polybius, vol. 2*, London, UK: MacMillan and Co., 1889. Sec. 43–44. [Online]. Available: <https://babel.hathitrust.org/cgi/pt?id=hvd.hxjupb&seq=53>. Accessed: July 27, 2023.
- [6] I. U. J. Chappe, "Histoire de la télégraphie," *Ch. Richelet*, 1840.
- [7] P. A. Loubere, "Overview," in *A History of Communication Technology*, New York, NY, USA: Routledge, 2021. pp. 5–13.
- [8] C. M., "An expeditious method of conveying intelligence." *The Scots Magazine*. pp. 73–74, Feb. 1753, [Online]. Available: <https://babel.hathitrust.org/cgi/pt?id=nyp.33433076839491&seq=87>. Accessed: July 27, 2023.
- [9] F. Ronalds, "Description of an electric telegraph," in *Descriptions of an Electrical Telegraph and of Some Other Electrical Apparatus*, London, UK: R. Hunter, 1823.

## REFERENCES

---

- pp. 1–24. [Online]. Available:  
<https://babel.hathitrust.org/cgi/pt?id=mdp.39015021065662&seq=7>.  
Accessed: July 27, 2023.
- [10] O. Heaviside, *Electrical papers*, vol. 2. London, UK: MacMillan and Co., 1894. [Online]. Available:  
[https://babel.hathitrust.org/cgi/pt?id=uc1.\\$b24585&seq=9](https://babel.hathitrust.org/cgi/pt?id=uc1.$b24585&seq=9). Accessed: July 27, 2023.
- [11] H. Hertz, *Electric Waves*. London, UK: MacMillan and Co., 1893. [Online]. Available: [https://babel.hathitrust.org/cgi/pt?id=uc1.\\$b104628&seq=9](https://babel.hathitrust.org/cgi/pt?id=uc1.$b104628&seq=9). Accessed: July 27, 2023.
- [12] G. Marconi, “A note on the effect of daylight upon the propagation of electromagnetic impulses over long distances,” *Proceedings of the Royal Society of London*, vol. 70, p. 4, Sept. 1902.
- [13] G. Johnson, *The All Red Line: The Annals and Aims of the Pacific Cable Project*. Ontario, Canada: J. Hope & Sons, 1903. [Online]. Available: [https://babel.hathitrust.org/cgi/pt?id=uc1.\\$b276871&seq=5](https://babel.hathitrust.org/cgi/pt?id=uc1.$b276871&seq=5). Accessed: Nov. 14, 2023.
- [14] “Imperial wireless chain: Progress at commercial stations.” *The Manchester Guardian*. pp. 12, Jan. 1926.
- [15] A. Joel, “Telecommunications and the IEEE communications society,” *IEEE Communications Magazine*, vol. 40, no. 5, pp. 6–8, 2002.
- [16] F. Stumpers, “The history, development, and future of telecommunications in Europe,” *IEEE Communications Magazine*, vol. 22, no. 5, pp. 84–95, 1984.
- [17] C. E. Shannon, “A mathematical theory of communication,” *The Bell System Technical Journal*, vol. 27, no. 3, pp. 379–423, 1948.
- [18] A. N. Netravali, “The impact of solid-state electronics on computing and communications,” *Bell Labs Technical Journal*, vol. 2, no. 4, pp. 126–154, 1997.
- [19] P. A. Loubere, “Electronic communication,” in *A History of Communication Technology*, New York, NY, USA: Routledge, 2021. pp. 211–212.

- 
- [20] R. Fields, C. Lunde, R. Wong, J. Wicker, D. Kozlowski, J. Jordan, B. Hansen, G. Muehlnikel, W. Scheel, U. Sterr, R. Kahle, and R. Meyer, "NFIRE-to-TerraSAR-X laser communication results: Satellite pointing, disturbances, and other attributes consistent with successful performance," in *Sensors and Systems for Space Applications III*, vol. 7330, (Orlando, FL, USA), pp. 211–225, 2009.
- [21] C. Fuchs, M. Brechtelsbauer, J. Horwath, A. Shrestha, F. Moll, D. Giggenbach, and C. Schmidt, "DLR's transportable optical ground station," in *Advanced Solid-State Lasers Congress*, (Paris, France), p. LTu1B.3, 2013.
- [22] C. M. Schieler, K. M. Riesing, B. C. Bilyeu, B. S. Robinson, J. P. Wang, W. T. Roberts, and S. Piazzolla, "TBIRD 200-Gbps cubesat downlink: system architecture and mission plan," in *2022 IEEE International Conference on Space Optical Systems and Applications (ICSOS)*, (Online conference), pp. 181–185, 2022.
- [23] K. C. Kao and G. A. Hockham, "Dielectric-fibre surface waveguides for optical frequencies," *Proceedings of the Institution of Electrical Engineers*, vol. 113, pp. 1151–1158, 1966.
- [24] D. B. Keck, R. D. Maurer, and P. C. Schultz, "On the ultimate lower limit of attenuation in glass optical waveguides," *Applied Physics Letters*, vol. 22, no. 7, pp. 307–309, 1973.
- [25] J. B. MacChesney and D. J. DiGiovanni, "Materials development of optical fiber," *Journal of the American Ceramic Society*, vol. 73, no. 12, pp. 3537–3556, 1990.
- [26] K. Kikuchi, "Fundamentals of coherent optical fiber communications," *Journal of Lightwave Technology*, vol. 34, pp. 157–179, 2016.
- [27] E. Lutz, "Towards the Terabit/s satellite – interference issues in the user link," *International Journal of Satellite Communications and Networking*, vol. 34, no. 4, pp. 461–482, 2016.
- [28] E. Peral, S. Statham, E. Im, S. Tanelli, T. Imken, D. Price, J. Sauder, N. Chahat, and A. Williams, "The radar-in-a-cubesat (RAINCUBE) and measurement results," in *IGARSS 2018 - 2018 IEEE International Geoscience and Remote Sensing Symposium*, (Valencia, Spain), pp. 6297–6300, July 2018.
- [29] P. Xaypraseuth, R. Satish, and A. Chatterjee, "NISAR spacecraft concept overview: Design challenges for a proposed flagship dual-frequency SAR mission," in *2015 IEEE Aerospace Conference*, (Big Sky, MT, USA), pp. 1–11, 2015.

## REFERENCES

---

- [30] H. Hemmati, A. Biswas, and I. B. Djordjevic, "Deep-space optical communications: Future perspectives and applications," *Proceedings of the IEEE*, vol. 99, no. 11, pp. 2020–2039, 2011.
- [31] M. N. Sweeting, "Modern small satellites: changing the economics of space," *Proceedings of the IEEE*, vol. 106, no. 3, pp. 343–361, 2018.
- [32] C. G. Niederstrasser, "The small launch vehicle survey a 2021 update: The rockets are flying," *Journal of Space Safety Engineering*, vol. 9, no. 3, pp. 341–354, 2022.
- [33] "Space-Track.org." Space-Track.org. <https://www.space-track.org/> (accessed: 2024-07-09).
- [34] A. Carrasco-Casado and R. Mata-Calvo, "Free-space optical links for space communication networks," in *Springer Handbook of Optical Networks*, pp. 1057–1103, Cham, Switzerland: Springer, 2020. [Online]. Available: <https://arxiv.org/ftp/arxiv/papers/2012/2012.13166.pdf>. Accessed: Aug. 24, 2022.
- [35] J. P. W. Stark and G. G. Swinerd, "Mission analysis," in *Spacecraft Systems Engineering*, 4th ed. Hoboken, NJ, USA: Wiley, 2011. pp. 111-175.
- [36] H. W. Leigh, L. A. Magruder, C. C. Carabajal, J. L. Saba, and J. F. McGarry, "Development of onboard digital elevation and relief databases for ICESat-2," *IEEE Transactions on Geoscience and Remote Sensing*, vol. 53, no. 4, pp. 2011–2020, 2014.
- [37] D. M. Boroson and B. S. Robinson, "The lunar laser communication demonstration: NASA's first step toward very high data rate support of science and exploration missions," *Space Science Reviews*, vol. 185, pp. 115–128, Dec. 2014.
- [38] Z. Sodnik, C. Heese, I. Carnelli, A. Galvez, and T. Dreischer, "Multi-purpose laser communication system for the asteroid impact mission (AIM)," in *2015 IEEE International Conference on Space Optical Systems and Applications (ICSOS)*, (New Orleans, LA, USA), pp. 1–7, 2015.
- [39] J. Poliak, R. M. Calvo, and F. Rein, "Demonstration of 1.72 Tbit/s optical data transmission under worst-case turbulence conditions for ground-to-geostationary satellite communications," *IEEE Communications Letters*, vol. 22, pp. 1818–1821, 2018.

- [40] A. Dochhan, J. Poliak, J. Surof, M. Richerzhagen, H. F. Kelemu, and R. M. Calvo, “13.16 Tbit/s free-space optical transmission over 10.45 km for geostationary satellite feeder-links,” in *Photonic Networks; 20th ITG-Symposium*, (Leipzig, Germany), pp. 1–3, 2019.
- [41] B. I. Bitachon, Y. Horst, L. Kulmer, T. Blatter, K. Keller, A. M. Bonnefois, J.-M. Conan, C. Lim, J. Montri, P. Perrault, *et al.*, “Tbit/s single channel 53 km free-space optical transmission—assessing the feasibility of optical GEO-satellite feeder links,” in *2022 European Conference on Optical Communication (ECOC)*, (Basel, Switzerland), pp. 1–4, 2022.
- [42] F. Heine, A. Brzoska, M. Gregory, T. Hiemstra, R. Mahn, P. M. Pimentel, and H. Zech, “Status on laser communication activities at Tesat-Spacecom,” in *Free-Space Laser Communications XXXV* (H. Hemmati and B. S. Robinson, eds.), p. 124130C, 2023.
- [43] J. C. McDowell, “The low earth orbit satellite population and impacts of the SpaceX Starlink constellation,” *Astrophysical Journal Letters*, vol. 892, no. 2, p. L36, 2020.
- [44] T. E. Humphreys, P. A. Iannucci, Z. M. Komodromos, and A. M. Graff, “Signal structure of the Starlink Ku-band downlink,” *IEEE Transactions on Aerospace and Electronic Systems*, pp. 1–16, 2023.
- [45] M. M. Kobayashi, F. Stocklin, M. Pugh, I. Kuperman, D. Bell, S. El-Nimri, B. Johnson, N. Huynh, S. Kelly, J. Nessel, A. Svitak, T. Williams, N. Linton, M. Arciaga, and A. Dissanayake, “NASA’s high-rate Ka-band downlink system for the NISAR mission,” *Acta Astronautica*, vol. 159, pp. 358–361, 2019.
- [46] C. Schieler, B. S. Robinson, O. Guldner, B. Bilyeu, A. S. Garg, K. M. Riesing, J. T. Chang, and F. Hakimi, “NASA’s terabyte infrared delivery (TBIRD) program: Large-volume data transfer from LEO,” in *Proceedings of the AIAA / USU Conference on Small Satellites*, (Logan, UT, USA), 2019. Communications, SSC19-VI-02. [Online], Available: <https://digitalcommons.usu.edu/smallsat/2019/all2019/107/>.
- [47] B. Denby, K. Chintalapudi, R. Chandra, B. Lucia, and S. Noghabi, “Kodan: Addressing the computational bottleneck in space,” in *Proceedings of the 28th ACM International Conference on Architectural Support for Programming Languages and Operating Systems, Volume 3*, pp. 392–403, 2023.

## REFERENCES

---

- [48] R. Sniffin and C. Chang, “General information,” in *DSN Telecommunications Link Design Handbook*, Pasadena, CA, USA: Jet Propulsion Laboratory, 2013. [Online]. Available: <https://deepspace.jpl.nasa.gov/dsndocs/810-005/208/208B.pdf>. Accessed: Feb. 25, 2022.
- [49] R. Martin and M. Warhaut, “ESA’s 35-meter deep space antennas at New Norcia/Western Australia and Cebreros/Spain,” in *2004 IEEE Aerospace Conference*, vol. 2, (Big Sky, MT, USA), pp. 1124–1133, 2004.
- [50] “Goonhilly lunar and deep space services.” Goonhilly Earth Station. [Online]. <https://www.goonhilly.org/deep-space> (Accessed: Jan. 14, 2024).
- [51] D. J. Geisler, “Modem module development for NASA’s Orion spacecraft: Achieving FSO communications over lunar distances,” in *Optical Fiber Communication Conference*, (San Diego, CA, USA), pp. Th3J–1, 2020.
- [52] I. J. O’Neill, “NASA’s tech demo streams first video from deep space via laser.” National Aeronautics and Space Administration. [Online]. <https://www.jpl.nasa.gov/news/nasas-tech-demo-streams-first-video-from-deep-space-via-laser> (Accessed: Feb. 8, 2024).
- [53] Z. Sodnik, C. Heese, P.-D. Arapoglou, K.-J. Schulz, I. Zayer, R. Daddato, and S. Kraft, “Deep-space optical communication system (DOCS) for ESA’s space weather mission to Lagrange orbit L5,” in *2017 IEEE International Conference on Space Optical Systems and Applications (ICSOS)*, (Naha, Japan), pp. 28–33, 2017.
- [54] *Optical Communications Physical Layer: Recommended Standard*, 141.0-B-1, Consultative Committee on Space Data Systems, Aug. 2019. [Online]. Available: <https://public.ccsds.org/Pubs/141x0b1.pdf> (Accessed: Dec. 15, 2021).
- [55] M. Srinivasan, E. Alerstam, E. Wollman, R. Rogalin, S. Meenehan, M. Shaw, A. E. Velasco, A. Biswas, N. Richard, D. Cho, V. Garkanian, J. Allmaras, G. Miles, and E. Grigorian, “The deep space optical communications project ground laser receiver,” in *Free-Space Laser Communications XXXV* (H. Hemmati and B. S. Robinson, eds.), vol. 12413, p. 124130R, 2023.
- [56] L. C. Andrews and R. L. Phillips, *Laser Beam Propagation Through Random Media*. 2nd ed., Bellingham, WA, USA: SPIE, 2005.

- 
- [57] B. P. Dix-Matthews, S. W. Schediwy, D. R. Gozzard, E. Savalle, F.-X. Esnault, T. Lévêque, C. Gravestock, D. D’Mello, S. Karpathakis, M. Tobar, and P. Wolf, “Point-to-point stabilized optical frequency transfer with active optics,” *Nature Communications*, vol. 12, p. 515, Dec. 2021.
- [58] B. P. Dix-Matthews, D. R. Gozzard, S. F. E. Karpathakis, C. T. Gravestock, and S. W. Schediwy, “Ultra-wideband free-space optical phase stabilization,” *IEEE communications letters*, vol. 25, no. 5, pp. 1610–1614, 2021.
- [59] E. D. Caldwell, W. C. Swann, J. L. Ellis, M. I. Bodine, C. Mak, N. Kuczun, N. R. Newbury, L. C. Sinclair, A. Muschinski, and G. B. Rieker, “Optical timing jitter due to atmospheric turbulence: Comparison of frequency comb measurements to predictions from micrometeorological sensors,” *Optics Express*, vol. 28, pp. 26661–26675, Aug. 2020.
- [60] J. Surof, J. Poliak, and R. M. Calvo, “Demonstration of intradyne BPSK optical free-space transmission in representative atmospheric turbulence conditions for geostationary uplink channel,” *Optics Letters*, vol. 42, no. 11, pp. 2173–2176, 2017.
- [61] L. C. Andrews, R. L. Phillips, C. Y. Hopen, and M. A. Al-Habash, “Theory of optical scintillation,” *J. Opt. Soc. Am. A*, vol. 16, pp. 1417–1429, June 1999.
- [62] F. Bennet, K. Ferguson, K. Grant, E. Kruzins, N. Rattenbury, and S. Schediwy, “An Australia/New Zealand optical communications ground station network for next generation satellite communications,” in *Free-Space Laser Communications XXXII* (H. Hemmati and B. S. Robinson, eds.), vol. 11272, pp. 1 – 7, 2020.
- [63] Y. Arimoto, M. Toyoshima, M. Toyoda, T. Takahashi, M. Shikatani, and K. Araki, “Preliminary result on laser communication experiment using engineering test satellite-VI (ETS-VI),” in *Free-Space Laser Communication Technologies VII* (G. S. Mecherle, ed.), vol. 2381, pp. 151–158, 1995.
- [64] M. Toyoshima, K. Takizawa, T. Kuri, W. Klaus, M. Toyoda, H. Kunimori, T. Jono, Y. Takayama, M. Mokuno, and K. Arai, “Results of ground-to-space optical communications experiments using a low earth orbit satellite,” in *LEOS 2006–19th Annual Meeting of the IEEE Lasers and Electro-Optics Society*, (Montreal, Canada), pp. 80–81, 2006.
- [65] T. Jono, Y. Takayama, K. Shiratama, I. Mase, B. Demellenne, Z. Sodnik, A. Bird, M. Toyoshima, H. Kunimori, D. Giggenbach, N. Perlot, M. Knappek, and K. Arai,

## REFERENCES

---

- “Overview of the inter-orbit and the orbit-to-ground laser communication demonstration by OICETS,” in *Free-Space Laser Communication Technologies XIX and Atmospheric Propagation of Electromagnetic Waves*, vol. 6457, pp. 9–18, 2007.
- [66] Y. Takayama, M. Toyoshima, Y. Shoji, Y. Koyama, H. Kunimori, M. Sakaue, S. Yamakawa, Y. Tashima, and N. Kura, “Expanded laser communications demonstrations with OICETS and ground stations,” in *Free-Space Laser Communication Technologies XXII* (H. Hemmati, ed.), vol. 7587, p. 75870D, 2010.
- [67] K. E. Wilson, J. Kovalik, A. Biswas, M. Wright, W. T. Roberts, Y. Takayama, and S. Yamakawa, “Preliminary results of the OCTL to OICETS optical link experiment (OTOOLE),” in *Free-Space Laser Communication Technologies XXII* (H. Hemmati, ed.), vol. 7587, p. 758703, 2010.
- [68] Z. Sodnik, H. Smit, M. Sans, D. Giggenbach, P. Becker, R. Mata Calvo, C. Fuchs, I. Zayer, M. Lanucara, K.-J. Schulz, J. Widmer, F. Arnold, A. Alonso, and I. Montilla, “Results from a Lunar laser communication experiment between NASA’s LADEE satellite and ESA’s optical ground station,” in *International Conference on Space Optical Systems and Applications (ICSOS)*, 2014.
- [69] C. Fuchs, C. Schmidt, J. Keim, F. Moll, B. Rödiger, M. Lengowski, S. Gaißer, and D. Giggenbach, “Update on DLR’s OSIRIS program and first results of OSIRISv1 on Flying Laptop,” in *Free-Space Laser Communications XXXI* (H. Hemmati and D. M. Boroson, eds.), vol. 10910, pp. 171–180, 2019.
- [70] K. M. Riesing, C. M. Schieler, J. S. Chang, N. J. Gilbert, A. J. Horvath, R. S. Reeve, B. S. Robinson, J. P. Wang, P. S. Agrawal, and R. A. Goodloe, “On-orbit results of pointing, acquisition, and tracking for the TBIRD cubesat mission,” in *Free-Space Laser Communications XXXV* (H. Hemmati and B. S. Robinson, eds.), vol. 12413, p. 1241305, 2023.
- [71] C. M. Schieler, A. S. Garg, B. C. Bilyeu, J. P. Wang, and B. S. Robinson, “Demonstration of reliable high-rate optical communication over an atmospheric link using ARQ,” in *2019 IEEE International Conference on Space Optical Systems and Applications (ICSOS)*, (Portland, OR, USA), pp. 1–6, 2019.
- [72] P. V. Trinh, A. Carrasco-Casado, T. Okura, H. Tsuji, D. R. Kolev, K. Shiratama, Y. Munemasa, and M. Toyoshima, “Experimental channel statistics of drone-to-ground retro-reflected FSO links with fine-tracking systems,” *IEEE Access*, vol. 9, pp. 137148–137164, 2021.

- [73] M. Birch, N. Martínez, F. Bennet, M. Copeland, and D. Grosse, “The Mount Stromlo optical communication ground station,” in *2022 IEEE International Conference on Space Optical Systems and Applications (ICSOS)*, (Online conference), pp. 134–137, 2022.
- [74] K. Mudge, B. Clare, E. Jager, V. Devrelis, F. Bennet, M. Copeland, N. Herrald, I. Price, G. Lechner, J. Kodithuwakkuge, J. Magarelli, D. Bandara, C. Peck, M. Hollick, P. Alvino, P. Camp-Smith, B. Szumylo, A. Raj, and K. Grant, “DSTG laser satellite communications: Current activities and future outlook,” in *2022 IEEE International Conference on Space Optical Systems and Applications (ICSOS)*, (Online conference), pp. 17–21, 2022.
- [75] M. Birch, J. R. Beattie, F. Bennet, N. Rattenbury, M. Copeland, T. Travouillon, K. Ferguson, J. Cater, and M. Sayat, “Availability, outage, and capacity of spatially correlated, Australasian free-space optical networks,” *Journal of Optical Communications and Networking*, vol. 15, no. 7, pp. 415–430, 2023.
- [76] H. Chedzey, M. Lynch, B. Nener, and K. Mudge, “Clear sky availability for satellite communications in a sub-tropical region - Australia,” *IEEE transactions on Aerospace and Electronic Systems*, pp. 1–10, 2023.
- [77] M. F. Mesिया, *Contemporary Communication Systems*. New York, NY, USA: McGraw-Hill, 2013.
- [78] Analog Devices, Inc., *ADI-BERT user guide*. (2014). Accessed Feb. 16, 2024 [Online]. Available: <https://www.analog.com/media/en/technical-documentation/user-guides/UG-551.pdf>.
- [79] Analog Devices, Inc., *ADN2915: Continuous rate 6.5 Mbps to 11.3 Gbps clock and data recovery IC with integrated limiting amp/EQ*. (2016). Accessed: Feb. 16, 2024. [Online]. Available: <https://www.analog.com/media/en/technical-documentation/data-sheets/ADN2915.pdf>.
- [80] *OTU-4 long-reach interface, G709.2*, International Telecommunication Union, July 2018. [Online]. Available: <https://www.itu.int/rec/T-REC-G.709.2/> (Accessed: July 29, 2022).
- [81] *SDA OCT Standard*, SDA OCT 3.1.0, Space Development Agency, March 2023. [Online]. Available: [https://www.sda.mil/wp-content/uploads/2023/06/SDA\\_OCT\\_Standard-3.1.0\\_Signed\\_Web\\_Version.pdf](https://www.sda.mil/wp-content/uploads/2023/06/SDA_OCT_Standard-3.1.0_Signed_Web_Version.pdf) (Accessed: Feb. 12, 2024).

## REFERENCES

---

- [82] *Optical Communications Physical Layer: Draft Recommended Standard*, 141.0-P-1.1, Consultative Committee on Space Data Systems, July 2020. [Online]. Available: <https://public.ccsds.org/Lists/CCSDS%201410P11/141x0p11.pdf> (Accessed Nov. 21, 2023).
- [83] E. Agrell and M. Karlsson, “Power-efficient modulation formats in coherent transmission systems,” *Journal of Lightwave Technology*, vol. 27, no. 22, pp. 5115–5126, 2009.
- [84] D. M. Boroson, *Optical Communications: A Compendium of Signal Formats, Receiver Architectures, Analysis Mathematics, and Performance Characteristics*. Lexington, MA, USA: Massachusetts Institute of Technology, Lincoln Laboratory, 2005.
- [85] J. J. Degnan, “Millimeter accuracy satellite laser ranging: a review,” in *Contributions of Space Geodesy to Geodynamics: Technology*, pp. 133–162, Hoboken, NJ, USA: Wiley, 1993.
- [86] Y. Dikmelik and F. M. Davidson, “Fiber-coupling efficiency for free-space optical communication through atmospheric turbulence,” *Applied Optics*, vol. 44, no. 23, pp. 4946–4952, 2005.
- [87] J. W. Strohbehn, “Line-of-sight wave propagation through the turbulent atmosphere,” *Proceedings of the IEEE*, vol. 56, no. 8, pp. 1301–1318, 1968.
- [88] J.-M. Conan, G. Rousset, and P.-Y. Madec, “Wave-front temporal spectra in high-resolution imaging through turbulence,” *Journal of the Optical Society of America A*, vol. 12, no. 7, p. 1559, 1995.
- [89] S. M. Walsh and S. W. Schediwy, “Adaptive optics LEO uplink pre-compensation with finite spatial modes,” *Optics Letters*, vol. 48, no. 4, pp. 880–883, 2023.
- [90] N. Maron, S. Fernandez, F.-X. Esnault, T. Lévêque, T. Muzeau, and P. Wolf, “Free space optical link to a tethered balloon for frequency transfer and chronometric geodesy,” *Opt. Express*, vol. 32, pp. 4267–4276, Jan. 2024.
- [91] N. Martinez, “Atmospheric pre-compensation of ground-to-space communications with adaptive optics: Past, present and future—a field review,” *Photonics*, vol. 10, p. 858, 2023.
- [92] R. Hill and G. Ochs, “Fine calibration of large-aperture optical scintillometers and an optical estimate of inner scale of turbulence,” *Applied Optics*, vol. 17, no. 22, pp. 3608–3612, 1978.

- 
- [93] C. R. Zeisse, B. D. Nener, and R. V. Dewees, "Measurement of low-altitude infrared propagation," *Applied Optics*, vol. 39, pp. 873–886, Feb. 2000.
- [94] J. Martin and S. M. Flatté, "Intensity images and statistics from numerical simulation of wave propagation in 3-D random media," *Applied Optics*, vol. 27, no. 11, pp. 2111–2126, 1988.
- [95] E. M. Johansson and D. T. Gavel, "Simulation of stellar speckle imaging," in *Amplitude and Intensity Spatial Interferometry II*, vol. 2200, pp. 372–383, 1994.
- [96] K. D. Silva and B. D. Nener, "Efficient sub-harmonic phase-screen generation for modelling of free-space laser communications," in *2013 IEEE 8th International Conference on Industrial and Information Systems*, (Kandy, Sri Lanka), pp. 219–223, 2013.
- [97] D. R. Gozzard, L. A. Howard, B. P. Dix-Matthews, S. F. E. Karpathakis, C. T. Gravestock, and S. W. Schediwy, "Ultrastable free-space laser links for a global network of optical atomic clocks," *Phys. Rev. Lett.*, vol. 128, p. 020801, Jan. 2022.
- [98] R. K. Tyson and B. W. Frazier, *Field Guide to Adaptive Optics*. 2nd ed. Bellingham, WA, USA: SPIE, 2012.
- [99] T. M. Yarnall, D. J. Geisler, C. M. Schieler, and R. B. Yip, "Analysis of free-space coupling to photonic lanterns in the presence of tilt errors," in *2017 IEEE Photonics Conference (IPC)*, pp. 723–724, 2017.
- [100] A. Billaud, A. Orioux, F. Gomez, T. Michel, S. Bernard, D. Allieux, and O. Pinel, "10 Gbps free space optical communication link using multi-plane light conversion turbulence mitigation," in *International Conference on Space Optics (ICSO) 2022*, vol. 12777, pp. 2040–2054, 2023.
- [101] J. L. Meriam and L. G. Kraige, *Engineering Mechanics: Dynamics*. 7th ed. Hoboken, NJ, USA: John Wiley & Sons, 2013.
- [102] *Safety of laser products – Part 14: A user's guide*, AS/NZS IEC 60825.14:2011, Standards Australia Limited/Standards New Zealand, Oct. 2011.
- [103] A. M. Kowalevich Jr and F. Bucholtz, "Beam divergence from an SMF-28 optical fiber." Naval Research Laboratory, Washington, DC, USA, NRL/MR/5650–06-8996, 2006. [Online]. Available: <https://apps.dtic.mil/sti/pdfs/ADA456331.pdf> (Accessed: Jan. 11, 2024).

## REFERENCES

---

- [104] “Fixed focus collimation packages: FC/APC connectors.” Thorlabs. [Online]. [https://www.thorlabs.com/newgrouppage9.cfm?objectgroup\\_id=1696](https://www.thorlabs.com/newgrouppage9.cfm?objectgroup_id=1696) (Accessed: Jan. 11, 2024).
- [105] L. C. Sinclair, F. R. Giorgetta, W. C. Swann, E. Baumann, I. Coddington, and N. R. Newbury, “Optical phase noise from atmospheric fluctuations and its impact on optical time-frequency transfer,” *Physical Review A*, vol. 89, p. 023805, Feb. 2014.
- [106] C. Robert, J.-M. Conan, and P. Wolf, “Impact of turbulence on high-precision ground-satellite frequency transfer with two-way coherent optical links,” *Physical Review A*, vol. 93, pp. 1–13, Mar. 2016.
- [107] Q. Shen, J.-Y. Guan, J.-G. Ren, T. Zeng, L. Hou, M. Li, Y. Cao, J.-J. Han, M.-Z. Lian, Y.-W. Chen, X.-X. Peng, S.-M. Wang, D.-Y. Zhu, X.-P. Shi, Z.-G. Wang, Y. Li, W.-Y. Liu, G.-S. Pan, Y. Wang, Z.-H. Li, J.-C. Wu, Y.-Y. Zhang, F.-X. Chen, C.-Y. Lu, S.-K. Liao, J. Yin, J.-J. Jia, C.-Z. Peng, H.-F. Jiang, Q. Zhang, and J.-W. Pan, “Free-space dissemination of time and frequency with 10<sup>-19</sup> instability over 113 km,” *Nature*, vol. 610, pp. 661–666, Oct. 2022.
- [108] H. J. Kang, J. Yang, B. J. Chun, H. Jang, B. S. Kim, Y.-J. Kim, and S.-W. Kim, “Free-space transfer of comb-rooted optical frequencies over an 18 km open-air link,” *Nature Communications*, vol. 10, no. 1, pp. 1–8, 2019.
- [109] B. Dix-Matthews, D. Gozzard, S. Karpathakis, S. Walsh, A. McCann, A. Frost, and S. Schediwy, “Experimental demonstration of velocimetry by actively stabilized coherent optical transfer,” *Physical Review Applied*, vol. 19, p. 054018, May 2023.
- [110] B. P. Dix-Matthews, D. R. Gozzard, S. M. Walsh, A. S. McCann, S. F. E. Karpathakis, A. M. Frost, C. T. Gravestock, and S. W. Schediwy, “Towards optical frequency geopotential difference measurements via a flying drone,” *Optics Express*, vol. 31, p. 15075, Apr. 2023.
- [111] E. D. Caldwell, J.-D. Deschenes, J. Ellis, W. C. Swann, B. K. Stuhl, H. Bergeron, N. R. Newbury, and L. C. Sinclair, “Quantum-limited optical time transfer for future geosynchronous links,” *Nature*, vol. 618, pp. 721–726, June 2023.
- [112] S. Manning, B. A. Clare, K. J. Grant, and K. A. Mudge, “Development and implementation of a robust angle of arrival turbulence measurement system,” *Optical Engineering*, vol. 54, p. 114104, Nov. 2015.

- [113] M. F. Stell, C. I. Moore, H. R. Burris, M. R. Suite, M. J. Vilcheck, M. A. Davis, R. Mahon, E. Oh, W. S. Rabinovich, G. C. Gilbreath, W. J. Scharpf, and A. E. Reed, "Passive optical monitor for atmospheric turbulence and windspeed," in *Free-Space Laser Communication and Active Laser Illumination III*, vol. 5160, pp. 422–431, SPIE, 2004.
- [114] B. P. Dix-Matthews, S. F. E. Karpathakis, and S. W. Schediwy, *Retroreflected optical phase, angle-of-arrival, and intensity dataset*. figshare, July 2023.  
<https://doi.org/10.6084/m9.figshare.23721870>.
- [115] S. M. Walsh, A. M. Frost, L. A. Howard, D. R. Gozzard, S. F. E. Karpathakis, B. P. Dix-Matthews, C. T. Gravestock, A. S. McCann, and S. W. Schediwy, "Angle-of-arrival variability of retroreflected lasers despite atmospheric reciprocity," *Optics Letters*, vol. 47, p. 1920, Apr. 2022.
- [116] W. Riley and D. Howe, "Time domain stability," in *Handbook of Frequency Stability Analysis*, Gaithersburg, MD, USA: National Institute of Standards and Technology, 2008. [Online]. Available:  
[https://tsapps.nist.gov/publication/get\\_pdf.cfm?pub\\_id=50505](https://tsapps.nist.gov/publication/get_pdf.cfm?pub_id=50505). Accessed: Sept. 30 2023.
- [117] E. Pincemin, Y. Loussouarn, Y. Pan, G. Miller, A. Gibbemeyer, B. Mikkelsen, A. Gaibazzi, W. Way, T. Yamazaki, A. Hayashi, and K. Fujiyama, "Interoperable CFP-DCO and CFP2-DCO pluggable optic interfaces for 100G WDM transmission," in *2019 Optical Fiber Communication Conference (OFC)*, pp. 1–3, 2019.
- [118] O. Balasiano, E. Wohlgemuth, I. Attia, A. Roizman, T. Falk, R. Faig, A. Shapira, Y. Yoffe, R. J. Cohen, R. Vered, and D. Sadot, "10 km retro-reflected coherent atmospheric FSOC at 128 Gbps 16-QAM," in *Advanced Photonics Conference: Signal Processing in Photonic Communications*, p. SpTu3G.5, 2022.
- [119] *CFP MSA Management Interface Specification*, Version 2.6 r06a, CFP Multi Source Agreement Consortium, March, 2017. [Online]. Available:  
<https://www.cfp-msa.org/documents/> (Accessed: Oct. 26, 2021).
- [120] "Perth December 13 weather." weatherspark.com – The Weather Year Round Anywhere on Earth. [Online]. <https://weatherspark.com/d/128792/13/13/Average-Weather-on-December-13-in-Perth-Australia> (Accessed: 30 Jan. 2023).

## REFERENCES

---

- [121] P. J. Winzer, D. T. Neilson, and A. R. Chraplyvy, "Fiber-optic transmission and networking: the previous 20 and the next 20 years," *Opt. Express*, vol. 26, pp. 24190–24239, Sept. 2018.
- [122] Y. Kaymak, R. Rojas-Cessa, J. Feng, N. Ansari, M. Zhou, and T. Zhang, "A survey on acquisition, tracking, and pointing mechanisms for mobile free-space optical communications," *IEEE Communications Surveys & Tutorials*, vol. 20, no. 2, pp. 1104–1123, 2018.
- [123] X. Zhu and J. M. Kahn, "Free-space optical communication through atmospheric turbulence channels," *IEEE Transactions on Communications*, vol. 50, no. 8, pp. 1293–1300, 2002.
- [124] A. Belmonte and J. M. Kahn, "Capacity of coherent free-space optical links using atmospheric compensation techniques," *Opt. Express*, vol. 17, pp. 2763–2773, Feb. 2009.
- [125] E. Ip, A. P. T. Lau, D. J. F. Barros, and J. M. Kahn, "Coherent detection in optical fiber systems," *Opt. Express*, vol. 16, pp. 753–791, Jan. 2008.
- [126] M. Toyoshima, "Maximum fiber coupling efficiency and optimum beam size in the presence of random angular jitter for free-space laser systems and their applications," *J. Opt. Soc. Am. A*, vol. 23, pp. 2246–2250, Sept. 2006.
- [127] M. Soukup, J. Gailis, D. Fantin, A. Jochemsen, C. Aas, P.-J. Baeck, I. Benhadj, S. Livens, B. Delauré, M. Menenti, B. Gorte, S. Hosseini aria, M. Esposito, and C. Dijk, "Hyperscout: Onboard processing of hyperspectral imaging data on a nanosatellite," in *Small Satellites, System and Services Symposium (4S)*, (Valletta, Malta), May 2016.
- [128] S. Seel, H. Kämpfner, F. Heine, D. Dallmann, G. Mühlwinkel, M. Gregory, M. Reinhardt, K. Saucke, J. Muckherjee, U. Sterr, B. Wandernoth, R. Meyer, and R. Czichy, "Space to ground bidirectional optical communication link at 5.6 Gbps and EDRS connectivity outlook," in *2011 IEEE Aerospace Conference*, (Big Sky, MT, USA), pp. 1–7, 2011.
- [129] W. Chen, J. Sun, X. Hou, R. Zhu, P. Hou, Y. Yang, M. Gao, L. Lei, K. Xie, M. Huang, R. Li, H. Zang, Y. Wan, E. Dai, Y. Xi, W. Lu, S. Wei, L. Liu, and J. Li, "5.12Gbps optical communication link between LEO satellite and ground station," in *2017*

- 
- IEEE International Conference on Space Optical Systems and Applications (ICSOS)*, (Naha, Japan), pp. 260–263, 2017.
- [130] Y. Saito, H. Takenaka, K. Shiratama, Y. Munemasa, A. Carrasco-Casado, P. V. Trinh, K. Suzuki, T. Fuse, Y. Takahashi, T. Kubo-oka, and M. Toyoshima, “Research and development of a transportable optical ground station in NICT: The results of the first performance test,” *Frontiers in Physics*, vol. 9, 2021.
- [131] E. Fischer, M. Feriencik, K. Kudielka, T. Dreischer, P. Adolph, T. Berkefeld, D. Soltau, J. Perdignes-Armengol, and Z. Sodnik, “ESA optical ground station upgrade with adaptive optics for high data rate satellite-to-ground links-test results,” in *2019 IEEE International Conference on Space Optical Systems and Applications (ICSOS)*, (Portland, OR, USA), pp. 1–6, 2019.
- [132] H. Takenaka, M. Toyoshima, and Y. Takayama, “Experimental verification of fiber-coupling efficiency for satellite-to-ground atmospheric laser downlinks,” *Optics express*, vol. 20, pp. 15301–15308, July 2012.
- [133] C. Chen, A. Grier, M. Malfa, E. Booen, H. Harding, C. Xia, M. Hunwardsen, J. Demers, K. Kudinov, G. Mak, B. Smith, A. Sahasrabudhe, F. Patawaran, T. Wang, A. Wang, C. Zhao, D. Leang, J. Gin, M. Lewis, B. Zhang, D. Nguyen, D. Jandrain, F. Haque, and K. Quirk, “Demonstration of a bidirectional coherent air-to-ground optical link,” in *Free-Space Laser Communication and Atmospheric Propagation XXX* (H. Hemmati and D. M. Boroson, eds.), vol. 10524, pp. 120 – 134, 2018.
- [134] L. Li, R. Zhang, Z. Zhao, G. Xie, P. Liao, K. Pang, H. Song, C. Liu, Y. Ren, G. Labroille, *et al.*, “High-capacity free-space optical communications between a ground transmitter and a ground receiver via a uav using multiplexing of multiple orbital-angular-momentum beams,” *Scientific Reports*, vol. 7, no. 1, pp. 1–12, 2017.
- [135] L. Li, R. Zhang, P. Liao, Y. Cao, H. Song, Y. Zhao, J. Du, Z. Zhao, C. Liu, K. Pang, H. Song, A. Almainan, D. Starodubov, B. Lynn, R. Bock, M. Tur, A. F. Molisch, and A. E. Willner, “Mitigation for turbulence effects in a 40-Gbit/s orbital-angular-momentum-multiplexed free-space optical link between a ground station and a retro-reflecting UAV using MIMO equalization,” *Opt. Lett.*, vol. 44, pp. 5181–5184, Nov. 2019.
- [136] G. Parca, A. Shahpari, V. Carrozzo, G. M. T. Belevfi, and A. L. J. Teixeira, “Optical wireless transmission at 1.6-Tbit/s (16×100 Gbit/s) for next-generation convergent urban infrastructures,” *Optical Engineering*, vol. 52, no. 11, p. 116102, 2013.

## REFERENCES

---

- [137] X. Feng, Z. Wu, T. Wang, H. Jiang, Y. Su, H. Jiang, and S. Gao, “120 Gbit/s high-speed WDM-QPSK free-space optical transmission through 1 km atmospheric channel,” *Electronics Letters*, vol. 54, no. 18, pp. 1082–1084, 2018.
- [138] F. P. Guiomar, M. A. Fernandes, J. L. Nascimento, V. Rodrigues, and P. P. Monteiro, “Coherent free-space optical communications: Opportunities and challenges,” *Journal of Lightwave Technology*, vol. 40, no. 10, pp. 3173–3186, 2022.
- [139] J. H. Shapiro, “Reciprocity of the turbulent atmosphere,” *J. Opt. Soc. Am.*, vol. 61, pp. 492–495, Apr. 1971.
- [140] S. Walsh, A. Frost, W. Anderson, T. Digney, B. Dix-Matthews, D. Gozzard, C. Gravestock, L. Howard, S. Karpathakis, A. McCann, and S. Schediwy, “The Western Australian optical ground station,” in *IET Conference Proceedings*, pp. 71–78(7), 2022.
- [141] G. M. Pettersson, J. Perdignes, and Z. Sodnik, “Unmodified portable telescope for space-to-ground optical links,” in *2019 IEEE International Conference on Space Optical Systems and Applications (ICSOS)*, (Portland, OR, USA), pp. 1–7, 2019.
- [142] Y. Wang, H. Xu, D. Li, R. Wang, C. Jin, X. Yin, S. Gao, Q. Mu, L. Xuan, and Z. Cao, “Performance analysis of an adaptive optics system for free-space optics communication through atmospheric turbulence,” *Scientific Reports*, vol. 8, no. 1, pp. 1124–11, 2018.
- [143] S. G. Leon-Saval, A. Argyros, and J. Bland-Hawthorn, “Photonic lanterns,” *Nanophotonics*, vol. 2, no. 5, pp. 429–440, 2013.
- [144] R. M. Calvo, D. Allieux, A. Reeves, A. Billaud, J. Poliak, O. Pinel, H. F. Kelemu, G. Labroille, and M. Richerzhagen, “Alternative passive fiber coupling system based on multi-plane light conversion for satellite-to-ground communications,” in *Free-Space Laser Communications XXXII* (H. Hemmati and D. M. Boroson, eds.), vol. 11272, pp. 167 – 178, 2020.
- [145] S. Wang, P. Huang, T. Wang, and G. Zeng, “Atmospheric effects on continuous-variable quantum key distribution,” *New Journal of Physics*, vol. 20, p. 083037, Aug. 2018.
- [146] B. Laurent, G. Planche, and C. Michel, “Inter-satellite optical communications: From SILEX to next generation systems,” in *International Conference on Space Optics (ICSO) 2004*, (Toulouse, France), pp. 395–402, 2004.

- [147] “Artemis plan: NASA’s lunar exploration program overview.” National Aeronautics and Space Administration. [Online]. [https://www.nasa.gov/sites/default/files/atoms/files/artemis\\_plan-20200921.pdf](https://www.nasa.gov/sites/default/files/atoms/files/artemis_plan-20200921.pdf) (Accessed: Feb. 9, 2022).
- [148] L. C. Sinclair, H. Bergeron, W. C. Swann, I. Khader, K. C. Cossel, M. Cermak, N. R. Newbury, and J.-D. Deschênes, “Femtosecond optical two-way time-frequency transfer in the presence of motion,” *Physical Review A*, vol. 99, no. 2, p. 023844, 2019.
- [149] H. Bergeron, L. C. Sinclair, W. C. Swann, I. Khader, K. C. Cossel, M. Cermak, J.-D. Deschênes, and N. R. Newbury, “Femtosecond time synchronization of optical clocks off of a flying quadcopter,” *Nature communications*, vol. 10, no. 1, pp. 1–7, 2019.
- [150] P. K. Esubonteng and R. Rojas-Cessa, “RESTORE: Low-energy drone-assisted NLoS-FSO emergency communications,” *IEEE Access*, vol. 10, pp. 115282–115294, 2022.
- [151] S. Janji, A. Samorzewski, M. Wasilewska, and A. Kliks, “On the placement and sustainability of drone FSO backhaul relays,” *IEEE Wireless Communications Letters*, vol. 11, no. 8, pp. 1723–1727, 2022.
- [152] H. D. Trung, “Performance of UAV-to-ground FSO communications with APD and pointing errors,” *Applied System Innovation*, vol. 4, no. 3, 2021.
- [153] A. Carrasco-Casado, K. Shiratama, P. V. Trinh, D. Kolev, Y. Munemasa, T. Fuse, H. Tsuji, and M. Toyoshima, “Development of a miniaturized laser-communication terminal for small satellites,” *Acta Astronautica*, vol. 197, pp. 1–5, 2022.
- [154] C. Quintana, Q. Wang, D. Jakonis, O. Oberg, G. Erry, D. Platt, Y. Thueux, G. Faulkner, H. Chun, A. Gomez, *et al.*, “A high speed retro-reflective free space optics links with UAV,” *Journal of Lightwave Technology*, vol. 39, no. 18, pp. 5699–5705, 2021.
- [155] J. R. Barry, *Wireless Infrared Communications*. 1st ed. New York, NY, USA: Springer, 1994.
- [156] “Perth March 18 weather.” weatherspark.com – The Weather Year Round Anywhere on Earth. [Online]. <https://weatherspark.com/h/d/149190/2022/3/18/Historical-Weather-on-Friday-March-18-2022-at-Perth-Airport-Australia> (Accessed: 11 Jan. 2023).

## REFERENCES

---

- [157] B. P. Dix-Matthews, S. W. Schediwy, D. R. Gozzard, S. Driver, K. U. Schreiber, R. Carman, and M. Tobar, “Methods for coherent optical Doppler orbitography,” *Journal of Geodesy*, vol. 94, p. 55, June 2020.
- [158] F. Moll, “Experimental analysis of channel coherence time and fading behavior in the LEO-ground link,” in *International Conference on Space Optical Systems and Applications (ICSOS)*, (Kobe, Japan), 2014.
- [159] R. Mata-Calvo, D. B. Calia, R. Barrios, M. Centrone, D. Giggenbach, G. Lombardi, P. Becker, and I. Zayer, “Laser guide stars for optical free-space communications,” in *Free-Space Laser Communication and Atmospheric Propagation XXIX*, vol. 10096, pp. 188–199, SPIE, 2017.
- [160] A. McCann, A. Frost, S. Karpathakis, B. Dix-Matthews, D. Gozzard, S. Walsh, and S. Schediwy, “Demonstration of a low-SWaP terminal for ground-to-air single-mode fiber coupled laser links,” *Photonics*, vol. 11, no. 7, p. 633, 2024.
- [161] “Digital optical ground station DOG suite from WORK microwave.” WORK Microwave GmbH. [Online].  
<https://work-microwave.com/digital-optical-groundstation/> (Accessed: Feb. 18, 2024).
- [162] D. J. Israel, B. L. Edwards, R. L. Butler, J. D. Moores, S. Piazzolla, N. du Toit, and L. Braatz, “Early results from NASA’s laser communications relay demonstration (LCRD) experiment program,” in *Free-Space Laser Communications XXXV* (H. Hemmati and B. S. Robinson, eds.), vol. 12413, p. 1241303, 2023.
- [163] T. D. Schmidt, T. Schuldt, G. Michalak, J. Surof, J. Poliak, G. Giorgi, C. Braxmaier, M. Meurer, and C. Günther, “Optical technologies for future global navigation satellite systems,” in *2023 IEEE/ION Position, Location and Navigation Symposium (PLANS)*, pp. 311–317, 2023.
- [164] E. D. Caldwell, L. C. Sinclair, J.-D. Deschenes, F. Giorgetta, and N. R. Newbury, “Application of quantum-limited optical time transfer to space-based optical clock comparisons and coherent networks,” *APL Photonics*, vol. 9, no. 1, p. 016112, 2024.
- [165] S. McSorley, D. R. Gozzard, S. F. Karpathakis, B. P. Dix-Matthews, and S. W. Schediwy, “Stabilized free space optical frequency transfer using digitally enhanced heterodyne interferometry,” *Optics Letters*, vol. 48, no. 14, pp. 3637–3640, 2023.

- [166] S. M. McSorley, B. P. Dix-Matthews, A. M. Frost, A. S. McCann, S. F. Karpathakis, D. R. Gozzard, S. M. Walsh, and S. W. Schediwy, “Free space optical frequency comparison over rapidly moving links,” *arXiv preprint arXiv:2402.08899*, 2024.
- [167] S.-K. Liao, W.-Q. Cai, W.-Y. Liu, L. Zhang, Y. Li, J.-G. Ren, J. Yin, Q. Shen, Y. Cao, Z.-P. Li, F.-Z. Li, X.-W. Chen, L.-H. Sun, J.-J. Jia, J.-C. Wu, X.-J. Jiang, J.-F. Wang, Y.-M. Huang, Q. Wang, Y.-L. Zhou, L. Deng, T. Xi, L. Ma, T. Hu, Q. Zhang, Y.-A. Chen, N.-L. Liu, X.-B. Wang, Z.-C. Zhu, C.-Y. Lu, R. Shu, C.-Z. Peng, J.-Y. Wang, and J.-W. Pan, “Satellite-to-ground quantum key distribution,” *Nature*, vol. 549, no. 7670, pp. 43–47, 2017.
- [168] M. Gündoğan, J. S. Sidhu, M. Krutzik, and D. K. L. Oi, “Time-delayed single satellite quantum repeater node for global quantum communications,” *Optica Quantum*, vol. 2, pp. 140–147, June 2024.
- [169] Texas Instruments, Inc., *ONET1151L: 11.3 Gbps low-power laser diode driver*. (2013). Accessed: Feb. 16, 2024. [Online]. Available: <https://www.ti.com/lit/ds/symlink/onet1151l.pdf>.
- [170] P. C. D. Hobbs, *Building Electro-Optical Systems: Making It All Work*. 2nd ed. Hoboken, NJ, USA: Wiley, 2009.
- [171] C. M. Schieler, K. M. Riesing, A. J. Horvath, B. C. Bilyeu, J. S. Chang, A. S. Garg, J. P. Wang, and B. S. Robinson, “200 Gbps TBIRD cubesat downlink: pre-flight test results,” in *Free-Space Laser Communications XXXIV* (H. Hemmati and B. S. Robinson, eds.), vol. 11993, p. 119930P, 2022.
- [172] C. M. Schieler, K. M. Riesing, B. C. Bilyeu, J. S. Chang, A. S. Garg, N. J. Gilbert, A. J. Horvath, R. S. Reeve, B. S. Robinson, J. P. Wang, S. Piazzolla, W. T. Roberts, J. M. Kovalik, and B. Keer, “On-orbit demonstration of 200-Gbps laser communication downlink from the TBIRD CubeSat,” in *Free-Space Laser Communications XXXV* (H. Hemmati and B. S. Robinson, eds.), vol. 12413, p. 1241302, 2023.
- [173] A. Biswas, J. M. Kovalik, M. W. Wright, W. T. Roberts, M. K. Cheng, K. J. Quirk, M. Srinivasan, M. D. Shaw, and K. M. Birnbaum, “LLCD operations using the Optical Communications Telescope Laboratory (OCTL),” in *Free-Space Laser Communication and Atmospheric Propagation XXVI* (H. Hemmati and D. M. Boroson, eds.), p. 89710X, 2014.



---

---

## APPENDIX A

---

# Supplementary Material: Chapter 2

This supplementary chapter provides background information for Chapter 2. Section A.1 gives two examples for binary usage, showing how binary words can be used to store numerical and text values. Section A.2 then introduces a device used to modulate the amplitude of optical frequency signals with electrical signals. For completeness, photodetectors, used for optical-to-electrical conversion are also briefly discussed in the section. Finally, Section A.3 shows how amplitude modulators are integrated into coherent modulators to create QPSK and  $m$ -QAM encoded signals. Coherent demodulators are also introduced, but interested readers are referred to the Kikuchi 2016 tutorial paper for further mathematical details [26].

### A.1 Binary Representation of Information

Digital information is stored as binary words, made up of bits [77]. Bits are discrete, meaning they can only take one of two defined values. These values are usually represented numerically as a ‘1’ or a ‘0’, although other abstractions are possible, such as the conditionals ‘true’ and ‘false’. Binary words can represent various types of data, for example, a digital sampling system can record a continuous electrical voltages signal and store it as discrete binary words. Figure A.1 depicts a example plot of this sampling process. In the figure, the voltages,  $\frac{3}{4}V_{pk}$  and  $-V_{pk}$  represent the maximum and minimum input voltage range of the sampler. The dark blue link represents the voltage signal being sampled, using three bits are used to quantise the signal. Three bits allows for  $2^3 = 8$  quantisation levels, each represented by a binary word to the left of the amplitude axis. Samples are taken at a regular interval. At the sample time, the binary word corresponding to the quantisation level nearest the voltage signal is sampled as a binary

output, below the time axis. The sampled signal, shown in light blue, can be reproduced elsewhere at a different time.

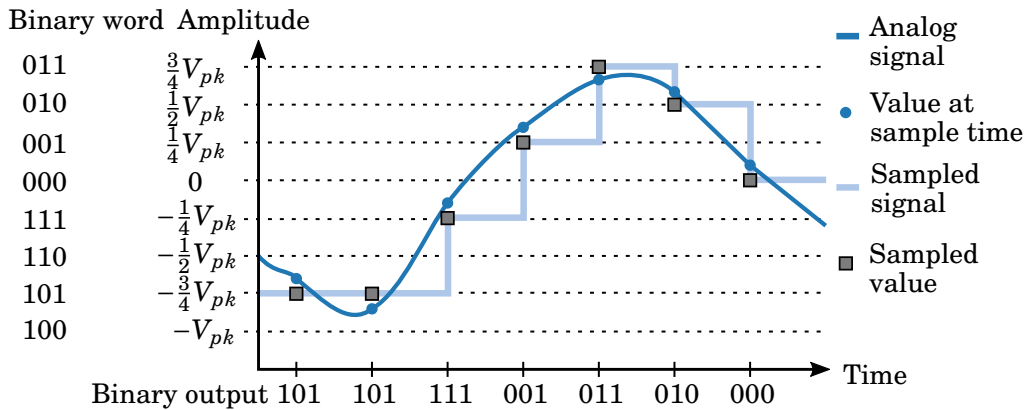


Figure A.1: A continuous analog signal, dark blue, is sampled using three bits, and quantised as an output sequence of binary words. The quantised signal, light blue, can be reproduced by a computer at any time.

Binary words are also used to encode printed characters, allowing human-readable text to be stored and used by a computer. Table A.1 shows a sample of mappings used in the American standard code for information interchange (ASCII) encoding scheme. In ASCII, seven bits are used, giving  $2^7$  or 128 possible values. Of these, 95 are print characters, and the remaining binary words refer to typesetting instructions, such as newlines and spaces. In practice, two computers communicating with each other will each have an internal ASCII encoding reference, so they can encode a text message into a binary message at the transmitter, and decode the binary message back into text at the receiver.

Table A.1: A selection of encodings from binary words to print characters in the ASCII encoding scheme.

Binary word	Print character	Binary word	Print character
011 0000	0	011 0011	3
011 0001	1	011 0100	4
011 0010	2	011 0101	5
110 0001	a	010 0001	!
110 0010	b	010 0010	"
110 0011	c	010 0011	#
110 0100	d	010 0100	\$
110 0101	e	010 0101	%
110 0110	f	010 0110	&
110 0111	g	010 011	'

## A.2 Amplitude Modulation

Amplitude modulation involves manipulating the amplitude of an optical carrier signal according to an electrical baseband message signal. Mathematically, the amplitude modulated signal,  $s_{AM}(t)$  is

$$s_{AM}(t) = A_m(t)A_L \cos(2\pi f_L t), \quad (\text{A.1})$$

where  $A_L$  is the optical signal amplitude, and  $f_L$  is the optical signal frequency, and  $A_m(t)$  is a function of the baseband message signal,  $m(t)$ . In some devices, a laser diode is used as the optical signal source, and the signal is amplitude modulated by directly modulating the power supply current to the diode [169]. In high-end use-cases, however, an external modulator will be used with a higher quality laser source. In optical communications, an external amplitude modulators called a Mach-Zehnder modulator (MZM) is used. A MZM based on a Mach-Zehnder interferometer, with the phase in each arm controlled by an electro-optic modulator (EOM). Figure A.2a shows an illustration of such an EOM. In the device, an optical signal is guided through a crystalline waveguide with electrodes bonded to it. Under an applied voltage signal, the waveguide's refractive index changes, altering the phase of the optical signal so the phase-modulated signal,  $s_{PM}(t)$  becomes

$$s_{PM}(t) = A_L \cos(2\pi f_L t) \exp\left(j \frac{m(t)}{V_\pi} \pi\right), \quad (\text{A.2})$$

where  $j$  is the imaginary number and  $V_\pi$  is the voltage required to induce a  $\pi$  radian phase shift. Figure A.2b illustrates the principle of a MZM, whereby the optical signal is split into two arms, each with an EOM, and then combined. If the two EOMs are driven by equal and opposite voltages  $m(t)$  and  $-m(t)$ , then the optical signal is amplitude modulated, with  $A_m(t)$  becoming

$$A_m(t) = \cos\left(\frac{m(t)}{V_\pi} \pi\right). \quad (\text{A.3})$$

The message signal,  $m(t)$ , has an offset voltage and peak-to-peak amplitude such that the cosine term of Equation A.3 is 1 for a binary 1, and 0 for a binary 0. A photodetector is required to demodulate the message signal from the carrier. Photodetectors generate an electrical current proportional to the square of the carrier signal's amplitude. Thus, the photocurrent due to the signal,  $i_s$ , will be proportional to the signal's amplitude:

$$i_s(t) \propto (A_m(t)A_L)^2. \quad (\text{A.4})$$

A transimpedance amplifier is then used to simply amplify and convert the current into a useful voltage readout for the receiver electronics.

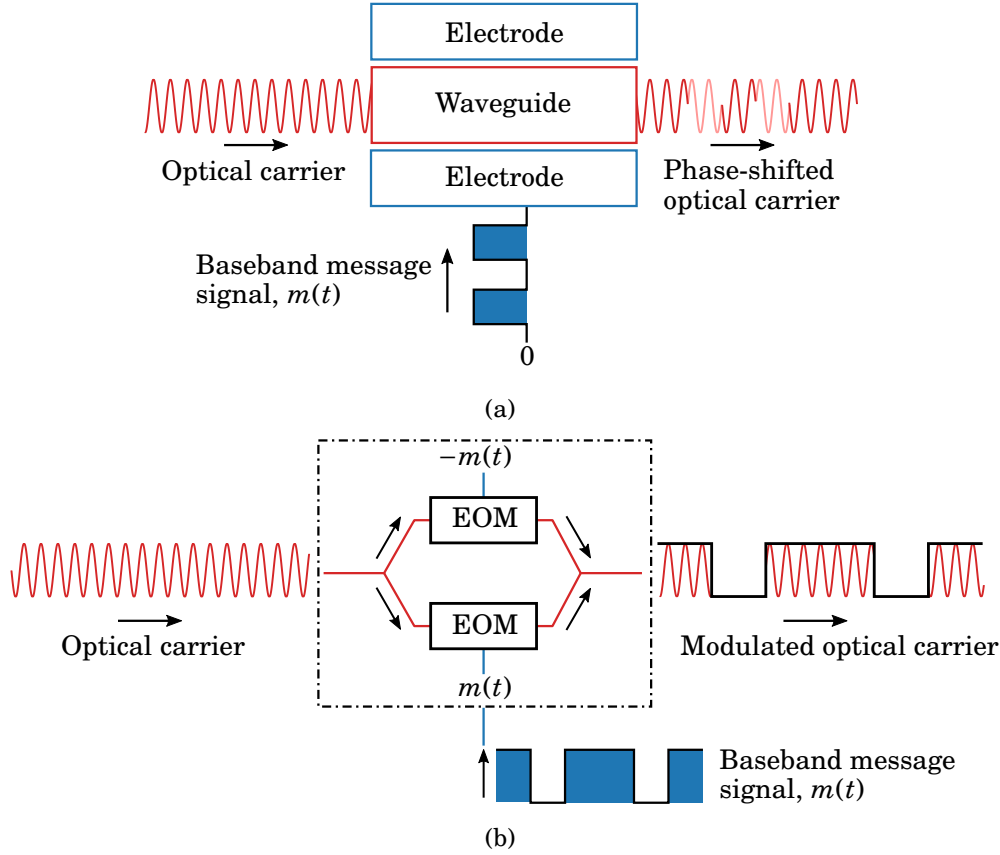


Figure A.2: (a) an illustration of an electro-optical modulator (EOM), used to change the phase of an optical carrier; (b) a Mach-Zehnder modulator, using two EOMs to change the amplitude of an optical carrier through interference.

### A.3 Coherent Modulation

Coherent modulation multiplies the data rate of an optical signal through additional control of phase in the modulator and sensitivity to phase and polarisation in the demodulator. In one polarisation, the coherent optical communications signal,  $s_{CM}(t)$  is

$$s_{CM}(t) = I_m(t)\cos(2\pi f_L t) + Q_m(t)\sin(2\pi f_L t), \tag{A.5}$$

where  $I_m(t)$  and  $Q_m(t)$  are the in-phase and quadrature amplitudes, respectively. Figure A.3a is an illustration of a dual-parallel Mach-Zehnder modulator (DPMZM), showing how the separate cosine and sine terms of Equation A.5 arise. The optical carrier signal is initially split, and one half undergoes a  $\pi/2$  radian phase shift, leading to the sine, or quadrature, term. The cosine term in the top branch is referred to as the in-phase term. In each branch of the DPMZM, a MZM is used to impart a phase shift, per the transfer function in Equation A.3. Figure A.3b shows the constellation diagram resulting QAM

encoding with the DPMZM, where the in-phase amplitude is the normalised amplitude of the cosine term in Equation A.5, and the quadrature amplitude is the normalised amplitude of the sine term. Polarisation diversity is achieved by combining two DPMZMs in parallel, with a polarising beam splitter and combiner before and after the two branches.

Coherent demodulation uses an arrangement of beamsplitters and a local optical signal, the LO, to measure the phase and amplitude of an incoming communications signal. Figure A.3c shows the structure of a coherent receiver.

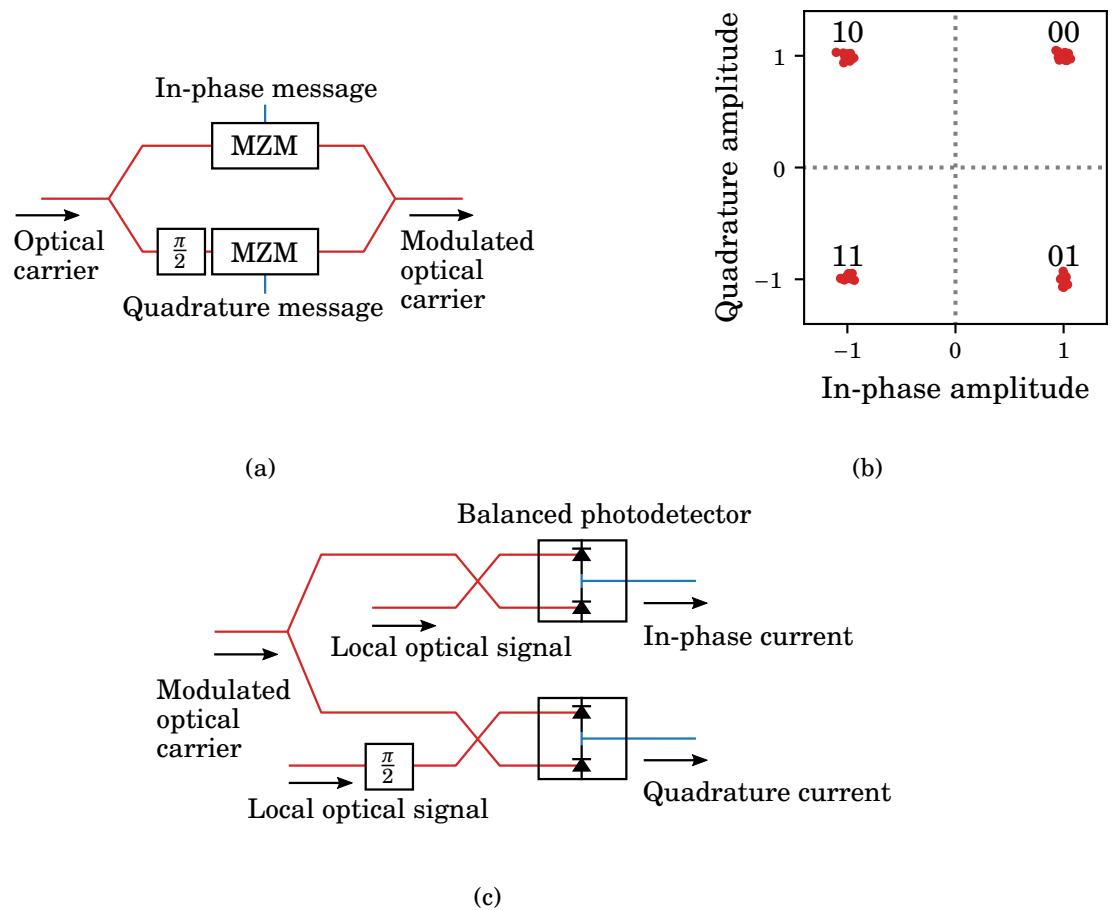


Figure A.3: (a) An illustration of a dual-parallel Mach-Zehnder modulator (MZM), used in coherent modulation; (b) a constellation diagram for quadrature phase-shift keying, a coherent modulation technique; (c) an illustration of a coherent receiver, for recovering the in-phase and quadrature components of the coherently-modulated optical carrier.

When two signals are incident on a photodetector, the output current,  $i_{QAM}$ , is proportional to the square of the summed amplitudes. It comprises multiple components:

$$i_{QAM} = i_s + i_{LO} + i_{mix}, \quad (\text{A.6})$$

where  $i_s$  is the signal's photocurrent,  $i_{LO}$  is the LO photocurrent, and  $i_{mix}$  is a photocurrent arising from the mixing between the two signals. The mixing effect is spatially-dependent; therefore, the communication signal and LO must have the same polarisation and be in the same spatial mode to mix efficiently. This condition also necessitates the use of SMF to ensure good mixing between the signal and LO. The mixing current is a function of the phase of the two signals [170],

$$i_{mix} = 2\sqrt{i_s i_{LO}} \cos(2\pi f_{IF} + \phi_s), \quad (\text{A.7})$$

where  $f_{IF}$  is the difference in frequency between the two signals, and  $\phi_s$  is the communication signal's phase. In the coherent receiver, the communications signal is mixed with the LO signal in the top branch to measure the communication signal's in-phase component. In the bottom branch, a copy of the LO signal is shifted by  $\pi/2$  radians to measure the quadrature component of the communication signal. The arrangement of beam splitters and balanced photodetectors isolates  $i_{mix}$  from the other currents of Equation A.6, for each of the in-phase and quadrature components of  $s_{CM}(t)$ . In a dual-polarisation scheme, two of these coherent receivers are used, in conjunction with a polarising beam splitter. Downstream, digital signal processing is used to further isolate each message current, synchronise  $f_{IF}$ , and then demodulate the message signals [26].

## A.4 Representative Link Budgets

Each demonstration described in this thesis was intended to map to certain space communication missions. However, a limitation of these terrestrial demonstrations is the shorter practicable link distances possible with this method. Although the integrated turbulence exhibited on kilometre-scale slanted terrestrial links can exceed that of ground-space links, geometric losses are significantly greater at ground-space scales. Larger receiver apertures will also be used in real OGS deployments. Considering these differences, the relevance of the terrestrial demonstrations to space-ground communications is assessed, with reference to prior FSO communications missions, with a focus on the link margin above receiver threshold power. At the receiver, the threshold optical power is limited by the modulation format and data rate. So, the remainder of this appendix section is organised into two sub-sections corresponding to the two modulation formats considered in the thesis, coherent QPSK and PPM.

### A.4.1 Coherent Communications Downlink

Table A.2 provides the link budget resulting from the TBIRD demonstration of two parallel 100 Gb/s transmitters based on the same coherent technology demonstrated in Chapters 4 and 5. In the demonstration, the receive power thresholds are quoted to be 42 dBm and 38 dBm for data rates of 100 Gb/s and 200 Gb/s, respectively [171, 172]. The ‘range loss’ given in published literature appears to incorporate both geometric loss and receiver gain [172]. The peak power in fibre was shown, in a figure, to exceed  $-30$  dBm when the downlink irradiance was  $-22.9$  dBm/m<sup>2</sup>. Applying Equation 2.6 to a link at 35000 km from GEO, at least an additional 30 dB of loss can be expected.

In light of these results, the link margins achieved in both Chapters 4 and 5 appear excessive. However, these systems were deployed without the higher-order AO necessary to stabilise dynamic fluctuations while coupling into SMF. A goal of the thesis project was to provide a low-risk platform for incrementally developing FSO communications capability. Further demonstrations, incorporating higher-order AO systems, may be conducted with transmission powers approximately 20 dB lower than documented. This would more accurately emulate the LEO link margin of Table A.2. The link budget results are also encouraging for the development of TeraNet 1 and TeraNet 2, as the 0.7 m apertures of these telescopes, anticipating similar implementation details to the TBIRD OGS, would lead to fibre-coupled power within the reported link margin. In the case of GEO feeder links, close attention must be paid to developments in high-power coherent optical amplifiers. The VERTIGO demonstration reported transmission power on the order of 100 W [41]. This is a substantial achievement and brings 100 Gb/s-class coherent GEO feeder links to within 10 dB of theoretical realisation.

Table A.2: Communication link budget for TBIRD to Optical Communications Telescope Laboratory.

Parameter	Value
Transmit power	29.5 dBm
Transmit optics loss	-0.3 dB
Transmit antenna gain	79.0 dB
Transmit pointing loss	-0.2 dB
Range loss (930 km, 1 m aperture)	-130.4 dB/m <sup>2</sup>
Atmospheric loss	-0.5 dB
Peak receive irradiance	-22.9 dBm/m <sup>2</sup>
Peak fibre power	-30 dB
Link margin (100 Gb/s)	12 dB
Link margin (200 Gb/s)	8 dB

**A.4.2 Pulse-Position Modulation Downlink**

FSO PPM reception from a lunar orbiter was demonstrated during the LLCD mission. The link budget for the ESA-managed OGS during LLCD is given in Table A.3 [68], while the budget for a NASA JPL-managed OGS is given in Table A.4 [173]. The threshold power in Table A.4 was not tabulated in the published results and is instead determined graphically from a published figure. The link margin in each of these examples are close to, or exceed, the order of the link margin maintained during the demonstration described in Chapter 6. In Chapter 6, the margin was kept slightly lower in order to probe the marginal BER versus SNR characteristic curve of Figure 6.3. With a 0.7 m aperture, the telescope gain of Teranet 1 and TeraNet 2 are likely to be sufficient for lunar communication, if equipped with an appropriate photon-counting receiver.

Table A.3: Communication link budget for the Lunar Laser Space Terminal to ESA Lunar Laser Optical Ground Station.

Parameter	Value
Downlink irradiance (at border of atmosphere)	-57.7 dBm/m <sup>2</sup>
Atmospheric loss	-1.50 dB
Telescope transmission loss	-3.20 dB
Seeing loss; beam splitting loss; fibre insertion loss	-1.40 dB
Receive loss per unit area (0.72 m <sup>2</sup> )	-1.40 dB/m <sup>2</sup>
Receive power	-65.2 dBm
Blue sky brightness	-78.7 dBm
Error-free link margin	13.5 dB

Table A.4: Communication link budget for the Lunar Laser Space Terminal to NASA JPL Optical Communications Telescope Laboratory.

Parameter	Value
LLST EIRP transmitting 0.5 W	129.1 dBm
LLST pointing loss	-0.6 dB
Space loss	-310.7 dB
Atmospheric loss	-0.5 dB
Ground net gain	114.4 dB
Net received power	-68.3 dBm
Error-free threshold (approximate)	-75 dBm
Link margin	6.7 dB

---

---

## APPENDIX B

---

# Supplementary Material: Chapter 4

## B.1 Space Communication

Reasoning and relevant calculations from Andrews 2005 [56] are presented here for reference.

### B.1.1 Uplink Versus Downlink Relevance

Assuming uniform refractive structure index constant,  $C_n^2$ , along the horizontal link path, Fried's parameter for a spherical wave from a point source is

$$r_0 = (0.16k^2C_n^2L)^{-\frac{3}{5}}, \quad (\text{B.1})$$

where  $k$  is the wavenumber for the wavelength, 1550 nm, and  $L$  is the path length, 5.15 km, considering the one-way trip. This returns  $r_0$  of 38 mm for a  $C_n^2$  of  $1.7 \times 10^{-14}$ . As this is slightly larger than the 34 mm  $1/e^2$  beam waist designed for the optical terminal, beam wander will not apply a sufficient angular disturbance to move the beam away from the corner cube retroreflector (CCR) at the end of the laser range, before the wavefront is large enough to undergo higher order disturbances. Furthermore, modelling a Gaussian beam with 34 mm  $1/e^2$  beam diameter and a 75 mm CCR at 5.15 km shows very little reduction in reflected power for angular deviations up to 5  $\mu\text{rad}$ , as shown in Figure B.1. Therefore, fade due to beam wander is unlikely, and the laser range is more relevant to a downlink.

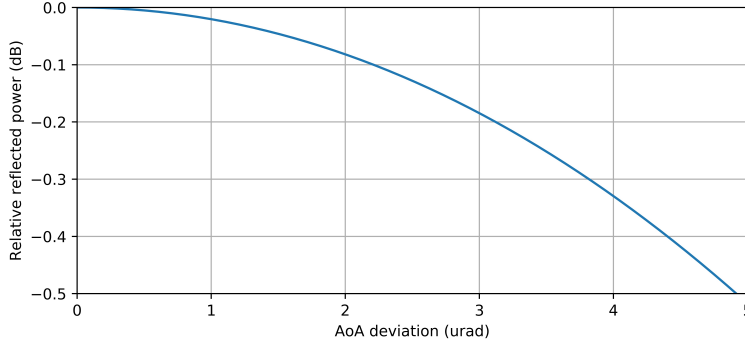


Figure B.1: Reflected power from a corner-cube retroreflector for range of deviation angles, relative to the reflected power from a perfectly-aligned, albeit clipped, Gaussian beam.

### B.1.2 Scintillation Index

Scintillation index,  $\sigma_I^2$  for a downlink channel are considered ‘high-turbulence’ for elevation angles below  $30^\circ$ . The scintillation index for a space-to-ground path is

$$\sigma_I^2 = \exp\left(\frac{0.49\sigma_R^2}{(1 + 1.11\sigma_R^{12/5})^{7/6}} + \frac{0.51\sigma_R^2}{(1 + 0.69\sigma_R^{12/5})^{5/6}}\right) - 1, \quad (\text{B.2})$$

where  $\sigma_R^2$  is the Rytov variance

$$\sigma_R^2 = 2.25k^2 \sec^{11/6}(\zeta) \int_{h_0}^H C_n^2(h)(h - h_0)^{5/6} dh, \quad (\text{B.3})$$

with  $h_0$  as the offset from ground,  $H$  as the maximum integration altitude, and  $\zeta$  is the azimuth angle, the complement to the elevation angle. The refractive index structure constant as a function of height,  $h$ ,  $C_n^2(h)$  is

$$C_n^2(h) = 0.00594(w/27)^2(10^{-5}h)^{10} \exp(-h/1000) + 2.7 \times 10^{-16} \exp(-h/1500) + A \exp(-h/100), \quad (\text{B.4})$$

where  $w = 21$  m/s and  $A = 1.7 \times 10^{-14} \text{ m}^{2/3}$  for the Hufnagel-Valley 5-7 profile. Scintillation index is plotted against elevation angle in Figure B.2. Figure B.2 shows scintillation index is 0.1 for  $50^\circ$  elevation and 0.4 for  $20^\circ$  elevation. These expressions, including the Rytov Variance, map to expressions for horizontal atmospheric laser links. The space link expressions differ from the horizontal expressions with the  $\zeta$ -dependence, as satellite links at different elevation angles pass through different atmospheric paths. The difference in  $C_n^2$  profile for three elevation angles are shown in Figure B.3 to illustrate this.

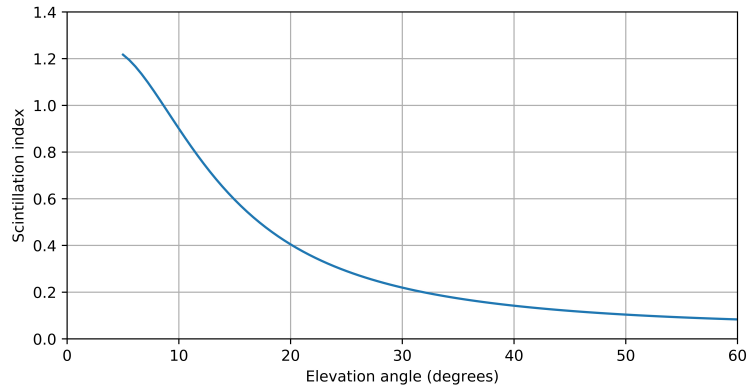


Figure B.2: Scintillation index for a space downlink to a point receiver on the ground, various elevation angles.

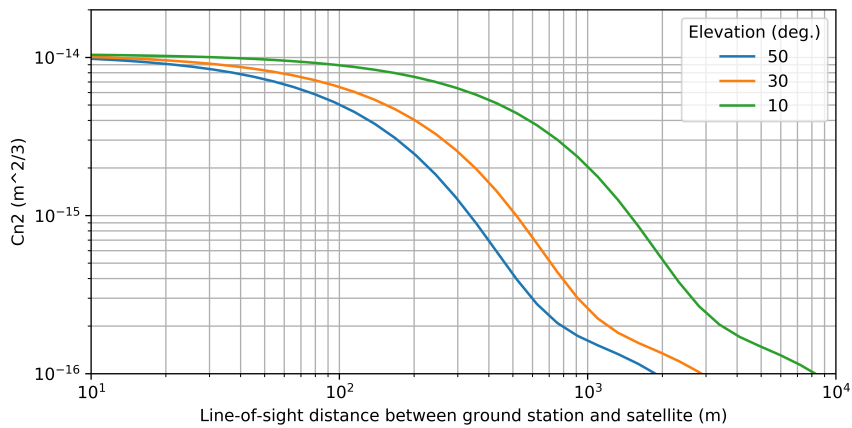


Figure B.3:  $C_n^2$  profile along the line-of-sight to a satellite at three different elevation angles, using the Hufnagel-Valley 5/7 profile.

## B.2 Results by Wavelength

Results for the coherent communications demonstration, including centre wavelength, measurement time, scintillation (SI), free-space to single-mode fibre (SMF) coupling, and percentage of transmissions with a bit error rate below the  $4.5 \times 10^{-3}$  FEC-correctable threshold specified in ITU-G.709.2, Table A.1 [80].

Table B.1: 111.8 Gb/s Communications demonstration 2022-12-13.

Wavelength	Time	SI	SMF coupling (dB)	% FEC-correctable
191.10 THz	17:55	0.231	-8.55	84
191.15 THz	17:59	0.198	-8.68	80

APPENDIX B. SUPPLEMENTARY MATERIAL: CHAPTER 4

---

Wavelength	Time	SI	SMF coupling (dB)	% FEC-correctable
191.20 THz	18:02	0.180	-8.70	85
191.25 THz	18:06	0.172	-8.78	87
191.30 THz	18:12	0.126	-8.71	90
191.35 THz	18:09	0.138	-8.87	91
191.40 THz	18:14	0.151	-9.03	85
191.45 THz	18:18	0.136	-9.12	85
191.50 THz	18:20	0.175	-9.54	69
191.55 THz	18:23	0.142	-9.26	84
191.60 THz	18:29	0.128	-9.11	86
191.65 THz	18:31	0.116	-9.29	80
191.70 THz	18:34	0.148	-9.30	79
191.75 THz	18:36	0.124	-9.14	90
191.80 THz	18:38	0.115	-9.11	80
191.85 THz	18:41	0.142	-9.50	70
191.90 THz	18:43	0.149	-9.54	74
191.95 THz	18:46	0.135	-9.55	76
192.00 THz	18:50	0.114	-8.90	96
192.05 THz	18:52	0.110	-8.69	97
192.10 THz	18:56	0.157	-9.28	87
192.15 THz	18:58	0.195	-9.13	78
192.20 THz	19:00	0.180	-9.27	86
192.25 THz	19:04	0.237	-9.26	74
192.30 THz	19:06	0.216	-9.36	74
192.35 THz	19:10	0.261	-9.32	70
192.40 THz	19:12	0.220	-9.56	65
192.45 THz	19:14	0.227	-9.42	68
192.50 THz	19:16	0.282	-9.24	61
192.55 THz	19:38	0.307	-9.79	42
192.60 THz	19:42	0.320	-9.53	52
192.65 THz	19:45	0.253	-10.2	39
192.70 THz	19:47	0.273	-9.88	39
192.75 THz	19:50	0.346	-10.4	29
192.80 THz	19:55	0.314	-11.3	9.1
192.85 THz	19:58	0.308	-11.4	6.6

---

## B.2. RESULTS BY WAVELENGTH

---

Wavelength	Time	SI	SMF coupling (dB)	% FEC-correctable
192.90 THz	20:02	0.308	-10.5	19
192.95 THz	20:04	0.302	-10.1	25
193.00 THz	20:07	0.272	-10.3	23
193.05 THz	20:09	0.292	-10.1	20
193.10 THz	20:15	0.272	-10.5	53
193.15 THz	20:17	0.271	-10.4	34
193.20 THz	20:19	0.306	-10.6	50
193.25 THz	20:22	0.323	-10.4	56
193.30 THz	20:26	0.260	-11.3	33
193.35 THz	20:28	0.282	-11.4	28
193.40 THz	20:31	0.345	-11.3	27
193.45 THz	20:33	0.323	-11.8	18
193.50 THz	20:35	0.303	-11.8	19
193.55 THz	20:37	0.248	-11.9	20
193.60 THz	20:41	0.236	-10.8	46
193.65 THz	20:43	0.289	-11.3	28

---



---

---

## APPENDIX C

---

# Supplementary Material: Published Work

---

### Chapter Contents

---

C.1 Atmospheric Turbulence Characterization with Simultaneous Measurement of Phase, Angle of Arrival, and Intensity in a Retroreflected Optical Link . . . . .	<b>135</b>
C.1.1 Introduction . . . . .	135
C.1.2 Phase Noise . . . . .	136
C.1.3 Angle of Arrival Variation . . . . .	137
C.1.4 Scintillation . . . . .	137
C.2 High-Bandwidth Coherent Optical Communication over 10.3 km of Turbulent Air . . . . .	<b>139</b>
C.2.1 Introduction . . . . .	139
C.2.2 Methods . . . . .	140
C.2.3 Channel Model . . . . .	140
C.2.4 Results . . . . .	141
C.2.5 Discussion . . . . .	142
C.2.6 Conclusion . . . . .	142
C.3 Demonstration of 100 Gbps Coherent Free-Space Optical Communications at LEO Tracking Rates . . . . .	<b>144</b>
C.3.1 Methods . . . . .	145
C.3.2 Results and Discussion . . . . .	150
C.3.3 Conclusion . . . . .	154

APPENDIX C. SUPPLEMENTARY MATERIAL: PUBLISHED WORK

---

C.4	Ground-to-Drone Optical Pulse Position Modulation Demonstration as a Testbed for Lunar Communications . . . . .	<b>156</b>
C.4.1	Introduction . . . . .	156
C.4.2	Materials and Methods . . . . .	157
C.4.3	Results . . . . .	161
C.4.4	Discussion and Conclusions . . . . .	162

---



## Atmospheric turbulence characterization with simultaneous measurement of phase, angle of arrival, and intensity in a retroreflected optical link

BENJAMIN P. DIX-MATTHEWS,<sup>\*,†</sup> SKEVOS F. E. KARPATHAKIS,<sup>†</sup> AND SASCHA W. SCHEDIWI

International Centre for Radio Astronomy Research, The University of Western Australia, WA 6009, Australia

<sup>†</sup>The authors contributed equally to this work.

\*benjamin.dix-matthews@uwa.edu.au

Received 26 July 2023; revised 30 September 2023; accepted 3 October 2023; posted 4 October 2023; published 17 October 2023

Free-space optical transmission through the Earth's atmosphere is applicable to high-speed data transmission and optical clock comparisons, among other uses. Fluctuations in the refractive index of the atmosphere limit the performance of atmospheric optical transmission by inducing phase noise, angle-of-arrival variation, and scintillation. The statistics of these deleterious effects are predicted by models for the spatial spectrum of the atmospheric refractive index structure. We present measurements of phase fluctuations, angle-of-arrival variations, and scintillation, taken concurrently and compared with models for the atmospheric refractive index structure. The measurements are also cross-compared by deriving independent estimates of the turbulence structure constant  $C_n^2$ . We find agreement within an order of magnitude for derived  $C_n^2$  values for all three metrics. © 2023 Optica Publishing Group

<https://doi.org/10.1364/OL.501346>

Understanding how atmospheric turbulence affects the propagation of optical beams is important when attempting to transmit optical signals over long distances, with motivating applications including high-speed data transmission [1] and frequency comparisons between optical clocks [2,3]. Horizontal or slanted optical links are used to connect terrestrial sites on the ground or in the air and can be point to point [4,5], folded with a mirror relay [6], or folded with a retroreflector [7–9]. Folded links are advantageous for only requiring access, power, and substantial shelter at one site as transmission and reception hardware can be co-located, with retroreflected links having less stringent pointing requirements. For all these optical links, refractive index fluctuations caused by atmospheric turbulence perturb the propagation of optical beams. Several models have been developed to describe the spatial spectrum of these refractive index fluctuations based on turbulence theory. In this Letter, we will focus on the Kolmogorov and Greenwood–Tarazano models [2,10,11].

These spatial spectrum models describe the physical structure of the refractive index fluctuations and are thus independent of any specific transmission signal. To determine the effect of the atmosphere on measurable quantities for a specific optical link architecture, the modeled refractive index fluctuations must be

integrated over the optical propagation path. To derive temporal statistics, Taylor's hypothesis of frozen turbulence [2,10] must be used to couple one spatial direction to the time axis by shifting the turbulence model transversely to the beam at a specific wind speed. Analytically derived statistics for phase noise, angle of arrival (AoA), and scintillation will drive engineering decisions for atmospheric optical transmission applications; however, these require understanding of the expected atmospheric turbulence strength. Thus, *in situ* characterization of the atmospheric turbulence conditions for a given optical link is important.

The strength of atmospheric turbulence is typically defined by the turbulence structure constant,  $C_n^2$ , which is obtained by comparing the predictions of atmospheric turbulence models with the statistics of experimentally measured quantities. Many commercial systems, known as scintillometers, rely on scintillation statistics to measure  $C_n^2$ ; however, they have a tendency to saturate in high-turbulence regimes [12]. Improved systems relying on AoA measurements to determine turbulence strength have been demonstrated within the free-space optical communication community [12,13]. An alternative method based on the measurement of optical phase fluctuations has been demonstrated within the frequency metrology community [11]. The  $C_n^2$  measurements based on phase-fluctuation data agreed within an order of magnitude with independent measurements taken by micrometeorological sensors. This previous investigation, conducted on a uniform range with distributed micrometeorological sensors, encourages the use of phase-fluctuation measurements on optical links where distributed sensors cannot be installed. However, this technique has not yet been compared to turbulence characterization techniques based on AoA and intensity measurements. In this Letter, we examine the agreement between the turbulence strength estimates derived from simultaneous phase, AoA, and scintillation measurements over a retroreflected link.

An apparatus for simultaneously measuring optical phase, AoA, and intensity was deployed over a 1.2 km horizontal atmospheric link to a  $\phi 50$  mm corner-cube retroreflector (CCR), as shown in Fig. 1. Power levels are indicated at key locations. This apparatus comprises a 1550 nm fiber laser source launched into free-space via a 15 $\times$  Galilean beam expander. The beam

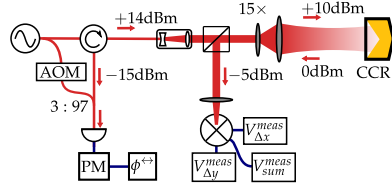


**Fig. 1.** Apparatus for measuring phase noise, angle-of-arrival variation, and scintillation. AOM, acousto-optic modulator; CCR, corner-cube retroreflector; PM, phase meter.

expander has a  $\phi 43.5$  mm aperture, and the outgoing beam has a 17 mm beam waist radius. In the free-space terminal, the reflected beam is split and partially directed to a quadrant photodetector (QPD) to measure AoA, via the voltages  $V_{\Delta x}^{\text{meas}}$  and  $V_{\Delta y}^{\text{meas}}$ , the difference in voltage between two opposite quadrants. The sum of the quadrant voltages is also recorded as  $V_{\text{sum}}^{\text{meas}}$  to derive the scintillation. The remaining beam power is coupled back into a single-mode fiber and beats with a prompt copy of the transmitted laser to measure the two-way phase shift,  $\phi^{\leftrightarrow}$ . The prompt copy of the laser passes an acousto-optic modulator to frequency-shift the signal, so the heterodyne interference beat can be input to a radio-frequency phase meter. QPD voltages were sampled at 1.25 kHz and the phase was sampled at 2 kHz. An anemometer was located on the rooftop, 4 m above the apparatus, recording wind speed and gusts at 300 s intervals.

Three one-hour long measurements were taken under different turbulence conditions and are consistently labeled “low,” “moderate,” and “high” in the remainder of this Letter for ease of reference. Phase, AoA, and intensity measurements in each of the low, moderate, and high data sets are compared with models derived from turbulence theory. Finally, rolling predictions of  $C_n^2$  are derived from the phase, AoA, and intensity measurements. The experimental data underlying the results presented in this Letter are made publicly available in a repository [14].

Phase fluctuations are a “zeroth-order” disturbance induced by atmospheric turbulence. Refractive index fluctuations on length scales physically larger than the propagating optical beam will cause variations in the time of flight and thus degrade the phase stability of the received optical beam. For a one-way transmission of a plane wave propagating through Kolmogorov turbulence [2,10,11], the single-sided power spectral density (PSD) of phase noise is expected to be

$$S_{\phi, \text{Kol}}^{\rightarrow}(f) = 0.033k^2 C_n^2 L V^{5/3} f^{-8/3}, \quad (1)$$

where  $C_n^2$  is the turbulence structure constant for the index of refraction,  $L$  is the path length,  $V$  is the perpendicular wind speed,  $f$  is the Fourier frequency,  $k = 2\pi/\lambda$  is the optical wavenumber, and  $\lambda$  is the optical wavelength.

Similarly, the Greenwood–Tarazano turbulence model for a plane wave results in an expected single-sided PSD of

$$S_{\phi, \text{Gre}}^{\rightarrow}(f) = 5.211k^2 C_n^2 L / V \int_0^{\infty} \left[ q_y^2 + \left( \frac{2\pi f}{V} \right)^2 + \frac{\sqrt{(2\pi f / V)^2 + q_y^2}}{L_0} \right]^{-11/6} dq_y, \quad (2)$$

where  $L_0$  is the outer scale of turbulence.

These phase noise models describe one-way propagation through atmospheric turbulence. For a two-way atmospheric link reflected by a CCR, the optical beam experiences a phase

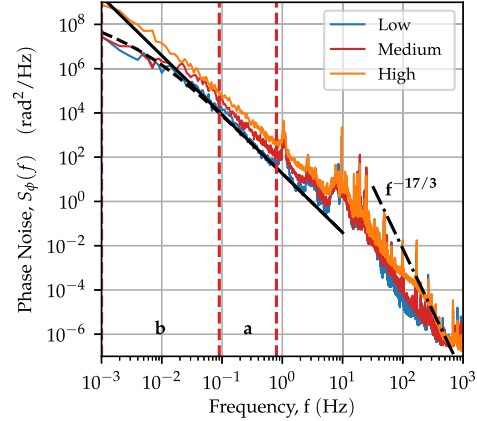


**Fig. 2.** Phase noise power spectral densities for three measurement runs. Two analytical models are fitted to the low turbulence measurement (blue). The solid black line is the Kolmogorov spectrum model. The dashed black line is the Greenwood–Tarazano spectrum model.

delay during forward propagation,  $\phi_{\rightarrow}(t)$ , and backward propagation,  $\phi_{\leftarrow}(t)$ . The phase delay caused by reflection of the CCR remains constant and may be ignored. Phase contributions at timescales below the round-trip time of the two-way link are reciprocal, and thus the total phase delay is  $\phi^{\leftrightarrow}(t) = 2\phi_{\rightarrow}(t)$ . Thus, the single-sided PSD of phase noise is

$$S_{\phi}^{\leftrightarrow}(f) = 4S_{\phi}^{\rightarrow}(f), \quad (3)$$

for  $f < 1/T$ , where  $T = L/c$  is the round-trip time of the link.

Three phase noise spectra observed are shown in Fig. 2, along with fitted lines for Kolmogorov (solid black) and Greenwood–Tarazano (dashed black) phase noise spectra for the low results. The low (blue) and medium (red) phase noise spectra in Fig. 2 show the characteristic downward inflection at low frequencies of the Greenwood–Tarazano model, Eq. (2), in the region labeled **b**. The high spectrum (orange) appears to follow the strict  $f^{-8/3}$  trend of the Kolmogorov model spectrum of Eq. (1) for most of the spectrum with a more subtle downward inflection at low frequencies. Outer scale,  $L_0$ , is estimated by fitting each spectra to Eq. (2) in the region **b**, and the estimates are given in Table 1. The estimates correspond to physically reasonable lengths, close to the approximately 30 m height above ground of the apparatus. The high spectrum (orange) in Fig. 2 exhibits a  $f^{-17/3}$  roll-off above 200 Hz consistent with aperture averaging [10], before dropping to a white

**Table 1. Summary of Turbulence Regimes, with Datum  $L_0$  and  $C_n^2$  Values Based on Observed Phase Noise Spectra<sup>a</sup>**

Name	$L_0$ [m]	$C_n^2$ [ $m^{-2/3}$ ]
Low	51.9	$1.25 \times 10^{-15}$
Medium	30.8	$4.84 \times 10^{-15}$
High	35.8	$1.52 \times 10^{-14}$

<sup>a</sup> $C_n^2$  is fit to the spectrum from 90 to 800 mHz.

## C.1. ATMOSPHERIC TURBULENCE CHARACTERIZATION WITH SIMULTANEOUS MEASUREMENT OF PHASE, ANGLE OF ARRIVAL, AND INTENSITY IN A RETROREFLECTED OPTICAL LINK

noise floor. An average  $C_n^2$  estimate was derived from each spectrum using a nonlinear least squares fit of Eq. (3) between 90 and 800 mHz, region **a** in Fig. 2, where all the spectra closely follow the  $f^{-8/3}$  Kolmogorov trend and do not contain any noise spurs. These values are given in Table 1. This technique is used to estimate rolling  $C_n^2$  from phase measurements later in this Letter.

“First-order” AoA variations lead to the optical beam wandering off-target. For a one-way link, the single-sided PSD of AoA fluctuations can be modeled in terms of the phase noise [2,10],

$$S_{\alpha}^{-}(f) = (\lambda f / V)^2 S_{\phi}^{-}(f). \quad (4)$$

Relating the AoA for a two-way link with a CCR to the one-way AoA is more complicated than in the phase case. For a perfectly flat wavefront, variations in AoA during the forward propagation are canceled in backward propagation, whether or not the beam underfills the CCR. However, for any other beam wavefront geometry, such as spherical or Gaussian, truncation at the CCR results in an additional AoA change not suppressed in the backward propagation, thus resulting in measurable AoA fluctuations over the two-way link [15]. Thus, the relationship between the one-way and two-way AoA fluctuations is  $\alpha_{\pm}(t) = b\alpha_{\pm}(t)$ , where  $b$  is a constant dependent on the specific geometry of the free-space link. Thus,

$$S_{\alpha}^{\pm}(f) = b^2 S_{\alpha}^{-}(f), \quad (5)$$

where  $b \approx 0.74$ , from numerical modeling based on the method in [15] of a  $\phi 50$  mm CCR at a distance of 1.2 km, with a beam waist radius of 17 mm and wavelength  $\lambda=1550$  nm.

If temporal information is not required, the expected AoA variance can be obtained from turbulence theory without the need for Taylor’s hypothesis of frozen turbulence. For a one-way link, the expected AoA variance is

$$\text{Var}[\alpha_{\pm}] = 1.093LC_n^2D_r^{-1/3}, \quad (6)$$

provided that  $(L\lambda)^{1/2} < D_r$ , where  $D_r$  is the receiver diameter [12,13]. The constant at the front of Eq. (6) is associated with the spherical wave approximation. Thus, by taking into account the relationship between the one- and two-way AoA,

$$\text{Var}[\alpha_{\pm}] = b^2 \text{Var}[\alpha_{\pm}] = 1.093b^2LC_n^2D_r^{-1/3}. \quad (7)$$

The AoA fluctuations of the retroreflected optical beam were measured using a QPD, where the incident angle is determined based on the voltage differences caused by the lateral deflections of the imaged beam. This QPD was at a focal point of the receiving optical system and operated in a regime where the returned optical beam was diffraction limited. The diameter of the imaged beam was significantly smaller than the full QPD size. In this regime, an incident AoA deflection in the  $x$ -axis by the diffraction-limited angular resolution of the optical system will entirely shift the imaged spot between the QPD  $x$  axis quadrants, causing the normalized voltage difference,  $\overline{V}_{\Delta x}$ , to span  $-1$  to  $+1$ . Thus, assuming linearity in the QPD response, the measured AoA deflections are given by

$$\theta_{\text{apd}}^x = \frac{\theta}{2} \overline{V}_{\Delta x}, \quad \theta_{\text{apd}}^y = \frac{\theta}{2} \overline{V}_{\Delta y}, \quad (8)$$

where  $\theta = 1.22\lambda/D_r$  is the diffraction-limited angular resolution of the optical system,  $\lambda$  is the optical wavelength, and  $\overline{V}_{\Delta x}$  and  $\overline{V}_{\Delta y}$

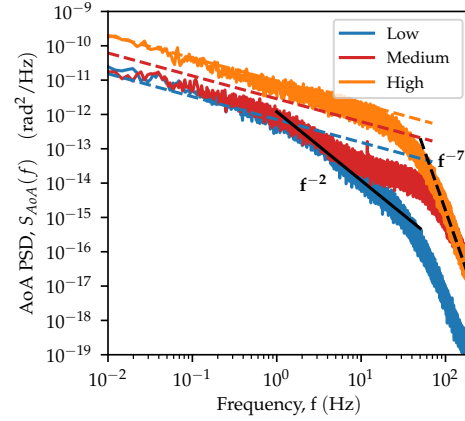


**Fig. 3.** Angle-of-arrival power spectral densities for three measurement runs. Fitted dashed lines are provided for each run, showing  $f^{-2/3}$  slopes predicted by the Kolmogorov model.

are the measured  $x$  and  $y$  QPD voltage differences normalized from  $-1$  to  $+1$ . The normalized voltage difference measurements are  $\overline{V}_{\Delta x} = V_{\Delta x}^{\text{meas}}/V_{\Delta x}^{\text{max}}$  and  $\overline{V}_{\Delta y} = V_{\Delta y}^{\text{meas}}/V_{\Delta y}^{\text{max}}$  where  $V_{\Delta x}^{\text{max}}$  is a design parameter of the QPD. Equation (8) will change slightly if the Fried parameter,  $r_0 = [1.46k^2C_n^2L]^{-3/5}$ , is smaller than the receive aperture. In this case, the angular resolution of the optical system is no longer diffraction limited, and instead  $\theta \approx \lambda/r_0$ . For the high-turbulence measurement in Fig. 3, the atmospherically limited angular resolution was used.

The AoA spectra for the three measurements are shown in Fig. 3. The three-dashed lines represent the expected AoA spectra given by Eq. (4) assuming the  $C_n^2$  values provided in Table 1. Substituting Eq. (1) into Eq. (4) predicts an  $f^{-2/3}$  trend, and this is exhibited in all spectra between 10 mHz and 2 Hz. Beyond 2 Hz the low (blue) and medium (red) spectra roll-off at  $f^{-2}$ , deviating from the expected trend, with the medium spectrum exhibiting an unexpected upwards inflection 10 Hz. This behavior is unlikely to be due to atmospheric effects, and may be caused by unexpected behavior in the QPD, such as sensitivities to spot size and incident power. Similarly, the sharp  $f^{-7}$  roll-off exhibited by all spectra at high frequencies is likely due to the instrumentation. The medium spectrum is also lower than expected for the first two measurement decades, the cause of which we are unsure.

“Higher-order” intensity fluctuations are caused when different sections of the wavefront pass through eddies with varying refractive indices before meeting at the receiver plane and interfering, thereby causing variation in the received power. This variance about the mean value is called scintillation [16] and is commonly expressed as the variance of log-intensity,  $\sigma_{\ln,I}^2$ ,

$$\sigma_{\ln,I}^2 = \ln\left(1 + \frac{\sigma_v^2}{\mu_v^2}\right), \quad (9)$$

where  $\mu_v$  is the mean and  $\sigma_v$  is the standard deviation of the voltage at the photodetector [17]. For a horizontal link with uniform  $C_n^2$ , the log-intensity variance is given by

$$\sigma_{\ln,I}^2 = 0.496C_n^2k^{7/6}L^{11/6}. \quad (10)$$

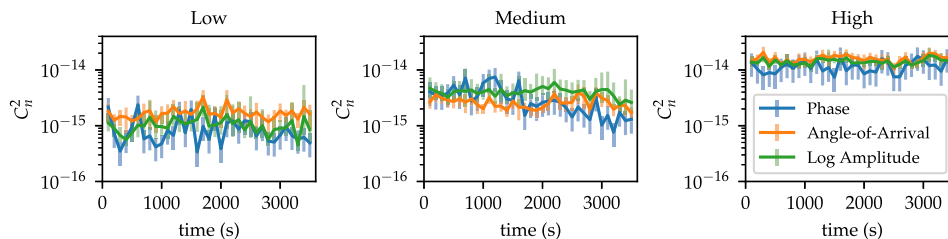


**Fig. 4.** Rolling measurement of turbulent structure constant  $C_n^2$ , based on 100 s samples of phase, angle-of-arrival, and intensity measurements. Three separate measurements are given in low, medium, and high turbulence. Error bars indicate the 90% confidence intervals for each parameter. For phase this is  $\pm 1.645\sigma$  calculated from the variance of the fit parameter. The angle-of-arrival and log-amplitude estimates depend on subsample variance  $s^2$ , the value of which is bounded by  $\left[ s^2 \frac{N}{\chi^2(0.95, N)}, s^2 \frac{N}{\chi^2(0.05, N)} \right]$ , where  $N$  is the number of independent samples [18], here defined as  $\frac{N_{total}}{2n_c}$ , where  $N_{total}$  is the total number of subsamples and  $n_c$  is the time taken, in samples, for the autocorrelation to drop below  $e^{-2}$ .

Retroreflected links have been analyzed in depth for laser ranging systems [16]. For this link geometry, the scintillation of the retroreflected link is equivalent to a link of the round-trip distance. The sum voltage from each quadrant of the QPD,  $V_{sum}^{meas}$ , was used to calculate a rolling log-intensity variance for each dataset, based on Eq. (9), and substituted into Eq. (10), to estimate  $C_n^2$ , as shown in Fig. 4. Rolling estimates of  $C_n^2$  based on phase and AoA measurements are also shown in Fig. 4. The phase estimate is derived by fitting Eq. (3) to region **a** in Fig. 2. The AoA estimates are derived using Eq. (7). Each rolling estimate is calculated from 100 s subsamples of the full measurement.

The rolling  $C_n^2$  estimates are encouraging, reinforcing the case for future development of these turbulence characterization techniques. Each measurement type agrees within an order of magnitude, with a maximum factor of 2.9 deviation between AoA and scintillation-derived  $C_n^2$  in all conditions and up to a factor of 6.6 between phase and AoA during low turbulence. In high turbulence, each measurement agrees within a factor of 2.5. Within the disagreement between the measurements, no one measurement appears to be biased to over- or underestimate the  $C_n^2$  in any of the three cases. Generally, the estimate based on phase noise has a lower tracking bandwidth, as it is based on PSD calculations involving averages over large time windows. The applicability of either technique will depend on the required time resolution, although the latter two measurements can be achieved with only one sensor device, the QPD. Anomalies in the AoA PSDs at high frequencies, as seen in Fig. 3, has motivated us to consider replacing the QPD with a charge-coupled device.

**Funding.** SmartSat Cooperative Research Centre (CRC Research Project 1-18).

**Acknowledgment.** This work has been supported by the SmartSat CRC, whose activities are funded by the Australian Government's CRC Program. S. Karpathakis is supported by a SmartSat CRC PhD Scholarship and a research award from The Andy Thomas Space Foundation and EOS Space Systems.

**Disclosures.** The authors declare no conflicts of interest.

**Data availability.** All data and software underlying the results presented in this paper are publicly available [14].

## REFERENCES

- S. Karpathakis, B. Dix-Matthews, D. Gozzard, and S. Schediwy, *Appl. Opt.* **62**, G85 (2023).
- L. C. Sinclair, F. R. Giorgetta, W. C. Swann, E. Baumann, I. Coddington, and N. R. Newbury, *Phys. Rev. A* **89**, 023805 (2014).
- C. Robert, J.-M. Conan, and P. Wolf, *Phys. Rev. A* **93**, 033860 (2016).
- B. Dix-Matthews, S. Schediwy, D. Gozzard, E. Savalle, F.-X. Esnault, T. Lévéque, C. Gravestock, D. D'Mello, S. Karpathakis, M. Tobar, and P. Wolf, *Nat. Commun.* **12**, 515 (2021).
- Q. Shen, J.-Y. Guan, and J.-G. Ren, *Nature* **610**, 661 (2022).
- H. J. Kang, J. Yang, B. J. Chun, H. Jang, B. S. Kim, Y.-J. Kim, and S.-W. Kim, *Nat. Commun.* **10**, 4438 (2019).
- B. Dix-Matthews, D. Gozzard, S. Walsh, A. McCann, S. Karpathakis, A. Frost, C. Gravestock, and S. Schediwy, *Opt. Express* **31**, 15075 (2023).
- B. Dix-Matthews, D. Gozzard, S. Karpathakis, S. Walsh, A. McCann, A. Frost, and S. Schediwy, *Phys. Rev. Appl.* **19**, 054018 (2023).
- E. D. Caldwell, J.-D. Deschenes, J. Ellis, W. C. Swann, B. K. Stuhl, H. Bergeron, N. R. Newbury, and L. C. Sinclair, *Nature* **618**, 721 (2023).
- J.-M. Conan, G. Rousset, and P.-Y. Madec, *J. Opt. Soc. Am. A* **12**, 1559 (1995).
- E. D. Caldwell, W. C. Swann, J. L. Ellis, M. I. Bodine, C. Mak, N. Kuczun, N. R. Newbury, L. C. Sinclair, A. Muschinski, and G. B. Rieker, *Opt. Express* **28**, 26661 (2020).
- S. Manning, B. A. Clare, K. J. Grant, and K. A. Mudge, *Opt. Eng.* **54**, 114104 (2015).
- M. F. Stell, C. I. Moore, H. R. Burris, M. R. Suite, M. J. Vilcheck, M. A. Davis, R. Mahon, E. Oh, W. S. Rabinovich, G. C. Gilbreath, W. J. Scharpf, and A. E. Reed, in *SPIE Proceedings* (SPIE, 2004).
- B. Dix-Matthews, S. Karpathakis, and S. Schediwy, "Retroreflected optical phase, angle-of-arrival, and intensity dataset," figshare (2023), <https://doi.org/10.6084/m9.figshare.23721870>.
- S. Walsh, A. Frost, L. Howard, D. Gozzard, S. Karpathakis, B. Dix-Matthews, C. Gravestock, A. McCann, and S. Schediwy, *Opt. Lett.* **47**, 1920 (2022).
- L. C. Andrews and R. L. Phillips, *Laser Beam Propagation through Random Media*, 2nd ed. (SPIE Press, 2005).
- C. R. Zeisse, B. D. Nener, and R. V. Dewees, *Appl. Opt.* **39**, 873 (2000).
- W. J. Riley, *Handbook of Frequency Stability Analysis* (US Gov. Printing Office, 2008).



## High-bandwidth coherent optical communication over 10.3 km of turbulent air

SKEVOS F. E. KARPETHAKIS,<sup>1,2,\*</sup> BENJAMIN P. DIX-MATTHEWS,<sup>1,2</sup> DAVID R. GOZZARD,<sup>1,2</sup> AND SASCHA W. SCHEDIWIY<sup>1,2</sup>

<sup>1</sup>International Centre for Radio Astronomy Research, The University of Western Australia, Crawley, WA 6009, Australia

<sup>2</sup>International Space Centre, The University of Western Australia, Crawley, WA 6009, Australia

\*skevos.karpathakis@uwa.edu.au

Received 24 March 2023; revised 1 May 2023; accepted 1 May 2023; posted 2 May 2023; published 22 May 2023

We demonstrate 111.8 Gb/s coherent optical communication throughput over a 10.3 km folded free-space laser range. Folded links are low complexity to establish and provide a high uptime for testing equipment. The communication signals were sourced from an un-modified commercial off-the-shelf transceiver intended for long-haul fiber networks. Wavelength dependence was explored by testing 52 optical C-band channels over the course of an evening. In the future, such high-bandwidth communications will be used in feeder links from satellites in geosynchronous orbit. Optical power measurements of the received signal are compared with atmospheric theory to determine the turbulence strength exhibited and therefore the applicability of the laser range to space-to-ground links. We show that the high-uptime, 10.3 km laser range is suitable for testing high-bandwidth space-to-ground optical communication systems intended for links to geosynchronous orbit at 20°–50° elevation. © 2023 Optica Publishing Group

<https://doi.org/10.1364/AO.491440>

### 1. INTRODUCTION

Space-to-ground communication using wireless radio and microwave transmissions is facing a bandwidth bottleneck due to increasing quantities of data acquired in space, and beam crowding due to divergence at orbital distances [1]. Free-space optical (FSO) communication promises to address these emerging issues in traditional space communication by offering improved bandwidth and lower divergence compared with wireless radio and microwave transmissions. Intensity modulation was used in early FSO communication experiments, including the first space-to-ground FSO communication demonstration in 1995 [2]. Intensity modulation has since been used in inter-satellite links [3], and in a cis-lunar space-to-ground link [4]. Coherent communication, using phase modulation, offers higher spectral efficiency than intensity modulation, and future FSO communications from geosynchronous orbit (GEO) and low-Earth orbit (LEO) to ground will use coherent optical communication transceivers to capitalize on commonly deployed, interoperable, terrestrial fiber technology [5,6]. In 2022, NASA's Tera-Byte Infra-Red Delivery (TBIRD) satellite began transmitting data from LEO at 200 Gb/s using two commercial off-the-shelf (COTS) 100 Gb/s coherent transceivers and wavelength-division multiplexing (WDM) [7–9]. TBIRD successfully transmits coherent optical signals from LEO to ground, through Earth's turbulent atmosphere, using an automatic repeat request (ARQ) protocol. This ARQ protocol

was developed using tests on a 3 km folded horizontal laser range [10].

Transceiver deployments over horizontal terrestrial laser ranges are used to inform system design choices to mitigate the effects of turbulence, because horizontal links can exhibit atmospheric turbulence equivalent to, or exceeding, space-to-ground links [11]. Dochhan, 2019 [12], demonstrated high-speed coherent communications on a 10.45 km point-to-point link. This demonstration utilized COTS transceivers as well as two optical combs, 200 Gb/s modulators, and WDM to simulate simultaneous transmission by many coherent transceivers. In doing so, 13.16 Tb/s transmission was achieved, utilizing the entire optical C-band, comprising center wavelengths from approximately 1530 to 1564 nm. Other relevant demonstrations over terrestrial laser ranges have been conducted using bespoke communication systems. Balasiano *et al.*, 2022 [13], tested a custom 128 Gb/s, single-wavelength transceiver over a 10 km folded laser range. Furthermore, Bitachon, 2022 [14], demonstrated the highest-capacity, longest-range demonstration yet. This was a point-to-point transmission over 53 km, achieving 1 Tb/s on a single wavelength by using technologies developed specifically for FSO communications, including adaptive optics and coherent beam combining. These publications describe the likely use-cases of high-bandwidth coherent communications to be feeder links from GEO.

This paper presents 111.8 Gb/s coherent communication over a 10.3 km folded horizontal laser range, using a

COTS coherent transceiver. Deploying the highly integrated COTS coherent transceiver highlights what is imminently possible with COTS components, versus the comparatively low-integration bespoke communication systems presented in Balasiano, 2022, [13] and Bitachon, 2022 [14]. Furthermore, at this distance, the folded link exceeds the 3 km distance presented in Schieler *et al.*, 2019 [10]. Folded laser links are extensively modeled in literature and exhibit comparable channel statistics to point-to-point links when monostatic terminals are used [15] and exhibit angle-of-arrival variability despite atmospheric reciprocity [16]. Folded links are also low complexity to establish, compared to point-to-point links such as in Dochhan, 2019, and are thus easier to replicate. Folded links also allow the internal loopback functions of COTS transceivers to be used for bit error rate (BER) testing, without requiring a fiber loopback between the sites. We analyze measurements of the received power to characterize the link conditions and demonstrate applicability of this low-complexity arrangement to a satellite FSO communication scenario. Data were transmitted on 52 channels over a turbulent channel with scintillation indices equivalent to a GEO-to-ground link between 20° and 50° elevation angle.

2. METHODS

A. Coherent Transceiver

The communications signal under test was generated by a COTS 111.8 Gb/s digital coherent optical (DCO) transceiver, employing quadrature phase-shift-keying modulation, and intended for use in a long-distance optical transport network. Functionality is standardized in the management interface specification [17]. The DCO contains a pseudo-random binary sequence (PRBS) generator and checker in its transmit and receive sections. The PRBS checker counts received bits and bit errors when enabled, and reports these quantities when disabled. The state of the PRBS checker may be toggled on the fly, allowing a real-time sub-sampling measurement of BER over the link. Figure 1 shows the logical mapping of these peripherals to the optical terminal.

In this demonstration, each sub-sampled measurement is considered to represent a transmission, and the duration of each transmission is a free parameter requiring constraint. Transmissions with duration of the order of 10 ms are useful for characterizing link quality due to atmospheric turbulence causing “bursty” data loss, on such time scales [10,12]. As the PRBS checker provides bit-by-bit comparisons, it does not give insight into the forward error correction (FEC) performance

internal to the DCO. A pre-FEC BER threshold of  $4.5 \times 10^{-3}$  was selected as the threshold for FEC-correctable transmission, based on the standards for staircase FEC [18].

The DCO emission wavelength was varied to characterize total throughput available with WDM and to search for any unexpected wavelength-dependent limitations. The laser inside the DCO is tunable between 1568.77 and 1527.60 nm, or 191.1 and 196.25 THz, in 50 GHz steps. Changing wavelength requires power-cycling the laser, approximately 60 s in duration. These processes, in conjunction with a 30 s measurement duration, limit the number of channels able to be tested during periods of low turbulence. An erbium-doped fiber amplifier (EDFA) was used to boost the DCO output to 26.8 dBm.

B. Optical Terminal

A schematic of the optical terminal is shown in Fig. 1. The terminal takes a fiber-fed laser input from the DCO and EDFA and collimates it to free space via a free-space to fiber collimator, FFC1. The beam splitter, BS1, splits the collimated beam. Half of the transmitted beam is directed to the 50 mm Galilean beam expander (GBE), expanding the beam to a 34 mm  $1/e^2$  waist diameter. The 63.5 mm corner cube retroreflector (CCR) reflects the beam back, and it passes BS1 before entering the receiver beam splitter, BS2. On passing BS2, half of the beam power is directed back into FFC2, to couple back into SMF for reception. BS2 and a separate receive FFC are required to provide separate transmit and receive fibers, as reflections off the fiber end-face can degrade the optical signal-to-noise ratio when the fibers are shared with a circulator. The other half of the received power is directed into a free-space photodetector (FS PD) to measure free-space power,  $P_{FS}$ . A 10% portion of the SMF-coupled power is directed to a fiber-coupled photodetector to measure received power,  $P_{rx}$ .

3. CHANNEL MODEL

Measurements of the communication channel are used to determine the relevance of this demonstration to FSO space-to-ground communication. The free-space laser range spans 5.15 km between the optical terminal site and the CCR. The optical terminal is located 29 m above sea level, and the CCR is placed 3 m above sea level. This slant path primarily spans the Swan River, Western Australia, and turbulence across the line of sight is relatively high at this distance above the ground and the river. Atmospheric turbulence causes random interference in the laser beam’s spatial profile as well as additional beam divergence, leading to time-varying scintillation of the received power and

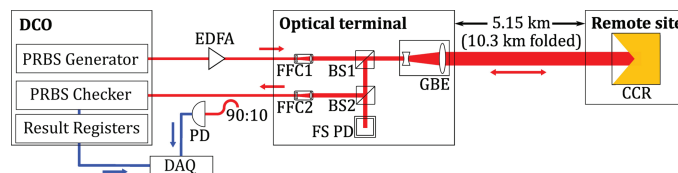


Fig. 1. Optical transceiver and terminal schematic for demonstration. BS, beam splitter; CCR, corner cube retro-reflector; DAQ, data acquisition; DCO, digital coherent optical module; EDFA, erbium-doped fiber amplifier; FFC, free-space to fiber collimator; FS PD, free-space photodetector; GBE, Galilean beam expander; PD, photodetector; PRBS, pseudo-random binary sequence.

## C.2. HIGH-BANDWIDTH COHERENT OPTICAL COMMUNICATION OVER 10.3 KM OF TURBULENT AIR

reducing the coupling efficiency of the free-space beam back into SMF.

Parameters used to characterize turbulence include the scintillation index, SI, atmospheric structure constant,  $C_n^2$ , and the Fried parameter [19]. The scintillation index is a measure of the scintillation in received optical power and is defined as

$$SI = \frac{\sigma_{P_{rx}}^2}{\mu_{P_{rx}}^2}, \quad (1)$$

where  $\sigma_{P_{rx}}$  and  $\mu_{P_{rx}}$  are the standard deviation and mean of received power  $P_{rx}$ , respectively. On a folded link, the attenuation due to turbulence is the product of two correlated random variables representing the forward and backward paths, and is treated similarly to a one-way point-to-point link [15]. The  $C_n^2$  can be derived from an angle-of-arrival spectrum measured with an angle-of-arrival scintillometer [20], and this requires a probe light source at the remote site in a folded link. The Fried parameter is a length scale decreasing with increasing turbulence along the link, and indicates the scale of the beam's spatial coherence. In an experiment, neither the  $C_n^2$  or Fried parameter is directly measurable and must be inferred indirectly from additional atmospheric measurements and knowledge of the experimental setup. The scintillation index was selected to relate the horizontal folded link to space channels because the parameter is a directly measurable value and is readily compared with previously published experiments.

Poliak, 2018 [11], discusses the relevance of horizontal ranges to uplink and downlink channels. They assert the 10 km ground-to-ground range most closely resembles an uplink because the atmospheric turbulence is close to the transmit aperture. The modeling supporting the demonstration suggested that scintillation indices of 0.2 and one corresponded to ground-to-space uplinks to GEO at 30° and 10° elevations, respectively. An elevation of 30° was stated to be the practical worst case for a GEO link. The aperture diameter in the modeling was not discussed. For the folded link concerned in this paper, with CCR at 5.15 km from the transmitter, calculations given in Supplement 1 show that the Fried parameter is close to the beam  $1/e^2$  waist diameter and receiver aperture diameter. Figure S1 in Supplement 1 shows that angular deviations will not lead to significant power variation. Instead, power scintillation is dominated by sub-aperture distortions or "speckle" as the beam front passes through multiple coherence regions. Speckle is observed in the space-to-ground downlink direction, and causes degraded free-space-to-SMF coupling. Therefore, the folded link is primarily subject to the characteristic issue of downlinks and is relevant to this transmission direction. Further modeling in Supplement 1, with a Hufnagel-Valley 5/7 profile [19], predicts scintillation indices between 0.1 and 0.4 for downlinks from satellites at 50° and 20° elevations, respectively. This modeling is based on plane wave propagation to a point receiver at the ground, and ground station receiver apertures of the order of 50–100 cm will be subject to lower scintillation indices due to aperture averaging. The scintillation indices measured during this demonstration are compared with the 0.1–0.4 scintillation index values for a point receiver, to show general applicability to a GEO feeder downlink.

**Table 1. Link Budget for the 10.3 km Folded Laser Range**

Quantity	Value	
Transmit power	26.8	dBm
Splitting loss (FFC1 to FFC2)	−9.00	dB
Geometric and clipping loss (optimum alignment)	−22.5	dB
Receiver cutoff power	−33.0	dBm
Link margin	28.3	dB

### A. Link Budget

A link budget is given in Table 1. The DCO cutoff is approximately −33.0 dBm of received optical power. Splitting losses are idealized to be 3 dB. For a transmit power of 26.8 dBm, a link margin of 28.3 dB accommodates excess losses due to misalignment, clipping, SMF coupling loss, and turbulence-induced fading. Additional loss will also be caused by scattering from sea-spray because the beam propagates close to the surface of the river.

## 4. RESULTS

Measurements were taken on 13 December 2022 between 17:55 and 20:43, while the scintillation index remained below 0.4. A scatterplot of BER measurements below the FEC threshold and SMF coupling against scintillation index is shown in Fig. 2. For each wavelength under test, the scintillation index, mean SMF coupling, and proportion of BER measurements below the  $4.5 \times 10^{-3}$  FEC threshold are shown in Fig. 3. The wavelengths shown were increased in chronological order, providing a time-sampling of the atmospheric turbulence. Reported wind direction and speed during the 3 h period is also given in Fig. 3. Wind direction was parallel to the direction of beam propagation for the first half of the demonstration, and transverse to the beam for the second half, and wind speed ranged from 11.1 to 27.8 km/h [21]. An additional 2 dB of transmit power was added at 20:15, increasing the power into FFC1 to 28.8 dBm, for wavelengths 193.10 THz and above, and causing a momentary increase in the proportion of BER above the FEC threshold. The minimum and maximum scintillation indices

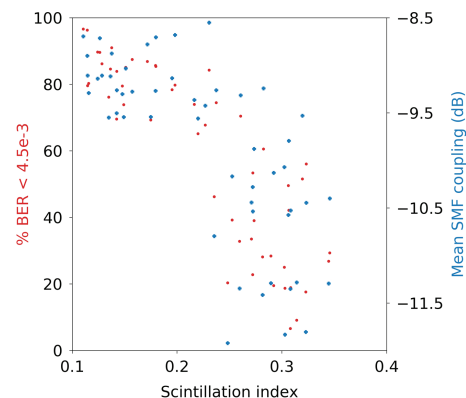


**Fig. 2.** Measurements during low turbulence. Scatterplot of low BER transmission % and fiber-coupling versus scintillation index.

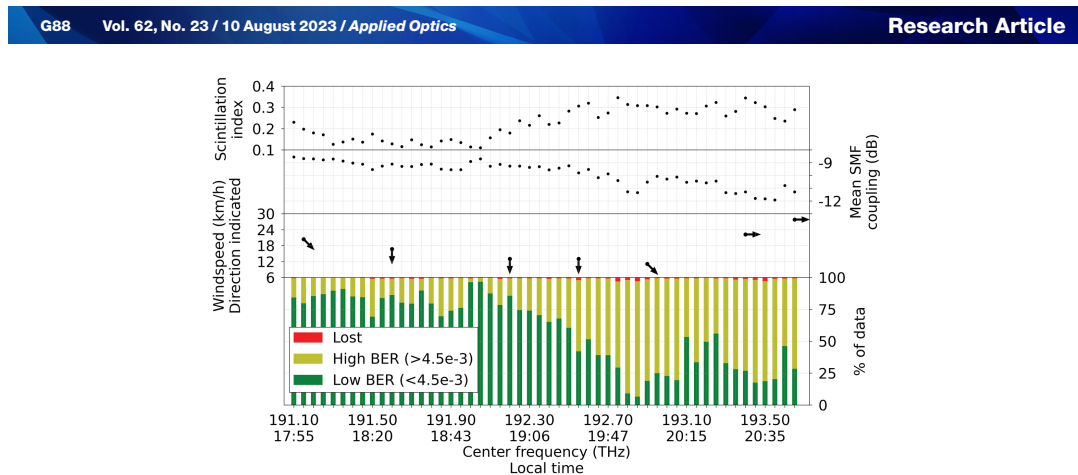


**Fig. 3.** Measurements during low turbulence. Per wavelength: scintillation index, single-mode fiber coupling, and proportions of lost, high bit error rate (BER) and low BER transmissions. Wind speed and direction as reported at Perth Airport [21]; downward arrows point south, parallel to the transmission.

were 0.110 and 0.346 for wavelengths 192.05 and 192.75 THz, respectively. Mean SMF coupling efficiency ranged between a maximum of  $-8.55$  dB and minimum of  $-11.9$  dB, corresponding to percentages of transmissions above threshold of 84% and 20%, respectively. Table S1 in Supplement 1 provides the full numerical results.

#### A. Transceiver Wavelength Dependence Characterization

For each wavelength used in the demonstration, loopback measurements of BER were taken in-fiber with fixed transmit power and attenuation to simulate channel loss. Of the first 10 channels, spanning 191.10–191.55 THz, BER decreased linearly from  $6.61 \times 10^{-4}$  to  $1.88 \times 10^{-4}$ . For the remaining 52 channels, spanning 191.60–194.15 THz, BER was randomly distributed within the range of  $1.05 \times 10^{-4}$  and  $2.11 \times 10^{-4}$ . This suggests a minor wavelength dependence in the DCO or EDFA only in the first 10 channels. Therefore, the variation in performance seen between 191.10 and 193.65 THz was likely caused by changing atmospheric turbulence.

## 5. DISCUSSION

The scintillation indices measured show the relevance of this laser range to a real ground-to-space laser links. The scintillation indices observed on 13 December 2022 spanned 0.1 to 0.4. These indices are equivalent to the scintillation indices modeled for a GEO downlink to a point receiver on the ground at  $20^\circ$ – $50^\circ$  elevation. A large proportion of transmissions for scintillation index values below 0.2 were below the FEC threshold, without any amplitude stabilization. From Fig. 2, the increasing scintillation index correlates with the decreasing SMF coupling efficiency, with a sharp drop-off around a scintillation index of 0.25. If a separate, smaller receiver aperture were used, beam disturbances would be limited to angular and phase-piston deviations. This aperture would be compatible with angular correction employing a fast-steering mirror to improve

SMF coupling and therefore BER performance [22,23], at the expense of greater geometric loss. For the best performance under speckle, a higher-order adaptive optics system would need to be employed to ensure robust reception, as in Dochhan, 2019 [12], or Bitachon, 2022 [14].

Additionally, at 20:00, a change in wind direction transverse to the beam path occurred close to the peak scintillation index observed at 19:50, and generally low number of transmissions below the FEC threshold between 19:55 and 20:15. The period of transverse wind may be more applicable to space communications than the period prior to 20:00 when the wind was parallel to the beam path, as winds encountered by a beam propagating from space-to-ground will necessarily travel transverse to the beam path. Also, wind generates sea spray on the surface of the river, resulting in additional power attenuation as the beam propagates close to the river surface. This effect will lead to an increase in high BER transmissions, in addition to atmospheric turbulence. The scattering cannot be isolated from the power measurements, but will clearly be correlated with wind velocity and the strength of the turbulence.

As GEO and LEO transmissions both pass through the same atmosphere, this link also has relevance to transmission from LEO. On a given day, the scintillation index for a LEO link will be higher than a GEO link because of the contribution of satellite slew rate to the pseudowind [19]. Furthermore, the Doppler shift imparted by the slew rate of a LEO satellite is not replicated by the stationary horizontal link.

## 6. CONCLUSION

High-speed coherent communication over a 10.3 km folded laser link was demonstrated without atmospheric turbulence correction, in varying turbulence conditions. The scintillation index for the demonstration was derived and showed the relevance of the horizontal ground-to-ground link to a typical and worst-case ground-to-space link. Performance under these conditions is challenging without employing a correction technology such as adaptive optics. However, transmission of

## C.2. HIGH-BANDWIDTH COHERENT OPTICAL COMMUNICATION OVER 10.3 KM OF TURBULENT AIR

data with BER below  $4.5 \times 10^{-3}$  is shown to be possible with unmodified fiber networking equipment, under the right conditions. A possible correlation between BER and wind direction was observed, and this may have implications for high-speed ground-to-ground FSO communication installations as an additional topic of interest.

The folded laser range utilizing a CCR is a relatively low-complexity arrangement, compared to a point-to-point link. This laser range intrinsically has a higher accessibility and potential uptime for commissioning activities than a link to a satellite. Having shown the relevance of this link, it can be used for further research and development activities. This includes commissioning other communication equipment prior to deployment in full-sized optical ground stations. Furthermore, the decline in BER with increasing the scintillation index demonstrates the need for adaptive optics correction to overcome high-order turbulence. As a priority, the optical terminal shown can be modified to incorporate an adaptive optics system, as the current arrangement clearly experiences speckle, and performance would be improved with adaptive optics to correct the wavefront. The adaptive optics system could then be tested, with high uptime, on this link with statistics representative of space-to-ground conditions.

**Funding.** SmartSat Cooperative Research Centre (CRC Research Project 1-18).

**Acknowledgment.** This work has been supported by the SmartSat CRC, whose activities are funded by the Australian Government's CRC Program. S. Karpathakis is supported by a SmartSat CRC PhD Scholarship and a research award from The Andy Thomas Space Foundation and EOS Space Systems. D. Gozzard is supported by a Forrest Research Foundation Fellowship.

The authors thank their CRC research partners at the Defence Science and Technology Group, Goonhilly Earth Station Ltd., Thales, Australia, Thales Alenia Space, and The University of South Australia. The authors thank Nicolas Maron from SYRTE-Observatoire De Paris for his assistance with the optical equipment, and Charles Gravestock from ICRAR for designing and building the free-space detector used in this work.

**Disclosures.** The authors declare no conflicts of interest.

**Data availability.** Data underlying the results presented in this paper are not publicly available at this time but may be obtained from the authors upon reasonable request.

**Supplemental document.** See Supplement 1 for supporting content.

### REFERENCES

1. E. Lutz, "Towards the terabit/s satellite-interference issues in the user link," *Int. J. Satell. Commun. Netw.* **34**, 461–482 (2016).
2. Y. Arimoto, M. Toyoshima, M. Toyoda, T. Takahashi, M. Shikatani, and K. Araki, "Preliminary result on laser communication experiment using Engineering Test Satellite-VI (ETS-VI)," *Proc. SPIE* **2381**, 151–158 (1995).
3. T. Jono, Y. Takayama, K. Shiratama, I. Mase, B. Demelenne, Z. Sodnik, A. Bird, M. Toyoshima, H. Kunimori, D. Giggenbach, N. Perlot, M. Knapek, and K. Arai, "Overview of the inter-orbit and the orbit-to-ground laser communication demonstration by OICETS," *Proc. SPIE* **6457**, 9–18 (2007).
4. D. M. Boroson and B. S. Robinson, "The lunar laser communication demonstration: NASA's first step toward very high data rate support of science and exploration missions," *Space Sci. Rev.* **185**, 115–128 (2014).
5. K. Kikuchi, "Fundamentals of coherent optical fiber communications," *J. Lightwave Technol.* **34**, 157–179 (2016).
6. E. Pincemin, Y. Loussouarn, Y. Pan, G. Miller, A. Gibbemeyer, B. Mikkelsen, A. Gaibazzi, W. Way, T. Yamazaki, A. Hayashi, and K. Fujiyama, "Interoperable CFP-DCO and CFP2-DCO pluggable optic interfaces for 100G WDM transmission," in *Optical Fiber Communication Conference (OFC)* (2019), pp. 1–3.
7. C. M. Schieler, K. M. Riesing, B. C. Bilyeu, B. S. Robinson, J. P. Wang, W. T. Roberts, and S. Piazzolla, "TBIRD 200-Gbps CubeSat downlink: system architecture and mission plan," in *IEEE International Conference on Space Optical Systems and Applications (ICSOS)* (2022), pp. 181–185.
8. A. Tantillo, "Communications system achieves fastest laser link from space yet," <https://news.mit.edu/2022/communications-system-achieves-fastest-laser-link-space-yet-1130> (Retrieved January 30, 2023).
9. C. M. Schieler, K. M. Riesing, B. C. Bilyeu, J. S. Chang, A. S. Garg, N. J. Gilbert, A. J. Horvath, R. S. Reeve, B. S. Robinson, J. P. Wang, S. Piazzolla, W. T. Roberts, J. M. Kovalik, and B. Keer, "On-orbit demonstration of 200-Gbps laser communication downlink from the TBIRD CubeSat," *Proc. SPIE* **12413**, 1241302 (2023).
10. C. M. Schieler, A. S. Garg, B. C. Bilyeu, J. P. Wang, and B. S. Robinson, "Demonstration of reliable high-rate optical communication over an atmospheric link using ARQ," in *IEEE International Conference on Space Optical Systems and Applications (ICSOS)* (2019), pp. 1–6.
11. J. Poliak, R. M. Calvo, and F. Rein, "Demonstration of 1.72 Tbit/s optical data transmission under worst-case turbulence conditions for ground-to-geostationary satellite communications," *IEEE Commun. Lett.* **22**, 1818–1821 (2018).
12. A. Dochhan, J. Poliak, J. Surof, M. Richerzhagen, H. F. Kelemu, and R. M. Calvo, "13.16 Tbit/s free-space optical transmission over 10.45 km for geostationary satellite feeder-links," in *20th ITG-Symposium on Photonic Networks* (2019), pp. 1–3.
13. O. Balasiano, E. Wohlgemuth, I. Attia, A. Roizman, T. Falk, R. Faig, A. Shapira, Y. Yoffe, R. J. Cohen, R. Vered, and D. Sadot, "10 km retro-reflected coherent atmospheric FSOC at 128 Gbps 16-QAM," in *Advanced Photonics Conference: Signal Processing in Photonic Communications* (2022), paper SpTu3G-5.
14. B. I. Bitachon, Y. Horst, L. Kulmer, et al., "Tbit/s single channel 53 km free-space optical transmission—assessing the feasibility of optical GEO-satellite feeder links," in *European Conference on Optical Communication (ECOC)* (2022), pp. 1–4.
15. P. V. Trinh, A. Carrasco-Casado, T. Okura, H. Tsuji, D. R. Kolev, K. Shiratama, Y. Munemasa, and M. Toyoshima, "Experimental channel statistics of drone-to-ground retro-reflected FSO links with fine-tracking systems," *IEEE Access* **9**, 137148 (2021).
16. S. Walsh, A. Frost, L. Howard, D. Gozzard, S. Karpathakis, B. Dix-Matthews, C. Gravestock, A. McCann, and S. Schediwy, "Angle-of-arrival variability of retroreflected lasers despite atmospheric reciprocity," *Opt. Lett.* **47**, 1920–1923 (2022).
17. "CFP MSA management interface specification," 2017, <https://www.cfp-msa.org/> [Retrieved October 26, 2021].
18. "ITU-T recommendation G709.2: OTU-4 long-reach interface," 2018, <https://www.itu.int/rec/T-REC-G.709.2/> [Retrieved July 29, 2022].
19. L. C. Andrews and R. L. Phillips, *Laser Beam Propagation through Random Media*, 2nd ed. (SPIE, 2005).
20. S. Manning, B. A. Clare, K. J. Grant, and K. A. Mudge, "Development and implementation of a robust angle of arrival turbulence measurement system," *Opt. Eng.* **54**, 114104 (2015).
21. "Perth December 13 2022 weather," 2022, <https://weather.spark.com/d/128792/13/13/Average-Weather-on-December-13-in-Perth-Australia> [Retrieved January 30, 2023].
22. S. M. Walsh, S. F. E. Karpathakis, A. S. McCann, B. P. Dix-Matthews, A. M. Frost, D. R. Gozzard, C. T. Gravestock, and S. W. Schediwy, "Demonstration of 100 Gbps coherent free-space optical communications at LEO tracking rates," *Sci. Rep.* **12**, 18345 (2022).
23. S. F. E. Karpathakis, B. P. Dix-Matthews, S. M. Walsh, A. S. McCann, D. R. Gozzard, A. M. Frost, C. T. Gravestock, and S. W. Schediwy, "Ground-to-drone optical pulse position modulation demonstration as a testbed for lunar communications," *Drones* **7**, 99 (2023).



OPEN

# Demonstration of 100 Gbps coherent free-space optical communications at LEO tracking rates

Shane M. Walsh<sup>✉</sup>, Skevos F. E. Karpathakis, Ayden S. McCann, Benjamin P. Dix-Matthews, Alex M. Frost, David R. Gozzard, Charles T. Gravestock & Sascha W. Schediwy

Free-space optical communications are poised to alleviate the data-flow bottleneck experienced by spacecraft as traditional radio frequencies reach their practical limit. While enabling orders-of-magnitude gains in data rates, optical signals impose much stricter pointing requirements and are strongly affected by atmospheric turbulence. Coherent detection methods, which capitalize fully on the available degrees of freedom to maximize data capacity, have the added complication of needing to couple the received signal into single-mode fiber. In this paper we present results from a coherent 1550 nm link across turbulent atmosphere between a deployable optical terminal and a drone-mounted retroreflector. Through 10 Hz machine vision optical tracking with nested 200 Hz tip/tilt adaptive optics stabilisation, we corrected for pointing errors and atmospheric turbulence to maintain robust single mode fiber coupling, resulting in an uninterrupted 100 Gbps optical data link while tracking at angular rates of up to 1.5 deg/s, equivalent to that of spacecraft in low earth orbit. With the greater data capacity of coherent communications and compatibility with extant fiber-based technologies being demonstrated across static links, ground-to-low earth orbit links of Terabits per second can ultimately be achieved with capable ground stations.

Communication at optical frequencies revolutionised terrestrial communications with the advent of optical fiber networks<sup>1</sup>, but the same is not yet true of free-space applications, which are still dominated by radio frequency (RF) communications. While the orders-of-magnitude increase in carrier frequency from RF (kHz–GHz) to optical frequencies (THz) enables a commensurate increase in data capacity, moving to the optical domain brings with it new challenges. Primary among these are the strict acquisition and tracking requirements<sup>2</sup>, and the effect of atmospheric turbulence that significantly influences optical beam propagation on millisecond timescales<sup>3</sup>. To realise the potential of free-space optical communications for ground-to-ground, ground-to-air, and ground-to-space links, the effects of atmospheric turbulence must be suppressed<sup>4</sup>.

The most straightforward implementations of free-space optical communications modulate data on the intensity of light, such as simple on-off keying (OOK) or pulse position modulation (PPM). These direct-detection methods only require a detector that can measure the intensity of the received light. Coherent detection methods, in contrast, maintain phase and polarisation information by mixing the received signal with a local oscillator (LO), giving extra degrees of freedom to encode data and capitalize fully on channel capacity<sup>5</sup> and compatibility with ubiquitous fiber-based technologies<sup>6</sup>. These coherent methods require coupling the received light into single mode fiber (SMF), which at a diameter of 8–10 μm, is more susceptible to pointing errors and turbulence compared with the larger multi-mode fiber (> 50 μm) or free-space detectors used with direct-detection schemes<sup>7</sup>.

Currently, earth observation satellites produce data at such high volumes that on-board compression is often required before transmission to the ground using available RF bandwidth (e.g.<sup>8,9</sup>), which is power intensive and can reduce data fidelity. For the case of low earth orbit (LEO), the time a spacecraft is visible to any particular ground station is only a few minutes per day, further constraining data transfer. A LEO spacecraft could transmit data via a relay spacecraft, typically in geosynchronous earth orbit (GEO), but the increased transmission distance (~ 35,000 km versus ~ 1000 km) further burdens the size, weight, and power (SWaP) of spacecraft communications systems. Relieving this bottleneck is the goal of NASA's Terabyte Infrared Delivery system (TBIRD) to develop cubesat-suitable optical terminals capable of 200 Gbps coherent LEO-to-ground downlink<sup>10</sup>.

International Centre for Radio Astronomy Research, The University of Western Australia, Perth 6009, Australia.  
✉email: shane.walsh@uwa.edu.au

### C.3. DEMONSTRATION OF 100 GBPS COHERENT FREE-SPACE OPTICAL COMMUNICATIONS AT LEO TRACKING RATES

www.nature.com/scientificreports/

The current 5.6 Gbps record for an optical data link between LEO to ground was demonstrated using coherent binary phase shift keying (BPSK) between two ESA TESAT laser communication terminals, one on board the NFIRE spacecraft and one on the ground at Tenerife, Spain<sup>11</sup>. These terminals were engineered for inter-satellite links, where atmospheric turbulence is not an issue and as such do not employ any active turbulence mitigation; only a reduction of the ground terminal aperture to reduce the effect of scintillation. The  $\sim 5$  m beam size would ensure that the occurrence of deep fades due to beam wander at the ground terminal are negligible, but given turbulence in a ground-to-space link is concentrated at the ground, beam wander is significantly greater for the uplink than the downlink. This is reflected in the disparity in link quality, with the downlink remaining error free while the uplink showed a bit-error rate (BER) of  $\sim 10^{-5}$ , despite the identical hardware at each end. To push the data rates into the 100+ Gbps regime requires, at a minimum, tip/tilt adaptive optics (AO) stabilisation to improve downlink fiber coupling efficiency and pre-compensate uplink beam wander. Such ground stations are currently in development<sup>12,13</sup> and have demonstrated AO-corrected SMF coupling from GEO<sup>14</sup>, but to our knowledge tip/tilt AO stabilised coupling has not been demonstrated at the more challenging tracking rates of LEO.

Tip/tilt AO stabilised high-speed coherent optical links between the ground and airborne platforms have been demonstrated previously. Chen et al.<sup>15</sup> demonstrated a 100 Gbps bi-directional quadrature amplitude modulation (QAM) link between a ground station and light aircraft over 10–20 km link distance. Li et al.<sup>16,17</sup> demonstrated an 80 Gbps link to a drone mounted retroreflector across a 100 m round trip distance with simulated turbulence, using two orbital-angular-momentum (OAM) multiplexed 40 Gbps quadrature phase shift keying (QPSK) links. These demonstrations reached angular tracking rates of  $\sim 0.2$  and  $\sim 0.1$  deg/s respectively, although maintaining fiber coupling at LEO-like tracking rates were not aims of those experiments.

The ultra-high capacity of coherent free-space optical communications has been demonstrated across static links by various groups. Parca et al.<sup>18</sup> used 16 channel QPSK to establish a 1.6 Tbps link over 80 m between buildings. Feng et al.<sup>19</sup> used 3 channel QPSK to achieve 160 Gbps over a 1 km link. The highest capacity link to date, by Docchan et al.<sup>20</sup>, achieved 13.16 Tbps with 54 channel QPSK with tip/tilt stabilisation across a turbulent 10.45 km link. Most recently, Guiomar et al. achieved the highest spectral efficiency to reach 800 Gbps in a single channel using probabilistic constellation shaping 64-ary QAM over 42 m.

To enable these high-capacity technologies for ground-to-space links requires a tracking system that can maintain SMF coupling in the presence of large angular velocities and atmospheric turbulence. In this paper, we present results of a coherent free-space optical link operating at 1550 nm between a deployable optical terminal and an airborne drone. Combining a tip/tilt AO system with concurrent closed loop machine vision (MV) tracking, we maintain the SMF coupled link at angular velocities up to  $\sim 1.5$  deg/s, representative of the apparent motion of spacecraft in LEO.

Our work uses the retroreflected signal serving as its own tip/tilt beacon<sup>21,22</sup>, which due to atmospheric reciprocity<sup>23</sup> allows our terminal to simultaneously demonstrate correction of the “downlink” beam to maintain fiber coupling as well as pre-compensation of the “uplink” to maintain pointing on target. An overview of the experiment is depicted in Fig. 1. Our deployable optical terminal serves as a development test-bed for the Western Australian Optical Ground Station (WAOGS-1)<sup>24</sup>, and also as a standalone unit, which with further optimisation could facilitate Tbps ground-to-ground, ground-to-air, and ground-to-LEO coherent optical links.

#### Methods

For this experiment our deployable optical terminal was located on the roof of the physics building at the University of Western Australia Crawley campus, approximately 34 m above sea level. An optical breadboard housing the optics, MV system, GPS receiver, and single board computer was fastened to the mount, shown in Fig. 2. Electrical cables and optical fiber carried signals to the tip/tilt AO control electronics on the mount base and communications equipment housed in a separate enclosure. To simulate a satellite pass, we used a drone carrying an optical payload that includes a corner-cube retroreflector (CCR), flying at an altitude of 120 m over the Swan River and a line-of-sight distance of 500–700 m for a folded link length of up to 1.4 km. Figure 3 details the interactions between components during the acquisition and tracking phases. CCRs installed at two fixed locations provided static links of 600 m and 2.4 km folded lengths, used for calibration and troubleshooting. A summary of the mount design parameters is presented in Table 1 and each subsystem is described in further detail in the following subsections.

**Mount.** Our deployable optical transceiver terminal was built around a PlaneWave Instruments L-350 precision altitude-azimuth astronomical mount. This mount provides smooth, accurate tracking and slew speeds of up to 50 deg/s for rapid acquisition. The mount is controlled by the remotely accessed single board computer located on the optical breadboard. Initial pointing of the mount can be provided by spacecraft two line element (TLE) ephemeris or aircraft automatic dependent surveillance-broadcast (ADS-B) retrieved over the internet, or in the case of this experiment, from GPS coordinates transmitted from the drone via 921.2 MHz LoRa signal. The vendor-provided mount API natively accepts TLEs and calculates the mount path accordingly, while ADS-B and GPS coordinates are converted into mount altitude and azimuth coordinates by our bespoke software layer above the mount API.

**Machine vision.** GPS and TLEs are not sufficiently precise to point an optical ground station accurately enough to acquire its target. To provide an intermediate acquisition and tracking stage between TLE/GPS and the tip/tilt AO system, an MV system is used for optical closed loop control of the mount. We use a commercially available MV camera with an  $f = 500$  mm lens, giving a  $1.0^\circ \times 0.75^\circ$  field of view. An example image is shown in Fig. 4. This is large enough to allow for errors in TLE/GPS-derived pointing, but with a fine  $9 \mu\text{rad}/\text{pixel}$

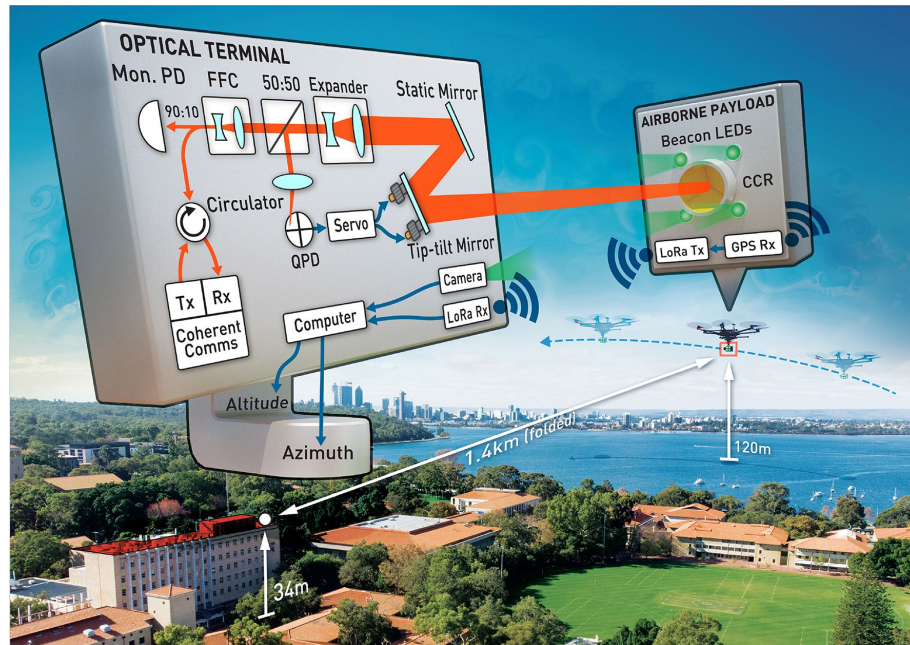


**Figure 1.** Schematic of the deployable optical terminal and experiment. *Mon. PD* monitoring photodetector, *FFC* fiber to free-space collimator, *QPD* quadrant photodetector, *CCR* corner-cube retroreflector, *LED* light emitting diode, *LoRa* “Long Range”, *Tx* transmitter, *Rx* receiver.

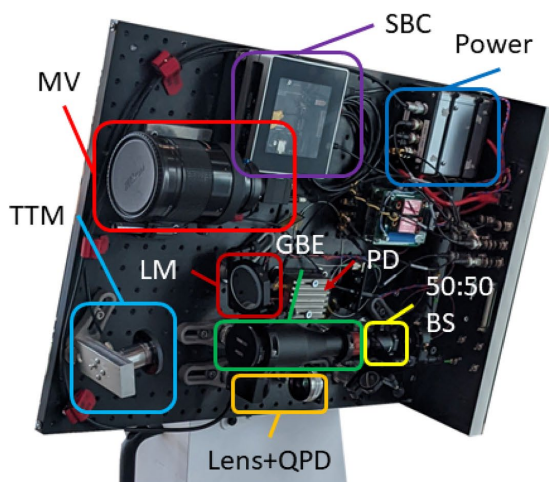


**Figure 2.** Left: the optical breadboard layout. *MV* Machine vision lens and camera, *TTM* tip/tilt mirror, *LM* static launch mirror, *GBE* Galilean beam expander, *QPD* quadrant photodetector, *SBC* single board computer, *PD* photodetector, *BS* beamsplitter. Right: the deployed optical terminal. Optics and *MV* are located on the far side of the breadboard. The tip/tilt control electronics are visible on the lower left of the mount base. The telescope mounted on the left was not used for this experiment.





**Figure 4.** Image from the machine vision tracking camera. The red cross shows the detected position of the beacon LEDs. The white circle shows the tip/tilt mirror actuation range, centred on the predetermined hotspot.

performance monitoring interval<sup>26</sup>. This 1 s sampling rate is suitable for deployment in fixed fiber networks, but will not capture amplitude shifts seen on a free space link due to the shorter atmospheric coherence time (a few to tens of milliseconds). In-fiber commissioning of the DCO module demonstrated the threshold power corresponding to a FEC-correctable BER of  $4.5 \times 10^{-3}$  is approximately  $-30$  dBm (optional registers reporting optical signal-to-noise ratio<sup>26</sup> were not implemented in this module). This BER value was taken to be the threshold for error-free communication, with the caveat that a 1 s period of reception averages out short duration bit error events over a free-space link and some instances may exceed the error-free threshold. Unfortunately, post-FEC BER nor QPSK constellations were available from this module.

As the DCO power measurements are taken at 1 Hz, fast power fluctuations due to atmospheric turbulence are subject to aliasing. Therefore, a 90:10 splitter sends 10% of the received light to a monitoring photodetector to capture received power information at 2 kHz. This sample rate is faster than the atmospheric coherence time, and allowed us to determine whether short duration deep fades due to turbulence or pointing errors were present; if signal is observed throughout the drone passes then the goal of robust SMF coupling is successful.

**Optics.** The communications signal is fiber fed from the DCO module to the mount via an erbium-doped fiber amplifier (EDFA) nominally providing 20 dB gain and  $< 5$  dB noise. The amplified output power was verified using a handheld power meter before feeding to the mount, where it is transmitted from a fiber to free-space collimator as a beam of waist radius  $w_0 = 1.14$  mm. The beam is directed to a 50:50 beamsplitter, needed for the tip/tilt AO correction of the returned beam, where 50% of the power is transmitted through the system. The transmitted portion of the beam is expanded by a  $15\times$  Galilean beam expander (GBE) to a waist radius of  $w_0 = 17.1$  mm from an aperture diameter of 50 mm. We chose this beam size to be as large as possible to minimize divergence due to diffraction, while remaining smaller than the expected worst-case Fried Parameter size ( $r_0$ , typically on the order of  $\sim 10$  cm at 1550 nm for strong turbulence). In this regime, scintillation is negligible and first-order tip/tilt AO alone is sufficient to correct for atmospheric turbulence. The expanded beam is reflected off the piezo-electric tip/tilt mirror to a static launch mirror before exiting from the system. Note that in Fig. 1, these two mirrors are swapped for graphical convenience, but this is functionally identical.

After propagating across the atmospheric channel to the drone, the beam is retroreflected and returned to the transceiver where it follows the reverse path through the optics. This time, at the beamsplitter, the transmitted light is coupled back into the SMF to be sent to the communications module and monitoring photodetector, while the reflected light is focused onto a position sensitive quadrant photodetector (QPD). Variations in angle-of-arrival of the retroreflected beam imparted by turbulence and/or pointing errors are translated into lateral spot movement on the QPD, which is used by the PID loop and control electronics to drive the tip/tilt mirror actuation to maintain the spot centering.

The tip/tilt AO system consists of a two-inch diameter mirror mounted to a commercial fast Piezo tip/tilt platform and its associated electronics. The Piezo platform has a specified closed-loop angular resolution of 50 nrad and actuation range of  $\pm 2$  mrad in two dimensions. During this experiment, the tip/tilt loop was operated at 200 Hz. Due to atmospheric reciprocity<sup>23</sup>, the tip/tilt loop has the dual effect of correcting beam wander of the outgoing beam to maintain pointing, as well as correcting the angle-of-arrival of the return beam to maintain fiber-coupling efficiency.

A link budget for the experiment is presented in Table 2. The in-fiber transmit power was limited to a maximum of 11.7 dBm to avoid saturation of the QPD and mitigate the effect of prompt reflections, largely from the refractive elements of the beam expander. The terminal optics imposed a combined 15.7 dB loss across transmission and reception, leaving 26 dB of link margin above the  $-30$  dBm threshold for pointing, geometric, and atmospheric losses.

### C.3. DEMONSTRATION OF 100 GBPS COHERENT FREE-SPACE OPTICAL COMMUNICATIONS AT LEO TRACKING RATES

www.nature.com/scientificreports/

Parameter	Value
In-fiber transmit power	11.7 dBm
Transmit beam split loss	- 3 dB
Geometric and clipping loss	- 1.7 dB
Receive beam split loss	- 3 dB
Single-mode fiber coupling loss	- 8 dB
Received power threshold for $10^{-4}$ BER	- 30 dBm
Link margin	26 dB

**Table 2.** Demonstration link budget.

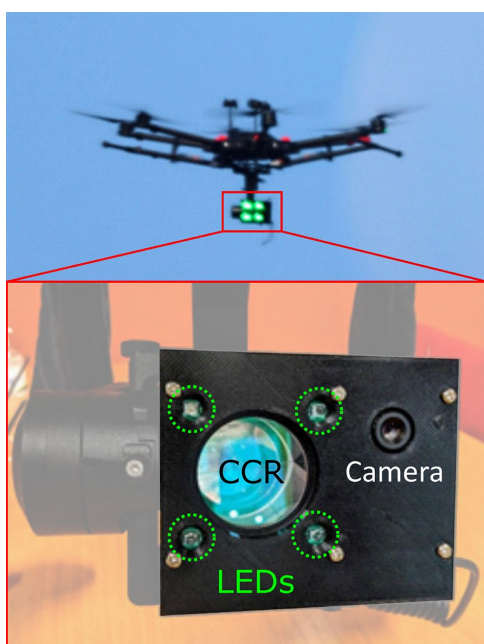


**Figure 5.** Top: the drone in operation, with MV beacon LEDs visible on the gimbal-mounted optical payload. Bottom: close-up of the optical payload showing the beacon LEDs, CCR, and camera.

**Drone.** To simulate the angular motion of a satellite in LEO, we use a professional grade drone carrying a gimbal-mounted optical payload consisting of a two-inch CCR to return the 1550 nm signal, four 532 nm beacon LEDs for MV tracking, and a camera for payload orientation. The drone also carries a GPS and barometric altimeter that relay coordinates to the optical terminal via LoRa for autonomous acquisition. The drone has a maximum horizontal velocity of 65 km/h, allowing us to easily mimic the  $\sim 1$  deg/s angular tracking rates of LEO across the  $\sim 700$  m distance to the optical terminal. Figure 5 shows the drone in flight with the payload LEDs illuminated (top), and a close up of the payload (bottom).

**Flight operations.** After take-off, the drone climbed to a regulation-limited 120 m altitude and moved into position over the Swan River, then adjusted the gimbal pointing so the beacon LEDs were oriented toward the mount. The onboard GPS module continuously transmitted the drone's position to the optical terminal computer, which was converted into altitude and azimuth angles to point the terminal at the drone. Once the LEDs were visible within the camera's field-of-view, the MV loop was closed and the mount pointing adjusted to acquire and maintain the drone beacons on the hotspot.

With the drone located on the MV hotspot, the laser was nominally incident on the CCR and signal was returned to the terminal. However, given the relatively short distance to the drone and its susceptibility to wind buffeting, return power was only intermittently observed until the tip/tilt loop was closed and signal was stable.

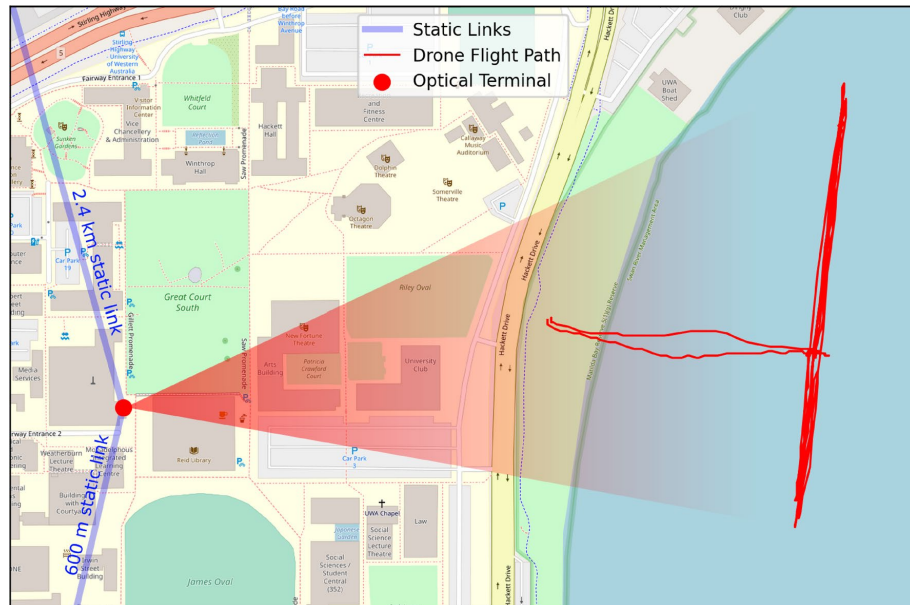


**Figure 6.** Map of flight area around the University of Western Australia campus in Perth, Western Australia. Red dot is the deployable optical terminal on the roof of the physics building, blue lines are static link paths, red line is the drone flight path during the 2022/04/21 flight. Map generated with OpenStreetMap data under the Open Database License ([openstreetmap.org/copyright](https://openstreetmap.org/copyright)).

Parameter	2022/04/07	2022/04/21
Temperature (°C)	30	25
Relative humidity (%)	25	34
Pressure (hPa)	1014	1023
Wind speed (km/h)	15	17
Wind direction	W	N
Cloud cover (%)	18	10
<b>Air quality (peak PM<sub>2.5</sub>, µg/m<sup>3</sup>)</b>		
Duncraig (16 km N)	< 10	160
Caversham (18 km NE)	10	> 200

**Table 3.** Atmospheric conditions in Perth for flight dates.

The MV and tip/tilt loops ran concurrently to track the drone correcting for macroscopic motion, whether intentional or due to wind buffeting, as well as beam wander from atmospheric turbulence. The MV controlled the mount for high-amplitude, low-frequency ( $\gtrsim 1$  Hz) errors and the tip/tilt loop controlled the tip/tilt mirror for low-amplitude ( $< 2$  mrad), high-frequency errors. With both tracking loops closed, we flew the drone in passes replicating the tracking rates needed for free-space optical links to spacecraft in LEO. Figure 6 shows a map of the drone flight path, which was limited in the north by obstructed line-of-sight, and to the south by dense marine traffic.

### Results and discussion

Flights were conducted on 2022/04/07 and 2022/04/21, with the former being a series of test flights and the latter being the culminating “high speed” flight. Atmospheric conditions for these dates are shown in Table 3. Figure 7 shows the BERs versus received optical power (top panel) for the flights with in-fiber measurements for reference, as well as histograms for the received power (bottom panel) for both days. During testing the received optical power ranged from  $-20$  to  $-12$  dBm, implying total pointing, atmospheric, and other losses of 8–16 dB. However, on 2022/04/21 smoke was present due to controlled burns by the Parks and Wildlife Service; air quality monitoring from sites 16 km north and 18 km north-east reported peak PM<sub>2.5</sub> densities over 150 and 200 µg/

### C.3. DEMONSTRATION OF 100 GBPS COHERENT FREE-SPACE OPTICAL COMMUNICATIONS AT LEO TRACKING RATES

www.nature.com/scientificreports/

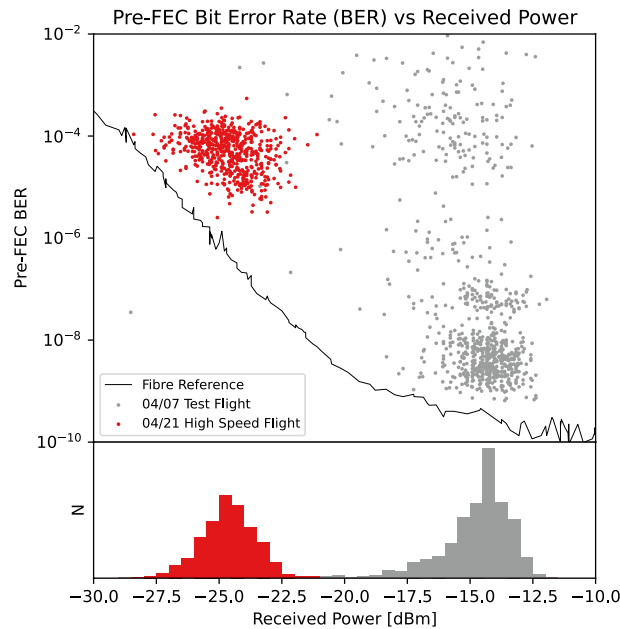


**Figure 7.** Top: pre-FEC BER versus received power. The black line is measurements taken in-fiber, delineating best possible performance. The gray dots are measurements from the 2022/04/07 test flights, red dots are from the 2022/04/21 high speed flight. Bottom: histogram of received power. Gray is from 2022/04/07 test flights, red is from 2022/04/21 high speed flight.

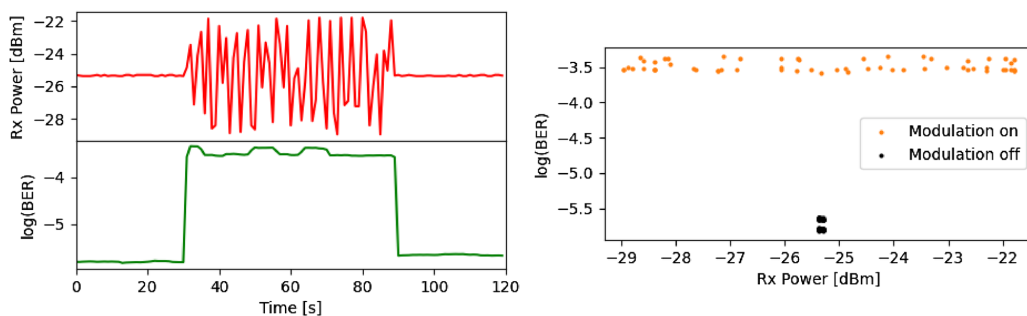


**Figure 8.** Left: time series for power (red) and log(BER) (green) for rapid power modulation test of DCO module. Right: scatter plot of BER versus power for modulation on (orange) and off (black).

$\text{m}^3$  respectively, compared with average values for those sites of  $\sim 20 \mu\text{g}/\text{m}^3$ . The increased density of micron-sized particulates imposed an apparent additional loss of  $\sim 10 \text{ dB}$  due to Mie scattering of the 1550 nm beam across the link, compared with the test measurements taken in the clearer  $\text{PM}_{2.5}$  conditions on 2022/04/07. This reduced power resulted in an associated increase in BER. The measurements deviate from the in-fiber reference due to aliasing of the turbulence-induced power fluctuations occurring faster than the 1 Hz sampling rate. In-fiber testing with a signal modulated by  $\pm 3 \text{ dB}$  at 220 Hz produced a two orders of magnitude increase in BER, with the aliased power measurements distributed near uniformly across the modulated range, as seen in Fig. 8. We therefore conclude the clustering of points at the top right of Fig. 7 is due to a period of particularly high turbulent variability across the link.

Figure 9 shows time-series data for the 2022/04/21 high speed flight, showing drone-terminal distance, drone velocity, mount azimuth tracking rate, MV tracking error, received optical power (from DCO module and

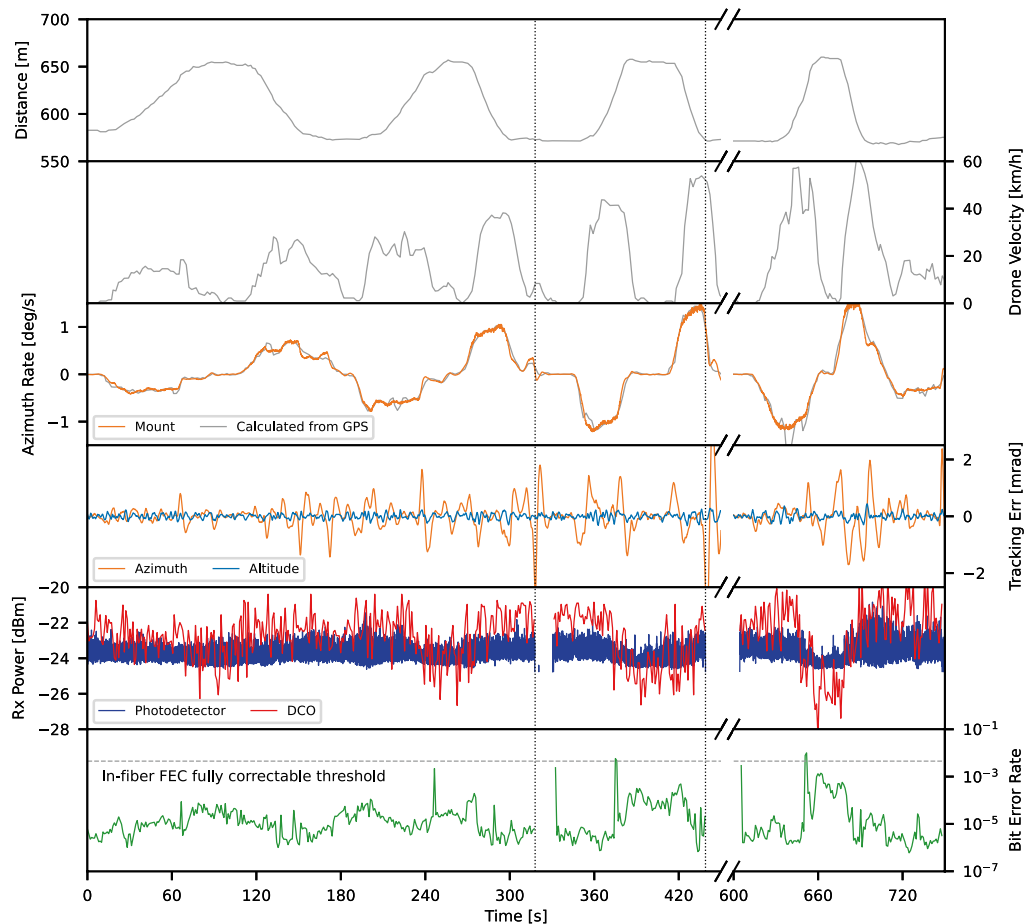


**Figure 9.** Time series data. From top to bottom: line-of-sight distance between the deployable optical terminal and drone as calculated from GPS. Drone horizontal velocity, as calculated from GPS. Mount azimuth tracking rate, as calculated from mount (orange) and GPS (grey). Machine vision tracking errors in azimuth (orange) and altitude (blue). Received optical power from photodetector (blue) and DCO module (red). BER. Times of link dropout are delineated with a dotted line ( $t = 318$  s and  $t = 439$  s).

photodetector), and pre-FEC BER. Drone distance and velocity were calculated from GPS coordinates, which also provide an independent measure of the mount azimuth tracking rate in addition to the values reported directly by the mount. The MV tracking errors are the offsets in milliradians between observed drone position and the hotspot.

The measurement series spans a total of eight drone passes over  $\sim 750$  s, with the longest uninterrupted link period of  $\sim 318$  s, or four drone passes. The link is only broken at the end of the fourth and sixth passes ( $t = 318$  s and  $t = 439$  s) when the drone decelerated abruptly at the flight area boundary, resulting in pointing errors too fast for the MV and too large for tip/tilt loops. When this occurred, the transmitted beam was no longer incident upon the CCR, and therefore no signal was returned; it is not the result of turbulence or poor link quality. During these periods of interruption, the MV tracking remains active as long as the drone remains visible in the  $1.0^\circ \times 0.75^\circ$  field of view. When the tracking returns the drone to the hotspot, the tip/tilt loop is closed again.

During the flight, the drone ranged from  $\sim 550$  to  $\sim 660$  m line-of-sight distance. The drone reached a maximum speed of 60 km/h, corresponding to an azimuth tracking rate of 1.5 deg/s. The MV tracking errors show the effect of wind buffeting, with the azimuth error frequently spiking well above 1 mrad while the altitude error remains stable below 0.25 mrad.

The returned optical power and BER plots show the link was lost only when the MV error exceeded 2.5 mrad during the drone deceleration; somewhat greater than the manufacturer specified 2 mrad actuation limit of

### C.3. DEMONSTRATION OF 100 GBPS COHERENT FREE-SPACE OPTICAL COMMUNICATIONS AT LEO TRACKING RATES

www.nature.com/scientificreports/

the tip/tilt mirror. The pre-FEC BER fluctuates between  $\sim 10^{-6}$  and  $\sim 10^{-3}$ . Given the millisecond scale of turbulence-induced atmospheric coherence time, instances of high BER will dominate the average within each 1 s sample. Therefore, the BER floor is very likely pessimistic compared to what would be observed with shorter and more frequent sample periods, which conversely would likely resolve more spikes above the FEC-correctable threshold. However, we can infer that for a practical communications link, when the pre-FEC BER approached and exceeded the (fiber-verified) FEC-correctable threshold of  $4.5 \times 10^{-3}$ , reliable communication could still be established with an appropriate retransmission protocol at the data layer. With this in mind, the results serve as confirmation that robust data transmission was maintained throughout the flight. Given the presence of smoke induced power loss and the limitations of the DCO for free-space links, the important result is the maintaining of the SMF coupling, rather than the specific BER behaviour.

The monitoring photodetector, receiving only 10% of the returned signal, was operating near the lower limit of its dynamic range, where its response is non-linear making measurements less accurate than the DCO reported values. The values shown in Fig. 9 were shifted by + 10.7 dB to account for the splitter and normalize the output to the DCO measurements. Due to the non-linearity it does not show the same variation in power as the DCO aliased measurements, but its 2 kHz sampling rate serves the critical purpose of showing that power fades are not occurring on timescales shorter than the 1 s DCO sample time; verifying that we maintained fiber coupling throughout the drone passes despite atmospheric turbulence, wind buffeting, and high angular velocity of the drone. To the best of our knowledge, this is the first such demonstration of tip/tilt AO-stabilised robust SMF coupling at the angular tracking rates needed for coherent ground-to-LEO links.

It is not possible to quantify the turbulence strength observed across the drone link from the data available as the power measurements are post-tip/tilt correction and any angle-of-arrival variations from turbulence are coupled with those from drone movement/vibration. Measurements without tip/tilt for comparison were also not possible as the tip/tilt loop was required to keep the beam on the CCR in the presence of wind buffeting. However, given the fact that tip/tilt was sufficient to keep the beam centered on the QPD, we can conclude that scintillation was negligible and the integrated turbulence resulted in a Fried parameter size  $r_0$  larger than the receiver diameter of 50 mm. For the round trip link distance of 1.2 km at 1550 nm, this would correspond to an upper bound  $C_n^2$  of  $5 \times 10^{-14} \text{ m}^{-2/3}$  throughout the experiment.

In some respects, a low-altitude drone link is more challenging than a link to a spacecraft. At the  $\sim 600$  m link length, the change in beam size due to divergence is negligible such that at the drone it is still only on the order of the CCR size. The drone was subjected to wind buffeting, causing motion at the scale of tens of centimeters even in mild winds and moving the CCR in and out of the beam when the tip/tilt AO loop was not closed. This motion was faster than the MV could correct the mount pointing, meaning that the tip/tilt AO system was correcting for this in addition to angle-of-arrival variations due to atmospheric turbulence. Furthermore, without a TLE spacecraft ephemeris providing an a priori coarse tracking path, the MV was responsible for tracking of the drone's large scale motion rather than making minor corrections to a pre-defined path. Despite these challenges the terminal maintained the link, with dropouts occurring only during abrupt deceleration of the drone as it approached flight boundaries, where the correction required was too rapid for the mount tracking and too large for the tip/tilt mirror. This situation is not analogous to any practical scenario of ground-to-LEO communications with a cooperative target.

A further drawback of the airspace and altitude restrictions on the drone was that tests were limited to tangential paths at a distance of  $> 550$  m. In this situation, the angular velocity is almost purely azimuthal, at a low altitude angle ( $\sim 8^\circ$ ). The mechanical azimuth rate of the mount needed to track a target on sky with a given angular velocity scales inversely with the cosine of the altitude angle, so the closer to zenith a satellite transits, the faster the azimuth axis must rotate. A more robust test would be a flight that transits close to zenith, more closely approximating the tracking demands on the mount axes where the required azimuth rate increases dramatically. We aim to address this in future experiments with light aircraft.

For this work we used the retroreflected beam as its own tip/tilt beacon, which provides an angle-of-arrival error signal despite atmospheric reciprocity due to the truncation of the Gaussian beam at the CCR on the drone payload<sup>22</sup>. This was convenient as it minimised the size and weight requirements of the drone. For a real LEO downlink, the spacecraft would either transmit a dedicated beacon signal at a separate wavelength from the data signal, or a portion of the data signal could be siphoned to use as the tip/tilt (or higher order AO) beacon. In either scenario, the operation of the tip/tilt loop remains unchanged from this work.

Our terminal has demonstrated the tracking capability for maintaining coherent ground-to-LEO communications, but to develop the terminal into a system capable of real uplink and downlink to LEO requires some optimizations. The line-of-sight velocity of the drone in this experiment produced a Doppler shift of at most  $\sim 1$  MHz, whereas the Doppler shift seen from a spacecraft at 500 km altitude LEO is of order  $\pm 10$  GHz during each orbital pass. For this experiment Doppler shift was negligible compared to the  $\pm 1.8$  GHz accuracy of the DCO module, but for coherent communications from LEO, a local oscillator capable of sweeping across a  $\sim 20$  GHz frequency range would be required.

The MV system would also need to be tailored to the beacon being used by the spacecraft. The limiting factor for our drone flights were the positional uncertainty from the GPS at a relatively short distance, requiring a large field of view. A simple lens and visible camera were sufficient as the beacon LEDs provided ample signal. A spacecraft beacon would be significantly fainter and therefore the MV system might be incorporated within the larger receiver optics using a dichroic/other beamsplitter to increase sensitivity and resolution. Depending on field-of-view constraints, separate coarse and fine MV systems may be needed<sup>25</sup>. It is possible the downlink signal itself could serve as both tip/tilt and MV beacons, which would require a camera sensitive at the signal wavelength. The demands placed on the MV for LEO would also be significantly less compared to the wind-buffed drone, meaning the control loop could operate at a slower rate and allow for longer integration time of the fainter beacon.

An increase in receiver aperture diameter is needed for more collecting power of the downlink signal, and an increase in transmitter aperture is needed to reduce beam divergence and geometric losses over the link distance to LEO. Aperture sizes of a few tens of centimeters are sufficient for ground-to-LEO links<sup>25,27,28</sup>. If the ratio of aperture size to Fried Parameter  $D/r_0$  is greater than one, either due to large aperture or strong turbulence, higher order correction beyond tip/tilt is required to efficiently couple into SMF. This can be accomplished with traditional AO<sup>15,29</sup>, or with novel “passive” methods such as photonic lanterns<sup>30</sup> or multi-plane light conversion<sup>31</sup>. In combination with atmospheric phase-stabilisation technology<sup>32–34</sup>, such a deployable optical terminal could even facilitate secure ground-to-LEO continuous variable quantum key distribution (CV-QKD)<sup>35</sup>.

### Conclusion

We have demonstrated a robust, high speed coherent free-space optical communications link between a deployable optical terminal and drone moving at LEO-like angular velocities. Combining MV optical tracking and large actuation range tip/tilt AO, we maintained transmitted beam pointing and retroreflected beam angle-of-arrival in the presence of atmospheric turbulence and macroscopic motion to sustain the 100 Gbps link. Single mode fiber coupling is requisite for high capacity coherent communications, and ground stations with capabilities such as described here will relieve the data bottleneck between earth and LEO and provide ubiquitous internet-like speeds to space.

### Data availability

The datasets used and/or analysed during the current study available from the corresponding author on reasonable request.

Received: 11 August 2022; Accepted: 7 October 2022

Published online: 31 October 2022

### References

- Winzer, P. J., Neilson, D. T. & Chraplyvy, A. R. Fiber-optic transmission and networking: The previous 20 and the next 20 years. *Opt. Express* **26**, 24190–24239. <https://doi.org/10.1364/OE.26.024190> (2018).
- Kaymak, Y. et al. A survey on acquisition, tracking, and pointing mechanisms for mobile free-space optical communications. *IEEE Commun. Surv. Tutor.* **20**, 1104–1123. <https://doi.org/10.1109/COMST.2018.2804323> (2018).
- Strohbehm, J. Laser beam propagation in the atmosphere. *Laser Beam Propag. Atmos.* **20**, 20 (1978).
- Zhu, X. & Kahn, J. Free-space optical communication through atmospheric turbulence channels. *IEEE Trans. Commun.* **50**, 1293–1300. <https://doi.org/10.1109/TCOMM.2002.800829> (2002).
- Belmonte, A. & Kahn, J. M. Capacity of coherent free-space optical links using atmospheric compensation techniques. *Opt. Express* **17**, 2763–2773. <https://doi.org/10.1364/OE.17.002763> (2009).
- Ip, E., Lau, A. P. T., Barros, D. J. F. & Kahn, J. M. Coherent detection in optical fiber systems. *Opt. Express* **16**, 753–791. <https://doi.org/10.1364/OE.16.000753> (2008).
- Toyoshima, M. Trends in satellite communications and the role of optical free-space communications. *J. Opt. Netw.* **4**, 300–311. <https://doi.org/10.1364/JON.4.000300> (2005).
- Soukup, M. et al. Hyperscout: Onboard processing of hyperspectral imaging data on a nanosatellite (2016).
- Peral, E. et al. The radar-in-a-cubesat (raincube) and measurement results. In *IGARSS 2018—2018 IEEE International Geoscience and Remote Sensing Symposium*, 6297–6300. <https://doi.org/10.1109/IGARSS.2018.8519194> (2018).
- Schieler, C. et al. NASA's terabyte infrared delivery (tbird) program: Large-volume data transfer from leo (2019).
- Seel, S. et al. Space to ground bidirectional optical communication link at 5.6 gbps and edrs connectivity outlook. In *2011 Aerospace Conference*, 1–7. <https://doi.org/10.1109/AERO.2011.5747331> (2011).
- Chen, W. et al. 5.12gbps optical communication link between leo satellite and ground station. In *2017 IEEE International Conference on Space Optical Systems and Applications (ICSOS)*, 260–263. <https://doi.org/10.1109/ICSOS.2017.8357402> (2017).
- Saito, Y. et al. Research and development of a transportable optical ground station in nict: The results of the first performance test. *Front. Phys.* **9**, 20. <https://doi.org/10.3389/fphy.2021.636696> (2021).
- Fischer, E. et al. Esa optical ground station upgrade with adaptive optics for high data rate satellite-to-ground links-test results. In *2019 IEEE International Conference on Space Optical Systems and Applications (ICSOS)*, 1–6. <https://doi.org/10.1109/ICSOS45490.2019.8978974> (2019).
- Chen, C. et al. Demonstration of a bidirectional coherent air-to-ground optical link. In *Free-Space Laser Communication and Atmospheric Propagation XXX* Vol. 10524 (eds Hemmati, H. & Boroson, D. M.) 120–134 (International Society for Optics and Photonics SPIE, 2018). <https://doi.org/10.1117/12.2292848>.
- Li, L. et al. High-capacity free-space optical communications between a ground transmitter and a ground receiver via a uav using multiplexing of multiple orbital-angular-momentum beams. *Sci. Rep.* **7**, 17427–12 (2017).
- Li, L. et al. Mitigation for turbulence effects in a 40-gbit/s orbital-angular-momentum-multiplexed free-space optical link between a ground station and a retro-reflecting uav using mimo equalization. *Opt. Lett.* **44**, 5181–5184. <https://doi.org/10.1364/OL.44.005181> (2019).
- Parca, G., Shahpari, A., Carrozzo, V., Beileffi, G. M. T. & Teixeira, A. L. J. Optical wireless transmission at 1.6-Tbit/s (16 × 100 Gbit/s) for next-generation convergent urban infrastructures. *Opt. Eng.* **52**, 116102. <https://doi.org/10.1117/1.OE.52.11.116102> (2013).
- Feng, X. et al. 120 gbit/s high-speed wdm-qpsk free-space optical transmission through 1 km atmospheric channel. *Electron. Lett.* **54**, 1082–1084. <https://doi.org/10.1049/el.2018.5450> (2018).
- Dochhan, A. et al. 13.16 tbit/s free-space optical transmission over 10.45 km for geostationary satellite feeder-links. In *Photonic Networks; 20th ITG-Symposium*, 1–3 (2019).
- Trinh, P. V. et al. Experimental channel statistics of drone-to-ground retro-reflected fso links with fine-tracking systems. *IEEE Access* **9**, 137148–137164. <https://doi.org/10.1109/ACCESS.2021.3117266> (2021).
- Walsh, S. et al. Angle-of-arrival variability of retroreflected lasers despite atmospheric reciprocity. *Opt. Lett.* **47**, 1920–1923. <https://doi.org/10.1364/OL.453869> (2022).
- Shapiro, J. H. Reciprocity of the turbulent atmosphere\*. *J. Opt. Soc. Am.* **61**, 492–495. <https://doi.org/10.1364/JOSA.61.000492> (1971).
- Walsh, S. et al. The western australian optical ground station. In *IET Conference Proceedings*, 71–78(7) (2022).

### C.3. DEMONSTRATION OF 100 GBPS COHERENT FREE-SPACE OPTICAL COMMUNICATIONS AT LEO TRACKING RATES

www.nature.com/scientificreports/

25. Pettersson, G. M., Perdignes, J. & Sodnik, Z. Unmodified portable telescope for space-to-ground optical links. In *2019 IEEE International Conference on Space Optical Systems and Applications (ICSOS)*, 1–7. <https://doi.org/10.1109/ICSOS45490.2019.8978992> (2019).
26. CFP MSA Management Interface Specification (2017).
27. Fuchs, C. *et al.* Dlr's transportable optical ground station. In *Advanced Solid-State Lasers Congress, LTu1B.3* (Optica Publishing Group, 2013). <https://doi.org/10.1364/LSC.2013.LTu1B.3>.
28. Saito, Y. *et al.* Research and development of a transportable optical ground station in nict: The results of the first performance test. *Front. Phys.* **9**, 25 (2021).
29. Wang, Y. *et al.* Performance analysis of an adaptive optics system for free-space optics communication through atmospheric turbulence. *Sci. Rep.* **8**, 1124–11 (2018).
30. Leon-Saval, S. G., Argyros, A. & Bland-Hawthorn, J. Photonic lanterns. *Nanophotonics (Berlin, Germany)* **2**, 429–440 (2013).
31. Calvo, R. M. *et al.* Alternative passive fiber coupling system based on multi-plane light conversion for satellite-to-ground communications. In *Free-Space Laser Communications XXXII* Vol. 11272 (eds Hemmati, H. & Boroson, D. M.) 167–178 (International Society for Optics and Photonics (SPIE), 2020).
32. Dix-Matthews, B. P., Gozzard, D. R., Karpathakis, S. F. E., Gravestock, C. T. & Schediwy, S. W. Ultra-wideband free-space optical phase stabilization. *IEEE Commun. Lett.* **25**, 1610–1614 (2021).
33. Dix-Matthews, B. P. *et al.* Point-to-point stabilized optical frequency transfer with active optics. *Nat. Commun.* **12**, 515–515 (2021).
34. Gozzard, D. R. *et al.* Ultrastable free-space laser links for a global network of optical atomic clocks. *Phys. Rev. Lett.* **128**, 020801. <https://doi.org/10.1103/PhysRevLett.128.020801> (2022).
35. Wang, S., Huang, P., Wang, T. & Zeng, G. Atmospheric effects on continuous-variable quantum key distribution. *New J. Phys.* **20**, 083037. <https://doi.org/10.1088/1367-2630/aad9c4> (2018).

#### Acknowledgements

The authors wish to acknowledge their SmartSat CRC research partners at Goonhilly Earth Station Ltd., The University of South Australia, the Defence Science and Technology Group, Thales Australia, and Thales Alenia Space. S.K. is supported by SmartSat CRC Scholarship. D.G. is supported by a Forrest Research Foundation Fellowship. A.M. is supported by a Defence Science Centre Higher Degree Student Grant. This work was funded by SmartSat Cooperative Research Centre (1-01, 1-18) and the Australian Space Agency (MTMDFG000001).

#### Author contributions

S.W. and S.K. wrote the manuscript with input from all authors. S.W. and A.M. developed the machine vision and mount control, S.K. provided and analyzed communications data, B.D., A.F., and D.G. designed and assembled optics, D.G. piloted the drone, C.G. provided engineering support, S.S. conceived the experiment. All authors reviewed the manuscript.

#### Competing interests

The authors declare no competing interests.

#### Additional information

**Correspondence** and requests for materials should be addressed to S.M.W.

**Reprints and permissions information** is available at [www.nature.com/reprints](http://www.nature.com/reprints).

**Publisher's note** Springer Nature remains neutral with regard to jurisdictional claims in published maps and institutional affiliations.



**Open Access** This article is licensed under a Creative Commons Attribution 4.0 International License, which permits use, sharing, adaptation, distribution and reproduction in any medium or format, as long as you give appropriate credit to the original author(s) and the source, provide a link to the Creative Commons licence, and indicate if changes were made. The images or other third party material in this article are included in the article's Creative Commons licence, unless indicated otherwise in a credit line to the material. If material is not included in the article's Creative Commons licence and your intended use is not permitted by statutory regulation or exceeds the permitted use, you will need to obtain permission directly from the copyright holder. To view a copy of this licence, visit <http://creativecommons.org/licenses/by/4.0/>.

© The Author(s) 2022



Technical Note

## Ground-to-Drone Optical Pulse Position Modulation Demonstration as a Testbed for Lunar Communications

Skevos F. E. Karpathakis <sup>1,2,\*</sup> , Benjamin P. Dix-Matthews <sup>1,2</sup> , Shane M. Walsh <sup>1,2</sup> , Ayden S. McCann <sup>1,2</sup>, David R. Gozzard <sup>1,2</sup>, Alex M. Frost <sup>1,2</sup>, Charles T. Gravestock <sup>1,2</sup> and Sascha W. Schediwy <sup>1,2</sup>

<sup>1</sup> International Centre for Radio Astronomy Research, The University of Western Australia, Crawley, WA 6009, Australia

<sup>2</sup> International Space Centre, The University of Western Australia, Crawley, WA 6009, Australia

\* Correspondence: skevos.karpathakis@uwa.edu.au

**Abstract:** Free-space optical (FSO) communication promises to bring fibre-like speeds to data transmissions between ground, sky and space. This is becoming more important in light of the increasing volume of data collected by aircraft and spacecraft. The University of Western Australia (UWA) is commissioning optical ground stations to support FSO communications payloads. We propose retroreflected laser links to drones as a useful step towards further ground-to-sky and ground-to-space FSO communications demonstrations. In this paper, we describe the operation of a hardware testbed for a high photon efficiency optical communication physical layer. This testbed was deployed over a slanted free space link to a drone to verify sub-systems required in communication between the ground station and a spacecraft in cis-Lunar space. Accomplishing this verification of the telescope pointing systems and communications systems would have otherwise been much harder or impossible without using a retroreflected drone link.

**Keywords:** applications of drones; free-space optical communication; pulse position modulation



Citation: Karpathakis, S.F.E.;

Dix-Matthews, B.P.; Walsh, S.M.;

McCann, A.S.; Gozzard, D.R.; Frost,

A.M.; Gravestock, C.T.; Schediwy,

S.W. Ground-to-Drone Optical Pulse

Position Modulation Demonstration

as a Testbed for Lunar

Communications. *Drones* **2023**, *7*, 99.

[https://doi.org/10.3390/](https://doi.org/10.3390/drones7020099)

[drones7020099](https://doi.org/10.3390/drones7020099)

Academic Editor: Mostafa Hassanalian

Received: 28 November 2022

Revised: 20 January 2023

Accepted: 27 January 2023

Published: 31 January 2023



**Copyright:** © 2023 by the authors.

Licensee MDPI, Basel, Switzerland.

This article is an open access article

distributed under the terms and

conditions of the Creative Commons

Attribution (CC BY) license ([https://creativecommons.org/licenses/by/](https://creativecommons.org/licenses/by/4.0/)

[https://creativecommons.org/licenses/by/](https://creativecommons.org/licenses/by/4.0/)

4.0/).

### 1. Introduction

From the Apollo era to today, deep space communication is conducted using radio-frequencies (RF), with the Deep Space Network currently able to provide speeds up to 150 Mb/s using the Ka band [1]. However, RF bandwidth presents a bottleneck to expanding deep-space communication capability. Free-space optical (FSO) communication between space and ground will enable the return of larger science data payloads, larger telemetry payloads, and streaming high-definition video to Earth. Pioneering experiments in FSO communication include NICT's 1994 space-to-ground laser downlink [2] and several space-to-space laser links in the 2000s [3–5]. In the 2013 Lunar Laser Communication Demonstration Mission, NASA demonstrated Moon-to-Earth optical communication at downlink speeds up to 622 Mb/s, using the Lunar Laser Space Transmitter (LLST) [6]. In the Artemis II Mission [7], a crew of NASA astronauts will orbit the Moon in the Orion spacecraft. This will be the first crewed Lunar orbit since Apollo 17, over 50 years ago. The Orion Artemis II Optical Communications Terminal (O2O) is the successor to the experimental LLST and will initially support space-to-ground downlink at speeds from 80 to 260 Mb/s and ground-to-space uplink at 20 Mb/s [8]. O2O will transmit information using the pulse-position modulation (PPM) format, standardised by the Consultative Committee for Space Data Systems (CCSDS) in the 141.0-B-1 Recommended Standard [9].

Earth's atmosphere remains a challenge to FSO communication because of the deleterious effects of atmospheric turbulence on optical propagation. Techniques for mitigating turbulence and correcting optical wavefronts, such as adaptive optics, have been successfully applied in optical astronomy for decades [10]. Therefore, organisations specialising in optical astronomy and space situational awareness are showing interest in establishing

optical ground station networks to support FSO communications, including several Australian institutions [11]. However, the limited accessibility of FSO communications-capable satellites in orbit remains a challenge for commissioning optical ground stations. Hardware testbeds in lieu of satellites and spacecraft are therefore useful for testing and verifying optical ground station systems and sub-systems.

Retroreflected laser links to drones are one such testbed and have been used by the frequency metrology community in preparation for tests of fundamental physics over satellite laser links [12,13]. For communications purposes, the channel statistics of retroreflected drone links have been analysed and tested for round-trip lengths up to 204 m [14]. A retroreflected communications link was demonstrated using orbital-angular momentum multiplexed light at 40 Gb/s over a round-trip distance of 100 m [15]. Extensions to this method are possible. For example, due to drone mobility, a drone may also be slewed, requiring the ground station to slew at equivalent angular rates to a low-Earth orbit satellite, therefore simulating low-Earth orbit satellite tracking [16]. However, in the context of Lunar and deep-space communication, a stationary, hovering drone is more analogous to communication with FSO payloads in cis-Lunar space, deep space or geosynchronous orbit. Furthermore, FSO communication demonstrations with stationary, long-distance drone platforms are also of interest to terrestrial network designers, as drones have been proposed as highly mobile nodes for FSO communication feeders in re-configurable networks for disaster recovery and urban centres [17,18]. Numerical studies of drone-to-ground communication have also been conducted [19]. True drone-to-ground communication for space simulation or terrestrial communication remains difficult to accomplish due to size, weight and power requirements. One drone-to-ground demonstration was conducted with a drone-borne active optical payload linked and powered with a tether to conduct loopback measurements over the aerial link [20]. However, the provision of a tether limits the drone's mobility and altitude, while also introducing vibrational modes associated with tension in the tether. However, advances in retroreflected links have led to achievements in drone-to-ground communications. In one case a 560 m, 500 Mb/s drone-to-ground link was demonstrated by using a modulating retroreflector [21].

In this paper, we present a 1.3 km round-trip retroreflected drone link, using a hardware transceiver based on CCSDS 141.0-B-1. Using a drone in this scenario is presented as a highly accessible, high-uptime testbed for FSO communications and flight operations. PPM symbols were transmitted and received over a 1.3 km folded link formed between an optical terminal and an optical payload, including a corner-cube retroreflector (CCR), mounted to a multi-rotor drone. Angle-of-arrival variations are exhibited by CCR-folded links despite atmospheric reciprocity [22], so the optical terminal must simultaneously demonstrate correction of the 'downlink' beam angle while pre-compensating for the 'uplink' beam pointing. The 4-PPM symbols with 8 ns slot widths were transmitted, received and demodulated for a line rate of 50 Mb/s, using commercial-off-the-shelf (COTS) components.

### 2. Materials and Methods

Figure 1 shows a photograph of the optical terminal in panel (a), alongside a photograph of the drone and drone-borne optical payload, in panel (b). Figure 2 shows a detailed schematic of the optical systems. As the link segment is a folded FSO range, the transmitter and receiver hardware are conveniently located in the same cabinet and are isolated in fibre with an optical circulator.

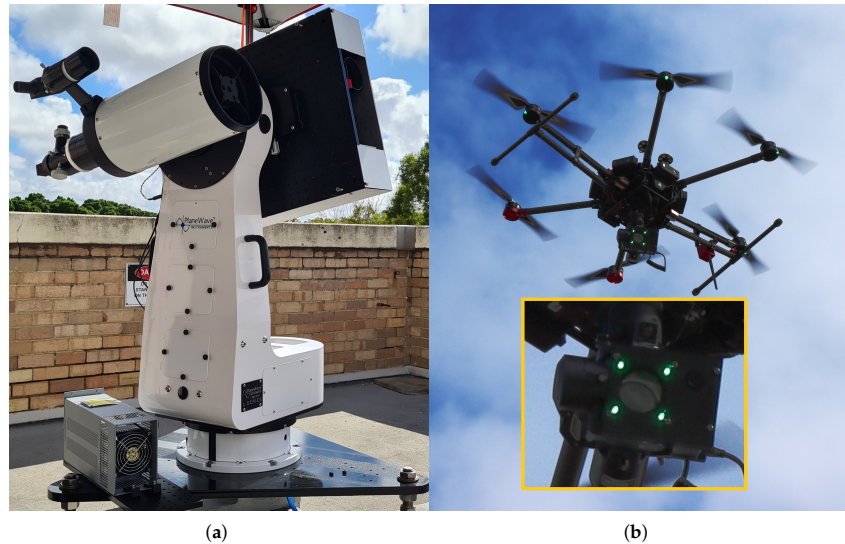


**Figure 1.** (a) Optical terminal. The upper-right box contains the free-space optics and machine vision system. The lower-left box is a tip-tilt mirror high voltage stage. The upper-left telescope is from an unrelated system. (b) Drone carrying the optical payload. Inset: close-up of the optical payload, consisting of LED array, pilot camera and corner-cube retroreflector.

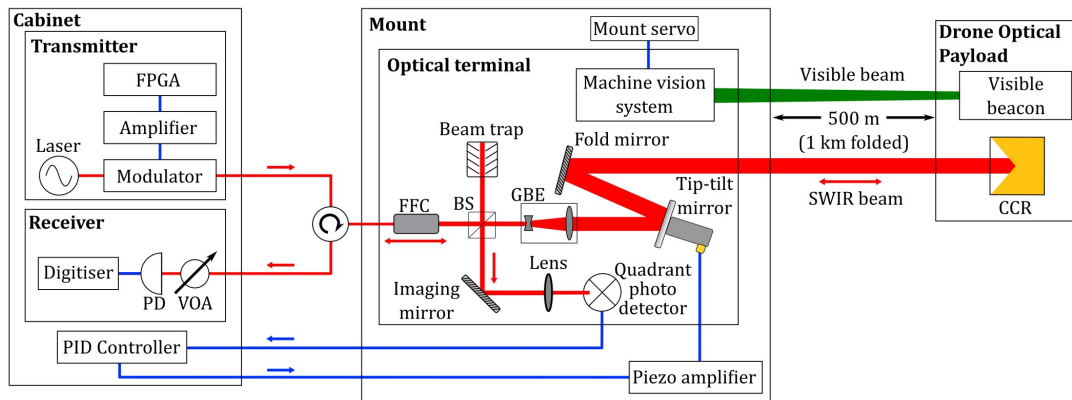


**Figure 2.** Schematic of the free-space optical pulse-position modulation demonstration. CCR: corner-cube retroreflector; FFC: fibre-to-free-space collimator; FPGA: field programmable gate array; GBE: Galilean beam expander; PD: photodetector; PID: proportional, integral, derivative; SWIR: short-wave infrared; VOA: variable optical attenuator.

2.1. Optical Systems

The optical terminal is a precursor to a field-deployable mobile optical ground station. Coarse pointing with the terminal mount (L-350, Planewave Instruments, Adrian, MI, USA) is achieved with a machine vision (MV) system, comprising a visible-light camera, lens and single board computer, used to image the drone and payload. The drone-borne optical payload includes a square array of visible wavelength (green) beacon LEDs, arranged uniformly around the centre of the CCR. This beacon-camera arrangement feeds back to the MV system to automatically servo the mount when engaged, keeping the beam within

## C.4. GROUND-TO-DRONE OPTICAL PULSE POSITION MODULATION DEMONSTRATION AS A TESTBED FOR LUNAR COMMUNICATIONS

the field of view of the optical terminal's laser path. The field-of-view of the machine vision system is  $17.5 \times 13.1$  mrad, with an angular resolution of  $9 \mu\text{rad}$ .

The optical terminal also houses the FSO components for directing the laser beam. Optical signals from the transmitter are fed to the terminal using fibre. At the fibre-to-free-space collimator (FFC), the signal is launched into free space. This beam passes through a 50:50 beam splitter to a Galilean beam expander with a clear aperture of 43.5 mm. The beam splitter is required to image the returning beam, so half of the outgoing power must be directed to a beam trap and is lost. The outgoing beam is then steered by the tip-tilt (TT) mirror and stationary fold mirror, out of the terminal. The incoming retroreflected beam follows the same path, but this time half of the power is coupled into the fibre via the FFC, and then to the optical receiver. At the link distance, no clipping due to beam divergence is caused by the aperture of the CCR or the Galilean beam expander. Half of the incoming beam is directed by the beam splitter to the imaging arm.

In the terminal's imaging arm, a lens focuses the incoming beam onto a 3 mm quadrant photodetector (QPD) with a field-of-view of  $2.9 \times 2.9$  mrad. Two position signals from the QPD are used to estimate angle-of-arrival variations and are input into a proportional, integral, derivative (PID) controller (one for each of the pitch and yaw mirror axes) and output to the TT mirror piezo actuators. The mirror has an actuation range of 4 mrad, covering the QPD field of view. Co-alignment between the QPD and FFC means the TT mirror provides high-frequency, narrow field-of-view pointing for fibre coupling.

Finally, the drone-borne optical payload also carries a camera to assist the drone pilot in pointing the payload towards the optical terminal. The optical payload chassis is a 3D-printed enclosure and mounts to the COTS gimbal controlled using the drone's native software and controller.

### 2.2. Transmitter and Receiver Hardware

A PPM transmitter and receiver are implemented to demonstrate the capability of the system as a testbed for Lunar FSO communications systems. A field-programmable gate array (FPGA) development board (STEMlab 125-14, Red Pitaya, Solkan, Slovenia) generates a pseudo-random binary sequence (PRBS), mapped to a 4- or 16-order PPM waveform output. A high-slew-rate amplifier (THS3491, Texas Instruments, Dallas, TX USA) matches the digital pin on the development board to the modulation port of a high-extinction-ratio optical amplitude modulator (MXER-LN-10, ixblue, Saint-Germain en Laye, France). A fibre-coupled seed laser (Koheras BASIK X15, NKT Photonics, Birkerød, Denmark) in the 1550 nm optical C-band is used, as it conveniently has polarisation-maintaining output fibre, avoiding polarisation-dependent losses in the modulator due to birefringence.

The transmitter PPM waveforms were measured over a 2 km fibre link in a lab environment to determine the minimum possible slot width due to bandwidth limitations of components. At 16 ns and 8 ns slot widths, the transmitted pulses exhibit well-defined edges shorter than 1 ns. At 8 ns width, the raw bitrates with 4- and 16-PPM mappings (and guard slots) are 50 Mb/s and 25 Mb/s, respectively. PPM symbols with 4 ns slot widths were tested but appeared distorted, most likely by the electrical transmission properties of the physical interconnect between the FPGA pin and the driver amplifier, limiting the achievable slot clock speed and, therefore, data rate. For the demonstration, the PRBS was framed into 15120 bit codewords, using the 4-PPM format with an 8 ns slot width. A faster slot clock could be achieved with a purpose-built electro-optical interface, to achieve the O2O-specified 260 Mb/s.

The receiver hardware comprises a single-mode fibre (SMF)-coupled InGaAs photodetector (Menlo Systems FPD510-FC-NIR, typical to the coherent detection systems more often used by the group) and digitiser (ATS9360, AlazarTech, Pointe-Claire, Canada), with sufficient bandwidth to observe the PPM waveforms. An SMF-coupled detector was used as it was available, but a multi-mode fibre-coupled or free-space detector would be better suited, as PPM communication is not mode-selective. Slot and symbol synchronisation and demodulation are conducted offline in MATLAB. The incoming PRBS is used to mea-

sure the bit-error rate (BER) of a sequence of PPM symbols, provided the first eight PPM symbols in a record are received without error. As the incoming light is coupled to SMF, the PPM signal experiences fading from angle-of-arrival variations caused by turbulence, wind-buffeting of the drone, and mechanical vibrations of the optical payload. A variable optical attenuator was also added ahead of the photodetector to manually control the link margin.

### 2.3. Receiver Software

The offline receiver achieves slot synchronisation for a codeword by edge detection, for an initial estimation of slot boundaries in the record of photodetector output voltage samples. Symbol synchronisation is then achieved by overlaying and summing a number of un-synchronised symbols and identifying the guard slot as the slot with the lowest cumulative sum. Maximum-likelihood demodulation of each symbol is implemented by summing the voltage values in each slot location and selecting the slot with the largest value. If the signal is lost at the beginning of a codeword, synchronisation fails and the codeword is discarded. However, if the signal is lost after a codeword is synchronised, the demodulator has an equal likelihood four-way decision on the pulse slot location for a given symbol.

### 2.4. Receiver Performance

For 4-PPM with a typical maximum-likelihood detector [23], errors arising from signal fade will lead to a BER,

$$BER = Q(\sqrt{SNR}), \quad (1)$$

where  $Q(x)$  is the  $Q$ -function and  $SNR$  is the signal-to-noise ratio. Analytical models for PPM error rates in terms of photodetector physics are complex to derive. In order to compare the demonstration data with this threshold, a simple model for  $SNR$  as a function of photodetector output voltage was developed for this demonstration. Three parameters are observed in the photodetector output voltage,  $v_d$ ,

$$v_d = v_s + v_o + v_n. \quad (2)$$

The photodetector voltage,  $v_d$  comprises the slot amplitude,  $v_s$ , an offset voltage,  $v_o$ , and additive white noise fluctuations,  $v_n$ , with zero-mean and variance  $\sigma_n^2$ . The optical signal itself is assumed to be otherwise noiseless because of the high extinction ratio of the modulator. Therefore, the  $SNR$  for each readout is

$$SNR = \frac{\langle v_s^2 \rangle - \langle v_o^2 \rangle}{\sigma_n^2}, \quad (3)$$

where  $\langle v^2 \rangle$  is the mean squared value of the voltage corresponding to  $v_s$  or  $v_o$  sampled over the entire codeword.

### 2.5. Demonstration Operations

The optical terminal, transmitter and receiver were located on the roof of the Department of Physics building at The University of Western Australia at an altitude of 32 m above sea level. The drone hovered at an altitude of 120 m (the maximum allowed by local regulations, without exemptions), with a 650 m slant distance from the terminal site, completing the 1.3 km slanted folded link. While the drone was hovering, the pilot would use the optical payload camera to coarsely align the CCR with the optical terminal. At the optical terminal side, the drone was pulled into the MV system's field of view by slewing the mount while viewing the MV camera feed. Upon entering the field-of-view of the machine vision system, the tracking system could be engaged, automatically moving the mount to locate the CCR within the field-of-view of the QPD. The TT system then dynamically corrected pointing errors. Operating concurrently, the two pointing and tracking

## C.4. GROUND-TO-DRONE OPTICAL PULSE POSITION MODULATION DEMONSTRATION AS A TESTBED FOR LUNAR COMMUNICATIONS

systems effectively maintained fibre coupling while the drone hovered in place. If the TT system was disengaged by disconnecting the PID controllers, the MV system was not able to couple the laser light back into the SMF on its own, due to the beam size, link distance and wind buffeting of the drone.

### 3. Results

Results are presented for a drone flight conducted during the day on 18 March 2022, at 2:30 p.m. The wind speed recorded at the local weather station, Perth Airport, was  $\approx 16.7$  km/h [24].

The link budget for the testbed is presented in Table 1. The optical sensitivity floor for the photodetector was determined to be  $-33$  dBm, corresponding to a mean output voltage of 1.4 mV. During measurements, the variable optical attenuator was adjusted such that the received power, after pointing losses, was near the threshold for error-free reception. Error-free reception occurred when the output voltage exceeded 2.9 mV, corresponding to an optical pulse power of  $-30.3$  dBm. Typically, less than one-third of the codewords were received without error, as the optical power received remained consistently above the  $-30$  dBm error-free threshold due to angle-of-arrival correction by the TT mirror. At this link distance, the beam size is smaller than the Fried parameter and, therefore, scintillation due to turbulence was not expected to cause any fading in excess of the angle-of-arrival errors caused by drone movement and beam wander.

**Table 1.** Link budget for retroreflected laser link to drone.

Parameter	Value
Transmit power	13.0 dBm
Modulator insertion loss	$-3.50$ dB
Circulator losses	$-2.40$ dB
Splitter loss (2 way)	$-6.00$ dB
Singlemode fibre coupling penalty	$-10.0$ dB
Receive power (error free)	$-30.3$ dBm
Combined pointing and variable attenuator loss	22.6 dB
Mean photodetector sensitivity	$-33.0$ dBm
Error-free link margin	2.70 dB

To confirm receiver functionality, BER was compared to Equation (1) using observations for SNR per Equation (3). The portion of transmissions received with bit errors, caused by partial or complete signal fading arising due to pointing errors, allow the receiver performance to be characterised. Figure 3 shows the SNR as derived from Equation (3) and BER for 720 codeword transmissions, with each data point representing a single 15,120-bit codeword. This record has a BER measurement sensitivity floor of  $1/15,120$  errors per bit, and a ceiling at  $1/2$  errors per bit, caused by failure to demodulate, though pulses were present. For comparison, the theoretical BER, from Equation (1), is plotted alongside the data as a black line in Figure 3.

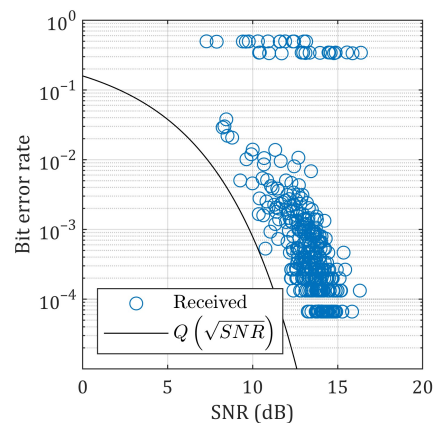


Figure 3. Bit-error rate versus signal-to-noise ratio (SNR) of 720 received 15120 bit 4-PPM codewords.

#### 4. Discussion and Conclusions

This demonstration involving a drone-borne CCR provided a useful return on experience towards FSO communications developments, including potential communication with O2O on a full-sized optical ground station. This was particularly true in the domain of flight operations, not otherwise accessible without enlisting the services of professional small aircraft operators, or operators of commercial high-altitude pseudo satellites or the few FSO communication-capable satellites in orbit. The drone link demonstration required the coordination of equipment and planning of methods within the research group and was subject to scheduling with the aviation authority and local government as well as uncontrollable go/no-go conditions such as wind warnings and rain. In effect, the availability of the drone provided a scaled-back simulation of space operations.

Interpreting Equation (3) implies the optical sensitivity floor represented by  $v_o$  is analogous to background counts in photon-counting receivers, and a comparison may be drawn between the drone link and LLCD results [25]. Downlink results from [25] reported error-free communication at 38.55 Mb/s with a link margin of 13.5 dB between signal and background photon counts. Per Table 1, the error-free link margin for the demonstration was 2.70 dB. While it is not possible for this testbed to recreate the transmission powers and link losses of a Lunar-to-ground link, the receiver may be similarly tested with the link margin at the limit of its sensitivity. This scales with detector technology, so a photon-counting detector with a lower sensitivity floor may be integrated into a future iteration of the testbed, and the receive power adjusted to recreate the link margin conditions.

Figure 3 shows a main cluster of BER versus SNR results following the theoretical relationship, confirming the expected performance of the receiver. However, the demodulation algorithm implemented often failed to completely demodulate a codeword if too many early symbols were faded, or if the slot or symbols synchronisation had failed, causing ‘synchronised’ pulses to fall across slot boundaries. These cases account for the outlying clusters at the top of the graph, stratified around BERs of 0.5 and 0.33, and indicate further margin for improvement of the offline receiver algorithm before investing engineering time into a real-time receiver.

The 1.3 km retroreflected drone link presented can be extended with materials and methods previously demonstrated over shorter retroreflected links such as verification of atmospheric channel modelling [14]; demonstration of other communication formats [15]; or demonstrations of modulating retroreflectors [21]. Further extensions previously demonstrated include links to tethered drones, carrying active optical payloads [20], or drones moving in paths tangential to the ground station, thus requiring the ground station to track at angular rates equivalent to satellite tracking [16]. Furthermore, results from FSO

## C.4. GROUND-TO-DRONE OPTICAL PULSE POSITION MODULATION DEMONSTRATION AS A TESTBED FOR LUNAR COMMUNICATIONS

communication demonstrations with stationary drones will be of interest to designers and analysts planning future terrestrial and disaster-response networks [17,18].

The drone provided a testbed to perform technical verification of the prototype communications equipment, intended for a future Lunar FSO communication link, over a real, time-varying channel. This also tests the mechanical robustness of the optical assembly and pointing systems. The effectiveness of the testbed is limited by dissimilarities to O2O in terms of modulation format and detector technology, as well as the relative differences in aperture sizes and optical power levels involved (intrinsically linked to detector technology and link distance). However, some of these limitations can be addressed with changes to the optics and launching the drone from a different location. Furthermore, without undertaking more fundamental demonstrations of capability, costly engineering upgrades to make the communications system more closely resemble O2O, such as the integration of photon-counting detectors, are risks and may not be supported by prudent systems engineering processes. The drone testbed will allow us to continue rapidly integrating and testing subsystems as work progresses to a more complete emulation of a cis-Lunar communication system. Therefore, this paper supports the case for retroreflected drone links as useful testbeds for developing FSO communication capabilities while access to FSO communications payloads in orbits remains limited.

**Author Contributions:** S.F.E.K. wrote the manuscript with input from all authors; S.M.W. and A.S.M. developed the machine vision and mount control; S.F.E.K. provided and analysed the data communications signals; B.P.D.-M., A.M.F. and D.R.G. designed and assembled the optics; D.R.G. piloted the drone; C.T.G. provided engineering support; experiment conceived by S.W.S. All authors have read and agreed to the published version of the manuscript.

**Funding:** This research was supported by the Australian Space Agency (Moon to Mars Demonstrator Feasibility Grant MTMDFG000001) and the SmartSat Cooperative Research Centre (CRC Research Project 1-18).

**Data Availability Statement:** The data presented in this study are available on request from the corresponding author.

**Acknowledgments:** The authors wish to thank their SmartSat CRC research partners at the Defence Science and Technology Group, Goonhilly Earth Station Ltd., Thales Australia, Thales Alenia Space and The University of South Australia. S. Karpathakis is supported by a SmartSat CRC PhD Scholarship and a research award from The Andy Thomas Space Foundation and EOS Space Systems. D. Gozzard is supported by a Forrest Research Foundation Fellowship. A. McCann is supported by a Defence Science Centre Research Higher Degree Student Grant.

**Conflicts of Interest:** The authors declare no conflict of interest.

### References

1. DSN Telecommunications Link Design Handbook. Available online: <https://deepspace.jpl.nasa.gov/dsndocs/810-005/208/208B.pdf> (accessed on 25 February 2022).
2. Arimoto, Y.; Toyoshima, M.; Toyoda, M.; Takahashi, T.; Shikatani, M.; Araki, K. Preliminary Result on Laser Communication Experiment Using Engineering Test Satellite-VI (ETS-VI). In Proceedings of the Free-Space Laser Communication Technologies VII, San Jose, CA, USA, 1–28 February 1995; Volume 2381, pp. 151–158.
3. Laurent, B.; Planche, G.; Michel, C. Inter-Satellite Optical Communications: From SILEX to Next Generation Systems. In Proceedings of the European Space Agency International Conference on Space Optics, ESA SP, Toulouse, France, 30 March–2 April 2004; pp. 395–402.
4. Jono, T.; Takayama, Y.; Shiratama, K.; Mase, I.; Demellenne, B.; Sodnik, Z.; Bird, A.; Toyoshima, M.; Kunimori, H.; Giggenbach, D.; et al. Overview of the Inter-Orbit and the Orbit-to-Ground Laser Communication Demonstration by OICETS. In Proceedings of the Free-Space Laser Communication Technologies XIX and Atmospheric Propagation of Electromagnetic Waves, San Jose, CA, USA, 20–25 January 2007; Volume 6457; pp. 9–18.
5. Fields, R.; Lunde, C.; Wong, R.; Wicker, J.; Kozlowski, D.; Jordan, J.; Hansen, B.; Muehlhnickel, G.; Scheel, W.; Sterr, U.; et al. NFIRE-to-TerraSAR-X Laser Communication Results: Satellite Pointing, Disturbances, and other Attributes Consistent with Successful Performance. In Proceedings of the Sensors and Systems for Space Applications III, Orlando, FL, USA, 13–17 April 2009; Volume 7330, pp. 211–225.

6. Boroson, D.M.; Robinson, B.S. The Lunar Laser Communication Demonstration: NASA's First Step Toward Very High Data Rate Support of Science and Exploration Missions. *Space Sci. Rev.* **2014**, *185*, 115–128. [[CrossRef](#)]
7. Artemis Plan: NASA's Lunar Exploration Program Overview. Available online: [https://www.nasa.gov/sites/default/files/atoms/files/artemis\\_plan-20200921.pdf](https://www.nasa.gov/sites/default/files/atoms/files/artemis_plan-20200921.pdf) (accessed on 9 February 2022).
8. Geisler, D.J. Modem Module Development for NASA's Orion Spacecraft: Achieving FSO Communications over Lunar Distances. In Proceedings of the Optical Fiber Communication Conference, Optica Publishing Group, San Diego, CA, USA, 8–12 March 2020; pp. Th3J-1.
9. Optical Communications Physical Layer: Recommended Standard. 2019. Available online: <https://public.ccsds.org/Pubs/141x0b1.pdf> (accessed on 15 December 2021).
10. Andrews, L.C.; Phillips, R.L. *Laser Beam Propagation Through Random Media*, 2nd ed.; SPIE: Ann Arbor, MI, USA, 2005; ISBN 978-081-945-948-0.
11. Bennet, F.; Ferguson, K.; Grant, K.; Kruzins, E.; Rattenbury, N.; Schediwy, S. An Australia/New Zealand Optical Communications Ground Station Network for Next Generation Satellite Communications. In Proceedings of the Free-Space Laser Communications XXXII, San Francisco, CA, USA, 1–6 February 2020; Volume 11272, pp. 1–7.
12. Sinclair, L.C.; Bergeron, H.; Swann, W.C.; Khader, I.; Cossel, K.C.; Cermak, M.; Newbury, N.R.; Deschênes, J.D. Femtosecond Optical Two-Way Time-Frequency Transfer in the Presence of Motion. *Phys. Rev. A* **2019**, *99*, 023844. [[CrossRef](#)]
13. Bergeron, H.; Sinclair, L.C.; Swann, W.C.; Khader, I.; Cossel, K.C.; Cermak, M.; Deschênes, J.D.; Newbury, N.R. Femtosecond Time Synchronization of Optical Clocks Off of a Flying Quadcopter. *Nat. Commun.* **2019**, *10*, 1819. [[CrossRef](#)] [[PubMed](#)]
14. Trinh, P.V.; Carrasco-Casado, A.; Okura, T.; Tsuji, H.; Kolev, D.R.; Shiratama, K.; Munemasa, Y.; Toyoshima, M. Experimental Channel Statistics of Drone-to-Ground Retro-Reflected FSO Links With Fine-Tracking Systems. *IEEE Access* **2021**, *9*, 137148–137164. [[CrossRef](#)]
15. Li, L.; Zhang, R.; Zhao, Z.; Xie, G.; Liao, P.; Pang, K.; Song, H.; Liu, C.; Ren, Y.; Labroille, G.; et al. High-Capacity Free-Space Optical Communications Between a Ground Transmitter and a Ground Receiver via a UAV Using Multiplexing of Multiple Orbital-Angular-Momentum Beams. *Sci. Rep.* **2017**, *7*, 17427. [[CrossRef](#)] [[PubMed](#)]
16. Walsh, S.M.; Karpathakis, S.F.; McCann, A.S.; Dix-Matthews, B.P.; Frost, A.M.; Gozzard, D.R.; Gravestock, C.T.; Schediwy, S.W. Demonstration of 100 Gbps Coherent Free-Space Optical Communications at LEO Tracking Rates. *Sci. Rep.* **2022**, *12*, 18345. [[CrossRef](#)] [[PubMed](#)]
17. Esubonteng, P.K.; Rojas-Cessa, R. RESTORE: Low-Energy Drone-Assisted NLoS-FSO Emergency Communications. *IEEE Access* **2022**, *10*, 115282–115294. [[CrossRef](#)]
18. Janji, S.; Samorzewski, A.; Wasilewska, M.; Kliks, A. On the Placement and Sustainability of Drone FSO Backhaul Relays. *IEEE Wirel. Commun. Lett.* **2022**, *11*, 1723–1727. [[CrossRef](#)]
19. Trung, H.D. Performance of UAV-to-Ground FSO Communications with APD and Pointing Errors. *Appl. Syst. Innov.* **2021**, *4*, 65. [[CrossRef](#)]
20. Carrasco-Casado, A.; Shiratama, K.; Trinh, P.V.; Kolev, D.; Munemasa, Y.; Fuse, T.; Tsuji, H.; Toyoshima, M. Development of a Miniaturized Laser-Communication Terminal for Small Satellites. *Acta Astronaut.* **2022**, *197*, 1–5. [[CrossRef](#)]
21. Quintana, C.; Wang, Q.; Jakonis, D.; Oberg, O.; Erry, G.; Platt, D.; Thueux, Y.; Faulkner, G.; Chun, H.; Gomez, A.; et al. A High Speed Retro-Reflective Free Space Optics Links With UAV. *J. Light. Technol.* **2021**, *39*, 5699–5705. [[CrossRef](#)]
22. Walsh, S.; Frost, A.; Howard, L.; Gozzard, D.; Karpathakis, S.; Dix-Matthews, B.; Gravestock, C.; McCann, A.; Schediwy, S. Angle-of-Arrival Variability of Retroreflected Lasers Despite Atmospheric Reciprocity. *Opt. Lett.* **2022**, *47*, 1920–1923. [[CrossRef](#)]
23. Barry, J.R. *Wireless Infrared Communications*, 1st ed.; Springer: New York, NY, USA, 1994; ISBN 978-1-4615-2700-8.
24. Climate and Average Weather Year Round at Perth Airport. Available online: <https://weatherspark.com/y/149190/Average-Weather-at-Perth-Airport-Australia-Year-Round> (accessed on 11 January 2023).
25. Sodnik, Z.; Smit, H.; Sans, M.; Giggenbach, D.; Becker, P.; Mata Calvo, R.; Fuchs, C.; Zayer, I.; Lanucara, M.; Schulz, K.J.; et al. Results from a Lunar Laser Communication Experiment Between NASA's LADEE Satellite and ESA's Optical Ground Station. In Proceedings of the International Conference on Space Optical Systems and Applications, Kobe, Japan, 7–9 May 2014.

**Disclaimer/Publisher's Note:** The statements, opinions and data contained in all publications are solely those of the individual author(s) and contributor(s) and not of MDPI and/or the editor(s). MDPI and/or the editor(s) disclaim responsibility for any injury to people or property resulting from any ideas, methods, instructions or products referred to in the content.